REPORT DOCUMENTATION PAGE

Form Approved
OMB No. 0704-0188

1. AGENCY USE ONLY (*Leave blank*)

2. REPORT DATE 9/23/99

3. REPORT TYPE AND DATES COVERED Final 10/1/92 to 9/30/96

4. TITLE AND SUBTITLE

A SPATIAL MODEL OF EROSION AND SEDIMENTATION ON CONTINENTAL MARGINS

5. FUNDING NUMBERS

G- NOOO14-93-1-0126

6. AUTHOR(S)

Lincoln F. Pratson, Bernard J. Coakley and Michael S. Steckler

7. PERFORMING ORGANIZATION NAME(S) AND ADDRESS(ES)

The Trustees of Columbia University
351 Engineering Terrace
500 W. 120th Street
New York, New York 10027

8. PERFORMING ORGANIZATION REPORT NUMBER

5-21717

9. SPONSORING/MONITORING AGENCY NAME(S) AND ADDRESS(ES)

The Office of Naval Research
Code 322GG
800 N. Quincy Street
Arlington, VA 22217-5660

10. SPONSORING/MONITORING AGENCY REPORT NUMBER

11. SUPPLEMENTARY NOTES

The view, opinions and/or findings contained in this report are those of the author(s) and should not be construed as an official Department of the Army position, policy, or decision, unless so designated by other documentation.

12a. DISTRIBUTION/AVAILABILITY STATEMENT

Approved for public release; distribution unlimited.

12b. DISTRIBUTION CODE

13. ABSTRACT (*Maximum 200 words*)

This project devised techniques to aid in predicting where and how mass movements could occur on submarine slopes, and how they would modify the seafloor. As part of a team of scientists in the ONR-sponsored STRATAFORM program, we developed: (i) quantitative methods for assessing past and present slope stability; and (ii) computer models that simulate the causes and morphologic consequences of submarine slope failure as they occur over geologic time. A computer model that simulates the evolution of continental slope morphology under the interaction of sedimentation, slope failure, and sediment flow erosion has been constructed and validated. It simulates to first order how slope failures shape continental slope terrains. High-resolution bathymetric grids of five U.S. continental slopes have been constructed and analyzed. Continental slopes on passive margins are steeper than those on active margins at both regional and local length scales. Process, tectonic, and lithologic differences among the margins are identifiable in the ranges of local seafloor slopes. A coupled sedimentologic-hydrologic computer model has been developed which constrains in 1-D ranges of geologic conditions that may lead to slope failure by liquefaction, frictional sliding, and normal faulting as a consequence of transient fluid flow and the high pore pressures.

14. SUBJECT TERMS

Continental slope, submarine canyons, seafloor erosion, submarine geomorphology

15. NUMBER OF PAGES

16. PRICE CODE

17. SECURITY CLASSIFICATION OF REPORT	**18. SECURITY CLASSIFICATION**	**19. SECURITY CLASSIFICATION OF ABSTRACT**	**20. LIMITATION OF ABSTRACT**
UNCLASSIFIED	UNCLASSIFIED	UNCLASSIFIED	UL

Form Approved
OMB No 9000-0095
Expires July 31, 1995

REPORT OF INVENTIONS AND SUBCONTRACTS

(Pursuant to "Patent Rights" Contract Clause (See Instructions on Reverse Side)

Public reporting for this collection of information is estimated to average 1 hour per response, including the time for reviewing instructions, searching existing data sources, gathering and maintaining the data needed and completing and reviewing the collection of information. Send comments regarding this burden estimate or any other aspect of this collection of information, including suggestions for reducing this burden, to Washington Headquarters Services, Directorate for Information Operations and Reports, 1215 Jefferson Davis Highway, Suite 1204, Arlington, VA 22203-4302, and to the Office of Management and Budget Paperwork Reduction Project (9000-0095), Washington, DC 20503.

PLEASE DO NOT RETURN YOUR COMPLETED FORM TO EITHER OF THESE ADDRESSES. RETURN COMPLETED FORM TO THE CONTRACTING OFFICER.

1a. NAME OF CONTRACTOR / SUBCONTRACTOR: The Trustees of Columbia Univ. in the City of NY
b. ADDRESS (Include ZIP Code):
1210 Amsterdam Avenue
351 Engineering Terrace
MC 2205, NY, NY 10027
c. CONTRACT NUMBER: NOOO14-93-1-0126
d. AWARD DATE (YYMMDD): 921001

2a. NAME OF GOVERNMENT PRIME CONTRACTOR: Office of Naval Research - Code 322GG
c. CONTRACT NUMBER: NOOO14-93-1-0126
b. ADDRESS (Include ZIP Code):
800 N. Quincy Street
Arlington, VA 22217-5660
d. AWARD DATE (YYMMDD): 921001

3. TYPE OF REPORT (X one): a. INTERIM X b. FINAL
4. REPORTING PERIOD (YYMMDD)
a. FROM 921001
b. TO 960930

SECTION 1 - SUBJECT INVENTIONS

5. "SUBJECT INVENTIONS" REQUIRED TO BE REPORTED BY CONTRACTOR / SUBCONTRACTOR *(If "None," so state)*

NAME(S) OF INVENTOR(S) (Last, First, MI) a.	TITLE OF INVENTION(S) b.	DISCLOSURE NUMBER, PATENT APPLICATION SERIAL NUMBER OR PATENT NUMBER c.	ELECTION TO FILE PATENT APPLICATIONS d. (1) UNITED STATES (a) YES	(1) UNITED STATES (b) NO	(2) FOREIGN (a) YES	(2) FOREIGN (b) NO	CONFIRMATORY INSTRUMENT OR ASSIGNMENT FORWARDED TO CONTRACTING OFFICER e. (1) YES	(2) NO
NONE								

f. EMPLOYER OF INVENTOR(S) NOT EMPLOYED BY CONTRACTOR / SUBCONTRACTOR
(1) (a) NAME OF INVENTOR (Last, First, MI)
(b) NAME OF EMPLOYER
(c) ADDRESS OF EMPLOYER (Include ZIP Code)
(2) (a) NAME OF INVENTOR (Last, First, MI)
(b) NAME OF EMPLOYER
(c) ADDRESS OF EMPLOYER (Include ZIP Code)

g. ELECTED FOREIGN COUNTRIES IN WHICH A PATENT APPLICATION WILL BE FILED
(1) TITLE OF INVENTION
(2) FOREIGN COUNTRIES OF PATENT APPLICATION

SECTION II - SUBCONTRACTS *(Containing a "Patents Rights" clause)*

6. SUBCONTRACTS AWARDED BY CONTRACTOR / SUBCONTRACTOR *(If "None," so state)*

NAME OF SUBCONTRACTOR(S) a.	ADDRESS (Include ZIP Code) b.	SUBCONTRACT NUMBER(S) c.	DFAR "PATENT RIGHTS" d. (1) CLAUSE NUMBER	(2) DATE (YYMMDD)	DESCRIPTION OF WORK TO BE PERFORMED UNDER SUBCONTRACT(S) e.	f. SUBCONTRACT DATES (YYMMDD) (1) AWARD	(2) ESTIMATED COMPLETION
NONE							

SECTION III - CERTIFICATION

7. CERTIFICATION OF REPORT BY CONTRACTOR / SUBCONTRACTOR (Not required if ☐ Small Business or ☐ *Non-Profit organization.) (X appropriate box)*

a. NAME OF AUTHORIZED CONTRACTOR / SUBCONTRACTOR OFFICIAL (Last, First, MI): Micheal Steckler
b. TITLE: Principal Investigator
c. I certify that the reporting party has procedures for prompt identification and timely disclosure of "Subject Inventions," that such procedures have been followed and that all "Subject Inventions" have been reported.
d. SIGNATURE
e. DATE SIGNED

DD Form 882, DEC 92

PREVIOUS EDITION IS OBSOLETE.

N/A = Not Applicable

An important goal of the Office of Naval Research is to devise techniques that can aid in predicting where and how mass movements could occur on submarine slopes, and how they would modify the seafloor. As part of the team of scientists working toward this goal in the ONR-sponsored STRATAFORM program, my long term goals are to develop: (i) quantitative methods for assessing past and present slope stability; and (ii) computer models that simulate the causes and morphologic consequences of submarine slope failure as they occur over geologic time.

On continental slopes, the dominant processes that affect the stratigraphic record are thought to be gravity driven, and commonly involve mass movements of sediments. These movements, which include sediment creep, slumps, slides, debris flows, and turbidity currents, are the primary means by which sediment is transferred from and across continental slopes to the deep sea. Their occurrence is significant in dictating where sediment is preserved on continental slopes and how continental slopes are shaped. The unconformable surfaces mass movements erode are complex, discontinuous and asynchronous, complicating the interpretation of continental slope stratigraphy in terms of both its physical makeup and origin. To date, my efforts have focused on understanding where and why submarine slope failures occur, and what affect they have on seafloor morphology.

We used two general approaches to investigate the causes and consequences of submarine slope failure. The first is quantitative analysis of slope stability from continental slope morphology and stratigraphy documented in multibeam bathymetry, side-scan sonar imagery, seismic reflection profiles, and sediment cores. The second is computer modeling of the processes that lead to slope failure and seafloor evolution. These approaches have led to three specific studies.

A computer model has been constructed that simulates the evolution of continental slope morphology under the interaction of sedimentation, slope failure, and sediment flow erosion. This first-generation seascape evolution model predicts that the morphologic evolution from open continental slope areas to submarine canyons occurs in three stages: 1) sediment flows triggered by depositional oversteepening of the upper slope erode narrow slope rills; 2) subsequent sediment flows deepen, and eventually destabilize the walls and/or thalweg of a rill, resulting in localized failure on mid to lower slope; and 3) continued sediment flow undercutting of its headwall transforms the failure into a headward eroding canyon that advances upslope along the rill by retrogressive failure. Model continental slope surfaces have been validated through geomorphic comparison with multibeam bathymetry of the continental slope in the New Jersey STRATAFORM study area. The intercanyon and canyon morphology produced by the model exhibits the same cross-cutting relations observed between Lindenkohl Canyon and adjacent erosional slope rills on the passive-margin New Jersey continental slope, and between slope failures and narrow dendritic tributaries of the Aoga Shima Canyon on the convergent-margin Izu-Bonin Forearc. The model of continental slope evolution appears to be correctly simulating to first order how slope failures shape continental slope terrains in both passive and active tectonic settings. It also reconciles morphologic evidence for headward canyon erosion by mass wasting with stratigraphic evidence for canyon inception by downslope-eroding sediment flows.

High-resolution bathymetric grids of five U.S. continental slopes in different sedimentary and tectonic settings have been constructed and analyzed. Principal findings from the tabulation and analysis of the ranges of seafloor gradients on continental slopes are: (i) U.S. continental slopes on passive margins are steeper than those on active margins at both regional (> 1,500 km^2) and local length scales (< 0.1 km^2); and (ii) process, tectonic, and lithologic differences among the margins are identifiable in the ranges of local seafloor slopes. The different morphologies of the U.S. continental slopes from this study have been described and analyzed. The bathymetric grids constructed in analyzing the slopes of continental slopes provide one the most comprehensive and detailed perspectives of continental margins to date, while the slope measurements suggest slope failures regulate the angles of continental slopes at regional scales, particularly in tectonically active margin settings.

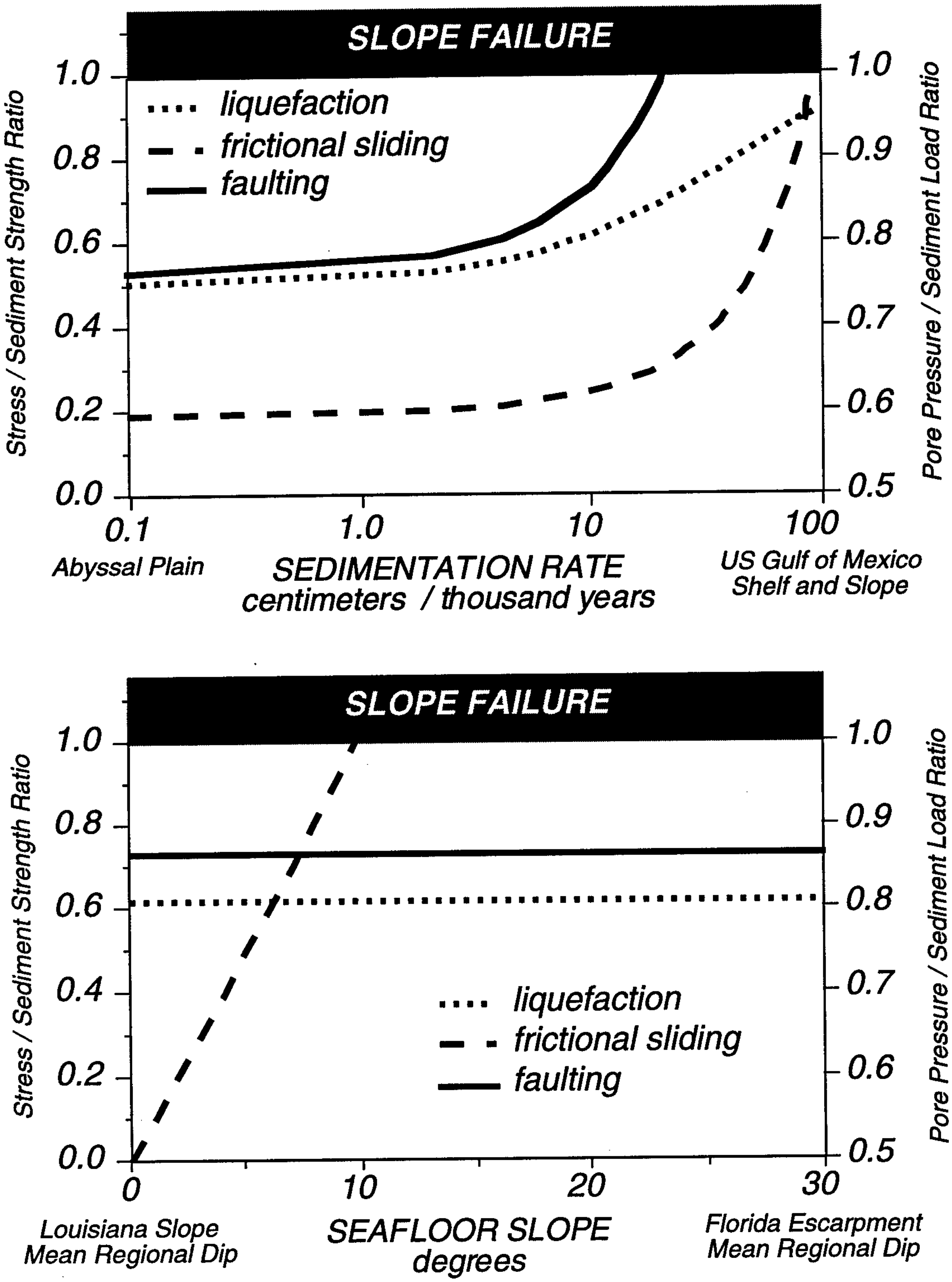

Figure 1.

A coupled sedimentologic-hydrologic computer model has been developed which constrains in 1-D ranges of geologic conditions (e.g., sedimentation rates, permeabilities, seafloor slopes, etc.) that may lead to slope failure as a consequence of transient fluid flow and the high pore pressures it can generate. The model constrains these ranges for three modes of slope failure: liquefaction, frictional sliding and faulting(Fig. 1). The 1-D sedimentologic-hydrologic model couples stress criteria for the initiation of the different failure modes to an analytical solution for the transient response of pore pressures to sedimentation. The model predicts that those factors that influence pore pressures (e.g., sedimentation rate, permeability) influence all three potential modes of slope failure (liquefaction, frictional sliding, and normal faulting), while those that do not (e.g., seafloor slope, internal angle of friction, lateral stress ratio) only influence one or two of the potential modes. The model prediction that slope failure is most likely to occur by normal faulting (Fig. 1) is important in that unlike frictional sliding, this mode of failure is not dependent on seafloor slope. Because the model only considers failure in one dimension, it is simplistic. In nature, seafloor failures may actually occur more often through some combination of listric faulting (at the headwall) and frictional sliding (along the basal shear plane). But what the model is indicating is that where faulting is involved, it may not be possible to discern from bathymetry the likelihood that a seafloor site will fail. Instead, additional information about the properties of the subsurface sediments appear to be critical for making this evaluation.

PUBLICATIONS SUPPORTED BY GRANT:

Goff, J., L. Mayer, J. Hughes-Clarke, and L.F. Pratson, 1996, , Swath mapping on the continental shelf and slope: the Eel River basin, Northern California: *Oceanography*, v. 9, p. 178-182.

Mello, U., and L.F. Pratson, 1999, Regional slope stability and slope-failure mechanics from the two-dimensional state of stress in an infinite slope: *Marine Geology*, v. 154, p 339-356.

Pirmez, C., L.F. Pratson, M.S. Steckler, in review, Clinoform development by advection-diffusion of suspended sediment: modeling and comparison to natural systems: *Journal of Geophysical Research*, v. 103; p. 24,141-24,157.

Pratson, L.F., and B.J. Coakley, 1996, A model for the headward erosion of submarine canyons induced by downslope eroding sediment flows: *Geological Society of America Bulletin*, v. 108, p. 225-234.

Pratson, L.F., and M. Edwards, 1996, An introduction to advances in seafloor mapping using side-scan sonar and multibeam bathymetry: *Marine Geophysical Research*, Special Issue, Advances in Seafloor Mapping using Side-scan Sonar and Multibeam Bathymetry, L.F. Pratson, and M. Edwards eds., v. 18.

Pratson, L.F., and W. Haxby, 1996, What is the slope of the U.S. continental slope?: *Geology*, v. 24 p. 3-6.

Pratson, L.F., and W.F. Haxby, 1997, Panoramas of the Seafloor: *Scientific American*, June, p. 66-71.

Pratson, L.F., and W. Haxby, in press, Bathymetry of U.S. continental slopes [CD-ROM]: *National Geophysical Data Centger, National Oceanic and Atmospheric Administration, Boulder, CO*

Pratson, L.F., and U. Mello, in prep., Pore pressure response to sedimentation, erosion, and sea level change and their influence on submarine slope stability: to be submitted to *Journal of Geophysical Research.*

Pratson, L.F., and W.B.F. Ryan, 1994, Pliocene to Recent infilling and subsidence of intraslope basins offshore Lousiana: *American Association of Petroleum Geologists Bulletin*, v. 78, p. 1483-1506.

Pratson, L.F. and W.B.F. Ryan, 1996, Automated drainage extraction in mapping the Monterey submarine drainage system, California, in L.F. Pratson and M. Edwards (eds.), Advances in Seafloor Mapping using Side-scan Sonar and Multibeam Bathymetry (special issue): *Marine Geophysical Researches,* v. 18, p. 757-777.

Pratson, L.F., H. Lee, G. Parker, M. Garcia, B.J. Coakley, D. Mohrig, J. Locat, U. Mello, J.D. Parsons, S.U. Choi, and K. Israel, 1996, Studies of mass movement processes on submarine slopes,*Oceanography*, v.9, p. 168-172.

Pratson, L.F., W.B.F. Ryan, Gregory S. Moutain, and David C. Twichell, 1994, Submarine canyon initiation by downslope eroding sediment flows; evidence in Late Cenozoic strata on the New Jersey continental slope: *Geological Society of America Bulletin*, v. 106, n. 3.

Seidl, M.A., J.K. Weissel, and L.F. Pratson, 1996, The kinematics and pattern of escarpment retreat across the rifted continental margin of southeast Australia: *Basin Research*, v. 8, p. 301-316.

Weissel, J.K., L.F. Pratson and A. Malinverno, 1994, The length-scaling properties of topography, M. Ellis and D. Merritts, eds, Tectonics and Topography (special section): *Journal of Geophysical Research*, v. 99, p. 13,997-14,012.

Published Abstracts

Coakley, B., and L.F. Pratson, 1993. A simple map view model of turbidite deposition; areal extent and accumulation: *Geological Society of America 1993 Annual Meeting*, v. 25, p. A-181.

Pratson, L.F., 1993. A spatial model of sedimentation, erosion and the evolution of continental margin morphology: *EOS Transactions American Geophysical Union*, v. 74, p. 294.

Pratson, L.F., U. Mello, C. Pirmez, C. Keeley, and B. Coakley, 1993, Morphologic analysis of submarine slope stability using gridded multibeam bathymetry and high frequency seismic reflection profiles: *EOS Transactions American Geophysical Union*, v. 74, No. 43, p. 316.

Weissel, J.K., L.F. Pratson, A. Malinverno, and D. Harding, 1993. Scaling properties of topographic surfaces: i*Geological Society of America 1993 Annual Meeting*, v. 25, p. A-343.

Weissel, J.K., L.F. Pratson and A. Malinverno, 1993. Scaling properties of topographic surfaces: *EOS Transactions American Geophysical Union*, v. 74, p. 194.

Pratson, L.F., 1994, What is the slope of the U.S. continental slope? (abs): *EOS Transactions American Geophysical Union*, v. 75, p. 319.

Coakley, B.J., and L.F. Pratson, 1994, A simple slope-based cellular automata model for the transport and accumulation of turbidites on passive margins (abs): 20th International Conference on Mathematical Geophysics.

Pratson, L.F., and Ulisses Mello, 1995, Pore pressure response to sedimentation, erosion, and sea level change and its influence on submarine slope stability: *EOS Transactions of the AGU*, v. 76, p. F192.

Pratson, L.F., and J.P. Syvitski, 1996, Modeling rates of submarine canyon evolution on continental slopes: *EOS Transactions of the American Geophysical Union*, v. 77, p. F329.

Syvitski, J.P.M., L. Pratson, M. Perlmutter, P. de Boer, G. Parker, M. Garcia, P. Wiberg, M. Steckler, D. Swift, and H. Lee, 1997, EARTHWORKS: a large-scale and complex numerical model to understand the flux and deposition of sediment over various time scales, in V. Pawlowsky-Glahn (ed.): *Proceedings of IAMG'97, the third annual conference of the International Association of Mathematical Geology*, CIMNE-Barcelona, v. 3, p. 29-33.

APPENDIX I

Copies of the following papers supported by grant:

1. Pratson, L.F., W.B.F. Ryan, Gregory S. Moutain, and David C. Twichell, 1994, Submarine canyon initiation by downslope eroding sediment flows; evidence in Late Cenozoic strata on the New Jersey continental slope: *Geological Society of America Bulletin*, v. 106, n. 3.
2. Weissel, J.K., L.F. Pratson and A. Malinverno, 1994, The length-scaling properties of topography, M. Ellis and D. Merritts, eds, Tectonics and Topography (special section): *Journal of Geophysical Research*, v. 99, p. 13,997-14,012.
3. Pratson, L.F., and W.B.F. Ryan, 1994, Pliocene to Recent infilling and subsidence of intraslope basins offshore Lousiana: *American Association of Petroleum Geologists Bulletin*, v. 78, p. 1483-1506.
4. Pratson, L.F. and W.B.F. Ryan, 1996, Automated drainage extraction in mapping the Monterey submarine drainage system, California, in L.F. Pratson and M. Edwards (eds.), Advances in Seafloor Mapping using Side-scan Sonar and Multibeam Bathymetry (special issue): *Marine Geophysical Researches,* v. 18, p. 757-777.
5. Pratson, L.F., and M. Edwards, 1996, An introduction to advances in seafloor mapping using side-scan sonar and multibeam bathymetry: *Marine Geophysical Research*, Special Issue, Advances in Seafloor Mapping using Side-scan Sonar and Multibeam Bathymetry, L.F. Pratson, and M. Edwards eds., v. 18, p. 601-605.
6. Pratson, L.F., and W. Haxby, 1996, What is the slope of the U.S. continental slope?: *Geology*, v. 24 p. 3-6.
7. Pratson, L.F., and B.J. Coakley, 1996, A model for the headward erosion of submarine canyons induced by downslope eroding sediment flows: *Geological Society of America Bulletin*, v. 108, p. 225-234.
8. Seidl, M.A., J.K. Weissel, and L.F. Pratson, 1996, The kinematics and pattern of escarpment retreat across the rifted continental margin of southeast Australia: *Basin Research*, v. 8, p. 301-316.
9. Pratson, L.F., H. Lee, G. Parker, M. Garcia, B.J. Coakley, D. Mohrig, J. Locat, U. Mello, J.D. Parsons, S.U. Choi, and K. Israel, 1996, Studies of mass movement processes on submarine slopes,*Oceanography*, v.9, p. 168-172.
10. Goff, J., L. Mayer, J. Hughes-Clarke, and L.F. Pratson, 1996, , Swath mapping on the continental shelf and slope: the Eel River basin, Northern California: *Oceanography*, v. 9, p. 178-182.
11. Pratson, L.F., and W.F. Haxby, 1997, Panoramas of the Seafloor: *Scientific American*, June, p. 66-71.
12. Pirmez, C., L.F. Pratson, M.S. Steckler, in review, Clinoform development by advection-diffusion of suspended sediment: modeling and comparison to natural systems: *Journal of Geophysical Research*, v. 103; p. 24,141-24,157.

Submarine canyon initiation by downslope-eroding sediment flows: Evidence in late Cenozoic strata on the New Jersey continental slope

LINCOLN F. PRATSON
WILLIAM B.F. RYAN
GREGORY S. MOUNTAIN } *Lamont-Doherty Earth Observatory, Columbia University, Palisades, New York 10964*
DAVID C. TWICHELL *U.S. Geological Survey, Woods Hole, Massachusetts 02543*

ABSTRACT

Multibeam bathymetry and seismic reflection profiles of the New Jersey continental slope reveal a series of abandoned and now-buried submarine canyons that have apparently influenced the development of modern canyons. The buried canyons are infilled along nine slope-wide unconformities separating upper-middle Miocene to Pleistocene sediments that thin downslope. Canyons infilled during the Miocene occur in the southwest part of the study area where Miocene sediments are thickest. Other canyons, infilled during the Pleistocene, occur in the northeast part of the study area where Pleistocene sediments are thickest. When followed downslope, each of the buried canyons arrives at a confluence with a modern canyon, usually where the downslope-tapering sediment cover has failed to smooth over the buried canyon, leaving a sea-floor trough. Seaward of the confluences, the modern canyons have exhumed the buried canyons and use the older valleys to reach the base of the slope.

Re-use of the lower slope reach of the buried canyons appears to have begun when the sea-floor troughs over the buried canyons captured sediment flows initiated along the upper slope and shelf break and confined them to follow the former path of the buried canyons to the base of the slope. The downslope erosion caused by the sediment flows is proposed to have initiated the modern canyons, which eventually excavated and deepened the former routes of the buried canyons seaward of the sites of sediment flow capture. The occurrence of buried canyons where strata thickens alongslope suggests that infilling of the buried canyons occurred seaward of shelf-edge depocenters. The heightened sediment input to the slope in these regions may have also led to the initiation and growth of modern-day canyons. The temporal relation between modern canyon formation, sediment supply, and sea level, however, remains to be established.

INTRODUCTION

Understanding of submarine canyons has progressed with advances in technology for studying the sea floor. The earliest studies used sounding charts made by marine surveyors of areas where heads of canyons indented the shelf break (for example, Dana, 1863). From the morphology of the canyon heads, these studies concluded that submarine canyons were subaerial river beds submerged during rising sea level at the end of the Pleistocene glaciations accompanied by downfaulting or downwarping of the margin (Spencer, 1903; Shepard, 1934). This idea had to be re-evaluated when subsequent bathymetric surveys using acoustic profiling (Veatch and Smith, 1939) revealed that submarine canyons extended seaward across continental slopes to depths too deep for subaerial exposure.

Soon after, investigations of submarine cable breaks (Heezen and Ewing, 1952) demonstrated the erosive power and canyon-forming potential of submarine sediment movements. Initially, these movements were thought to occur only as turbidity currents (Daly, 1936; Kuenen, 1937). But repeated soundings (Chamberlain, 1964), dives (Dill, 1964; Shepard and others, 1964), bottom photographs (Shepard and Dill, 1966), and current measurements (Drake and others, 1978; Shepard and others, 1979) began to reveal that other processes, including sand creep, localized slumps, currents, and even biological erosion were important in moving fill downslope and eroding canyon walls. In a broad review of submarine canyons, Shepard (1981) concluded that canyons were not the product of any single process but the composite result of a variety of processes, probably acting over long periods.

Until this time, studies of processes active within submarine canyons along the narrow continental shelf of the western United States had been emphasizing a relation between canyon formation and the supply of shelf sands (Gorsline, 1970). In this region, shifting sediment supply due to sea-level change, river-mouth migration, and their effect on longshore current regimes and shoreline configuration were found capable of causing movements in canyon position over time (Felix and Gorsline, 1971). Submarine canyons seaward of the broad continental shelf off the eastern United States came to be viewed as relict, having been formed under similar influences as the modern west coast canyons, but only when shorelines were near the shelf edge during glacio-eustatic lowerings (Emery and Uchupi, 1972).

This view of the east coast canyons began to change in the early 1980s when new, side-scan sonar images of the New Jersey continental slope documented an abundance of slope gullies and submarine canyons with heads occurring well below the shelf break (Twichell and Roberts, 1982). The separation of the canyon heads from the shelf edge raised the possibility that submarine canyons could be formed by agents unrelated to the supply of shelf sands. The common association of failure scars with the slope-confined canyons and the occurrence of base-of-slope mass wasting deposits in the place of submarine fans led to the idea that retrogressive slope failures could initiate submarine canyons (Farre and others, 1983). Once these canyons breached the shelf break, they then became subject to the same processes active in the canyons off the western United States.

With the discovery of numerous slope-confined canyons along other continental

---

Geological Society of America Bulletin, v. 106, p. 395–412, 11 figs., March 1994.

slopes, this *upslope* erosion theory of canyon initiation has come to be as widely accepted (for example, McGregor, 1985; Dingle and Robson, 1985; Nelson and Maldanado, 1988; Klaus and Taylor, 1991) as Daly's (1936) original theory that submarine canyons initiate by the *downslope* erosion of shelf-edge–sourced turbidity currents. It is important to note, however, that both of these theories are primarily derived from observations of the morphology of modern submarine canyons and the processes active within them.

The question of canyon initiation is addressed in this study by taking a more historical approach and using both slope morphology and stratigraphy to examine how modern canyons have exploited older, buried canyons along an 80-km stretch of the New Jersey continental slope from Lindenkohl to Hendrickson Canyon (Fig. 1). In this region, nine submarine canyons that cross the breadth of the slope have formed on top of at least thirteen older canyons buried at various depths beneath the upper slope by sediments that range in age from upper middle Miocene to Pleistocene. Downslope, each of these older, buried canyons is exhumed and is now re-used by one of the modern canyons. This re-use of the older canyons by modern canyons is examined with the objective of learning whether initiation of the modern canyons offshore New Jersey was more the result of downslope-sediment-flow erosion or upslope, retrograde-failure erosion.

CONTINENTAL SLOPE STUDY AREA

Geologic Background

The New Jersey continental slope is composed of semilithified to lithified, truncated, tapering Tertiary strata that is overlain by Quaternary silts and clays (Fig. 2) (Robb and others, 1981; Poag, 1985). The Quaternary sediments thin from >400 m near the shelf break to being locally absent along parts of the lower slope (>1,500 m). Where absent, expansive outcrops of Eocene chalk occur (Hollister and others, 1972a).

The Eocene chalk was deposited during warm climate and high sea level. Beginning in the Miocene the depositional environment changed (Farre, 1985; Poag, 1985). Climate cooled and sea level dropped, accompanied by a massive influx of terrigenous sediment. By the mid-Miocene, large deltas had prograded out to the former shelf edge, and submarine canyons were cut into post-Eocene clastic sediments (Mountain, 1987). Clastic sedimentation continued through the Quaternary, the amount fluctuating with the movement of the shoreline across the shelf by glacially induced sea-level changes (Emery and Uchupi, 1984).

Sea-Floor Morphology

Figure 3 is a perspective image of a grid constructed from near-complete SeaBeam bathymetry of the New Jersey continental slope and uppermost rise between Lindenkohl and Hendrickson Canyons (thick solid outline, Fig. 1). The image shows that the slope is incised by numerous submarine canyons, while the upper rise is morphologically subdued and crossed by only a few channels. The canyons on the slope are of two general types: long canyons that cross the entire breadth of the slope, and shorter, box-shaped canyons with almost vertical headwalls in exposures of Eocene Chalk, which occur on the mid- to lower slope generally beneath the 1,500-m isobath (Pratson and others, 1989).

Closer inspection of the slope bathymetry reveals that the divides between the submarine canyons are commonly incised by narrow (20–300 m), downward-trending slope rills (Fig. 4). Also seen are a series of broader (0.5–2 km), shallow-relief, downward-trending troughs (Fig. 5). These troughs begin well beyond the shelf break at 500- to 800-m water depth and deepen seaward until being truncated by an intersecting canyon. At these sites, the troughs are left hanging above the canyon floors and are commonly sites of mass wasting of canyon fill materials. An example is the recess left in a hanging trough by a large slump block that has calved into Hendrickson Canyon (Fig. 5).

BURIED SUBMARINE CANYONS

Single-channel seismic reflection profiles indicate the intercanyon troughs are the surficial expression of buried, slope-crossing canyons whose former relief has been subdued but not entirely erased by sediment infilling. Successive alongslope profiles show that as the thickness of the sediments that infill the canyons decreases downslope, the troughs over the buried canyons become pronounced. The profiles reveal that other buried canyons occur in the area as well.

Characteristics

Slope. In the seismic reflection profiles, the buried canyons are generally V-shaped in cross section, outlined by the unconformity between the seismic reflectors truncated at the canyon walls and the draping reflectors of the canyon fill (Fig. 6). Truncated reflectors are also seen within the canyon fill, indicating that burial was periodically interrupted by renewed erosion down the canyon axis. Above these unconformities, reflectors within the fill commonly continue onto the surrounding slope (Figs. 6, 7A–7C), signifying that the latter part of canyon infilling was accomplished during periods of broader slope deposition.

Knowledge of the sediments that infill the buried canyons is limited to DSDP Site 612 (Fig. 1), which was drilled into a buried canyon formed during the middle Miocene 9–11 m.y. BP (Miller and others, 1987). The 135 m of upper Miocene, Pliocene, and Pleistocene sediments that fill the buried canyon are generally fine grained, consisting of muds with an interval of interbedded upper Miocene and Pliocene glauconitic sands (Shipboard Scientific Party, 1987a). The sediments show no evidence of debris flows, have few shallow-water biofacies, and exhibit only minor amounts of reworked older material, suggesting little downslope transport (Katz and Miller, 1987).

Upper Rise. Buried, former slope canyons cut into Eocene Chalk have been mapped beneath the upper rise where it onlaps the continental slope (Mountain, 1987). But buried channels in the Miocene, Pliocene, and Pleistocene strata that overlie the Chalk and form the apron of upper-rise sediments that thickens away from the slope cannot be identified seaward of the present-day canyons. The upper-rise strata appear in the seismic reflection profiles as relatively chaotic units of intermittent reflectors. Forms that might be channels cannot be traced downslope between seismic lines. The late Miocene sediments on the rise infill the Eocene canyons where the rise onlaps the former slope. The sediments were sampled at DSDP Sites 604 and 613 and consist of coarse sands, gravels, and conglomerates (Shipboard Scientific Party, 1987b, 1987c). The overlying Pliocene and Pleistocene sediments, which were also sampled, are a mixture of clays, silts, and sandy turbidites, interspersed with clasts of Eocene chalk and chaotic slump/debris-flow deposits.

A modern analogue for the upper-rise deposits appears to be the upper-rise surface. Although the bathymetry shows channels extending from the mouths of Lindenkohl and Toms Canyons, only subtle, shallow-floored, linear depressions are seen extending seaward of most of the other canyons. In the seismic reflection profiles (for example, GS

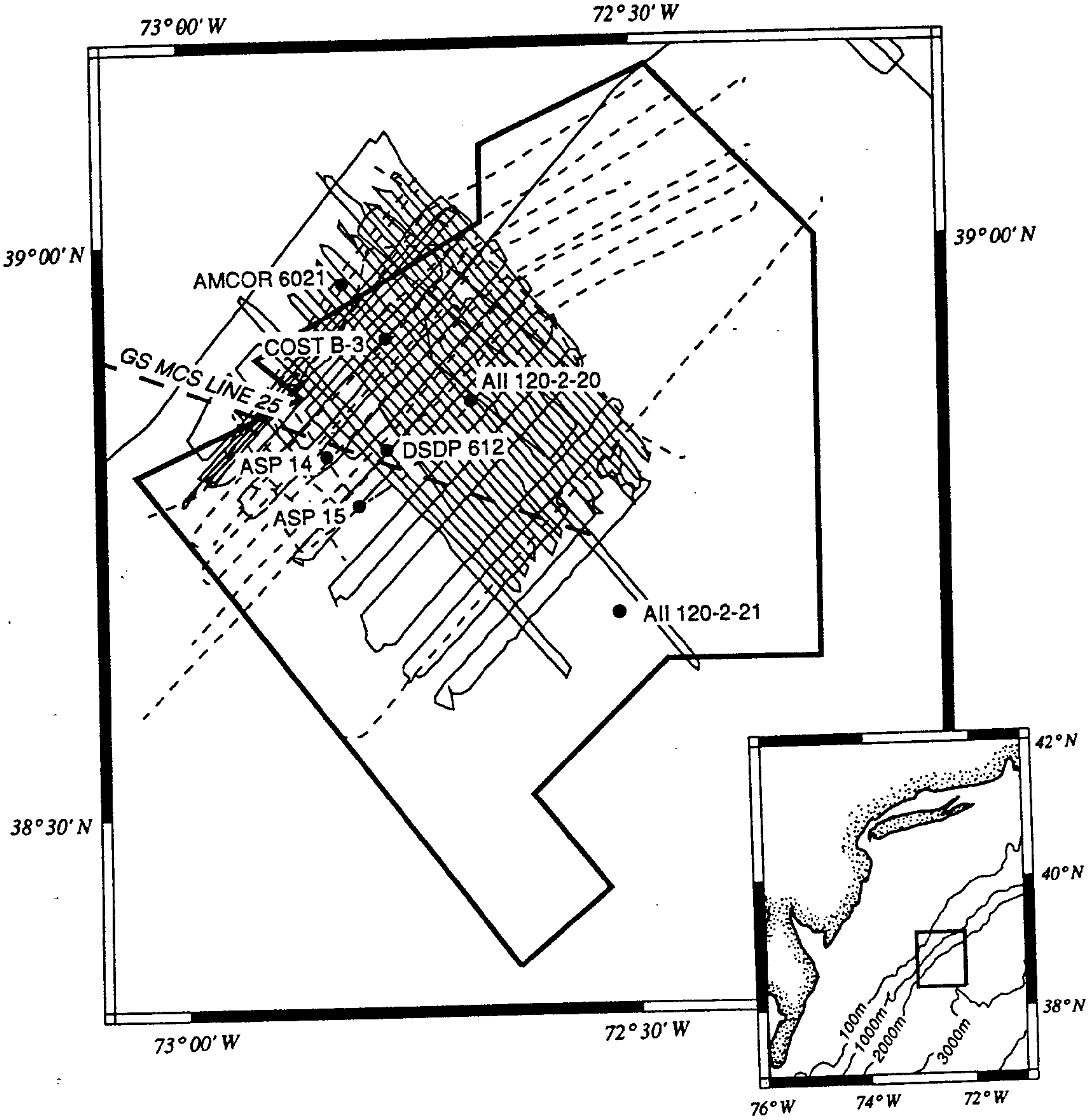

Figure 1. Location map of single-channel seismic reflection profiles, SeaBeam bathymetry, boreholes, and piston cores. Thin solid lines are the profiles collected by the U.S. Geological Survey (USGS) (Robb and others, 1981); thin dashed lines are the profiles collected by Lamont-Doherty Geological Observatory (L-DGO) and Rutgers University (Mountain, 1991); thick solid line outlines the SeaBeam coverage; and thick dashed line is USGS multichannel seismic line 25 (Grow and others, 1983), an interpretation of which is shown in Figure 2. Boreholes are the AMCOR 6021 (Hathaway and others, 1976), ASP 14 and 15 (Poag, 1985), COST B-3 (Scholle, 1980), and DSDP Site 612 (Shipboard Scientific Party, 1987a). Piston cores are AII 120-2-20 and AII 120-2-21. Inset shows location of study area offshore New Jersey.

101, Fig. 7D), these linear depressions exhibit slight erosion in their thalwegs, and what appears to be minor levee construction along their sides. Piston core AII 120-2-21 (Fig. 1) was cored in one of the linear depressions (Fig. 7D, Line GS 101—"Rise Linear Depression") 10 km seaward of the base of the slope and contained slide debris buried beneath 1–2 m of hemipelagic sediments. Identical debris was recovered in AII 120-2-20 (Fig. 1) cored in the thalweg of Northeast Valley Canyon directly upslope. Physical property measurements made by K. Moran (unpub. data) suggest that such debris acts as a sound scatterer and is the cause for the downslope-trending trails of high acoustic reflectivity seen by Schlee and Robb (1991) in GLORIA side-scan so-

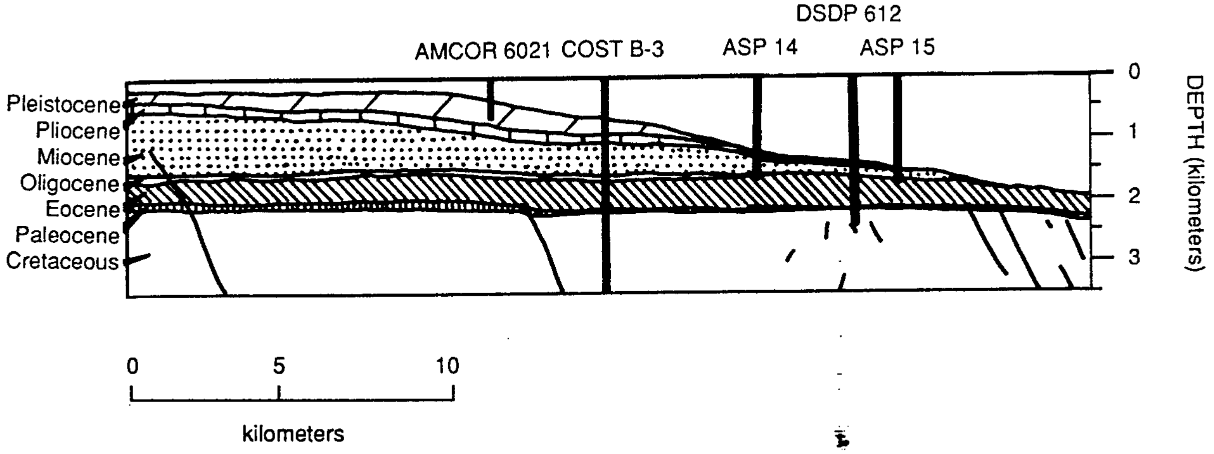

Figure 2. General stratigraphy of the New Jersey continental slope based on an interpretation of USGS line 25 (Fig. 1). Note that Pleistocene sediments are thickest on the upper slope near the shelf break. Interpretation is modified from Poag (1985).

nar imagery of the New Jersey–Delaware slope and rise.

Relation to Slope-Wide Unconformities

The surfaces of truncation that delineate the walls of the buried canyons in the seismic reflection profiles can be traced as surfaces of erosion across the continental slope. Commonly, several buried canyons occur along the same surface. Nine such surfaces (Figs. 7A–7C) are mapped across the slope in the area of the seismic surveys (Fig. 1). The surfaces are interpreted to represent slope-wide unconformities.

Dating of the unconformities is hampered by the patchy stratigraphic record of late Cenozoic sediments cored on the New Jersey slope. At the sites where the ASP 14 and 15 and DSDP Site 612 (Fig. 8A) boreholes were drilled, stratigraphic intervals are missing (Poag, 1985; Scientific Party, 1987a). At the COST B-3 site (Fig. 8B), coring did not commence until 312 m subbottom in middle Miocene strata (Scholle, 1980). And at the AMCOR 6021 site (Fig. 8B), coring was stopped after recovering ~300 m of Pleistocene sediments (Poag, 1985).

Because of the stratigraphic gaps between the boreholes in the study area, only approximate ages are assigned to the nine unconformities. The oldest is the M0, which, based on the stratigraphy at DSDP Site 612 (Fig. 8A) (Shipboard Scientific Party, 1987a), appears to have formed during the late middle Miocene. The second oldest is the M1 unconformity, which Miller and others (1987) date as separating upper middle Miocene and lower upper Miocene strata. The third oldest, M2, does not appear to have been sampled at any borehole. Poag and Mountain (1987) have mapped the same unconformity as separating Tortonian and Messinian strata, however, and this age is used here. The fourth oldest unconformity, P1, apparently has also not been sampled. Across this unconformity, the seismic character changes from truncated reflectors below to draping reflectors above. This change is interpreted to represent an erosional boundary between upper Miocene sediments below and Pliocene sediments above. The P2 unconformity was sampled at DSDP Site 612 and appears to be Pliocene in age (Fig. 8A). The younger P3 surface apparently has not been sampled, but the cores recovered at DSDP Site 612 and AMCOR 6021 constrain its age as Pliocene to Pleistocene. The three youngest unconformities, P11, P12, and P13, are Pleistocene, occurring within the ~300 m penetrated at the AMCOR 6021 borehole.

Distribution

Although tentative, the ages for the unconformities provide a framework as to when the buried canyons were last active. Buried canyons that were active in the Miocene occur where intercanyon Miocene sediments are thickest, which is in the vicinity of Lindenkohl Canyon (Figs. 7A–7C and 9). These intercanyon sediments thin and are truncated to the north by thickening sequences of overlying Pleistocene sediments. Miocene canyons may have existed in this area as well, but only one is preserved (BC1, Fig. 7B). Buried canyons that were active in the Pleistocene, however, are restricted to where intercanyon Pleistocene sediments are thickest (Figs. 7A–7C and 9). This suggests that their development was directly linked to the greater slope deposition occurring to the north.

The map of the submarine canyons in Figure 9 also shows that when traced downslope, all of the buried canyons arrive at a confluence with a nearby modern canyon. These confluences commonly occur downslope of where a trough appears over the buried canyon. Basinward of the confluences, the modern canyons do not cross the buried canyons but instead re-use the paths of the former canyons to reach the base of the slope. This re-use of the former canyon pathways provides a new insight into submarine canyon formation offshore New Jersey.

DISCUSSION

Canyon Initiation by Upslope versus Downslope Erosion

The Upslope Erosion Model. The slope failure theory of Twichell and Roberts (1982) and Farre and others (1983) is based on observations of submarine canyons offshore New Jersey and nearby mid-Atlantic states. The theory's success lies in its recognition that canyons are eroded not just by turbidity currents, but also by retrogressive mass wasting of the slope. It explains the origin of the numerous canyons that do not breach the shelf break, and the densely gullied walls of the relatively few that do. The theory is based on observations that were made almost solely from side-scan sonar imagery, however, which was incapable of revealing the buried canyons underlying the slope.

When viewed in light of the buried canyons, the idea that submarine canyons erode

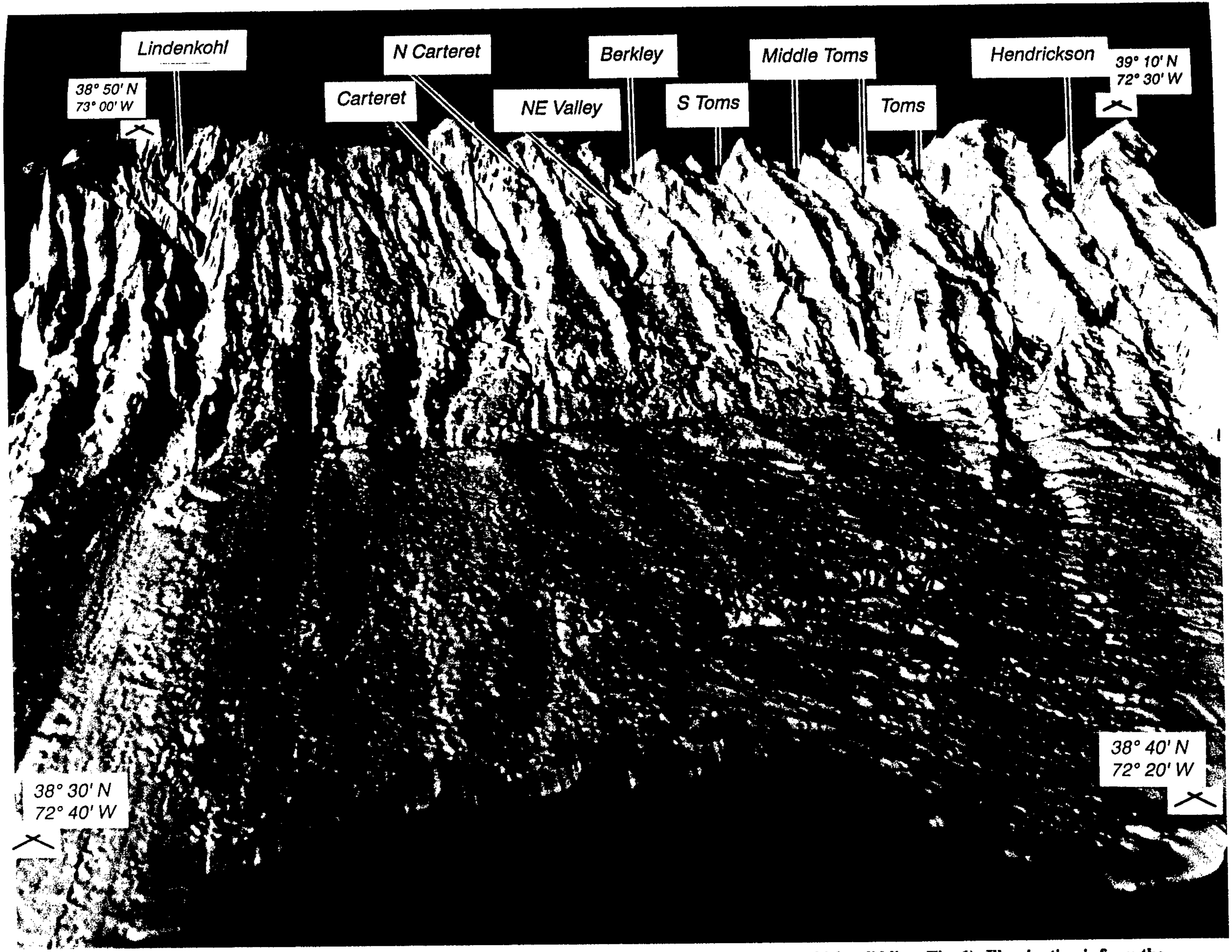

Figure 3. Perspective image of a gridded version of the SeaBeam bathymetry (area outlined by thick solid line, Fig. 1). Illumination is from the left, grid spacing is 50 m, and vertical exaggeration is ~5:1. Image depicts the sea floor extending from the upper continental slope (200–400 m) to the upper continental rise (2,600–2,700 m). Slope-rise boundary (~2,100 m) appears as a sharp contrast change from light to dark gray in mid-part of image, best seen beneath Northeast Valley. Image constructed by W. Haxby, Lamont-Doherty Earth Observatory.

Figure 4. Close-up of slope rills on the intercanyon divide between Lindenkohl (left) and Carteret (right) Canyons. Contours show that approximately 11 rills, each on average 20–40 m deep and 300 m wide, initiate on the upper slope at 250- to 500-m water depth. The rills join one another downslope forming several rill networks that enter into three lower-slope, box-shaped canyons that are more than 100 m deep and a kilometer wide.

upslope by mass wasting appears limited in its ability to reproduce the modern canyon–buried canyon confluences observed in the study area. For example, were a developing canyon to encounter a buried canyon filled with sediments more difficult to erode than the surrounding slope, the developing canyon would probably avoid the buried canyon and cut its own path to the shelf break (Fig. 10A). This possibility is ruled out by the modern canyons having exploited former canyons to reach the base of the slope.

Alternatively, if the sediments filling the buried canyon were easier to erode than the surrounding slope, then the developing canyon would probably erode into the buried canyon but excavate and re-use the buried canyon's upslope reach (Fig. 10B). The opposite is observed in the study area; modern canyons re-use the downslope reach of buried canyons.

For mass wasting to initiate canyons that excavate and re-use the downslope reach of buried canyons, it appears a developing canyon would first have to erode headward through lower slope sediments filling a buried canyon, then at some point erode out of the buried canyon and cut a new path toward the shelf break (Fig. 10C). Although this scenario is possible, it is unclear what would cause a developing canyon to adopt such a change of course in erosion.

Another difficulty with the mass-wasting theory is that no modern analog is seen for a "youthful," slope-confined canyon eroding upslope by headwall failure (Fig. 3). The box-shaped canyons on the mid- to lower slope were initially thought to be examples (Farre and others, 1983). But petrographic analyses by McHugh and others (1993) indicate that the mass wasting in these canyons is associated with diagenetic fracturing and jointing of the Eocene chalk. The structural and lithologic influences on the origin of these canyons explains their highly segmented nature and lack of significant headward growth into the upper-slope siliciclastic lithologies. Joints and fractures have also influenced erosion in the longer, slope-crossing canyons where they incise the Eocene chalk. The similarities suggest that when some of the slope-crossing canyons first formed, they exploited existing lower-slope, box-shaped canyons.

The Downslope Erosion Model. An alternate explanation for the origin of the New Jersey canyons is that they were begun by turbidity current, or more inclusively, sediment-flow erosion begun on the upper continental slope and/or shelf break. On the upper slope, most former canyons are completely filled, and sediment flows beginning their passage downslope would not be influenced by buried topography (Fig. 11B). By the mid- to lower slope, however, sediment cover thins, and sea-floor impressions of buried topography (that is, the troughs) become pronounced. Upon entering a sea-floor trough above a buried canyon, a sediment flow would be captured and constrained to retrace the course of the buried canyon to the base of the slope (Fig. 11C). Through repeated capture, subsequent sediment flows would excavate the lower part of the buried canyon while eroding a new headward extension

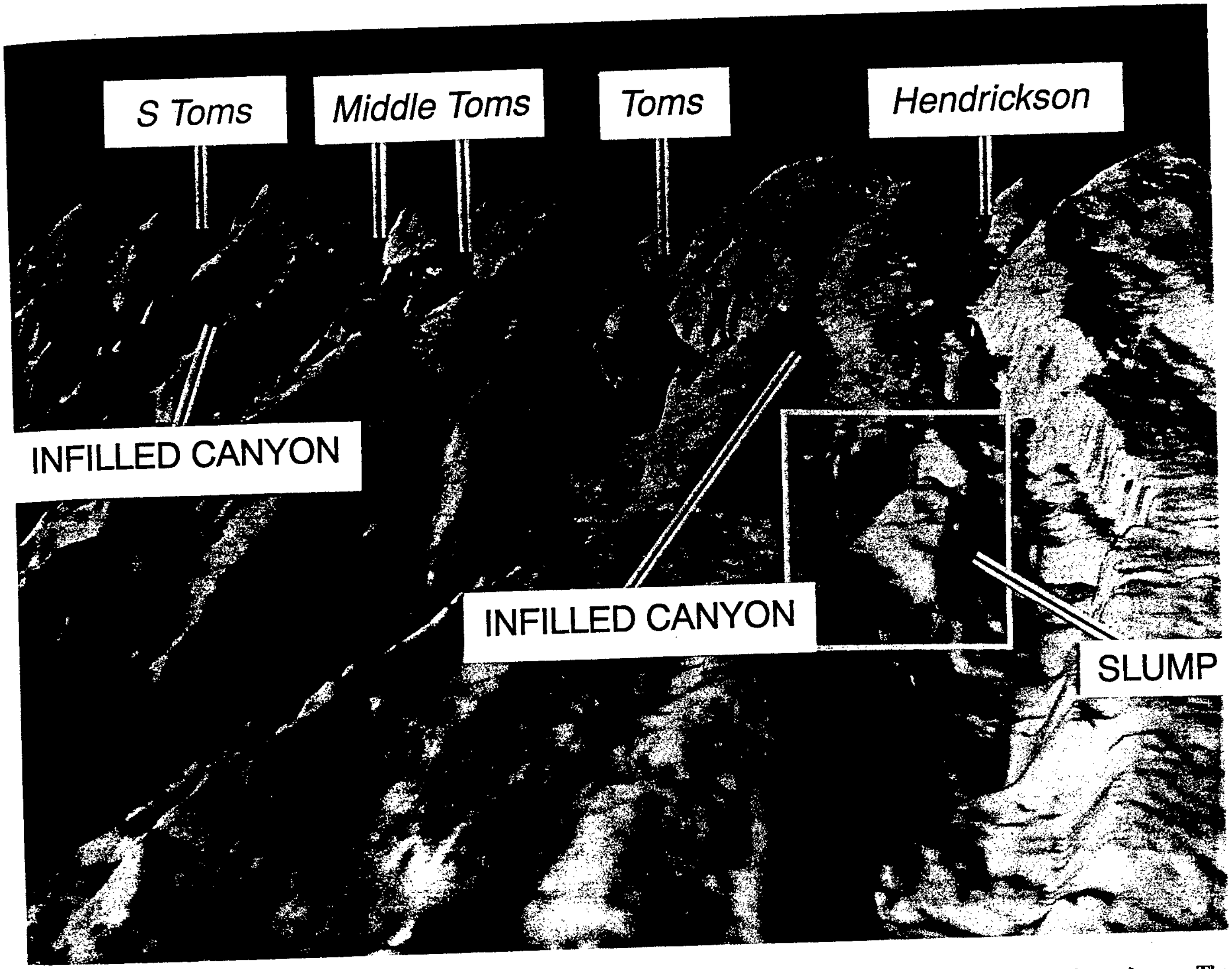

Figure 5. Close-up of downslope-trending sea-floor troughs located between submarine canyons in the northeastern part of the study area. The troughs overlie and reflect the form of older submarine canyons buried beneath the troughs. Note the large slump block (within box, lower right) that has calved from a sea-floor trough into Hendrickson Canyon. Image constructed by W. Haxby, Lamont-Doherty Earth Observatory.

(Fig. 11D). Canyon entrenchment would leave the sea-floor trough over the buried canyon hanging above the developing canyon floor. Eventually the entrenchment would undercut the buried canyon, causing portions of its exposed fill to slump into the developing canyon's thalweg (for example, Figs. 5 and 11D). The result would be a truncated confluence between modern and buried canyons with the same geometry as that observed in the study area (Figs. 10D and 11D).

Causes for the initiation of the sediment-flow erosion called for above remain open to speculation. Earthquakes, such as the 1929 Grand Banks event (Heezen and Ewing, 1952), are capable of triggering erosive, canyon-forming sediment flows (Hughes-Clarke, 1988) and are a possible cause in the formation of other submarine canyons off the U.S. east coast (O'Leary, 1986). The recurrence time of large (magnitude > 7, Richter Scale) earthquakes along the North American Atlantic seaboard may be as often as one event in each 100-km portion of the seaboard every 2,000 yr (Seeber and Armbruster, 1988). It seems unlikely, however, that the multitude of canyons off the U.S. Atlantic margin were only initiated by earthquake-generated sediment flows.

A temporal relation is generally believed to exist between sediment-flow erosion, sediment supply, and sea level (for example, Vail and others, 1977). Sediment flows continue to erode the New Jersey continental slope today (Stanley and others, 1984), but substantial slope erosion by sediment flows is believed to have last occurred during the sea-level lowstands of the Pleistocene (Prior and others, 1984). An abundance of shelf sands and shallow, cold-water fauna occur within Pleistocene turbidites cored on the rise and abyssal plain (Ericson and others, 1961; Ewing and others, 1963; Hollister and others, 1972a, 1972b). These reworked materials are identical to materials deposited on the outer shelf when glacially induced sea-level lowerings moved shorelines out near the shelf edge (Emery, 1968). The shoreline migration apparently resulted in heightened sediment input to the nearby slope and the frequent triggering of erosive sediment flows, which

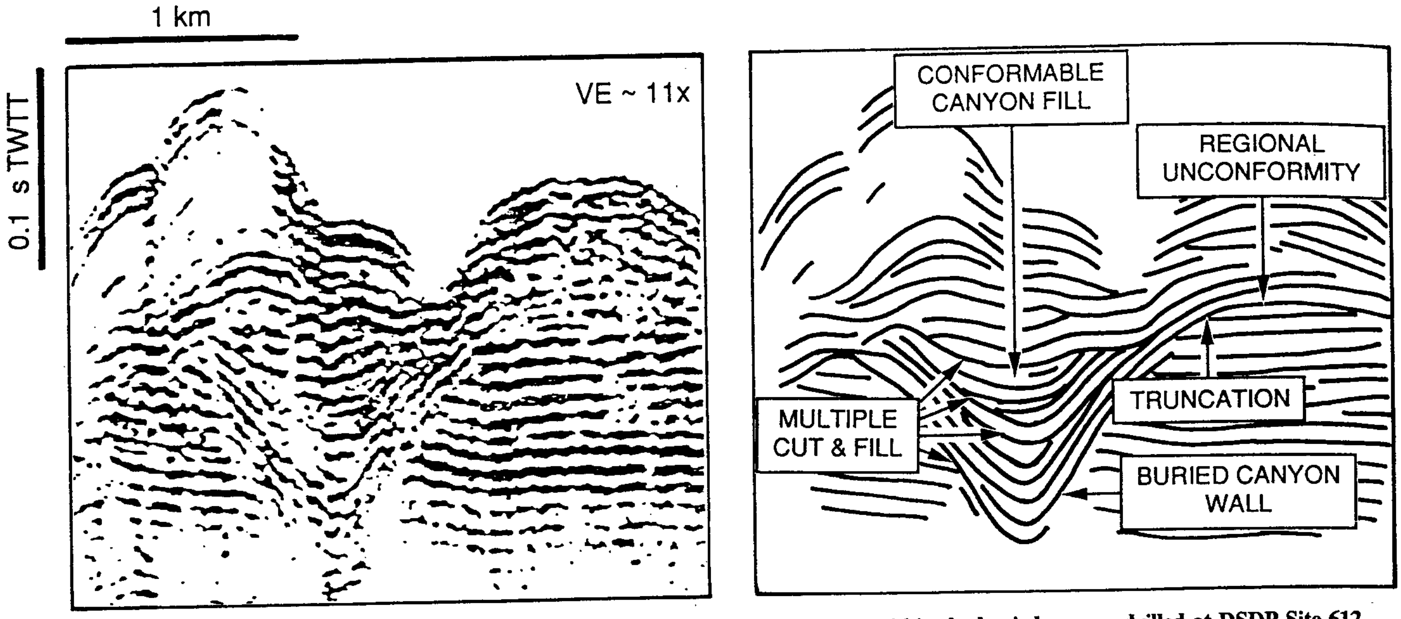

Figure 6. Detail from USGS seismic line GS 89 (BC 5, Fig. 7) of the stratal geometry within the buried canyon drilled at DSDP Site 612.

undoubtedly contributed to submarine canyon erosion.

Whether canyon initiation is exclusively the result of erosion by sediment flows carrying shelf materials that bypass the slope is debatable. The submerged Nichols and Franklin shorelines mapped by Veatch and Smith (1939) approximately coincide with the present shelf break offshore New Jersey (~120 m). The proximity of these shorelines, which are Pleistocene in age (Dillon and Oldale, 1978), indicates that sediment flows consisting of materials deposited by rivers and longshore currents could have initiated at the shelf edge. This would suggest that at least during the last (Wisconsin) Pleistocene sea-level lowstand, the slope was a surface of erosion and sediment bypassing, with submarine canyons likely being cut by shelf-derived sands.

Stanley and others (1983), however, have shown that along clastic margins, a transition between erosion and deposition occurs where there is a balance between the energy conditions of the water column and the supply of terrigenous sediments. Offshore New Jersey, this transition presently exists over the upper slope between 200- and 400-m water depth. Over this depth range, the turbulent waters of the shelf give way to the quieter waters over the upper slope in which suspended materials can settle out of the water column. This depth range also coincides with the thickest accumulation of Pleistocene sediments (Fig. 2). The accumulation suggests sedimentation has been focused over the upper slope since the beginning of the Quaternary. Diminishing sediment supply seaward of the upper slope transition zone would explain why Pleistocene sediments thin downslope and have not completely smoothed over former mid- to lower-slope canyon topography. Upbuilding of the upper slope could have led to periodic oversteepening, failure, and the triggering of erosive sediment flows (Coleman and others, 1983). These in turn could have initiated submarine canyons with heads that occur on the upper slope below the shelfbreak, such as those first observed by Twichell and Roberts (1982) and Farre and others (1983).

Multiple Submarine Canyons: The Influence of Shelf Sedimentation and the Impact on Rise Deposition

An important source of sediment to the slope at times of lowered sea level were rivers that crossed the exposed continental shelf. In some instances, these rivers transported sediments directly to the heads of submarine canyons (Twichell and others, 1977; Knebel and others, 1979). But the paucity of buried river valleys on the shelf suggests that rivers were few relative to the large number of canyons incising the slope (Shor and McClennen, 1988).

Rivers could still have contributed to the formation of multiple submarine canyons by their lateral movement along the shelf during both sea-level lowstands and highstands. During sea-level lowstands, the Hudson River, which last fed Hudson Canyon, migrated over a broad region of the shelf off New York and New Jersey (Knebel and others, 1979) and may have fed sediment to submarine canyons as far south as Wilmington Canyon ~200 km away (Veatch and Smith, 1939; Kelling and Stanley, 1970; Kelling and others, 1975). During sea-level highstands, mouths of rivers along the mideast United States (for example, Delaware and Susquehana) have been forced to migrate southward by southerly longshore current deposition (Colman and others, 1990), possibly since as far back as the Miocene (Poag and Sevon, 1989). With each sea-level lowering, and possibly even during a single sea-level lowstand, these movements have allowed rivers to source different sections of the eastern U.S. margin.

Such a shift in river-fed shelf-edge sedimentation is a likely cause for the alongslope change in thickness of the stratigraphic intervals mapped in the study area. Both the isopach maps of Poag and Mountain (1987) and the profiles in Figures 7A–7C show that slope deposition moved from the vicinity of Lindenkohl Canyon to northeast of Toms Canyons sometime at the end of the Pliocene. The increased deposition in the northeast part of the study area was probably caused by enhanced sediment input from the Hudson and possibly Delaware Rivers during Pleistocene sea-level lowstands (Knebel and Spiker, 1977). It may also have been contributed to by sediments from glacial melt waters (Milliman and others, 1990). The increased

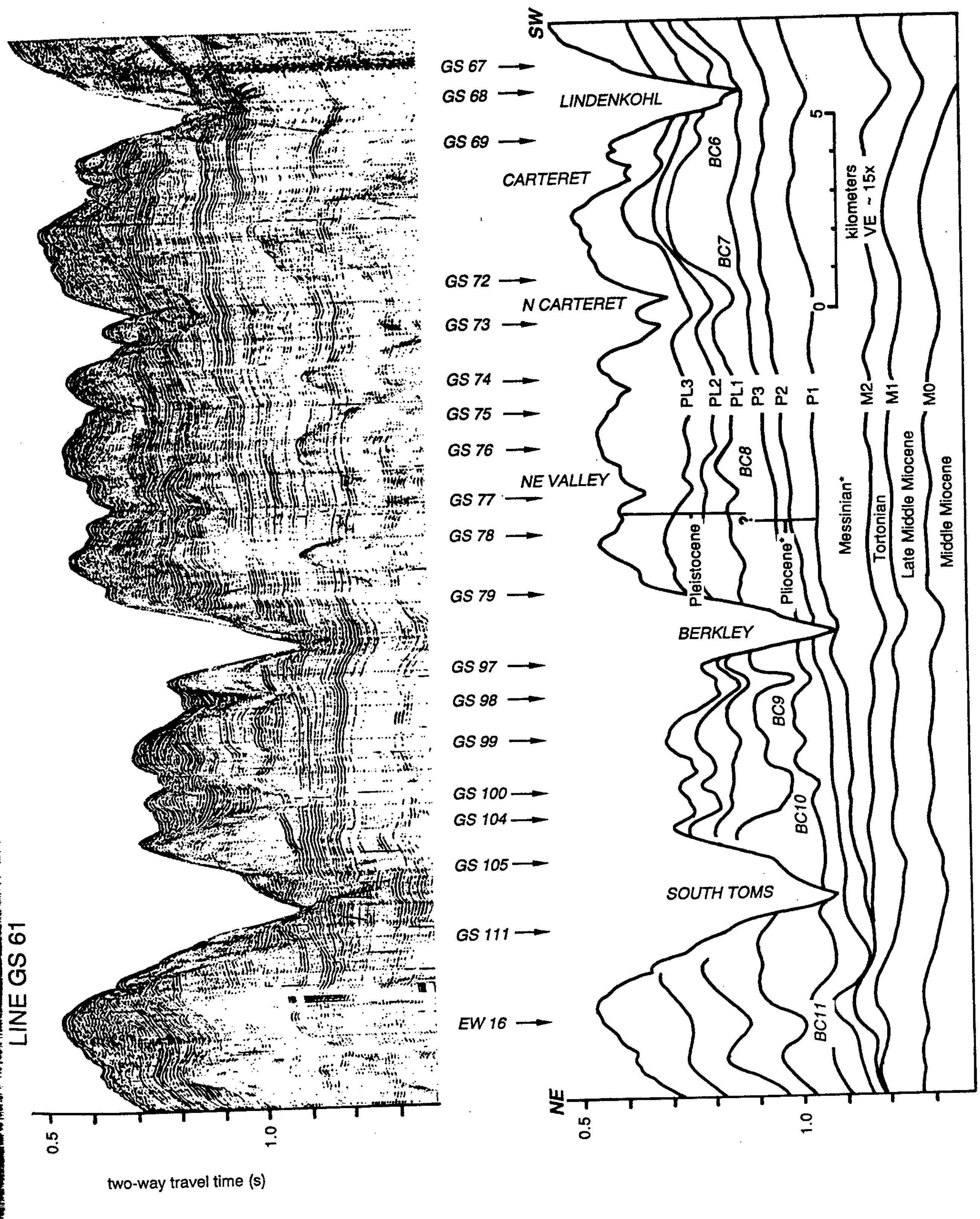

Figure 7A. Example strike line GS 61, collected by the U.S. Geological Survey (Robb and others, 1981). Location of profile is shown in Figure 10.

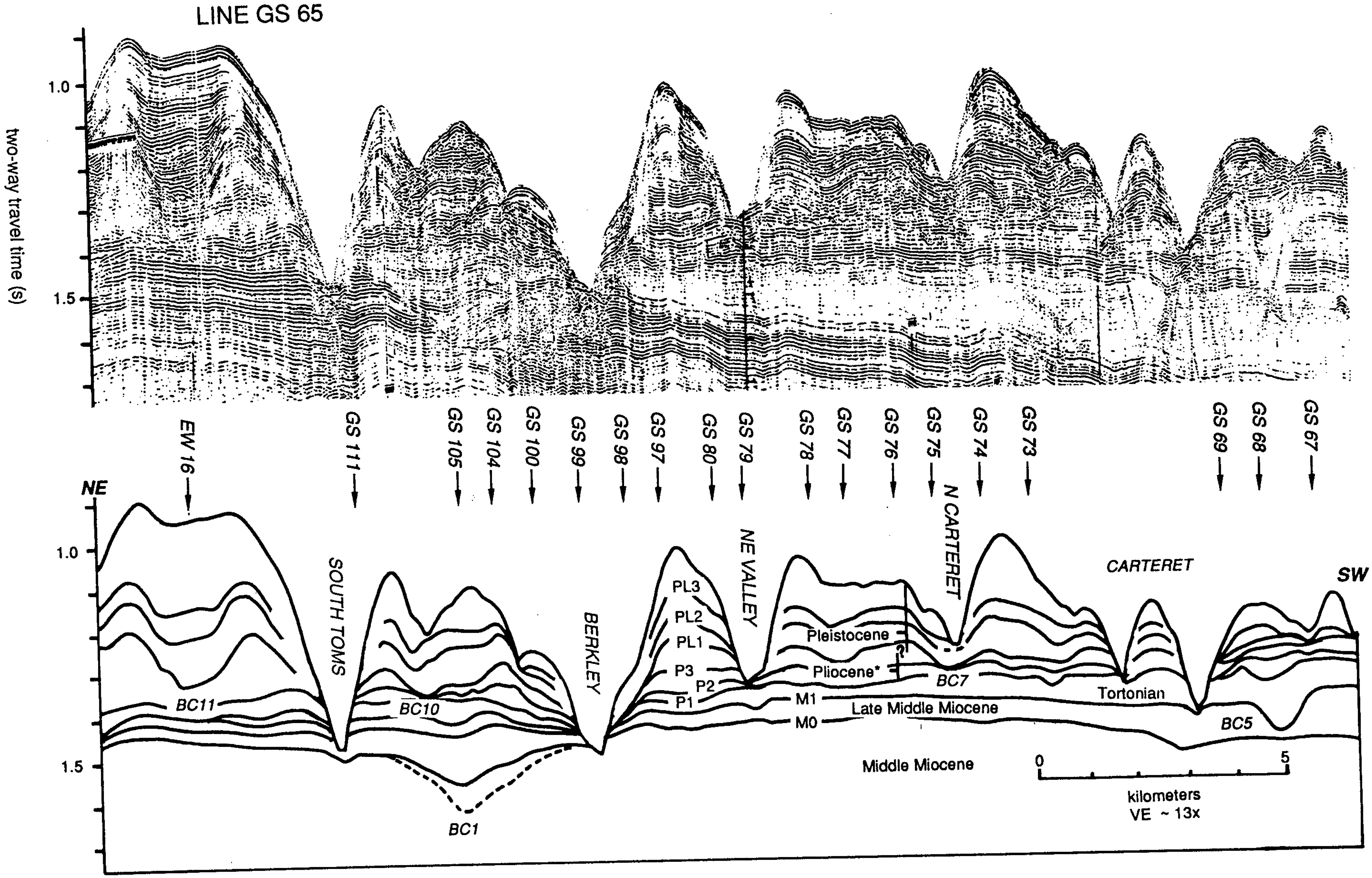

Figure 7B. Example strike line GS 65, collected by the U.S. Geological Survey (Robb and others, 1981). Location of profile is shown in Figure 10.

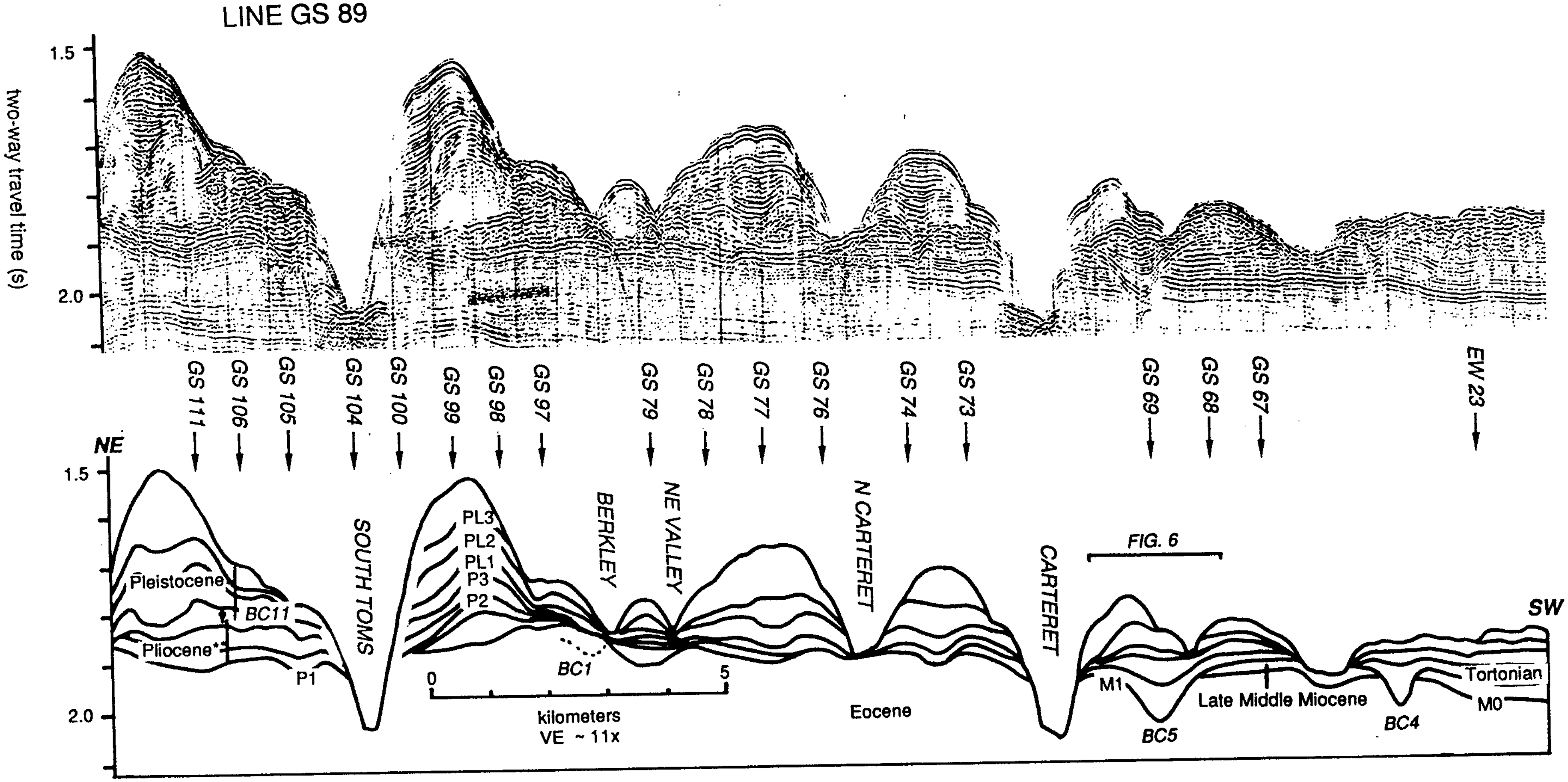

Figure 7C. Example strike line GS 89, collected by the U.S. Geological Survey (Robb and others, 1981). Location of profile is shown in Figure 10.

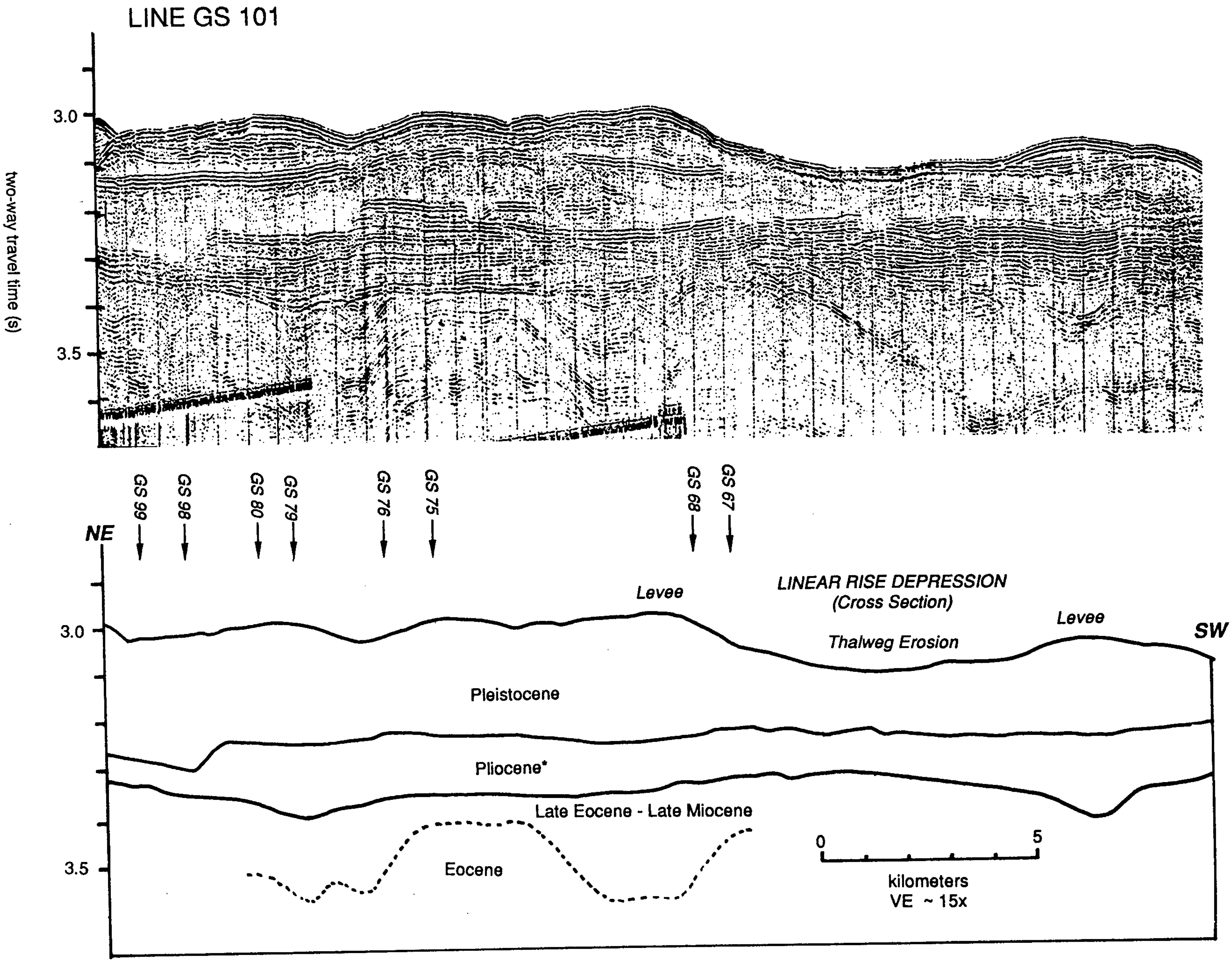

Figure 7D. Example strike line GS 101, collected by the U.S. Geological Survey (Robb and others, 1981). Location of profile is shown in Figure 10.

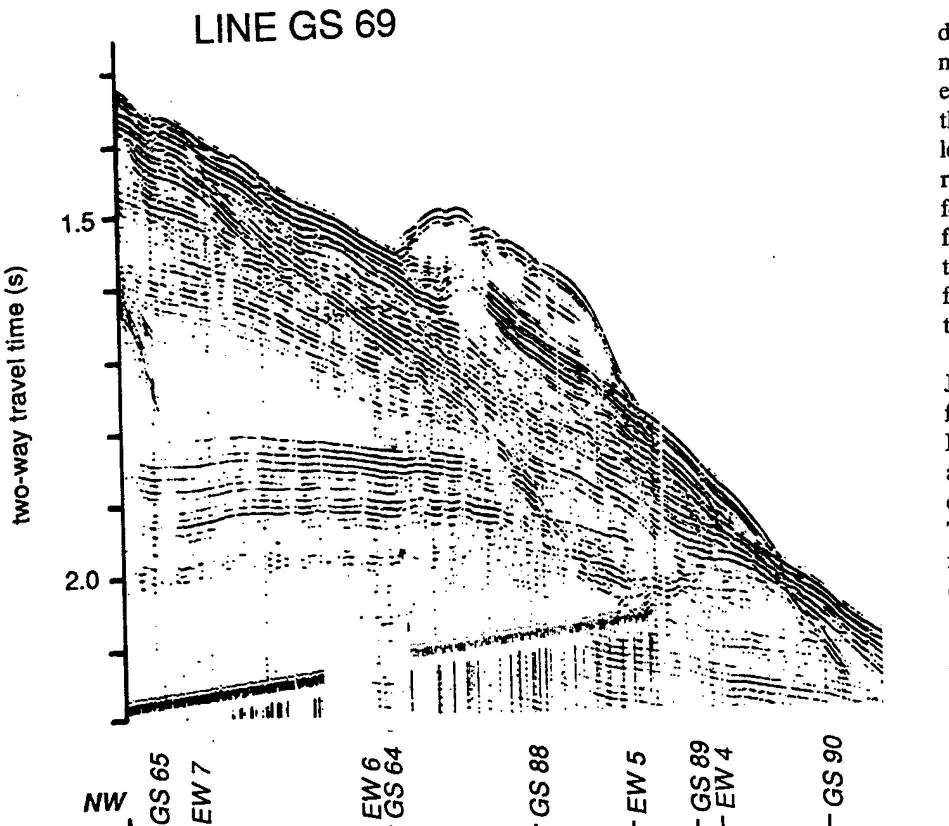

Figure 8A. Example dip line GS 69, collected by the U.S. Geological Survey (Robb and others, 1981). Location of profile is shown in Figure 10. Seismic sequences are tied to published stratigraphy for DSDP Site 612 (Shipboard Scientific Party, 1987a).

deposition appears to have led to the abandonment and infilling of the buried Pleistocene canyons between Carteret and Hendrickson Canyon. As discussed in the downslope erosion model above, the increased sedimentation may have also led to the initiation and growth of many of the submarine canyons that occur in the area today.

An example of where shifting shelf-edge depocenters apparently have initiated submarine canyons is the Ebro margin off northeastern Spain. Lateral shifts in the location of the Ebro River during the Plio-Pleistocene led to the formation of shelf-edge deltas (Farran and Maldonado, 1990), in front of which formed submarine canyons that fed deep-sea fans (Field and Gardner, 1990). At least four to five such canyons are believed to have formed as a consequence of the movement of this one river (Bellaiche and others, 1981).

The Ebro margin is also similar to the New Jersey margin in that some of these canyons feed directly into channels that cross the Ebro rise, while others empty into debris aprons at the base of the slope (Bellaiche and others, 1981; Alonso and others, 1985). Those canyons that feed into channels on the rise only occur seaward of former shelf-edge deltas. This has led Nelson and Maldonado (1988) to suggest that the submarine canyons that empty into debris aprons were formed by mass wasting along parts of the margin removed from significant deltaic sedimentation.

The debris aprons and lack of channel development in front of many of the submarine canyons on the New Jersey slope could similarly be interpreted to signify that canyon formation has largely been the consequence of erosion by mass wasting rather than sediment flows. Differences exist between the Ebro and New Jersey margins, however. Along the Ebro margin, interleaving of channel-levee complexes seaward of the canyons suggests that each shelf-edge depocenter fed only one canyon at a time (Alonso and others, 1990). In contrast, along the New Jersey margin, the large number of present-day canyons and the occurrence of several canyons along a number of the slope-wide unconformities suggest that multiple canyons actively transported shelf-derived materials during the same periods. And although slide debris has been cored on the upper rise offshore New Jersey seaward of canyons that end at the base, so have Plio-Pleistocene turbidites containing shallow-water fauna (Shipboard Scientific Party, 1987b, 1987c). This suggests that all of the canyons in the study area periodically issued sediment flows initiated along the shelf edge and upper slope.

Rather than a lack of sediment supply, the sparcity of channels on the upper rise in the study area may be the result of overlapping sediment delivery from many closely spaced canyons active during the same period. The chaotic nature of the Pliocene and Pleistocene sequences underlying the upper rise

Figure 8B. Example dip line GS 77, collected by the U.S. Geological Survey (Robb and others, 1981). Seismic sequences are tied to published stratigraphy for the AMCOR 6021 borehole (Poag, 1985) and the COST B-3 borehole (Poag, 1985).

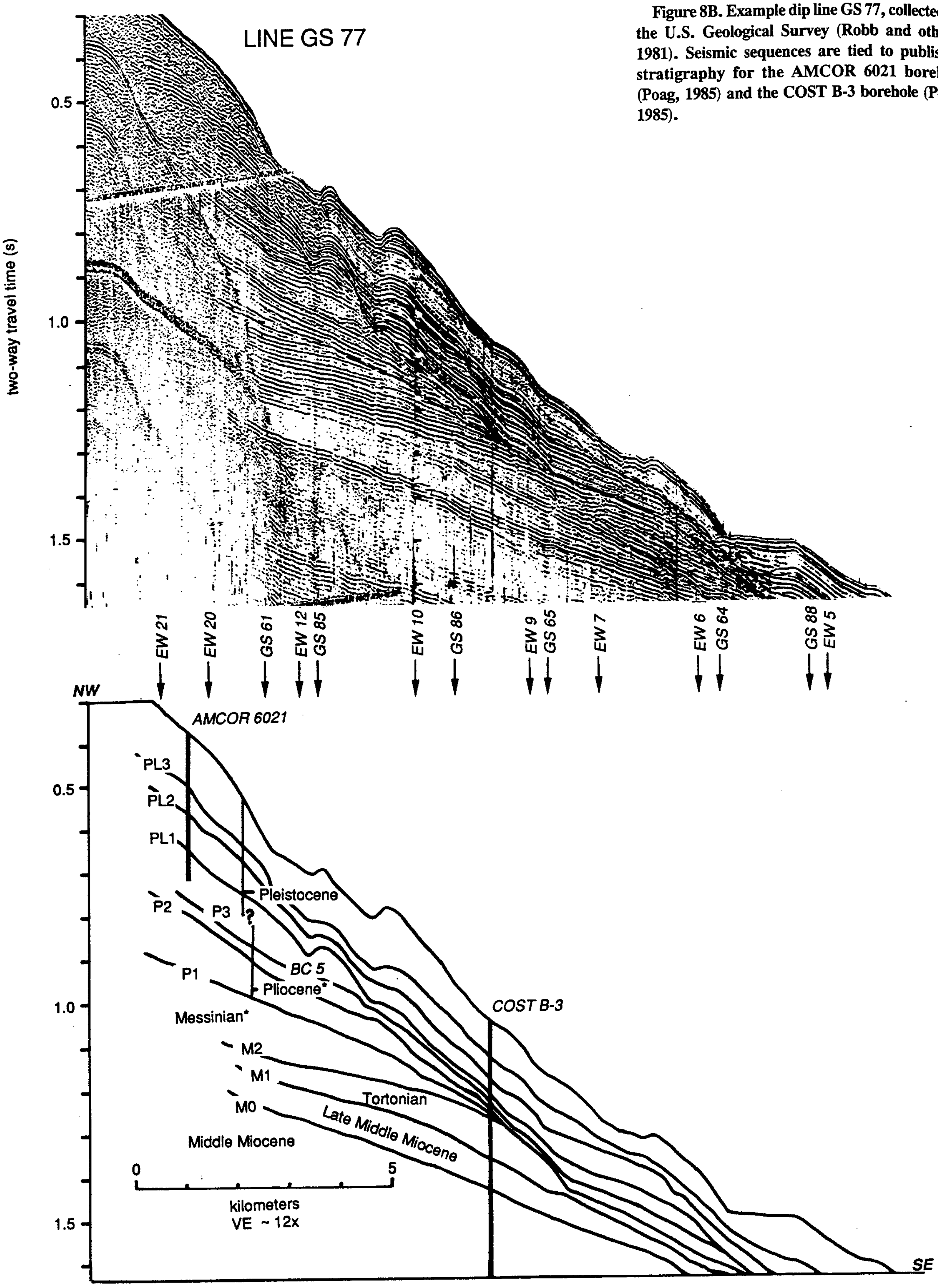

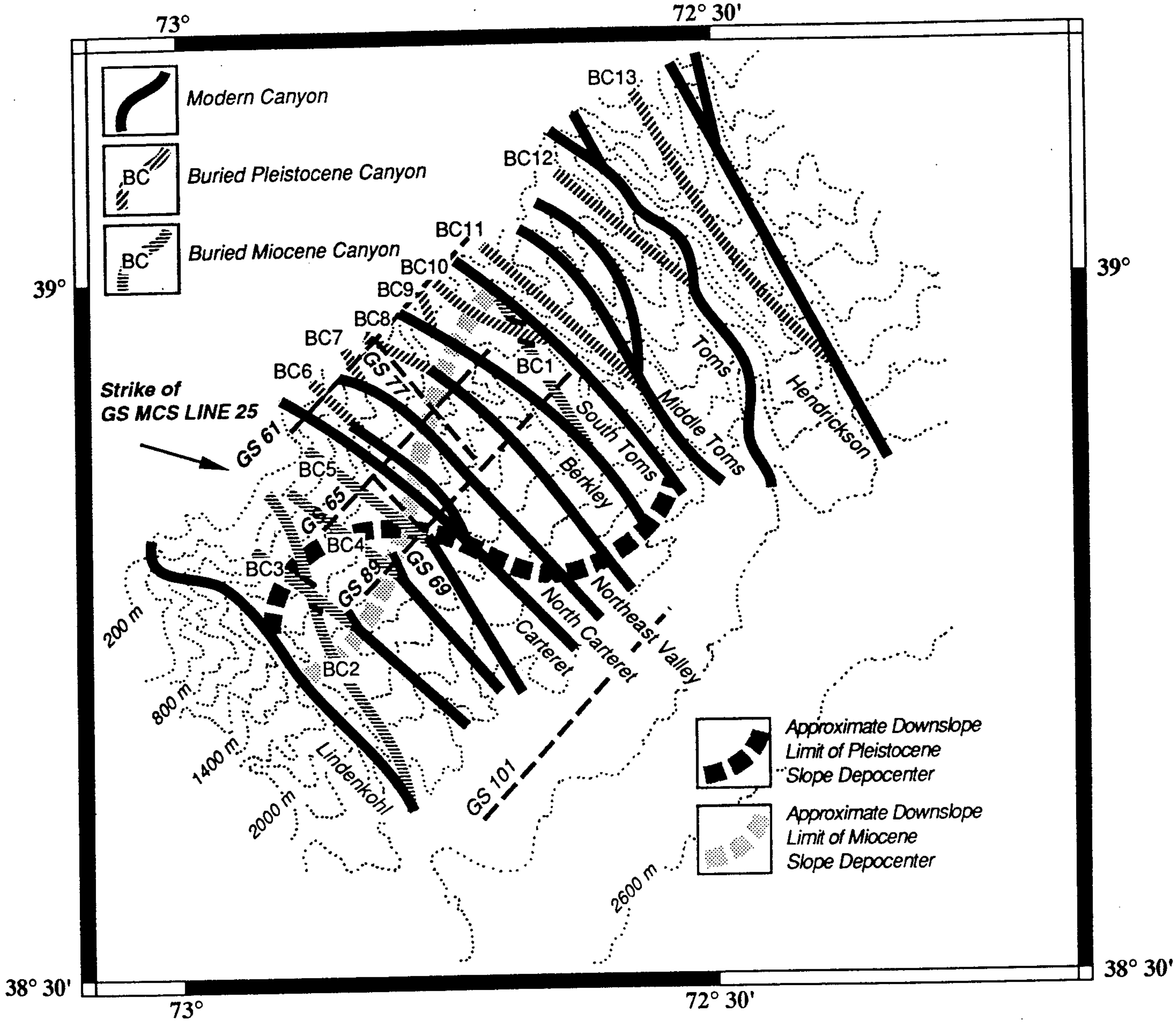

Figure 9. Map view of the distribution of modern and buried canyons within the study area. Also shown are the downslope limits of the mid- to upper Miocene and Pleistocene slope depocenters. Downslope limits are approximate and represent where strata of those ages are <0.05-s (two-way travel time) thick. Note that although buried canyons cross buried canyons, none of the modern canyons cross a buried canyon. Rather the modern canyons truncate the buried canyons and then must follow the former path of the buried canyons to the base of the slope. Buried Miocene canyons occur in the vicinity of the Miocene depocenter to the southwest, and buried Pleistocene canyons occur in the vicinity of the Pleistocene depocenter to the northeast.

suggests that the linear depressions seaward of many of the canyons are ephemeral features. These linear depressions could represent an early stage of channel development, formed by one or several sediment flows issued from a canyon. Further channel development is then arrested by erosion and deposition by sediment flows issued from adjacent canyons. More mature channels may only form seaward of canyons where sediment flows are frequent enough to outcompete flows from adjacent canyons, acting to preserve and further channel growth.

Although sediment input from the multiple canyons in the study area has possibly inhibited channel development near the base of the slope, it appears to have fostered the erosion of a "master channel" farther seaward on the rise. As noted above, the trails of high acoustic backscatter seen in the GLORIA imagery are most likely caused by tracts of coarse debris that lead from the submarine canyons out onto the rise. The distribution of this debris reveals the paths followed by sediment flows upon issuing from the canyons. Schlee and Robb (1991) have mapped these paths to gather ~100 km seaward into the large, erosional, Wilmington Deep-Sea Valley. In the absence of a single major canyon, the New Jersey Canyons, along with canyons along

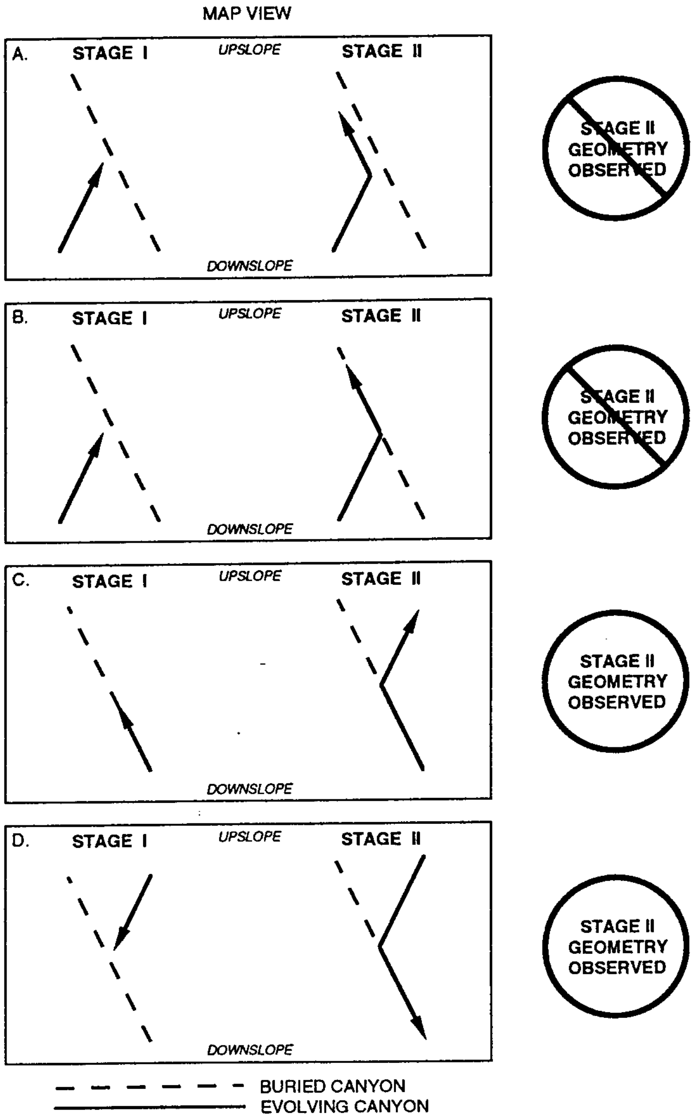

Figure 10. Map view schematic of possible ways a canyon eroding the slope would respond upon encountering a buried canyon: (A) upslope-eroding canyon encounters a buried canyon filled with sediments more difficult to erode than the surrounding slope, (B) upslope-eroding canyon encounters a buried canyon filled with sediments more easily eroded than the surrounding slope, (C) upslope-eroding canyon erodes up a buried canyon but then changes course and cuts a new path toward the shelf break, and (D) downslope-eroding canyon is captured by a sea-floor trough overlying a buried canyon. Scenarios C and D reproduce the confluence geometry between existing and buried canyons observed in the study area.

the Delaware slope to the south, appear to have formed a line source, along which the occurrence of episodic sediment flows issuing from the multiple canyons collectively eroded the Wilmington Deep-Sea Valley.

Topography and Submarine Canyon Initiation

Parallels exist between the way sea-floor topography (for example, the troughs over the buried canyons) appears to have influenced the formation of slope-crossing canyons offshore New Jersey, and the way Horton (1945) envisions that land topography influences the formation of streams and rivers. On land, variations in hillslope topography focus precipitation runoff, which results in the erosion of a series of small channels, known as rills. Through pirating and slope failure, some rills grow at the expense of others until a master channel is formed. The initial slope is then replaced by slopes that slant toward a main drainage line. These become subject to erosion as well, resulting in the development of tributaries and the expansion of the channel's drainage area.

Aspects of Horton's (1945) theory may be applicable to the submarine environment. Sediment flows initiated on the upper slope could begin unconfined and then become channelized by topography that directs their course downslope. In intercanyon areas, sediment-flow channelization may at first cause the erosion of a number of slope rills. Randomness in the location at which sediment flows initiate and the erosion each sediment flow causes, however, should lead some slope rills to deepen and widen faster than their neighbors. This would result in the failure of divides between slope rills and the piracy of adjacent sediment drainage. The eventual focusing of sediment drainage into a single slope conduit may lead to the formation of a submarine canyon.

Such early canyon development appears to be occurring on the slope divide between Lindenkohl and Carteret Canyon (Fig. 4). In this region, at least eleven slope rills initiate on the upper slope between 250- and 500-m water depth. When traced downslope, many of the slope rills join with their neighbors to form several broader slope rills by about the 1,300-m isobath. The broader slope rills shoal across the middle slope, possibly because of the greater erosional resistance of the more-lithified middle Miocene and Eocene strata that occur just beneath the thinning cover of Pleistocene sediments. The slope rills then enter three of the box-shaped canyons on the lower slope (~1,500 m) thought to have formed by mass wasting along diagenetic fractures in exposed Eocene chalk.

Other areas of New Jersey Slope illustrate that even after burial, topography can continue to influence where canyon initiation occurs. Buried topography in the study area has imposed a topographic grain to the continental slope surface. This grain appears to have anchored canyon formation at specific sites along the slope. Repeated canyon formation at these sites likely contributed to the size difference between the buried submarine canyons and the canyons that exist today. Only two buried canyons (BC9 and BC10 along the P2 unconformity between South Toms and Berkley Canyons, Fig. 7A) approach the size of the modern canyons, and none incise older substratum as deeply (Figs. 7A–7C). This suggests that the erosion that produced the relief of the modern canyons was not achieved by the latest phase of

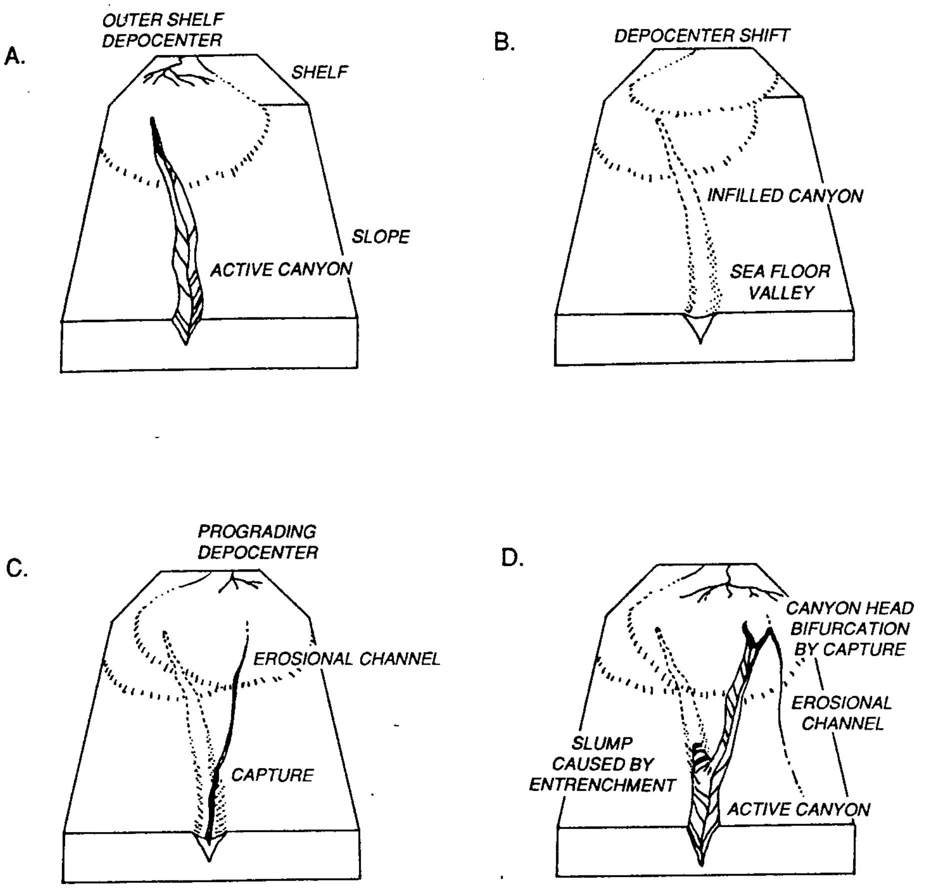

Figure 11. Schematic model of how the interaction between existing and buried canyons in the study area is thought to have developed. (A) Former canyons transported failed, upper-slope sediments from shelf-edge depocenters to the deep sea. (B) Former canyons began to infill when slope sedimentation diminished, probably during sea-level highstands. (C) With the resumption of high-slope sedimentation rates along a new section of the margin due to a shift in depocenter location, sediment flows induced by slope failure began to cut erosional channels, which in some cases were captured by sea-floor troughs formed over buried canyons. (D) Where continued slope failure led to repeated sediment flows, erosional channels matured into canyons that eventually excavated and deepened the underlying buried canyons.

canyon formation but was contributed to by one or more phases of canyon formation in approximately the same locations (for example, cyclic canyon cut and fill [Ryan and others, 1978]).

CONCLUSIONS

The re-use of existing downslope conduits by the present-day canyons offshore New Jersey is evidence for the initiation of the canyons by the downslope erosion of sediment flows begun along the shelf break and upper slope. This type of canyon formation was first proposed by Daly (1936) and later refined by others studying contemporary processes in active submarine canyons (Shepard, 1981). More recent investigations have shown that there do appear to be submarine canyons that have grown from slope failures (Orange and Breen, 1992). The findings of this study, however, do not support the present working hypothesis of Farre and others (1983) that slope-crossing canyons on the New Jersey slope were initiated and evolved from retrograding sea-floor failures begun on the continental slope.

The important role of mass wasting in triggering sediment flows makes clear that the initiation of the canyons studied offshore New Jersey cannot be attributed exclusively to either slope failure or sediment-flow erosion. Rather, it is likely that each process had a specific role in submarine canyon formation. As reviewed here, mass wasting initiated the subsea sediment flows that began canyon formation and enhanced canyon growth by widening the canyons through retrogressive sea-floor failures (for example, the gullying of canyon walls observed by Farre and others [1983]). Subsea sediment flows on the other hand generated submarine canyons, for the path their erosion took downslope determined the course along which canyon development ensued.

Abandonment and infilling of buried canyons offshore New Jersey appear to have occurred in association with shifts in the location of shelf-edge depocenters. Modern canyons may also have been initiated by the depocenter movements, which were likely brought about during changes in sea level. This study has principally relied on geophysical data, however, and the timing of canyon formation remains speculative. Until a more complete understanding of the stratigraphy of the New Jersey slope is achieved, it will not be possible to establish the temporal relation between sea level, sediment supply, and canyon formation offshore New Jersey.

ACKNOWLEDGMENTS

This study represents part of Pratson's Ph.D. dissertation at Columbia University. Thanks is extended to W. Haxby for his perspective images of the New Jersey slope and rise constructed from the SeaBeam bathymetry. The initial manuscript benefited from the suggestions of C. Pirmez, N. Driscoll, and B. Coakley. Reviews by S. O'Connell and D. Gorsline helped to clarify points in the manuscript and to place the study findings in the context of earlier investigations of submarine canyons. Funds for this study were provided by the National Science Foundation (Grant No. OCE 88-17563) and the Office of Naval Research (Contract No. N0014-87-K-0204).

REFERENCES CITED

Alonso, B., Kastens, K. A., Maldonado, A., Malinverno, A., Nelson, C. H., O'Connell, S., Palanques, A., and Ryan, W.B.F., 1985, Morphology of the Ebro Fan valleys from SeaMARC and Sea Beam Profiles: Geo-Marine Letters, v. 5, p. 141–148.

Alonso, B., Field, M. E., Gardner, J. V., and Maldonado, A., 1990, Sedimentary evolution of the Pliocene and Pleistocene Ebro margin, northeastern Spain: Marine Geology, v. 95, p. 313–331.

Bellaiche, G., Droz, L., Aloisi, J. L., Bouye, G., Got, H., Monaco, A., Maldonado, A., Serra-Raventos, J., and Mirabile, L., 1981, The Ebro and the Rhone deep-sea fans; first comparative study: Marine Geology, v. 43, p. M75–M85.

Chamberlain, T. K., 1964, Mass transport of sediment in the heads of Scripps Submarine Canyon, California, *in* Miller, R., ed., Papers in marine geology, Shepard Commemorative Volume: New York, Macmillan, p. 42–64.

Coleman, J. M., Prior, D. B., and Lindsay, J. F., 1983, Deltaic influences on shelfedge instability processes, *in* Stanley, D. J., and Moore, G. T., eds., The shelf-break: Critical interface on continental margins: Society of Economic Paleontologists and Mineralogists Special Publication No. 33, p. 121–137.

Colman, S. M., Halka, J. P., Hobbs, C. H., Mixon, R. B., and Foster, D. S., 1990, Ancient channels of the Susquehanna River beneath Chesapeake Bay and the Delmarva Peninsula: Geological Society of America Bulletin, v. 102, p. 1268–1279.

Daly, R. A., 1936, Origin of submarine "canyons": American Journal of Science, Ser. 5, v. 31, p. 401–420.

Dana, J. D., 1863, A manual of geology: London, England, Truber, 798 p.

Dill, R. F., 1964, Sedimentation and erosion in Scripps Submarine Canyon head, *in* Miller, R., ed., Papers in marine geology, Shepard Commemorative Volume: New York, Macmillan, p. 23–41.

Dillon, W. P., and Oldale, R. N., 1978, Late Quaternary sea-level curve: Reinterpretation based on glaciotectonic influence: Geology, v. 6, p. 56–60.

Dingle, R. V., and Robson, S., 1985, Slumps, canyons and related features on the continental margin off East London, SE Africa (SW Indian Ocean): Marine Geology, v. 67, p. 37–54.

Drake, D. E., Hatcher, P. G., and Keller, G. M., 1978, Suspended particulate matter and mud deposition in upper Hudson Submarine Canyon, *in* Stanley, D. J., and Kelling, G. E., eds., Sedimentation in submarine canyons, fans and trenches: Stroudsburg, Pennsylvania, Dowden, Hutchinson and Ross, p. 33–41.

Emery, K. O., 1968, Relict sediments on continental shelves of the world: American Association of Petroleum Geologists Bulletin, v. 52, p. 445–464.

Emery, K. O., and Uchupi, E., 1972, Western North Atlantic, topography, rocks, structure, water, life, and sediments: American Association of Petroleum Geologists Memoir 17, 532 p.

Emery, K. O., and Uchupi, E., 1984, The geology of the Atlantic Ocean: New York, Springer-Verlag, 1,050 p.

Ericson, D. B., Ewing, M., Wollin, G., and Heezen, B. C., 1961, Atlantic deep-sea sediment cores: Geological Society of America Bulletin, v. 72, p. 193–268.

Ewing, J. I., LePichon, X., and Ewing, M., 1963, Upper stratification of Hudson apron region: Journal of Geophysical Research, v. 68, p. 6303–6316.

Farran, M., and Maldonado, A., 1990, The Ebro continental shelf, Quaternary seismic stratigraphy and growth patterns, *in* Nelson, C. H., and Maldonado, A., eds., Marine geology of the Ebro continental margin, northwestern Mediterranean Sea: Marine Geology, v. 95, p. 289–312.

Farre, J. A., 1985, The importance of mass wasting processes on the continental slope [Ph.D. dissert.]: New York, Columbia University, 226 p.

Farre, J. A., McGregor, B. A., Ryan, W.B.F., and Robb, J. M., 1983, Breaching the shelf-break: Passage from youthful to mature phase in submarine canyon evolution, *in* Stanley, D. J., and Moore, G. T., eds., The shelf-break: Critical interface on continental margins: Society of Economic Paleontologists and Mineralogists Special Publication No. 33, p. 25–39.

Felix, D. W., and Gorsline, D. S., 1971, Newport Submarine Canyon, California; An example of the effects of shifting loci of sand supply upon canyon position: Marine Geology, v. 10, p. 177–198.

Field, M. E., and Gardner, J. V., 1990, Pliocene-Pleistocene growth of the Rio Ebro margin, northeast Spain: A prograding-slope model: Geological Society of America Bulletin, v. 102, p. 721–733.

Gorsline, D. S., 1970, Submarine canyons; an introduction: Marine Geology, v. 8, p. 183–186.

Grow, J. A., Hutchinson, D. R., Klitgord, K. D., Dillon, W. P., and Schlee, J. S., 1983, Representative multichannel seismic profiles over the U.S. Atlantic continental margin: American Association of Petroleum Geologists Studies in Geology No. 15, v. 2, p. 2.2.3-1–2.2.3-19.

Hathaway, J. C., Schlee, J. S., Poag, C. W., Valentine, P. C., Weed, E.G.A., Bothner, M. H., Kohout, F. A., Manheim, F. T., Schoen, R., Miller, R. E., and Schultz, D. M., 1976, Preliminary summary of the 1976 Atlantic Margin Coring Project of the U.S. Geological Survey: U.S. Geological Survey Open-File Report 76-844, 217 p.

Heezen, B. C., and Ewing, M., 1952, Turbidity currents and submarine slumps and the 1929 Grand Banks earthquake: American Journal of Science, v. 250, p. 849–873.

Hollister, C. D., Ewing, J. I., Habib, D., Hathaway, J. C., Lancelot, Y., Luterbacher, H., Paulus, F. J., Poag, C. W., Wilcoxon, J. A., and Worstell, P., 1972a, Site 108—Continental slope, *in* Hollister, C. D., Ewing, J. I., and others, Initial reports of the Deep Sea Drilling Project, Volume 11: Washington, D.C., U.S. Government Printing Office, p. 357–364.

Hollister, C. D., Ewing, J. I., Habib, J. C., Lancelot, Y., Luterbacher, H., Paulus, F. J., Poag, C. W., Wilcoxon, J. A., and Worstell, P., 1972b, Site 106, *in* Hollister, C. D., Ewing, J. I., and others, Initial reports of the Deep Sea Drilling Project, Volume 11: Washington, D.C., U.S. Government Printing Office, p. 313–349.

Horton, R. E., 1945, Erosional development of streams and their drainage basins: Hydrophysical approach to quantitative morphology: Geological Society of America Bulletin, v. 56, p. 275–370.

Hughes-Clarke, J. E., 1988, The geologic record of the 1929 "Grand Banks" earthquake and its relevance to deep-sea clastic sedimentation [Ph.D. dissert.]: Nova Scotia, Canada, Dalhousie University, 171 p.

Katz, M. E., and Miller, K. G., 1987, Neogene benthic foraminiferal biofacies of the New Jersey Transect, *in* Poag, C. W., Watts, A. B., and others, Initial reports of the Deep Sea Drilling Project, Volume 95: Washington, D.C., U.S. Government Printing Office, p. 299–311.

Kelling, G., and Stanley, D. J., 1970, Morphology and structure of Wilmington and Baltimore submarine canyons, eastern United States: Journal of Geology, v. 78, p. 637–660.

Kelling, G., Sheng, H., and Stanley, D. J., 1975, Mineralogic composition of sand-sized sediment on the outer margin off the mid-Atlantic states; Assessment of the influence of the ancestral Hudson and other fluvial systems: Geological Society of America Bulletin, v. 86, p. 853–862.

Klaus and Taylor, 1991, Submarine canyon development in the Izu-Bonin Forearc; a SeaMARC II and seismic survey of Aoga Shima Canyon: Marine Geophysical Researches, v. 13, p. 105–130.

Knebel, H. J., and Spiker, E., 1977, Thickness and age of surficial sand sheet, Baltimore Canyon Trough Area: American Association of Petroleum Geologists Bulletin, v. 61, p. 861–871.

Knebel, H. J., Wood, S. A., and Spiker, E. C., 1979, Hudson river, evidence for extensive migration on the exposed continental shelf during Pleistocene time: Geology, v. 7, p. 254–258.

Kuenen, Ph. H., 1937, Experiments in connection with Daly's hypothesis on the formation of submarine canyons: Leidshe Geologische Mededelingen, v. 8, p. 327–351.

McGregor, B. A., 1985, Role of submarine canyons in shaping the rise between Lydonia and Oceanographer canyons, Georges Bank: Marine Geology, v. 62, p. 277–293.

McHugh, C. M., Ryan, W.B.F., and Schreiber, B. C., 1993, The role of diagenesis in exfoliation of submarine canyons: American Association of Petroleum Geologists Bulletin, v. 77, p. 145–172.

Miller, K. G., Melillo, A. J., Mountain, G. S., Farre, J. A., and Poag, C. W., 1987, Middle to late Miocene canyon cutting on the New Jersey continental slope: Biostratigraphic and seismic stratigraphic evidence: Geology, v. 15, p. 509–512.

Milliman, J. D., Jiezao, Z., Anchun, L., and Ewing, J. I., 1990, Late Quaternary sedimentation on the outer and middle New Jersey continental shelf; result of two local deglaciations?: Journal of Geology, v. 98, p. 966–976.

Mountain, G., 1987, Cenozoic margin construction and destruction offshore New Jersey, *in* Ross, C., and Haman, D., eds., Cushman Foundation for Foraminiferal Research Special Publication 24, p. 57–83.

Mountain, G., 1991, Cenozoic slope failure offshore New Jersey inferred from seismic, litho-, and bio-stratigraphy: Eos (American Geophysical Union Transactions), v. 72, p. 164.

Nelson, C. H., and Maldonado, A., 1988, Factors controlling depositional patterns of Ebro turbidite systems, Mediterranean Sea: American Association of Petroleum Geologists Bulletin, v. 72, p. 698–716.

O'Leary, D. W., 1986, The Munson-Nygren Slide: A major lower-slope slide off Georges Bank: Marine Geology, v. 72, p. 101–114.

Orange, D. L., and Breen, N. A., 1992, The effects of fluid escape on accretionary wedges 2. Seepage force, slope failure, headless submarine canyons, and vents: Journal of Geophysical Research, v. 97, p. 9277–9295.

Poag, C. W., 1985, Depositional history and stratigraphic reference section for the central Baltimore Canyon trough, *in* Poag, C. W., ed., Geologic evolution of the United States Atlantic margin: New York, Van Nostrand Reinhold, p. 217–264.

Poag, C. W., and Mountain, G. S., 1987, Late Cretaceous and Cenozoic evolution of the New Jersey continental slope and upper rise: An integration of borehole data with seismic reflection profiles, *in* Poag, C. W., Watts, A. B., and others, Initial reports of the Deep Sea Drilling Project, Volume 95: Washington, D.C., U.S. Government Printing Office, p. 673–724.

Poag, C. W., and Sevon, W. D., 1989, A record of Appalachian denudation in postrift Mesozoic and Cenozoic sedimentary deposits of the U.S. middle Atlantic continental margin: Geomorphology, v. 2, p. 119–157.

Pratson, L. F., Ryan, W., Miller, K., Farre, J., Pirmez, C., Wright, J., Moran, K., McHugh, C., Edwards, M., Mars, H., Hall, F., Christensen, B., and Barone, A., 1989, Ground-truthing side-scan sonar imagery, bathymetry and seismic reflection profiles of the New Jersey continental slope [abs.]: Eos (American Geophysical Union Transactions), v. 70, p. 1346.

Prior, D. B., Coleman, J. M., and Doyle, E. H., 1984, Antiquity of the continental slope along the middle Atlantic margin of the United States: Science, v. 223, p. 926–928.

Robb, J. M., Hampson, J. C., Kirby, J. R., and Twichell, D. C., 1981, Geology and potential hazards of the continental slope between Lindenkohl and South Toms canyons, offshore mid-Atlantic states: U.S. Geological Survey Open-File Report 81-600, p. 1–33.

Ryan, W.B.F., Cia, M. B., Miller, E. L., Hanselman, D., Nesteroff, W. D., Hecker, B., and Nibbelink, M., 1978, Bedrock geology in New England submarine canyons: Oceanologica Acta, v. 1, p. 233–254.

Schlee, J. S., and Robb, J. M., 1991, Submarine processes of the middle Atlantic continental rise based on GLORIA imagery: Geological Society of America Bulletin, v. 103, p. 1090–1103.

Scholle, P. A., ed., 1980, Geological studies of the COST No. B-3 well, United States Mid-Atlantic Continental Slope area: U.S. Geological Survey Circular 833, 132 p.

Seeber, L., and Armbruster, J. G., 1988, Seismicity along the Atlantic seaboard of the U.S.; Intraplate neotectonics and earthquake hazards, *in* Sheridan, R. E., and Grow, J. A., eds., The geology of North America, Volume I-2, The Atlantic Continental Margin, U.S.: Boulder, Colorado, Geological Society of America, p. 565–582.

Shepard, F. P., 1934, Canyons off the New England Coast: American Journal of Science, v. 27, p. 24–36.

Shepard, F. P., 1981, Submarine canyons; multiple causes and long-time persistence: American Association of Petroleum Geologists Bulletin, v. 65, p. 1062–1077.

Shepard, F. P., and Dill, R. F., 1966, Submarine canyons and other sea valleys: Chicago, Rand McNally, 381 p.

Shepard, F. P., Curray, J. R., Inman, D. L., Murray, E. A., Winterer, E. L., and Dill, R. F., 1964, Submarine geology by diving saucer: Science, v. 145, p. 1042–1046.

Shepard, F. P., Marshall, N. F., McLoughlin, P. A., and Sullivan, G. G., 1979, Currents in submarine canyons and other sea-valleys: American Association of Petroleum Geologists Studies in Geology No. 8, 173 p.

Shipboard Scientific Party, 1987a, Site 612, *in* Poag, C. W., Watts, A. B., and others, Initial reports of the Deep Sea Drilling Project, Volume 95: Washington, D.C., U.S. Government Printing Office, p. 31–153.

Shipboard Scientific Party, 1987b, Site 613, *in* Poag, C. W., Watts, A. B., and others, Initial reports of the Deep Sea Drilling Project, Volume 95: Washington, D.C., U.S. Government Printing Office, p. 155–241.

Shipboard Scientific Party, 1987c, Sites 604 and 605, *in* van Hinte, J. E., Wise, S. W., and others, Initial reports of the Deep Sea Drilling Project, Volume 93: Washington, D.C., U.S. Government Printing Office, p. 277–413.

Shor, A. N., and McClennen, C. E., 1988, Marine physiography of the U.S. Atlantic margin, *in* Sheridan, R. E., and Grow, J. A., eds., The geology of North America, Volume I-2, The Atlantic Continental Margin, U.S.: Boulder, Colorado, Geological Society of America, p. 9–18.

Spencer, J. W., 1903, Submarine valleys off the American coasts and in the North Atlantic: Geological Society of America Bulletin, v. 14, p. 207–226.

Stanley, D. J., Addy, S. K., and Behrens, E. W., 1983, The mudline; variability of its position relative to shelfbreak, *in* Stanley, D. J., and Moore, G. T., eds., The shelf-break: Critical interface on continental margins: Society of Economic Paleontologists and Mineralogists Special Publication No. 33, p. 279–298.

Stanley, D. J., Nelsen, T. A., and Stuckenrath, R., 1984, Recent sedimentation on the New Jersey slope and rise: Science, v. 226, p. 125–133.

Twichell, D. C., and Roberts, D. G., 1982, Morphology, distribution and development of submarine canyons on the United States Atlantic continental slope between Hudson and Baltimore canyons: Geology, v. 10, p. 408–412.

Twichell, D. C., Knebel, H. J., and Folger, D. W., 1977, Delaware River; evidence for its former extension to Wilmington Submarine Canyon: Science, v. 195, p. 438–485.

Vail, P. R., Mitchum, R. M., Jr., Todd, R. G., Widmier, J. M., Thompson, S., III, Sangree, J. B., Bubb, J. N., and Hatlelid, W. G., 1977, Seismic stratigraphy and global changes of sea level, *in* Payton, C. E., ed., Seismic stratigraphy—applications to hydrocarbon exploration: American Association of Petroleum Geologists Memoir 26, p. 49–212.

Veatch, A. C., and Smith, P. A., 1939, Atlantic submarine valleys of the United States and the Congo Submarine Valley: Geological Society of America Special Paper 7, 101 p.

Manuscript Received by the Society December 11, 1992
Revised Manuscript Received June 14, 1993
Manuscript Accepted July 6, 1993
Lamont-Doherty Earth Observatory Contribution No. 5145

Printed in U.S.A.

JOURNAL OF GEOPHYSICAL RESEARCH, VOL. 99, NO. B7, PAGES 13,997–14,012, JULY 10, 1994

The length-scaling properties of topography

Jeffrey K. Weissel and Lincoln F. Pratson
Lamont-Doherty Earth Observatory of Columbia University, Palisades, New York

Alberto Malinverno
Schlumberger-Doll Research, Ridgefield, Connecticut

Abstract. The scaling properties of synthetic topographic surfaces and digital elevation models (DEMs) of topography are examined by analyzing their "structure functions," i.e., the qth order powers of the absolute elevation differences: $\Delta h_q(l) = E\{|h(x+l) - h(x)|^q\}$. We find that the relation $\Delta h_1(l) \approx cl^H$ describes well the scaling behavior of natural topographic surfaces, as represented by DEMs gridded at 3 arc sec. Average values of the scaling exponent H between ~0.5 and 0.7 characterize DEMs from Ethiopia, Saudi Arabia, and Somalia over 3 orders of magnitude range in length scale l (~0.1-150 km). Differences in apparent topographic roughness among the three areas most likely reflect differences in the amplitude factor c. Separate determination of scaling properties in the x and y coordinate directions allows us to assess whether scaling exponents are azimuthally dependent (anisotropic) or whether they are isotropic while the surface itself is anisotropic over a restricted range of length scale. We explore ways to determine whether topographic surfaces are characterized by simple or multiscaling properties. The difference between scaling exponents of $\Delta h_1(l)$ and $\sqrt{\Delta h_2(l)}$ for the DEMs is small, but positive, and such divergence in the scaling exponents of the structure functions is consistent with multiscaling behavior. Exceedance and perimeter sets of fractional Brownian surfaces fail to yield the trivial fractal dimensions expected of sets of known monofractals, suggesting a practical limitation arising from the use of finite resolution data sets in the analysis. By comparing the hypsometry of "real" topography (represented as DEMs) with that of fractional Brownian surfaces, we show that synthetic surfaces based on Gaussian statistics are limited as models for natural topography. Hypsometric curves, which probably reflect the relative importance of tectonic and erosional processes in shaping topography, clearly show that statistical moments higher than the second are important in describing topographic surfaces. Scaling analysis is a valuable tool for assessing the quality and accuracy of DEM representations of the Earth's topography.

Introduction

Many natural surfaces evolve under processes that add and/or remove material. A familiar example is the Earth's surface. In this case, however, only limited success has been achieved in establishing a quantitative understanding of the processes important to its evolution. Information on processes that shape many natural surfaces is provided through their space- and time-scaling properties [*Family and Vicsek*, 1991]. Therefore much effort has been directed in recent years toward determining and understanding the scaling properties of topographic and other natural surfaces.

Vening Meinesz [1951] showed that the power spectral density of topographic amplitude decayed according to a power law at an approximately uniform rate over a broad wavelength range. This early study and others reviewed later provide the basis for believing that Earth's topography possesses length-scaling properties over a wide range of scales.

The purpose of this paper is to develop a better understanding of the scaling properties of topography through analyses of synthetic surfaces and digital elevation models (DEMs) of topography. A definition of scaling properties is presented, followed by a discussion of the analytical techniques that permit their determination and a summary of knowledge about the scaling properties of topography from previous work. We mainly employ an analytical technique which examines scaling properties of elevation increments, or topographic relief. This technique is applied to a planar surface, simulated fractional Brownian surfaces, and DEMs

Paper number 94JB00130.
0148-0227/94/94JB-00130$05.00

to illustrate how anisotropy affects the scaling properties of natural surfaces and how it can be quantified. Synthetic surfaces and DEMs are then examined empirically for statistical indications that allow the distinction between simple and multiscaling behavior (characteristic of monofractal functions, and multifractal fields, respectively). Finally, the hypsometry of natural surfaces is compared to that of fractional Brownian surfaces in order to show the limitations of synthetic surfaces based on Gaussian statistics as models for topography.

Scaling Properties and Their Determination

What is meant by scaling, or more aptly, scale invariance? The short answer is that phenomena which lack a characteristic or intrinsic length scale are called "scaling functions". *Feder* [1988, p. 26] provides a useful definition, citing that functions $f(s)$ which satisfy the homogeneity relation

$$f(\lambda s) = \lambda^{\alpha} f(s) \tag{1}$$

for all positive values of the scale factor λ, are called scaling functions. This is a broad definition, encompassing multivalued as well as single valued functions and self-similar as well as self-affine scaling behavior. Note that in (1), the scaling exponent α is constant and independent of s, which in this study will have units of length. The power law function

$$f(s) = cs^{\alpha}, \tag{2}$$

for example, satisfies (1). A definition more applicable to multidimensional functions that allows for anisotropy in scaling properties is [*Family and Vicsek,* 1991]

$$f(\lambda_1 s_1, \lambda_2 s_2, ...) = \lambda_1^{\alpha_1} \lambda_2^{\alpha_2} ... f(s_1, s_2, ...). \tag{3}$$

In general, a topographic surface is defined as a collection of height or elevation values $h(\mathbf{x})$ distributed in two dimensions, where $\mathbf{x}$ is a vector denoting position, i.e., $\mathbf{x} = (x_1, x_2)$. In this paper we examine the scaling properties of topography through the determination of "structure functions" [*Monin and Yaglom,* 1971; *Parisi and Frisch,* 1985]. Specifically, we consider how topographic relief, defined here as the absolute elevation difference between pairs of points separated by a "lag" vector $\mathbf{l} = (l_1, l_2)$, varies with the distance or length scale over which it is measured. The qth order structure function of topography is defined as

$$\Delta h_q(\mathbf{l}) \equiv E\{|h(\mathbf{x}+\mathbf{l}) - h(\mathbf{x})|^q\}, \tag{4}$$

where $E\{\cdot\}$ is the expected value operator and q is an exponent that takes positive values. In this paper, we restrict our attention to values for q of 1 and 2. For $q = 1$, Δh_1 is the expected value of the absolute elevation differences (or topographic relief). For $q = 2$, Δh_2 is the expected value of the squares of the elevation differences, and it is also known as the "variogram" [*Journel and Huijbregts,* 1978].

In practice, we must analyze finite samples of topographic surfaces. As a consequence, we estimate $\Delta h_q(\mathbf{l})$ from

$$\widehat{\Delta h}_q(\mathbf{l}) = \langle |h(\mathbf{x}+\mathbf{l}) - h(\mathbf{x})|^q \rangle, \tag{5}$$

where the "hat" denotes an estimate and the angular brackets denote averaging over the sample. Unless the sample size is infinite, $\widehat{\Delta h}_q(\mathbf{l})$ will not, in general, equal $\Delta h_q(\mathbf{l})$.

Notice in (4) and (5) that $\Delta h_q(\mathbf{l})$ and $\widehat{\Delta h}_q(\mathbf{l})$ depend on the vector quantity $\mathbf{l}$. There is no a priori reason for assuming that the statistical properties of topographic surfaces, including scaling properties, are isotropic. We address the anisotropy question simply by modifying (5) to examine the length-scaling properties of topography in the x_1 and x_2 coordinate directions separately. This is straightforward to do because both synthetic surfaces and DEMs commonly comprise equally spaced elevation values in rectangular arrays. For the DEMs analyzed in this paper, the x_1 direction (or simply the x direction) is east-west, and the x_2 direction (or the y direction) is north-south.

Using this approach, we investigate two kinds of anisotropy: The first is anisotropy in which the scaling properties of topography depend on the orientation $\theta = \tan^{-1}(l_2/l_1)$ of the lag vector. This case, where the exponents α_i, i=1, 2 in (3) are different, has been addressed previously by *Klinkenberg and Goodchild* [1992] using azimuth-dependent variograms. The second kind of anisotropy is the situation where topographic surfaces have isotropic scaling properties; i.e., the exponents α_1 and α_2 in (3) are equal, while the surfaces themselves are anisotropic over a defined range of length scale.

If, instead, we assume that the scaling properties of topography are effectively isotropic, the direction of the lag vector $\mathbf{l}$ does not matter, and we can rewrite (4) and (5) in terms of the distance $l = \sqrt{l_1^2 + l_2^2}$ between the observation points. From (1) and (2), scaling behavior implies that the structure functions of topography (4) should be related to length scale l through a power law such as

$$\Delta h_q(l) = c_q l^{K_h(q)}, \tag{6}$$

where coefficients c_q and the exponents $K_h(q)$ depend on q but not on l. The central question concerning the scaling properties of topography is how well they are described by (6). In other words, to what extent are the scaling properties of topographic surfaces homogeneous (i.e., independent of length scale and location)? We examine this question by using (5) to estimate the $q = 1$ and $q = 2$ structure functions of several DEM representations of topography in northeastern Africa and Arabia.

Note that if topography possesses "simple" scaling properties describable by a single scaling exponent, (6) simplifies to

$$\Delta h_q(l) = c_q l^{qH}, \tag{7}$$

and the scaling exponents of the structure functions become a simple linear function of the order q. In this case, H, the Hurst parameter, which is the scaling exponent of $\Delta h_1(l)$, is the only exponent required to describe the scaling properties of topography. The self-affine fractional Brownian surfaces first defined by *Mandelbrot and Van Ness* [1968] are familiar examples of "fractal" surfaces which possess simple scaling properties characterized by a single scaling exponent. We present simulations of fractional Brownian surfaces and examine their properties in more detail later.

A critical question remains, however. Is H in (7) sufficient by itself to describe the scaling properties of topography or do we need to examine the exponents of the higher-order structure functions in (6)? In other words, do topographic surfaces possess simple scaling or multiscaling properties? This question was addressed recently by *Lavallee et al.* [1993], who concluded that topography is indeed multiscaling and suggested some ways to distinguish multiscaling from simple scaling behavior. Here, we provide a brief, intuitive explanation of multiscaling behavior, and in a later section we report on our own analyses designed to determine whether topography is characterized by simple scaling or multiscaling properties.

Multiscaling Behavior

Muzy et al. [1991, 1993] recently presented a readily understood explanation of multiscaling behavior as applied to "fractal" signals. Let us consider a Taylor series expansion of a signal or function $s(x)$ (approximating a topographic profile) about the point x_0:

$$s(x_0+l)-s(x_0)=l\cdot s^{(1)}(x_0)+\ldots+(l^n/n!)\cdot s^{(n)}(x_0)+C\cdot|l|^{h(x_0)}+0(|l|^{h(x_0)}), \tag{8}$$

where (n) denotes the nth derivative of s. In the limit $l\to 0$, (8) indicates that $s(x)$ has a local scaling exponent h at the point x_0. Because s is differentiable n times, the value of $h(x_0)$ lies between n and $n+1$. Alternatively, we can say that $s(x)$ possesses a "singularity" of strength $n<h(x_0)<n+1$ at the point x_0. Notice that the left-hand side of (8) can be related to the elevation increments used to estimate the structure functions of topography (4) using (5). Simple scaling functions like fractional Brownian profiles are not differentiable $(n=0)$, and thus no derivative terms will appear on the right-hand side of (8). Fractional Brownian profiles are therefore singular everywhere with a uniform singularity strength $h(x)=H$, where $0<H<1$. There is, however, no a priori reason for assuming that topographic profiles (and by analogy, topographic surfaces) should be characterized by a single, spatially homogeneous singularity strength. Therefore we must allow that, in general, topographic surfaces are characterized by a range of singularity strengths (or, equivalently, local scaling exponents), and not just one. In other words, we should expect topographic surfaces to exhibit multiscaling properties.

Our purpose here is not to develop techniques for the determination of the multiscaling properties of topography but to implement some simple tests to distinguish simple scaling from multiscaling behavior. Multiscaling analysis of fractal signals generally involves the determination of the "singularity spectrum" of the signal. Briefly, this means first finding the range of singularity strengths (say, $h_{min}<h(x)<h_{max}$) present in a given signal sample, then determining the Hausdorff (fractal) dimension $D(h)$ of the subset of points associated with each singularity strength h, i.e.,

$$D(h)=dim\{x|h(x)=h\}.$$

A plot of $D(h)$ versus h yields the required singularity spectrum.

The structure function approach is but one method for doing this. However, it is only applicable to signals with $0<h(x)<1$ [*Muzy et al.*, 1993], which should generally be the case for topography. As (6) and (7) show, $K_h(q)$ depends linearly on q for simple scaling functions. For multiscaling functions, $K_h(q)$ will, in general, be a nonlinear convex function of q. The reason for this is that strong singularities (small h values) will dominate the structure function for large values of q. Singularity strength h is reflected in the gradient $d(K_h(q))/dq$, which therefore becomes less with increasing q as the stronger singularities become dominant. Thus, to demonstrate multiscaling behavior using the first- and second-order structure functions, we need to show that $2K_h(1)-K_h(2)>0$, allowing for the effects of estimation errors as discussed below. For simple scaling, the difference should not be resolvable from zero, again, subject to the estimation errors.

Estimation Errors

Returning now to (5), let us denote the error in estimating $\Delta h_q(l)$ by $\widehat{\Delta h}_q(l)$ as

$$\epsilon_q(l)=\widehat{\Delta h}_q(l)-\Delta h_q(l).$$

Generally speaking, the larger our sample size, the closer the estimate will be to the true value. A most important feature of estimation errors is whether values of $\epsilon_q(l)$ for neighboring values of l are correlated. In other words, if, say, $\epsilon_q(l_0)$ is positive, is $\epsilon_q(l_0+\Delta l)$ also likely to be positive if Δl is small? We can gain some insight into this issue for the case where $q=2$ (the second-order structure function or variogram). For a topography profile with zero mean and a finite variance σ^2, $\Delta h_2(l)$ is related to the autocovariance $C(l)$ as follows:

$$C(l)=E\{h(x)h(x+l)\}=\sigma^2-\frac{1}{2}\Delta h_2(l).$$

The estimation errors of $\widehat{C}(l)$ are reasonably well understood, and *Priestley* [1981, p. 333] has shown that the estimation errors of the sample autocovariance will be positively correlated if the autocovariance has a decaying form (which will always be the case in practice for the autocovariance of topography). We can then reasonably conclude that the estimation errors of $\widehat{\Delta h}_2(l)$ will also be positively correlated over neighboring values of l.

There are two important consequences of this result: First, if the estimation errors of $\widehat{\Delta h}_2(l)$ and, by analogy, $\widehat{\Delta h}_q(l)$ are positively correlated, then apparently systematic changes in the slope of the log-log plot of $\widehat{\Delta h}_q(l)$ versus l might be due to correlated estimation errors. Second, if one were to conclude that there was a unique slope to the log-log plot, and the mean slope and its error were obtained using a standard least squares method, the error associated with that slope might be grossly underestimated. This is because standard linear regression by least squares assumes that the errors about a best fitting straight line are uncorrelated.

This discussion of estimation errors is intended to alert the reader to be cautious in interpreting apparently systematic departures from linearity in log-log plots of structure functions of topography in terms of the length-scale dependence of geomorphic processes.

Notes

It is important at this point to note a few things which will help place our summary of previous work in perspective. First, in principle, the variogram, autocovariance function, and power spectral density are equivalent ways of expressing how the variance of topography is distributed on various length scales [*Mark and Aronson*, 1984; *Saupe*, 1988; *Voss*, 1986, 1988; *Goff and Jordan*, 1988]. In practice, however, there may be good reasons for preferring one of these techniques over the others [*Carr and Benzer*, 1991; *Klinkenberg and Goodchild*, 1992]. Second, scaling behavior in the space domain translates to scaling behavior in the wavenumber domain. For simple scaling functions, the exponent α describing the decay of power spectral amplitude with wavenumber can be expressed in terms of the Hurst exponent H in (7): $\alpha = -(2H + 1)$ for topographic profiles; and $\alpha = -2(H + 1)$ for topographic surfaces [*Saupe*, 1988; *Voss*, 1988; *Goff and Jordan*, 1988]. As H ranges from 0 to 1, α ranges from -1 to -3 for topographic profiles and from -2 to -4 for topographic surfaces. Third, we prefer to use exponents such as H rather than fractal dimensions to characterize scaling because H is independent of the dimension of the observing space, i.e., it is the same for topographic profiles and surfaces. Finally, we want to emphasize that at least two parameters are required to describe completely the scaling properties of topography. Referring to (2), (6), and (7), scaling behavior is specified by two parameters, an amplitude parameter and a scaling exponent. The amplitude parameter describes the amplitude of the surface roughness (say, at unit length scale), while the exponent describes how the roughness varies

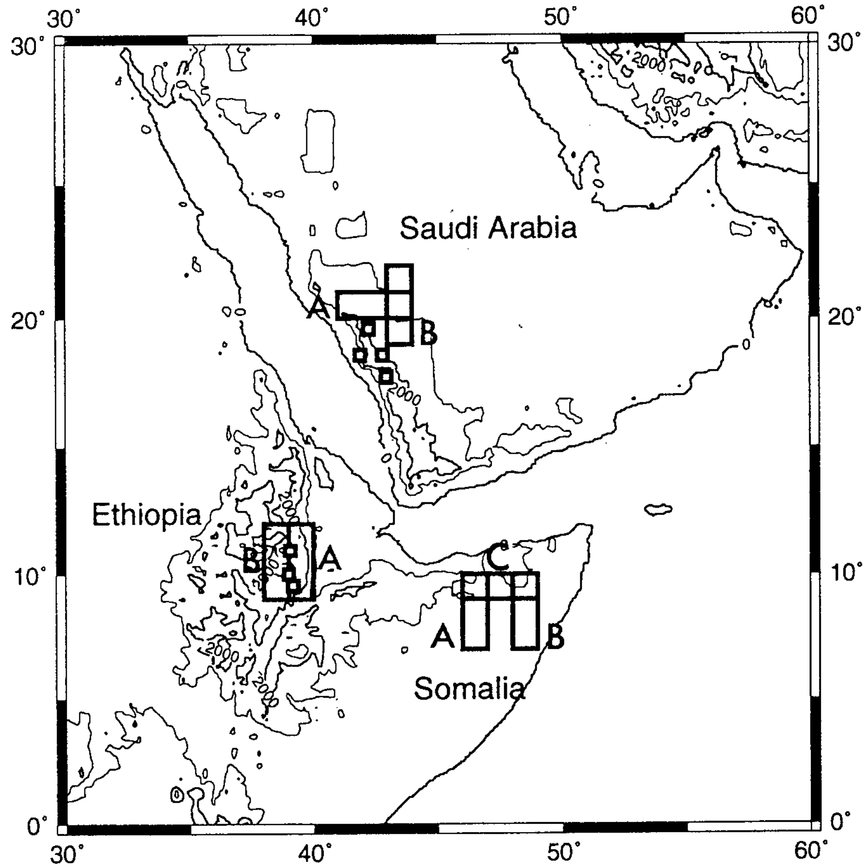

Figure 1. Map showing the location of the digital elevation models (DEMs) analyzed in this study. Length-scaling analyses for the DEMs spanning either 3° of latitude and 1° of longitude (3600×1200 grid points), or 1° of latitude and 3° of longitude are shown in Figures 2-4. Hypsometric curves for the smaller DEMs (500×500 grid points) in Ethiopia and Saudi Arabia are shown in Figure 14. Elevation contours are every 1000 m.

with length scale. In our opinion it is a mistake to focus exclusively on the scaling exponent because it is well known that the scaling exponents of natural surfaces do not vary very much (see below). For example, *Sayles and Thomas* [1978] showed that the scaling exponent of "smooth" surfaces, such as airport runways, is quite similar to that of "rough" surfaces, such as mountainous terrains. The amplitude parameters, however, are very different.

Previous Studies of the Scaling Properties of Topography

Following the pioneering work of *Vening Meinesz* [1951] mentioned earlier, *Bell* [1975] compiled power spectra of continental and ocean floor topographic profiles into a composite spectrum that decayed as a power law (2) with an exponent of $\alpha \approx -2$ for wavelengths between about 0.5 and 10^4 km. *Sayles and Thomas* [1978] showed that many other natural and some artificial surfaces exhibit the same negative power law form of spectral density over 8 orders of magnitude range in length scale. They also pointed out that although the spectra seemed to be associated with a remarkably constant power law exponent $\alpha \approx -2$, a value for the amplitude of variation (with dimensions of length) at a given length scale was required for a complete characterization of surface topography. *Brown and Scholz* [1985] examined the power spectra of natural rock surfaces for wavelengths between about 20 μm to 1 m and noted that the spectral exponent varied between -2 and -3. *Power and Tullis* [1991] investigated the spectral properties of natural fault and fracture surfaces in the wavelength range 10 μm to 40 m. Overall, they found that the composite spectra decayed with an exponent of -3, implying self-similar scaling but that exponents > -3, indicative of self-affine scaling, characterized smaller ranges in wavelength. The variation in scaling exponents with length scale (wavelength range) noted in several of these studies indicates that the homogeneity relation (1) is not always obeyed in detail. Such behavior indicates that the scaling properties of topographic surfaces could be inhomogeneous (i.e., dependent on length scale and/or location), which could (in turn) provide important insight into the processes affecting topography. Overall, however, the previous studies provide good reason to believe that topographic surfaces are scaling functions and can be analyzed as such.

A number of studies cited below have noted that there is an upper limit in length scale in the scaling properties of natural surfaces. Equation (2), for instance, implies that the variance of a scaling function increases without bound as the length scale increases. Clearly, this is physically unrealistic, and all natural scaling phenomena should have an upper limit of length scale. For topography, the implication is that for some $l > l_{max}$, $\widehat{\Delta h}_1(l)$ behaves as l^0; i.e., the relief tends toward a constant value. In the ocean basins, several studies have shown that power spectral density plots for abyssal hill topography are essentially flat for wavelengths greater than a few tens of kilometers, whereas for shorter wavelengths the spectra decay according to the power law form given above with $\alpha \approx -2$ [*Bell,* 1975; *Gilbert and Malinverno,* 1988; *Goff and Jordan,* 1988; *Malinverno and Cowie,* 1993]. In a static situation, we could surmise that the upper bound for relief is determined by whether the weight of the rocks exceeds their intrinsic strength. We leave aside the question of the minimum length scale for which scaling behavior is observed for topographic surfaces.

Scaling Properties of DEMs

Digital elevation models (DEMs), which are two-dimensional arrays of elevations equally spaced in a specified map projection, are intended to represent real topography, nominally at the resolution of the gridding interval. The digital nature of DEMs is a great advantage where computers are used to process and analyze topographic information, to make maps, for example. Where quantitative knowledge about topography is required, however, it becomes important to know how well DEMs represent the "real" topography. DEMs are constructed using many different techniques, digitization of existing topographic contour maps, and photogrammetric methods applied to stereo imagery are but two examples. One practical application of the techniques developed to determine the length-scaling properties of topography is in the assessment of the quality of DEMs, as we discuss later.

The DEMs used here are gridded at 3 arc sec of latitude and longitude. Information on the source and methods of construction of these DEMs is given by the *U.S. Geological Survey (USGS)* [1987]. Most likely the DEMs we analyze here were produced by manual correlation of stereo pairs acquired on adjacent, high-inclination satellite orbits. This would be consistent with the WNW-ESE lineated artifacts that we can discern in these products (see discussion section). Figure 1 shows the location of the DEMs. They cover portions of Ethiopia (two DEMs), Saudi Arabia (two DEMs), and Somalia (three DEMs). Each DEM spans either 3° of latitude and 1° of longitude (3600×1200 grid points), or 1° of latitude and 3° of longitude (Figure 1). Grids of these sizes allow us to determine scaling properties for over 3 orders of magnitude range in length scales.

The calculation procedure is described in (5). Essentially, we make separate and independent determinations of $\widehat{\Delta h}_1(l)$ for the x and y coordinate directions (columns and rows, respectively,) of the Ethiopia, Saudi Arabia, and Somalia DEMs shown in Figure 1. For all columns (x direction) and all rows (y direction) of each DEM we compute all possible independent estimates of relief (the absolute elevation differences) at a given length scale l, which is constrained to be a multiple of the gridding interval. The "expected value" of relief $\Delta h_1(l)$ in the x and y directions is then estimated as the mean of all relief values at that length scale. The procedure is then repeated for a suite of length scales ranging over 3 orders of magnitude. The grid interval itself is the smallest length scale considered, while the largest length scales are kept less than half the DEM sizes in the x and y directions. Even at the largest length scales considered, the number of independent relief estimates is more than 2.5 million. We first validated the technique by determining the scaling properties of fractional Brownian surfaces and profiles for which the scaling exponent H was known a priori in Monte Carlo simulation experiments.

Figures 2, 3, and 4 display the scaling properties of the Ethiopia, Saudi Arabia, and Somalia DEMs, respectively. In these plots we display the logarithm of mean relief $\widehat{\Delta h}_1$ against the logarithm of length scale l, for the x and y directions of each DEM separately. Values of the scaling exponent H found from simple least squares fits to the individual scaling plots are shown on each of the figures. In essence, the scaling exponents for all DEMs are $0.5 \leq H < 0.7$. The Saudi Arabia DEM is distinguished by a very small range of 0.51-0.55 in the scaling exponent (Figure 3). In detail, the scaling plots for all DEMs reveal small but systematic variations in scaling exponent over the length scale range considered. This shows some degree of inhomogeneity in the scaling properties of the DEMs. The "roll off" of relief with increasing length scale observed in the Ethiopia y direction scaling plots and the Somalia scaling plots for both directions indicates that an upper bound in scaling behavior is attained for length scales greater than about 50 km (Figures 2 and 4). We can compare topographic roughness among the three areas by choosing a particular length scale and reading the value of mean relief at that length scale on the ordinates of the scaling plots. From Figures 2-4 we find that the mean relief for Ethiopia is greater than for the other two regions over all length scales considered. This underscores the fact that the scaling exponent does not uniquely characterize topography, an amplitude parameter (e.g., the relief at a given length scale) is also required.

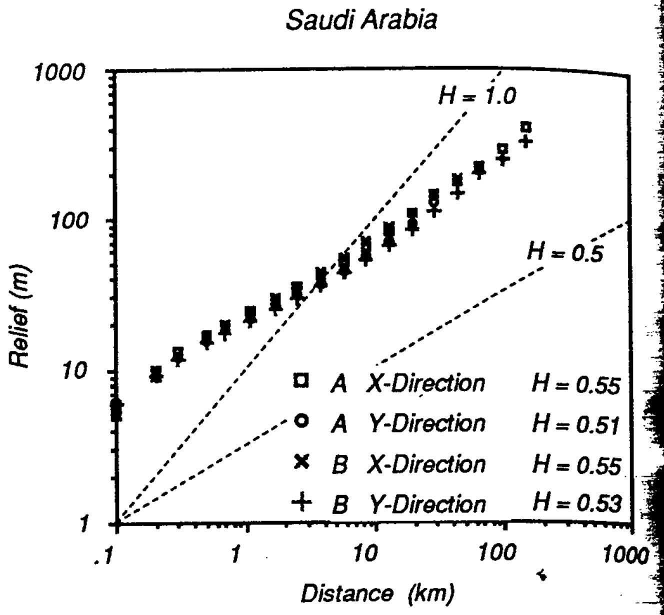

Figure 3. Plots of log $\widehat{\Delta h}_1(l)$ (mean topographic relief) against log l (length scale) for the DEMs from Saudi Arabia (Figure 1). The best fitting value for the scaling exponent H for each plot is shown on the right. Dashed lines with slopes of 1 and 0.5 are shown for reference purposes.

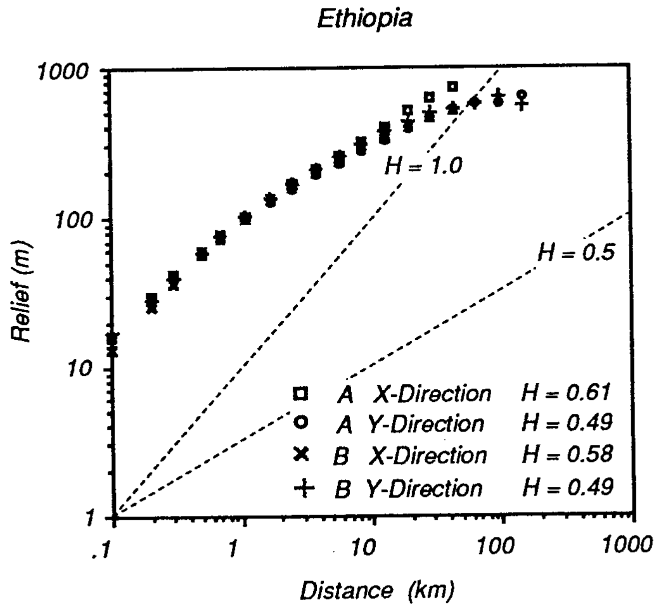

Figure 2. Plots of log $\widehat{\Delta h}_1(l)$ (mean topographic relief) against log l (length scale) for the DEMs from Ethiopia (Figure 1). The best fitting value for the scaling exponent H for each plot is shown on the right. Dashed lines with slopes of 1 and 0.5 are shown for reference purposes.

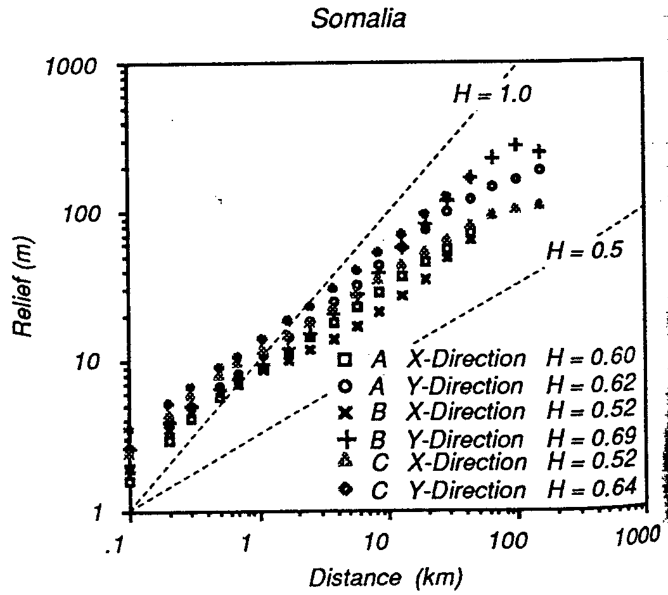

Figure 4. Plots of log $\widehat{\Delta h}_1(l)$ (mean topographic relief) against log l (length scale) for the DEMs from Somalia (Figure 1). The best fitting value for the scaling exponent H for each plot is shown on the right. Dashed lines with slopes of 1 and 0.5 are shown for reference purposes.

Anisotropic Surfaces

To better understand the scaling properties of the DEMs analyzed above, we first consider the scaling properties of an inclined plane $h = a + bx + cy$, an example of which is shown in Figure 5. Starting at an arbitrary point on the plane and moving along each coordinate axis separately, we can determine how the surface elevation changes with distance in the x and y directions using (5). If we plot elevation difference (relief) linearly against distance (Figure 6a), we find as expected that the relief increases linearly with distance at a rate of b in the x direction and c in the y direction. This is always true irrespective of the starting point on the plane surface. If instead of a linear plot, we display the logarithm of the relief against the logarithm of distance, we get quite a different representation of the same information (Figure 6b). We now see that the plane is an exact (as opposed to a statistical) scaling function and that the scaling exponent H is identically equal to 1 for both the x and y directions.

It is important to note that while the scaling properties of the plane are isotropic, the surface itself is anisotropic and can be characterized by an anisotropy factor b/c. On the logarithmic plot (Figure 6b), the x and y scaling plots are offset horizontally by $(\log b - \log c)$ and vertically by $H(\log b - \log c)[= \log b - \log c]$. Notice also that the anisotropy factor will vary according to the orientation of the coordinate axes with respect to the plane, a feature also true for topographic surfaces. Thus, unless the x and y coordinate axes correspond to the principal axes of anisotropy, we will need to conduct a second set of scaling estimates along a second pair of orthogonal directions (e.g., along the diagonals of the topography grid) in order to measure anisotropy correctly.

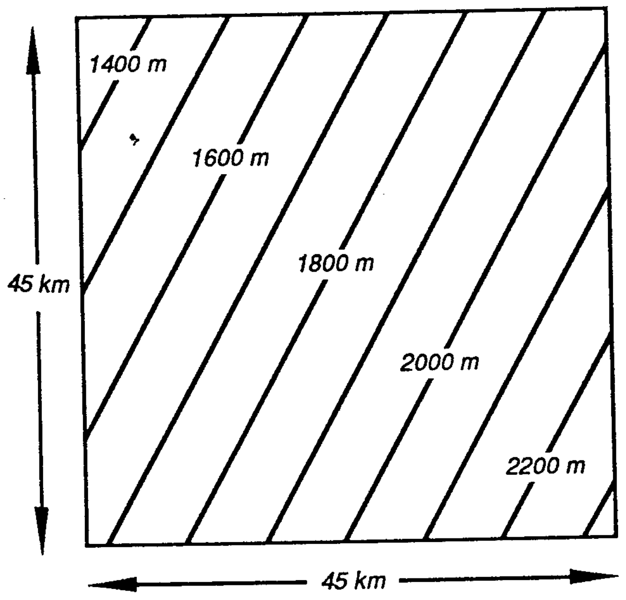

Figure 5. Elevation contours of a best-fitting planar surface for a 500×500 grid point DEM from Ethiopia. The DEM is gridded at 3 arc sec of latitude and longitude.

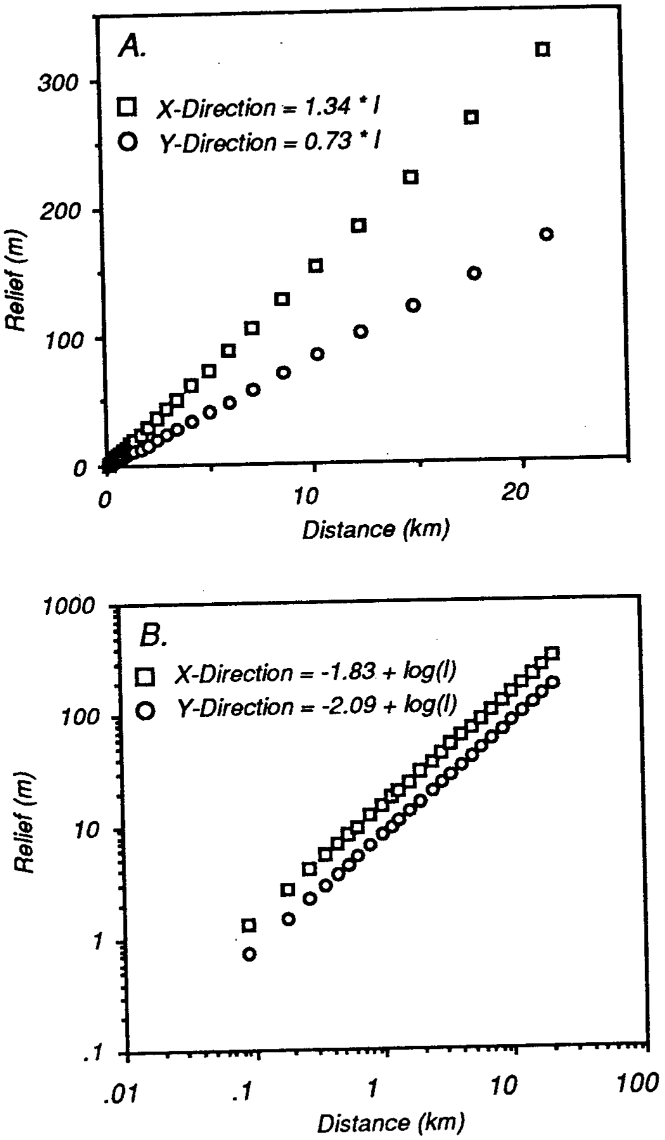

Figure 6. (a) Topographic relief for the plane in Figure 5 in the x and y directions versus distance, plotted with linear scales. (b) Topographic relief for the plane in Figure 5 in the x and y directions versus distance, plotted with logarithmic scales.

We now address the issue of topographic surfaces which have isotropic scaling properties but are anisotropic over a defined range in length scale. To illustrate this, we construct synthetic surfaces in which the height increments Δh are drawn from a zero-mean Gaussian distribution. Such surfaces are known as fractional Brownian surfaces [*Mandelbrot and Van Ness*, 1968; *Voss*, 1986, 1988], and a vertical cut through such a surface corresponds to the trace of random walk (Brownian motion) for the particular value of $H = 0.5$. Fractional Brownian surfaces are readily generated by filtering (actually, fractionally integrating) a randomly generated two-dimensional field of Gaussian white noise in the wavenumber k domain. In order to incorporate the effects of anisotropy, we consider the following expression for the power spectral density $P(k_x, k_y)$ of a quasi-fractional Brownian surface [after *Goff and Jordan,* 1988]:

$$P(k_x, k_y) = \frac{aH\sigma^2}{2\pi k_2^2 \left[1 + \frac{a^2k_x^2 + k_y^2}{k_2^2}\right]^{H+1}} \tag{9}$$

where k_x and k_y are wavenumbers corresponding to the x and y directions, respectively, H is the Hurst exponent (see (4)), σ^2 is the total variance of the surface, k_2 is the characteristic wavenumber corresponding to the y direction, and a is the anisotropy factor defined as $a = k_2/k_1$, and k_1 is the characteristic wavenumber corresponding to the x direction. We can also define characteristic length scales $\lambda_i = 2\sqrt{2(H + 1/2)}/k_i$, ($i$=1, 2) corresponding to k_1 and k_2 [*Goff and Jordan,* 1988].

Figure 7 schematically shows vertical cuts through $P(k_x,\ k_y)$ along the wavenumber coordinate axes. Note from Figure 7 that (1) $P(k_x, k_y)$ is a scaling function only for $k_x, k_y > k_2$, where it follows a power law with an exponent of $-2(H+1)$; (2) the anisotropy factor a is given by the shift of $P(0, k_y)$ relative to $P(k_x, 0)$ parallel to the wavenumber axis; and (3) $P(k_x, k_y)$ tends to a constant value for $(k_x^2 + k_y^2)^{1/2} < k_1$. That is, an upper bound in scaling behavior is attained at such wavelengths. Because "true" fractional Brownian surfaces do not have an upper bound (such surfaces are scaling over an infinite range, in principle), we refer to surfaces generated using (9) as quasi-fractional Brownian surfaces. Later, we employ the "midpoint displacement" algorithm of *Saupe* [1988] to get synthetic surfaces closer to the fractional Brownian model.

Each of the synthetic surfaces in Figure 8 was obtained by Fourier transforming a single realization of a quasi-fractional Brownian surface with a power spectral density given by (9). There are four free parameters in (9), namely, k_2, σ, H, and a. Only the anisotropy factor a is varied in Figure 8. The effect of increasing a from 1 (isotropy) to 10 can be clearly seen in the progressive "smearing" of the plots in the x direction. Essentially, the ratio of the characteristic lengths λ_1/λ_2 increases with the anisotropy factor a.

We can express the scaling properties in the x and y directions separately by modifying (5) and (7) to give

$$\widehat{\Delta h}_{1,x}(l) \approx \widehat{\Delta h}_{1,y}(l) \propto l^H, \tag{10}$$

where the symbol $\propto$ denotes proportionality. Equation (10) explicitly refers to the case where the scaling properties and the surface itself are isotropic. If the surface is anisotropic, however, the statistical properties of the fluctuations over distance l in the y direction will be on average, the same as over distance al in the x direction. If $\widehat{\Delta h}_{1,x}(l) \propto l^H$, then $\widehat{\Delta h}_{1,y}(l) \propto (al)^H$. Thus, $\widehat{\Delta h}_{1,y}(l) \approx a^H \widehat{\Delta h}_{1,x}(l)$, or, referring to the plots in Figure 9,

$$\log \widehat{\Delta h}_{1,y}(l) \approx H \log a + \log \widehat{\Delta h}_{1,x}(l). \tag{11}$$

The length-scaling properties of the quasi-fractional Brownian surfaces (Figure 8) determined following (4) and (5) are shown in Figure 9. The scaling properties in the y direction are shown only for a = 1, the isotropic case, because these do not change appreciably as a is varied. The construct of the four vertical dashed lines (Figure 9) demonstrates that the x direction scaling plots for a =2, 5, and 10 are each shifted from the a = 1 plot parallel to the distance axis by an amount approximately equal to log a, in agreement with equation (11). The effect of anisotropy is only seen for length scales much less than $2\pi/k_2$ (approximately λ_2), a feature already noted from the power spectrum plot in Figure 7. Figure 9 shows that it should be possible

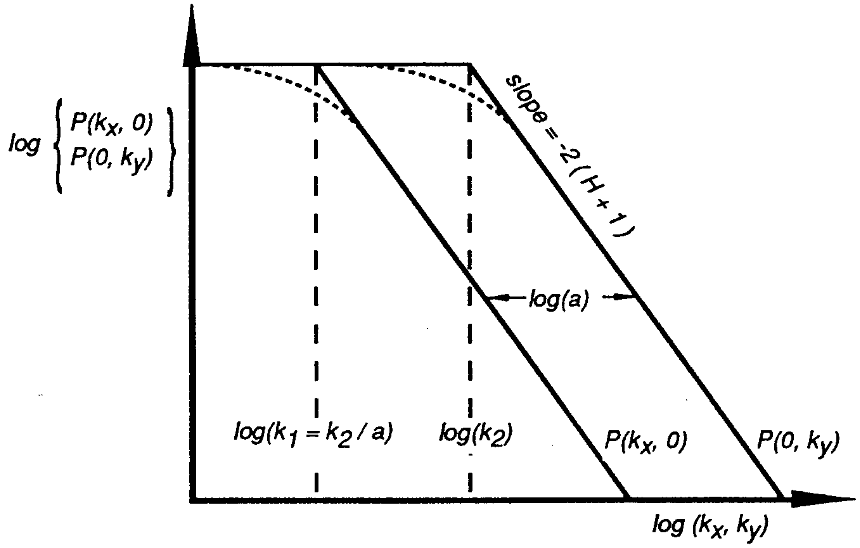

Figure 7. Schematic diagram showing vertical cuts along the wavenumber coordinate axes through the power spectral density $P(k_x, k_y)$ (equation (9)) of a quasi-fractional Brownian surface. See text for explanation.

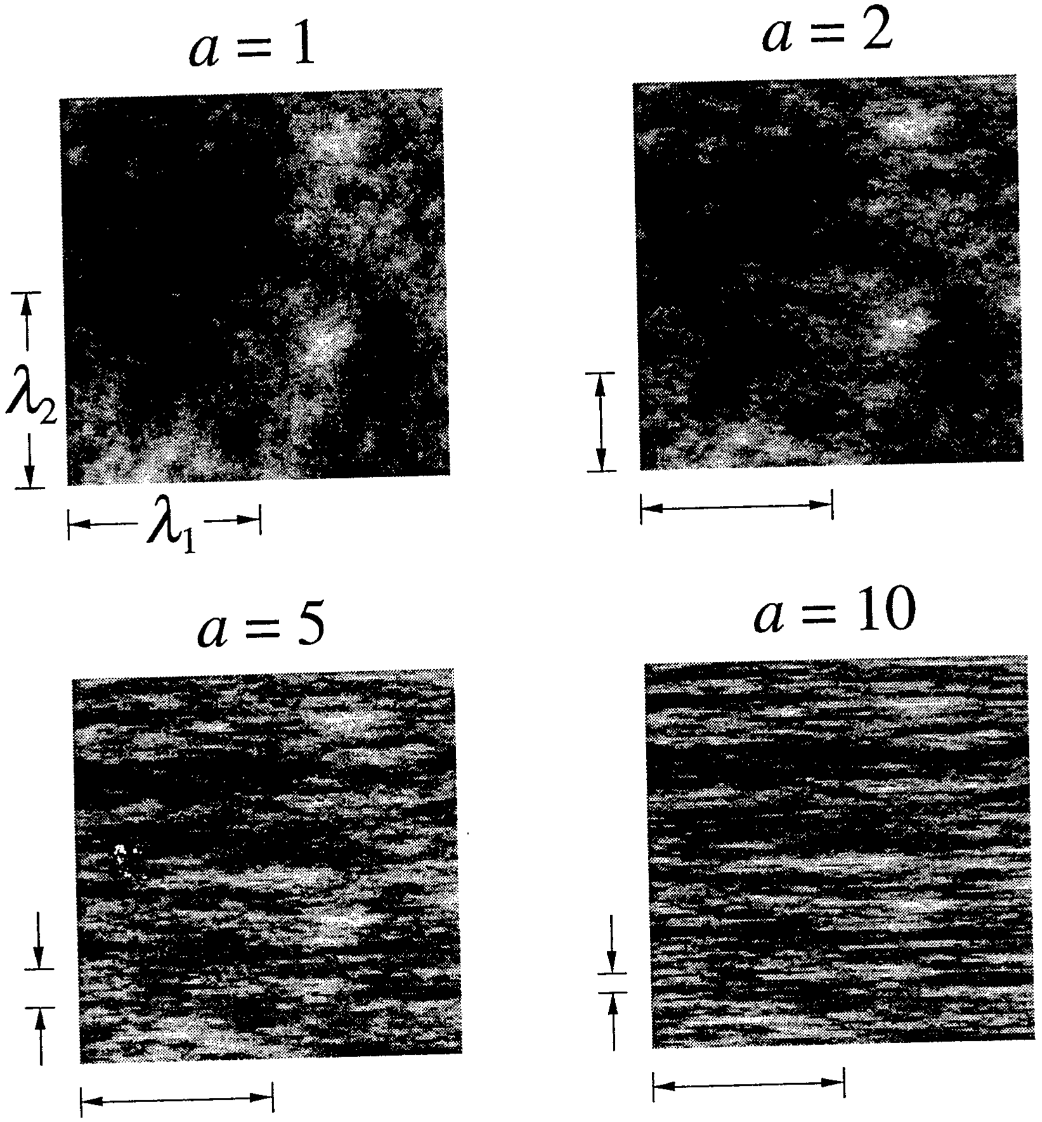

Figure 8. Contour maps with an arbitrary grey scale for quasi-fractional Brownian surfaces whose power spectral densities are given by equation (9) and shown schematically in Figure 7. The effect of varying the anisotropy factor a is clearly seen by the progressive "smearing" of the plots in the x direction as a is increased.

to detect anisotropy in topographic surfaces when it is not scale dependent.

In Figure 10 we show length scaling plots of DEMs from Saudi Arabia and Somalia (see Figure 1 for location). The DEMs are gridded at 3 arc sec of latitude and longitude, and their general scaling properties were discussed in more detail earlier. The purpose here is to examine these topographic surfaces for evidence of anisotropy. While approximately isotropic scaling exponents characterize the Somalia DEM (a slope of $H \approx 0.5$ satisfies both the x and y direction plots), we note that the average relief in the y direction is consistently greater than in the x direction over the 2 orders of magnitude range in length scale considered (Figure 10). This implies that the Somalia DEM is anisotropic over this range. In contrast, the x and y direction scaling plots for the Saudi DEM appear to show slightly different average slopes over the range in length scale considered. Anisotropic scaling behavior might therefore provide a better explanation for the Saudi DEM scaling plots.

Simple versus Multiscaling Behavior

Scaling Properties of the $q = 1$ and $q = 2$ Structure Functions

Lavallee at al. [1993] suggested that simple and multiscaling behavior could be distinguished by examining the scaling properties of $\Delta h_q(l)$, the qth order structure function of topography $h(\mathbf{x})$, as q is varied following (4)-(6). Generally for multifractal fields, the scaling exponents $K_h(q)$ of the structure functions depend nonlinearly on order q, and in particular, $d(K_h(q))/dq$ decreases with increasing q, as discussed earlier. *Lavallee et al.* [1993] determined the length scaling properties

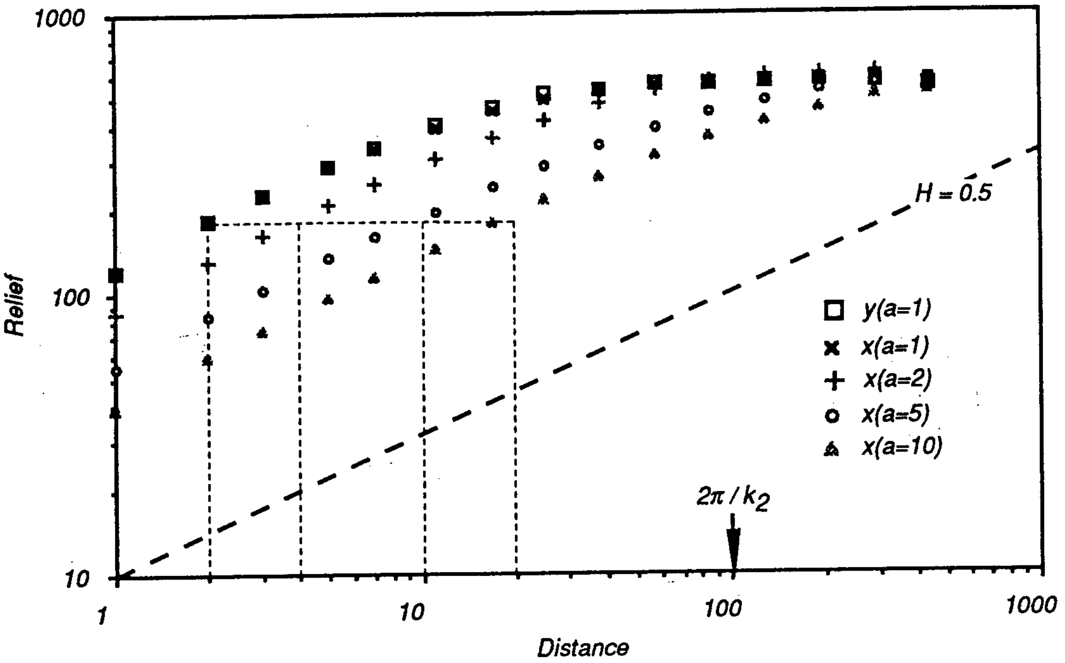

Figure 9. The length-scaling behavior of the quasi-fractional Brownian surfaces shown in Figure 8. The scaling properties in the y direction are shown only for $a = 1$, the isotropic case. The abscissa intercepts of the four vertical dashed lines demarcate horizontal shifts of log a from the dashed line at log 2, as a takes values 1, 2, 5, and 10. This illustrates the effects of anisotropy and shows that the anisotropy factor can, in principle, be obtained from length-scaling plots.

of the first- and second-order ($q = 1$ and $q = 2$, respectively) structure functions from a DEM gridded at 50-m intervals for Deadman's Butte, Wyoming. They found that $2K_h(1)[= 2H] - K_h(2) > 0$, consistent with multiscaling behavior. Although the value found was small 0.055 ± 0.01, Lavallee et al. pointed out that it agreed with results obtained using a more accurate technique called the "double trace moment."

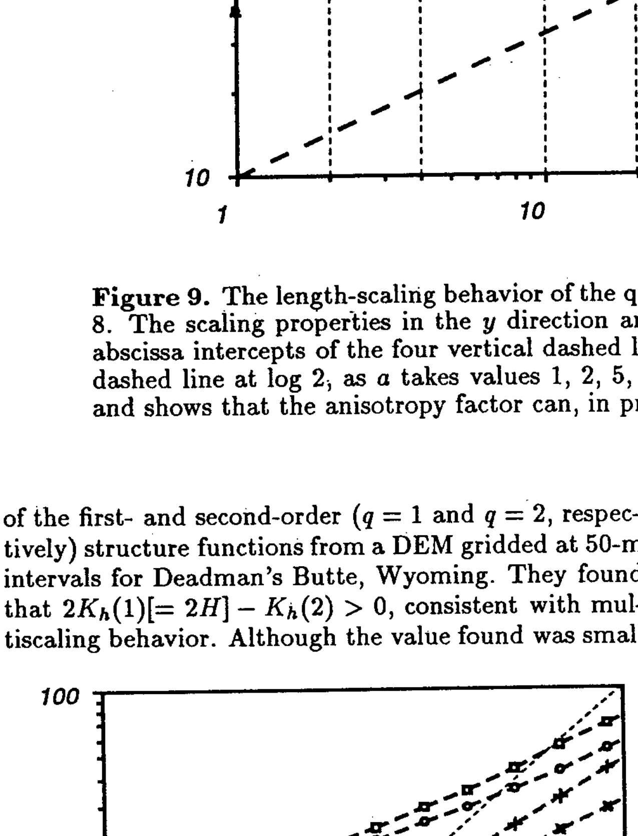

Figure 10. Details of the scaling behavior of selected DEMs from Saudi Arabia and Somalia. Notice that the x and y direction scaling plots for Somalia are approximately parallel over the 2 orders of magnitude range in length scale. This indicates isotropic scaling properties but an anisotropic surface. The Saudi Arabia DEM, on the other hand, shows evidence for anisotropic scaling properties.

For simple scaling functions (monofractals), on the other hand, the scaling exponents should be a linear function of moment q, i.e., $K_h(q) = qH$ (equation (7)). As verification of theory, we performed a Monte Carlo experiment in which we determined the scaling properties for moments $q = 1$, 2, and 3 of 100 realizations of a fractional Brownian profile with $H = 0.5$. Each profile realization was obtained using the mid-point displacement method of *Saupe* [1988]. Using (5), we found that $K_h(q) = qH$ is satisfied to 2 decimal places for $q = 1 - 3$. Thus the scaling properties of an a priori known monofractal appear to behave according to theory.

We then determined and compared the scaling properties of the first- and second-order structure functions for the DEMs from Ethiopia, Saudi Arabia, and Somalia (Figure 1). As representative results (Figure 11), we show $\widehat{\Delta h}_1(l)$ and $(\widehat{\Delta h}_2(l))^{1/2}$ as functions of length scale l for selected Ethiopia and Saudi Arabia DEMs. It is apparent in Figure 11 that the scaling exponents for the first- and (square-rooted) second-order moments are slightly different. In fact, for all of the DEMS we obtained a mean value for $K_h(1) - 0.5K_h(2)$ of 0.054 ± 0.036 (the uncertainty given as 2 times the standard deviation) which is positive, and consistent with results obtained by *Lavallee at al.* [1993] for the Deadman's Butte DEM. Although the difference in the scaling exponents is small, the fact that the difference

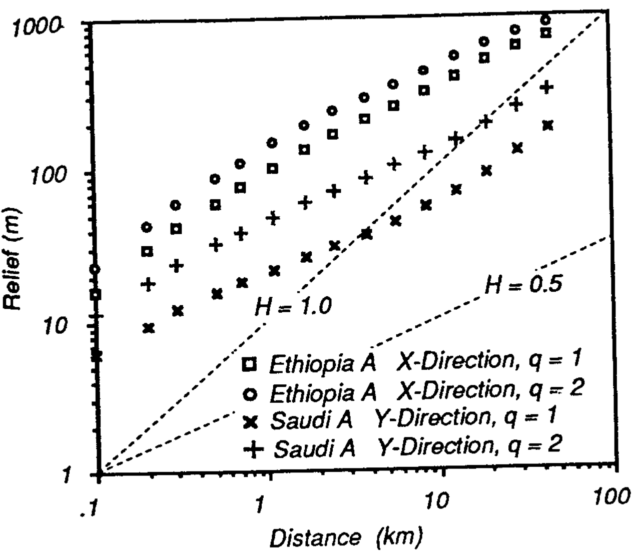

Figure 11. Plots of log $\widehat{\Delta h_1}(l)$ and 0.5 log $\widehat{\Delta h_2}(l)$ (first- and second-order structure functions of topography) against log l (length scale) for the DEMs from Ethiopia and Saudi Arabia (see Figure 1 for locations). The slightly different slope of the $q = 1$ and $q = 2$ plots is evidence that topography possesses multiscaling properties.

is positive leads us to conclude, as Lavallee et al. did, that topographic surfaces, or at least DEM representations of topography, are characterized by multiscaling properties.

Exceedance Sets and Perimeter Sets of Topography

A second way to distinguish simple from multiscaling behavior is through the analysis of exceedance and perimeter sets of topographic surfaces [*Lavallee et al.*, 1993]. An exceedance set for topography $h(\mathbf{x})$ is defined as the set of points $S_{\geq T}$ for which the elevation equals or exceeds a threshold elevation T. The perimeter set P_T comprises the boundary points of the exceedance set. Perimeter sets can be qualitatively equated to topographic contours.

The theory of fractal sets suggests that if topography is a single-valued function and if $T_1 > T_2$, the exceedance set $S_{\geq T_1}$ is a subset of $S_{\geq T_2}$, and the Hausdorff dimension $D(S_{\geq T_1})$ of $S_{\geq T_1}$ will be less than or equal to the dimension $D(S_{\geq T_2})$ of $S_{\geq T_2}$. Furthermore, because the perimeter set P_T is a subset of the corresponding exceedance set $S_{\geq T}$, $D(P_T)$ will be less than or equal to $D(S_{\geq T})$. *Schertzer and Lovejoy* [1990] and *Lavallee et al.* [1993] noted, however, that in the case of simple scaling (monofractals), $S_{\geq T}$ will not be a fractal set at all and that its dimension $D(S_{\geq T})$ will equal the dimension of the space in which the set is "embedded," i.e., 2 for surfaces and 1 for profiles. Furthermore, for simple scaling, perimeter sets of topographic surfaces will have dimension $D(P_T) = 2 - H$, independent of the value of T. The foregoing suggests that by determining the dimensions of exceedance and perimeter sets, we should be able to show whether topography is characterized by simple scaling or multiscaling properties. *Lavallee et al.* [1993], for example, showed that the dimensions of exceedance sets obtained from a DEM for France (1-km spacing) decreased from 1.92 to 0.84 as threshold elevations increased from 28 to 3600 m. They concluded from this result that topography displays multiscaling properties.

Because the theory given by *Schertzer and Lovejoy* [1990] and *Lavallee et al.* [1993] regarding the trivial dimensions of exceedance and perimeter sets for simple scaling functions seemed counterintuitive to us at first, we performed a Monte Carlo experiment in which we determined the dimension of exceedance and perimeter sets for 100 realizations of a fractional Brownian surface with $H = 0.5$. The realizations were done using the midpoint displacement algorithm described by *Saupe* [1988]. A box counting technique was applied to determine the dimensions of exceedance and perimeter sets defined by the intersection of the fractional Brownian surfaces with 50 elevation thresholds equally spaced across the elevation range of each surface realization. The results, showing mean dimension and two times its standard deviation as a function of elevation threshold, are displayed in Figure 12. Also shown in Figure 12 are the expected dimensions for exceedance sets (the dashed line at $D = 2$) and for perimeter sets (the dotted line at $D = 1.5$), according to theory advanced by *Schertzer and Lovejoy* [1990] for simple scaling surfaces with $H = 0.5$. While the results for the perimeter sets are ambiguous in relation to the theoretically predicted value of $D = 1.5$, the dimensions found for the exceedance sets are clearly less than the predicted value

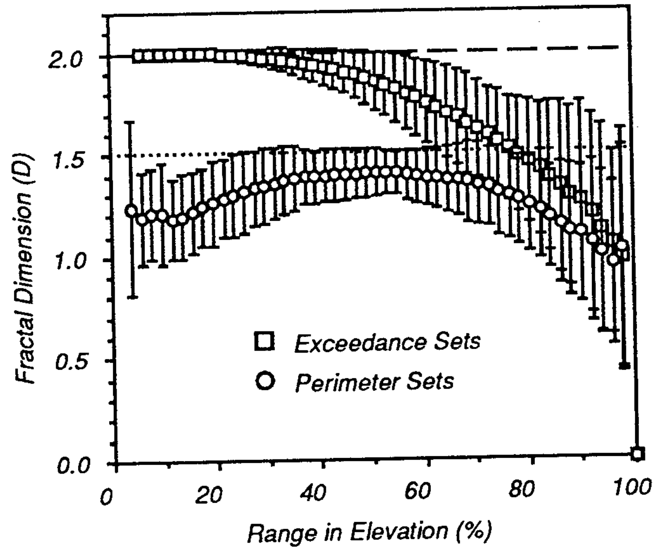

Figure 12. Dimensions of exceedance and perimeter sets of $H = 0.5$ fractional Brownian surfaces versus relative elevation threshold. The theoretical dimensions for simple scaling surfaces, such as fractional Brownian surfaces, are $D = 2$ for exceedance sets (dashed line) and $D = 1.5$ for perimeter sets (dotted line). Our analysis of exceedance set dimensions does not conform to theory. See text for discussion.

of $D = 2$ for threshold elevations greater than 60 percent of the elevation range in the surfaces (Figure 12). The dimensions of the exceedance sets for the fractional Brownian surfaces, in fact, behave in a similar fashion to those for the French DEM, which *Lavallee et al.* [1993] interpreted as evidence for multiscaling behavior.

A possible reason for these paradoxical results may be found by considering the method for determining the fractal dimensions of sets. A box counting scheme is commonly employed to determine the dimensions of fractal sets. Briefly, the number $N(l)$ of boxes of size l required to cover the set S completely varies as

$$N(l) \propto l^{-D(S)}. \qquad (12)$$

$D(S)$ is known as the box counting (fractal) dimension or simply, box dimension, and it is estimated from the slope of $\log N(l)$ plotted against $\log l$. A problem we perceive is that, in practice, we must apply the box counting technique to "data," such as DEMs, which have a finite lower bound in resolution. Caution should be exercised in interpreting the results of applying (12) to finite resolution sets. The explanation we favor for the unexpected behavior of the exceedance set dimensions (Figure 12) is that we are effectively prevented from obtaining an accurate measurement of set dimension at high elevation thresholds because of the finite resolution of the data. As we go to higher elevation thresholds the exceedance sets get sparser. In principle, if we had infinite resolution data, we should see the level of detail in the set expected for the given value of H at all box sizes. With finite resolution data this cannot be achieved, and our determined values for dimension $D(S)$ at high elevation thresholds will be inaccurate. Because of this practical limitation, we conclude that determination of the dimensions of exceedance and perimeter sets is not a reliable way to distinguish simple from multiscaling behavior.

Limitations of Fractional Brownian Surfaces as Models for Topography

The models of synthetic topography discussed above and in the literature [e.g., *Voss,* 1988] are based on Gaussian statistics. The statistical properties of these synthetic surfaces are completely specified by their first- and second-order moments, such as the mean and covariance (or, equivalently, the mean and power spectral density). *Sayles and Thomas* [1978] noted that a Gaussian form for topography might reasonably be expected from the central limit theorem of statistics, which states that a variable will be normally distributed if it is the sum of many random independent causes. Normally distributed topography is symmetrical: If we were to generate a fractional Brownian surface, its overall appearance would not change if we multiplied the elevation scale by -1. A general observation is that although such Gaussian fractal surfaces might closely resemble freshly fractured rock surfaces, they lack the distinctive drainage features that are so characteristic of eroded terrains.

Voss [1988] suggested that the aesthetic appeal of synthetic topography could be enhanced simply by rescaling the elevations of a fractional Brownian surface according to a power law. He found that if elevations were cubed, the peaks in the synthetic landscape became sharper, and the areas of low elevation broadened and took on the appearance of sedimented lowlands. In essence, non linear rescaling of elevations of a fractional Brownian surface introduces statistical moments higher than the second. This appears to be necessary in order to make synthetic surfaces look more realistic. We note also that *Goff and Jordan* [1988] found it necessary to consider statistical moments up to the fourth in order to describe fully the systematic slope asymmetries and the presence of smooth, sedimented valleys in ocean floor topography.

We suggest that fractional Brownian surfaces, while useful as a model for natural topography as shown above, have definite limitations (see also *Mark and Aronson* [1984] for a comparison between simulated and actual topography). Our contention is best illustrated by comparing the hypsometric curves determined from fractional Brownian surfaces with those from "real" topography, as represented by DEMs. A hypsometric curve graphs the relative proportion of a region's area that lies at or below (or, at or above) a given height [e.g., *Strahler,* 1952]. Hypsometric curves are often made nondimensional by normalizing the heights relative to the elevation range in the area under consideration. The region of interest is arbitrary, it might comprise a single drainage basin [e.g., *Strahler,* 1952], or it might include entire continents [e.g., *Harrison et al.,* 1983].

Hypsometric analysis is easily done on synthetic topographic surfaces and DEMs because each elevation value is representative of $(m \times n)^{-1}$ of the total area of the elevation array (assuming the gridding of the $m \times n$ array is approximately equal area). In practice, we can divide the total elevation range into a convenient number of intervals and simply "bin" all the elevation values for the array in their appropriate intervals. A height-frequency histogram is constructed in this way. If this histogram is normalized by the total number of elevation values in the array $(m \times n)$, we get a curve analogous to a probability density function in statistics. The ordinate gives the probability of finding any binned relative height. The integral of this curve with respect to relative height will then be equivalent to a cumulative distribution function. A hypsometric curve is therefore the cumulative height distribution function for a given region.

The hypsometric curves for fractional Brownian surfaces (Figure 13) resemble error functions turned on their side. This is to be expected because the height increments are drawn from a Gaussian distribution, and thus the entire surface is governed by Gaussian statistics, as discussed above. The hypsometric curves are symmetric, with the 50th percentile of the relief associated with the 50th percentile of the area. The changes in shape of the hypsometric curves as the value of the scaling exponent H is varied (Figure 13) are consis-

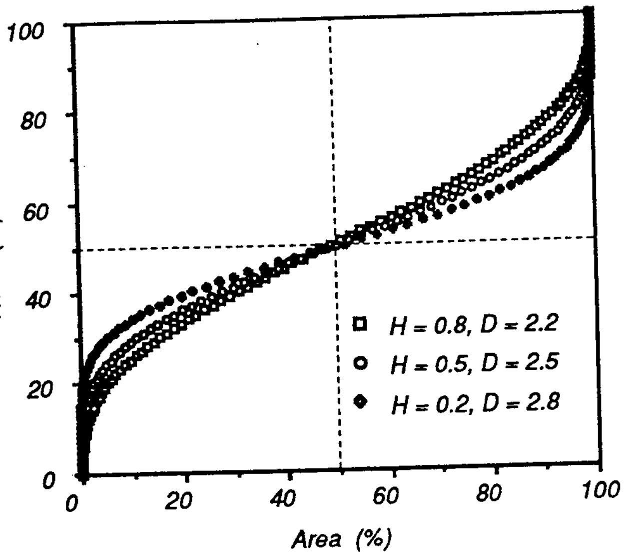

Figure 13. Hypsometry of fractional Brownian surfaces as the scaling exponent H takes values of 0.2, 0.5, and 0.8. Corresponding fractal dimensions $D = 3 - H$ are the values on the right. Note the symmetry of the hypsometric curves.

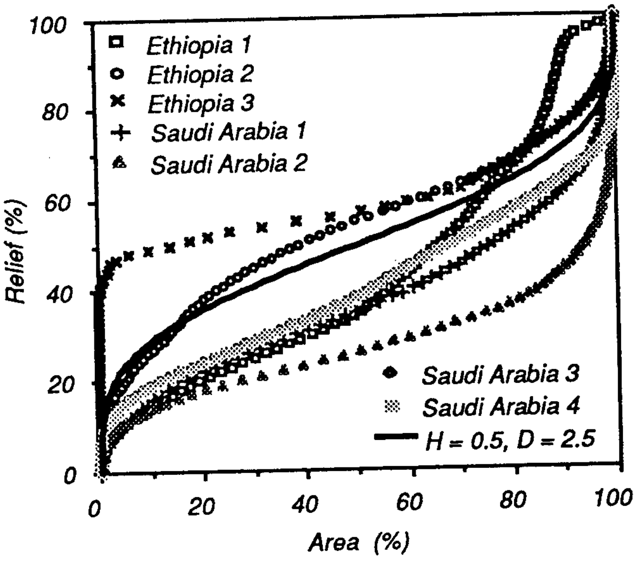

Figure 14. Hypsometric curves for various 500x500 point DEMs from Ethiopia and Saudi Arabia (see Figure 1 for locations). The hypsometric curve for the Brownian surface ($H = 0.5$) from Figure 13 is shown for comparison. Note that the hypsometric curves for natural topography are biased toward either higher or lower elevation compared to the synthetic surface hypsometry.

tent with the properties of fractional Brownian surfaces. The ratio of standard deviations for surfaces characterized by different scaling exponents should behave as $l^{\Delta H}$, where ΔH is the difference in scaling exponents.

The hypsometric curves for several 500×500 point DEMs from Ethiopia and Saudi Arabia (Figure 14), on the other hand, are definitely not symmetric. We do not intend to argue from the hypsometric curves whether the DEM landscapes can be characterized by terms such as "youth," "maturity," or "old age" as sometimes inferred from hypsometry [*Strahler*, 1952; *Scheidegger*, 1970]. Our purpose is simply to point out, by comparing the hypsometry of natural surfaces and fractional Brownian surfaces, that synthetic surfaces based on Gaussian statistics are of limited use as models for topography.

Discussion

Assessment of DEM Quality

Determination of length-scaling properties helps us assess DEM quality. Although the Ethiopia, Saudi Arabia, and Somalia DEMs show consistent scaling behavior over 3 orders of magnitude range in length scale, we did note that there are systematic departures from strict linearity in the scaling plots of Figures 2-4. Such behavior might indicate that landscape-forming processes are effective over limited and different ranges of length scale. However, if we focus on the scaling properties of the DEMs for length scales less than a few kilometers, we find systematic behavior that could be attributed to "flaws" in the DEMs themselves.

All of the x direction scaling plots and several of the y direction plots are marked by an increase in slope (scaling exponent) with decreasing length scale. In other cases, the plots for the y direction actually decrease in slope with decreasing length scale. Both kinds of "anomalous" scaling behavior at short length scales can be observed in the scaling plots for the Saudi Arabia and Somalia DEMs in Figure 10. It is important to understand whether such behavior is a true reflection of landscape forming processes, whether it is an artifact stemming from the analytical technique used, or whether it reflects "noise" introduced into the DEMs during their construction.

We can probably eliminate concerns about methodology in explaining the "anomalous" scaling behavior, because we have examined the scaling properties of many hundreds of realizations of fractional Brownian surfaces and profiles using (4)-(7) during the course of this work and have observed the expected scaling behavior at all length scales. Furthermore, high scaling exponents at short length scales have also been found in previous studies where variograms have been the main analysis tool [*Mark and Aronson*, 1984; *Chase*, 1992; *Klinkenberg and Goodchild*, 1992; *Lifton and Chase*, 1992].

We suggest that the anomalous steep slopes (high scaling exponents) frequently observed in scaling plots of DEMs (Figures 2-5) at short length scales reflects excessive smoothing of relief at those scales introduced during construction of the DEMs. DEMs are averaged "models" for the real Earth topography, created by interpolation between points of known elevation. Many commonly used interpolation schemes involve smoothing, and several methods have been developed for identifying interpolation artifacts in DEMs [e.g., *Polidori et al.*, 1991]. We illustrate our point about excessive smoothing at short length scales by taking a single realization of a fractional Brownian profile with a scaling exponent $H = 0.5$, decimating it by factors 1, 4, and 8 and using a cubic spline interpolation scheme to reconstruct the decimated profiles at the original data spacing. The scaling plots for the original profile, and the decimated and reconstructed profiles are shown in Figure 15a. There is a clear relationship between the degree of interpolation involved in reconstructing the decimated profiles, and the progressive smoothing of the relief and resulting increase in scaling exponent with decreasing length scale. The slope of the scaling plots for the interpolated profiles approaches $H = 1$ at the shortest length scales, and the length scale at which the scaling plots depart from the $H = 0.5$ slope of the original Brownian profile appears to be a direct reflection of the decimation factor (Figure 15a).

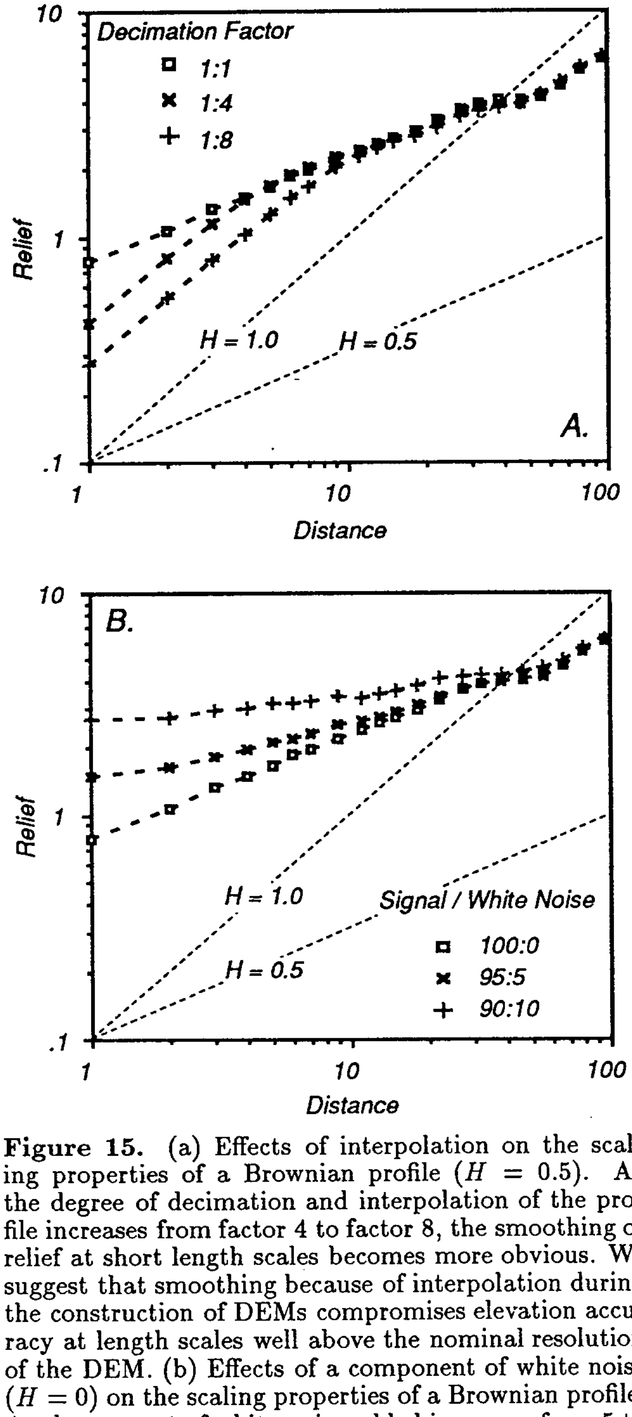

Figure 15. (a) Effects of interpolation on the scaling properties of a Brownian profile ($H = 0.5$). As the degree of decimation and interpolation of the profile increases from factor 4 to factor 8, the smoothing of relief at short length scales becomes more obvious. We suggest that smoothing because of interpolation during the construction of DEMs compromises elevation accuracy at length scales well above the nominal resolution of the DEM. (b) Effects of a component of white noise ($H = 0$) on the scaling properties of a Brownian profile. As the amount of white noise added increases from 5 to 10 percent, the scaling plots flatten (i.e., slopes tend to zero) with decreasing length scale.

The anomalous behavior of the y direction scaling plots in Figure 10 at short length scales is more likely related to a directionally dependent noise field present in the DEMs used. If the DEM surfaces are illuminated by an artificial sun placed to the north or south, lineations trending in a ESE-WNW direction become readily visible. These lineations are probably artifacts introduced during the manual correlation between the stereo images from which the DEMs were produced. Because this noise field is almost orthogonal to the y direction of the scaling plots, it is preferentially registered in the y direction scaling plots as an anomalous increase in topographic roughness and a corresponding decrease in scaling exponent with decreasing length scale. We test this explanation in Figure 15b where small amounts of white noise are added to the realization of Brownian noise ($H = 0.5$). As the amount of white noise is increased, the scaling plots (Figure 15b) flatten (decrease in slope) with decreasing length scale. We thus suggest that the scaling plots for the Saudi and Somalia DEMs in Figure 10 reveal a component of white noise which is lineated at a high angle to the y direction of the DEMs.

Detrending of Topographic Data

The work reported above on the scaling properties of planar surfaces (Figures 5 and 6b) made us rethink the wisdom of removing a best fitting planar trend from data before analysis. Scaling functions, as stated earlier, have spectra which approximate a wavenumber power law like (2) with an exponent $\alpha \leq -2$. Such spectra are called "red." Detrending is a common "prewhitening" technique applied to data to improve the estimation of power spectra in situations where the spectrum is expected to be red. However, detrending is an inappropriate prewhitening method to use if the objective of the analysis is to estimate the scaling properties of the data from the spectral exponent.

We illustrate our concern by considering what happens when a planar trend which scales as $H = 1$ is removed from data which scales as $0 < H < 1$. We ask does the residual data possess scaling properties? Because the scaling exponents of the natural surface and the plane are different, the answer will generally be no. Further consideration of the scaling properties of natural surfaces and their best fitting planar trend provides the following insight. At short length scales, the natural surface has greater relief compared to the planar trend. As we go to longer and longer length scales, the relief of the plane rapidly approaches that of the data because the scaling exponent of a plane $H = 1$ is significantly higher than the real surface $H \approx 0.5$. Removing a planar trend therefore disproportionately affects relief at the larger length scales, and in this way the scaling behavior of the original surface is destroyed.

Controls on Hypsometry

We have seen above that we can manufacture synthetic surfaces obeying Gaussian statistics which have scaling exponents H approximately equal to those of natural topography. Yet the hypsometric curves for natural and synthetic surfaces appear distinctly different (Figures 13 and 14). Thus length-scaling behavior is not a complete or unique characterization of surfaces. The statistics of real surfaces, as emphasized above, involve moments higher than order 2. In other words, the elevation distribution for real surfaces is "biased" either up or down.

We suggest this reflects the underlying processes that shape the Earth's topographic surface. These are generally grouped under two categories. First, tectonic forces modify elevation patterns because the surface deforms under their action. Work is done against gravity by these forces in moving rock mass from low to high elevations. Second, erosional processes operate on the surface of Earth to move material from higher to lower elevation (thereby expending gravitational potential energy). We include weathering, transportation and depositional processes under the general term, erosional processes. Surface water and groundwater flows are the principal agents for the removal and transport of the eroded products of continental topography, although ice and wind are locally important. Two things to note here are that (1) we should expect that topography at any given time reflects the interaction of tectonic and erosional processes and (2) gravity introduces a directional "bias" (down is not the same as up, water does not flow uphill). Geomorphologists have used hypsometric curves to infer the relative "age" of landscapes, as mentioned above. We suggest that hypsometry might better reflect the relative importance of tectonic and erosional processes in shaping topography. Tectonism, particularly compressional tectonics, bias landscapes toward a greater proportion of area at higher elevation, whereas erosional/depositional processes bias landscapes toward a greater proportion of area at lower elevation. Gravity provides the fundamental control on the elevation bias in natural landscapes, since tectonic uplift represents work done against gravity by tectonic forces, whereas erosion represents work done by gravity in redistributing topographic mass to lower elevations.

Conclusions

We draw the following conclusions from our consideration of the techniques for measuring the length-scaling properties of topography and the application of those techniques to natural and synthetic surfaces:

1. The relation $\widehat{\Delta h}_1(l) \approx cl^H$ describes well the scaling behavior of natural topographic surfaces (as represented by DEMs gridded at 3 arc sec). Over 3 orders of magnitude range in length scale (about 0.1 to 150 km), average values of the scaling exponent H between about 0.5 to 0.7 characterize DEMs from Ethiopia, Saudi Arabia, and Somalia. Differences in apparent topographic roughness among the three areas most likely reflect differences in the amplitude factor c.

2. By considering the scaling properties of topographic surfaces in the x and y directions separately, we can assess the extent to which the scaling exponents are azimuthally dependent (anisotropic), or whether the scaling properties of the surface are isotropic while the surface itself is anisotropic over a restricted range of length scale. In this case, the degree of surface anisotropy can also be determined from the scaling plot.

3. We conducted two experiments with DEMs and synthetic surfaces to test whether topography possess multiscaling as opposed to simple scaling properties. The scaling exponents of the first- and second-order structure functions (or scaling of the relief and the variogram, respectively) determined for the DEMs are different. Although the difference in the scaling exponents is small, it is positive, and provides evidence that topographic surfaces are characterized by multiscaling properties. Our experiment with the exceedance and perimeter sets of fractional Brownian surfaces failed to yield the trivial fractal dimensions expected of sets of known monofractals. We suggest that this is a practical limitation arising from the use of finite resolution data sets in the analysis.

4. By comparing the hypsometry of natural surfaces with fractional Brownian surfaces, we illustrated the limitation of Gaussian synthetic surfaces as models for natural topography. We suggest that hypsometry might better be viewed as reflecting the relative importance of tectonic and erosional processes in shaping topography, rather than simply an indicator of the relative "youth" or "maturity" of the landscape.

5. Scaling analysis provides a means to assess the quality of DEMs and, in particular, to recognize artifacts that might be introduced into DEMs during their construction.

6. Finally, we suggest it is unwise to remove a planar trend from topography if the objective of the resulting analysis is to estimate scaling properties.

Acknowledgments. We thank Mike Ellis, James Carr, and Brian Klinkenberg for careful and constructive reviews of the manuscript. The work was supported in part by NASA award NAGW-2114 to J.K.W. and A.M., and ONR grant N00014-93-1-0126 to L.F.P. This is Lamont-Doherty Earth Observatory publication 5174.

References

Bell, T.H., Statistical features of sea-floor topography, *Deep Sea Res.*, *22*, 883-892, 1975.

Brown, S.R., and C.H. Scholz, Broad bandwidth study of the topography of natural rock surfaces, *J. Geophys. Res.*, *90*, 12,575-12,582, 1985.

Carr, J.R., and W.B. Benzer, On the practice of estimating fractal dimension, *Math. Geol.*, *23*, 945-958, 1991.

Chase, C.G., Fluvial landsculpting and the fractal dimension of topography, *Geomorphology*, *5*, 39-57, 1992.

Family, F., and T. Vicsek, *Dynamics of Fractal Surfaces*, 480 pp., World Scientific, Singapore, 1991.

Feder, J., *Fractals*, 283 pp., Plenum, New York, 1988.

Gilbert, L.E., and A. Malinverno, A characterization of the spectral density of residual ocean floor topography, *Geophys. Res. Lett., 15,* 1401-1404, 1988.

Goff, J.A., and T.H. Jordan, Stochastic modeling of seafloor morphology: Inversion of Sea Beam data for second order statistics, *J. Geophys. Res., 93,* 13,589-13,608, 1988.

Harrison, C.G.A., K.J. Miskell, G.W. Brass, E.S. Saltzman, and J.L. Sloan II, Continental hypsography, *Tectonics, 2,* 357-378, 1983.

Journel, A.G., and C.J. Huijbregts, *Mining Geostatistics,* 600 pp., Academic, San Diego, Calif., 1978.

Klinkenberg, B., and M.F. Goodchild, The fractal properties of topography: A comparison of methods, *Earth Surf. Processes Landforms, 17,* 217-234, 1992.

Lavallee, D., S. Lovejoy, D. Schertzer, and P. Ladoy, Nonlinear variability of landscape topography: Multifractal analysis and simulation, in *Fractals in Geography,* edited by L. De Cola and N. Lam, pp. 158-192, Prentice-Hall, Engelwood Cliffs, N.J., 1993.

Lifton, N.A., and C.G. Chase, Tectonic, climatic and lithologic influences on landscape fractal dimension and hypsometry: Implications for landscape evolution in the San Gabriel Mountains, *Geomorphology, 5,* 77-113, 1992.

Malinverno, A., and P. A. Cowie, Normal faulting and the topographic roughness of mid-ocean ridge flanks, *J. Geophys. Res., 98,* 17,921-17,939, 1993.

Mandelbrot, B.B., Self-affine fractals and fractal dimension, *Phys. Scr., 32,* 257-260, 1985.

Mandelbrot, B.B., and J.W. Van Ness, Fractional Brownian motions, fractional noises and applications, *SIAM Rev., 10,* 422-437, 1968.

Mark, D.M., and P.B. Aronson, Scale-dependent fractal dimensions of topographic surfaces: An empirical investigation, with applications in geomorphology and computer mapping, *Math. Geol., 16,* 671-683, 1984.

Monin, A. S., and A. M. Yaglom, *Statistical Fluid Mechanics,* vol. II, MIT Press, Cambridge, Mass., 1971.

Muzy, J.F., E. Bacry, and A. Arneodo, Wavelets and multifractal formalism for singular signals: Application to turbulence data, *Phys. Rev. Lett, 67,* 3515-3518, 1991.

Muzy, J.F., E. Bacry, and A. Arneodo, Multifractal formalism for fractal signals: The structure-function approach versus the wavelet modulus-maxima method, *Phys. Rev. E, 47,* 875-884, 1993.

Parisi, G., and U. Frisch, Fully developed turbulence and intermittency, in *Proceedings of the International School on Turbulence and Predictability in Geophysical Fluid Dynamics and Climate Dynamics,* edited by M. Ghil, R. Benzi, and G. Parisi, pp. 84-88, North-Holland, New York, 1985.

Polidori, L., J. Chorowicz, and R. Guillande, Descriptio of terrain as a fractal surface, and application to digital elevation model quality assessment, *Photogramm. Eng. Remote Sens., 57,* 1329-1332, 1991.

Power, W.L., and T.E. Tullis, Euclidian and fractal models for the description of rock surface roughness, *J. Geophys. Res., 96,* 415-424, 1991.

Priestley, M. B., *Spectral Analysis and Time Series,* Academic, San Diego, Calif., 890 pp., 1981.

Saupe, D., Algorithms for random fractals, in *The Scienc of Fractal Images,* edited by H.-O. Peitgen, and D. Saupe, pp. 71-136, Springer-Verlag, New York, 1988.

Sayles, R.S., and T.R. Thomas, Surface topography as non-stationary random process, *Nature, 271,* 431-434, 1978.

Scheidegger, A.E., *Theoretical Geomorphology,* 2nd ed., 43 pp., Springer-Verlag, New York, 1970.

Schertzer, D., and S. Lovejoy, Non-linear variability in geophysics: Analysis and simulation, in *Fractals,* edited b L. Pietronero, pp. 49-79, Plenum, New York, 1990.

Strahler, A.N., Hypsometric (area-altitude) analysis of erosional topography, *Geol. Soc. Am. Bull., 63,* 1117-1142, 1952.

U.S. Geological Survey (USGS), Department of the Interior Digital elevation models; data users guide, National Mapping Program, Technical Instructions, *Data Users Guide 5,* 38 pp., Reston, Va., 1987.

Vening Meinesz, F.A., A remarkable feature of the Earth's topography, *Proc. K. Ned. Akad. Wet. Ser. B Phys. Sci., 54,* 212-228, 1951.

Vicsek, T., *Fractal Growth Phenomena,* 2nd ed., 518 pp., World Scientific, Singapore, 1992.

Voss, R.F., Random fractals: Characterization and measurement, *Phys. Scr., T13,* 27-32, 1986.

Voss, R.F., Fractals in nature: From characterization to simulation, in *The Science of Fractal Images,* edited by H.-O. Peitgen, and D. Saupe, pp. 21-70, Springer-Verlag, New York, 1988.

A. Malinverno, Schlumberger-Doll Research, Old Quarry Road, Ridgefield, CT 06877. (e-mail: alberto@sdr.slb.com)

L. F. Pratson and J. K. Weissel, Lamont-Doherty Earth Observatory, P.O. Box 1000, Palisades, NY 10964. (e-mail: lincoln @ ldeo.columbia.edu, jeffw@ldeo.columbia.edu)

(Received April 13, 1993; revised November 16, 1993; accepted January 13, 1994.)

Pliocene to Recent Infilling and Subsidence of Intraslope Basins Offshore Louisiana[1]

Lincoln F. Pratson and William B. F. Ryan[2]

ABSTRACT

Intraslope basins on the lower eastern Louisiana continental slope are modern analogs of large oil- and gas-charged basins infilled on the upper Louisiana slope and buried landward beneath the shelf. High-resolution, gridded multibeam bathymetry and single-channel seismic reflection profiles are used to (1) characterize the morphology and shallow stratigraphy of 46 intraslope basins within the outer slope region; and (2) look for surficial evidence among the basins of slope channelways that fed sediment flows to the Mississippi Fan during the Pliocene-Pleistocene. Computer algorithms, traditionally employed for automatically mapping river networks in gridded land topography, are used to extract morphologic measurements of the intraslope basins from the gridded bathymetry. The basins are found to average approximately 15 km in length, 10 km in width, and 200 m in depth and occur over a map area of about 50 km^2. These dimensions, however, can range over an order of magnitude.

The intraslope basins examined exhibit (1) distinctive plots of basin area vs. relief (i.e., hypsometric curves) and (2) different near-surface (<2 seconds two-way travel time) stratal geometries, which together appear to reflect a continuum between two intraslope basin end-member morphologies. Analysis of the hypsometric curves suggests that the transformation between basin end members is a result of differences in amounts of basin subsidence relative to basin infilling. Comparison with intraslope basins along a canyon-channel system offshore Texas suggests that the transformation occurs as the basins are progressively infilled downslope. However, seismic stratigraphic unconformities within basin strata indicate asymmetric subsidence, presumably along growth faults bounding the basins, which complicates this infilling by periodically deepening the intraslope basins and staving off their burial. Such subsidence appears to have occurred over the Quaternary, deepening the intraslope basins and helping mask any regional bathymetric imprint of the slope pathways eroded by sediment flows during the Pliocene and Pleistocene.

INTRODUCTION

Numerous isolated and enclosed sea-floor depressions, termed intraslope basins (Bouma et al., 1978), populate the Texas-Louisiana continental slope (Figure 1). The basins are shouldered by salt diapirs and are often bounded by growth faults (Worrall and Snelson, 1989). Similar features occur in the subsurface of the Louisiana continental shelf and are interpreted to be intraslope basins that have been infilled and prograded over by the continental shelf (Pacht et al., 1990).

A number of both the buried shelf basins [e.g., Eugene Island Block 330 (Holland et al., 1980, 1990)] and modern slope basins [e.g., Jolliet field, Green Canyon 184 (Brannon et al., 1993); South Timbalier 295 field (Mason et al., 1993); Bullwinkle, Green Canyon 65 field (McCarthy et al., 1993)] are now known to contain thick intervals (up to tens of meters) of clean sands, which in some cases reservoir large volumes (millions of metric barrels) of oil and gas. Like the sands in the modern slope basins, the sands deep in the infilled shelf basins were deposited in bathyal water depths (200–2000 m: Mitchum et al., 1990). These sands, which are distinct in well logs (Figure 2), generally occur in a

---

[1] Revised manuscript submitted February 11, 1994; final revisions submitted May 18, 1994; final acceptance June 10, 1994.

[2] Lamont-Doherty Earth Observatory, Columbia University, Palisades, New York 10964.

This study, which represents part of Pratson's Ph.D. dissertation at Columbia University, benefited from the help of a number of people. The bathymetry for the project was made available by the National Oceanic and Atmospheric Administration, with thanks owed to M. Lockwood and P. Grim. The project evolved from conversations with P. Flemings, V. Kolla, and C. Pirmez. The initial manuscript was improved by the ideas and suggestions of D. Twichell, N. Driscoll, P. Flemings, G. Karner, and P. Grim. Critical reviews by P. Weimer, R. J. Scolaro, J. W. Tucker, and D. H. Wilson clarified ideas and helped place the study in the context of recent Gulf of Mexico findings. Thanks is also owed to P. Weimer for well logs from the Green Canyon area, and to A. Pulham for permission to reproduce his seismic profiles and interpretations of buried submarine canyons on the Louisiana continental slope. Funds for this study were provided by the National Science Foundation (Grant No. OCE 89-12241), the Office of Naval Research (Contract Nos. N0014-87-K-0204 and N00014-93-1-0126), and the Department of Energy (Project No. DE-FC22-93BC1496). This is L-DEO contribution no. 5203.

AAPG Bulletin, V. 78, No. 10 (October 1994). P. 1483–1506.

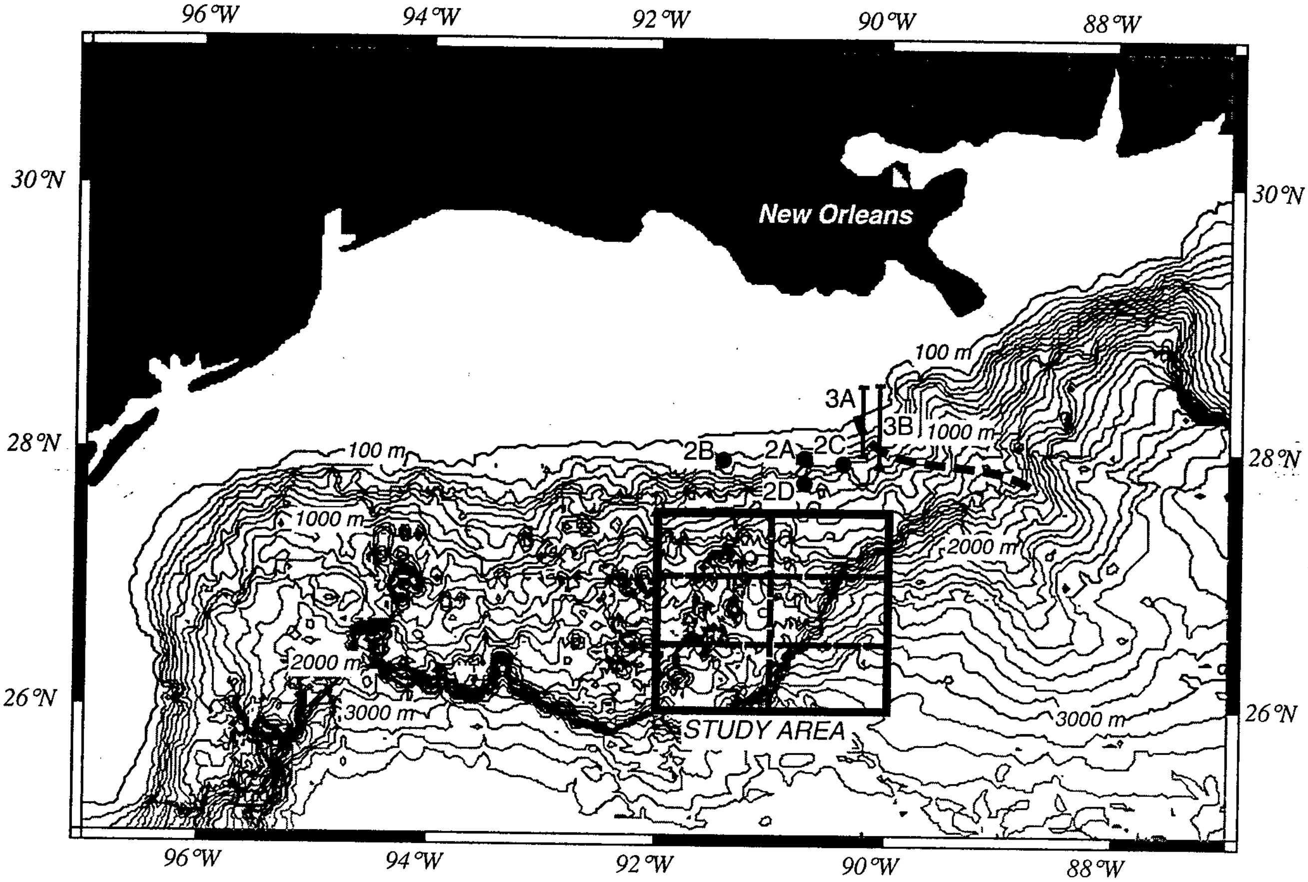

Figure 1—Bathymetry of the northwest U.S. Gulf Coast margin. Boxed region is the study area. Dashed lines within study area outline the six NOAA bathymetric grids used to create the composite grid shown in Figure 4. Solid circles represent the locations of the boreholes from which the well logs in Figure 2 are taken. Solid lines represent locations of seismic profiles showing buried Pliocene and Pleistocene submarine canyons. Dotted line marks main axis of an upper Pleistocene canyon mapped by Pulham (in 1993). Contour map was made from bathymetry derived from GeoBase (Menke et al., 1991) using GMT software (Wessel and Smith, 1991).

repeating vertical succession of (1) thick, laterally continuous sheet sands interpreted to be basin floor fans overlain by (2) more localized massive sands interpreted to be amalgamating channels, overlain in turn by (3) thinning-upward interbedded sands and silts interpreted to be levee/overbank deposits (Mitchum et al., 1990; McGee et al., 1993; Pulham, 1993). In the case of the modern slope basins, the sands were delivered through buried canyons (Figure 3), which, in at least one instance (Pulham, 1993), have been documented to extend to the Mississippi Fan (Figure 1).

Regional mapping of possible buried canyon systems and of the intraslope basins through which the systems passed would present an important aid in the search for sand reservoirs on the Texas-Louisiana slope. It would also be of help in determining the timing of intraslope basin evolution and sediment accumulation. Segments of the buried canyons have been imaged in multichannel seismic reflection profiles (Mann et al., 1992; Pulham, 1993), and a comprehensive map of buried canyons on the eastern Louisiana slope is being compiled (Weimer and Dixon, in press). So far, slope morphology has been of limited help in locating these fairways, for unlike other continental margins, not even modern canyon/channel systems are evident in the region's lunar-like bathymetry. But if, as suggested by Bouma et al. (1990), intraslope basins associated with former canyon/channel systems are in some way unique, the identification and linking of these basins could yield a first-order map of potential sand reservoirs across the continental slope.

One criterion for differentiating the intraslope basins might be their shape. The basins are irregular in form and size. Until recently, they had been best depicted in hand-drawn bathymetric maps of the Texas-Louisiana slope constructed by Bryant et al. (1990) from seismic reflection profiles spaced at

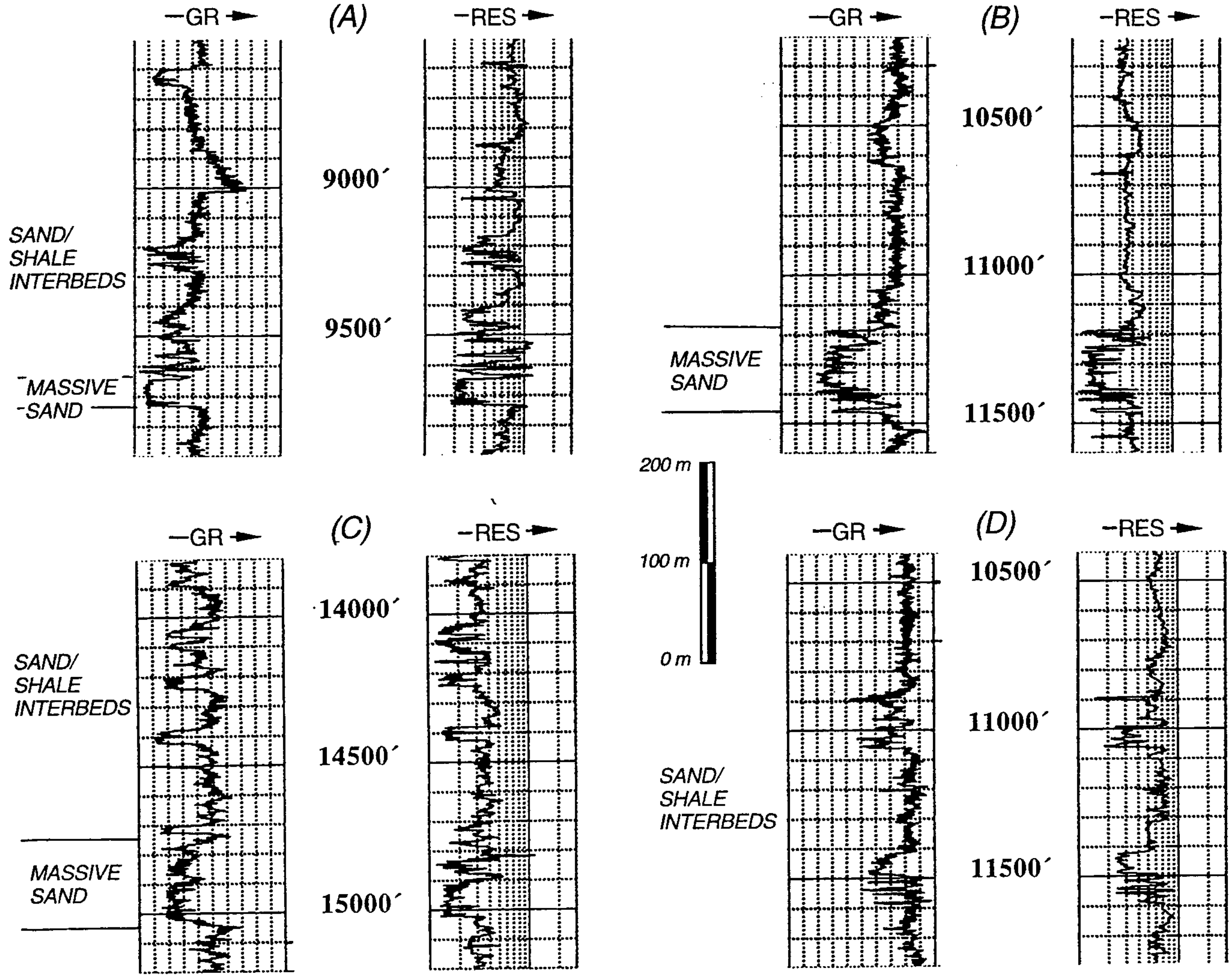

Figure 2—Example gamma-ray and resistivity well-log responses to Pliocene–Pleistocene turbidite sands drilled in different intraslope basins immediately north of the study area (locations A–D shown in Figure 1). The sands, which produce distinct low gamma-ray and resistivity kicks, are characteristically massive at the base, giving rise to a relatively "blocky" log shape with clear top and bottom. Thinner sand units spaced apart by shale interbeds often occur above. The overall well-log signal through the sands reflects a fining upward. The well logs are courtesy of P. Weimer.

least 8 km apart. Much higher-resolution gridded bathymetry of this region (Figure 4) has now been released by the National Oceanic and Atmospheric Administration (NOAA). This bathymetry, which derives from complete multibeam bathymetric mapping of areas within the Gulf of Mexico, accurately documents the morphology of intraslope basins at a resolution of 250 m.

The purpose of this paper is to use NOAA's gridded version of the bathymetry for the eastern Louisiana continental slope (26–27.5°N, 90–92°W; Figure 4) to obtain a better understanding of the morphology of the intraslope basins—both as a modern analog for the morphology of salt-shouldered, oil-producing basins now buried beneath the Louisiana continental shelf and as a means of distinguishing patterns among the intraslope basins that might lead to insights on the locations of buried slope channelways. Computer algorithms that delineate lows in gridded elevation data are used to extract from the bathymetry measures of the sizes and shapes of 46 intraslope basins that occur within the study area. Single-channel seismic reflection profiles collected by the U.S. Geological Survey (USGS) are then used to relate the morphology of these basins to general differences in the stratal geometry of their upper sediment fill. Although two end members and a transitional type

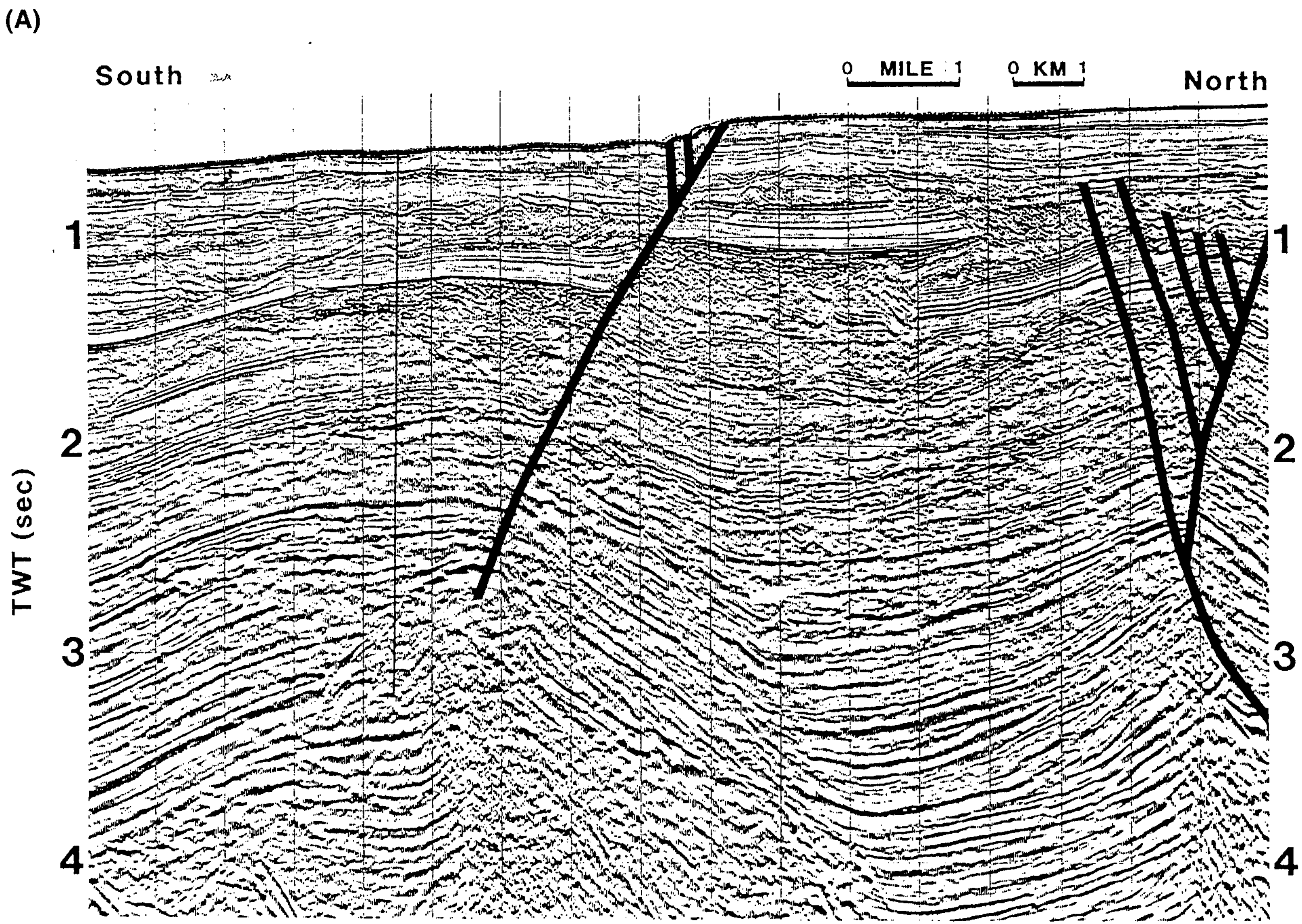

Figure 3—(A and B) Dip-oriented seismic reflection profiles (uninterpreted [a] and interpreted [b]) across the upper slope in the northeast corner of the study area (locations 3A and 3B shown in Figure 1), showing buried canyons (highlighted) incising middle and late Pleistocene sediments (from Pulham, 1993).

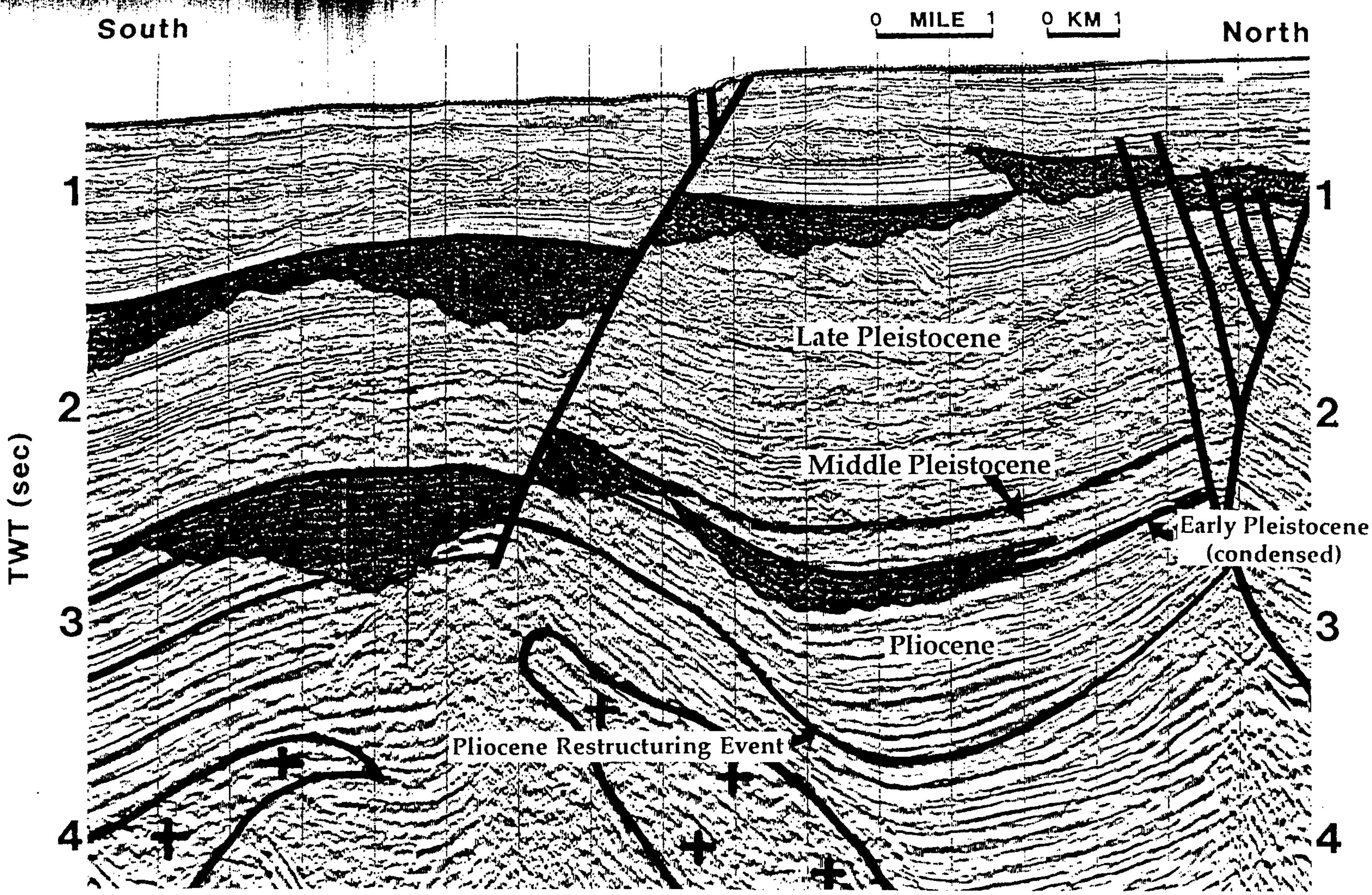

Figure 3—Continued.

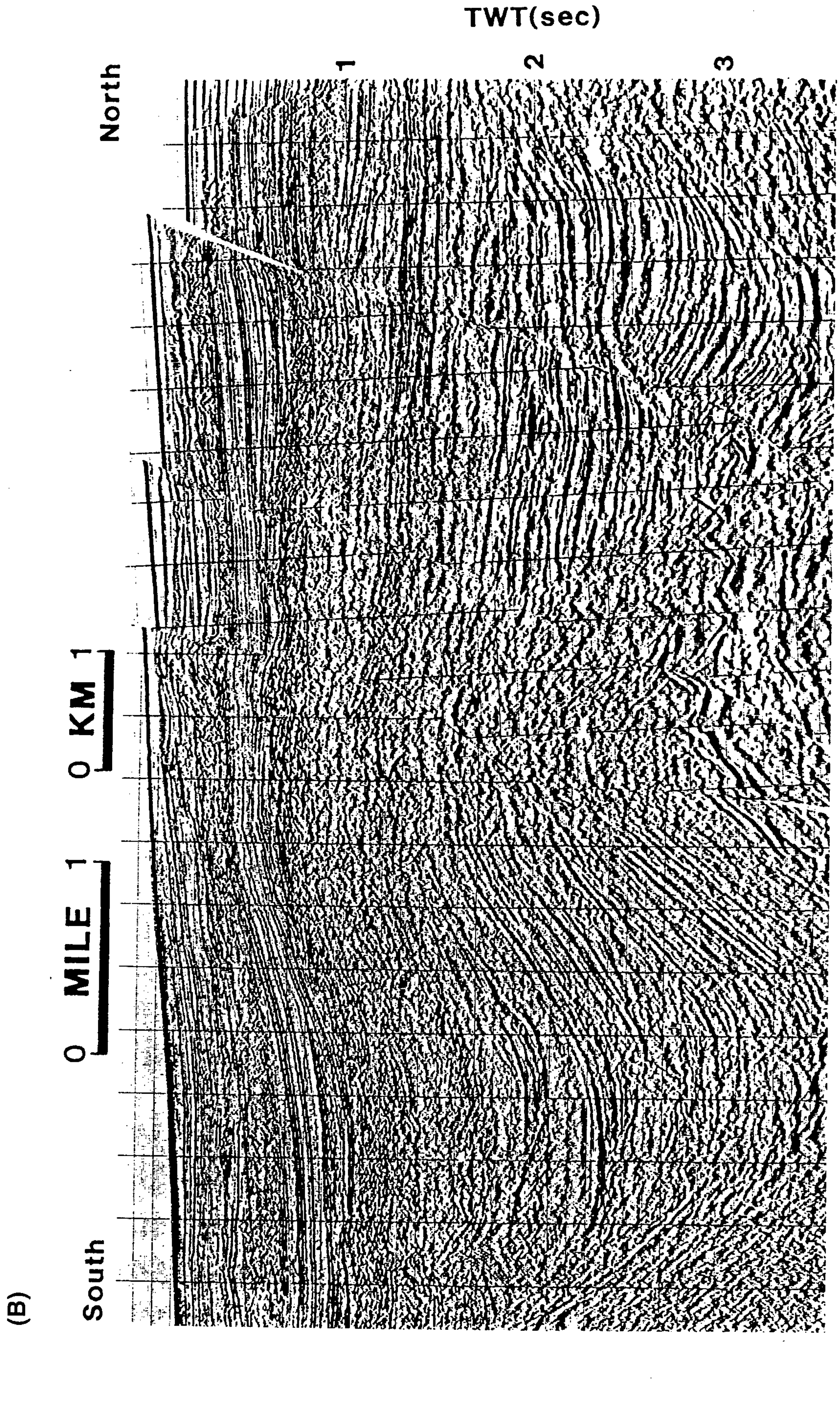

Figure 3—Continued.

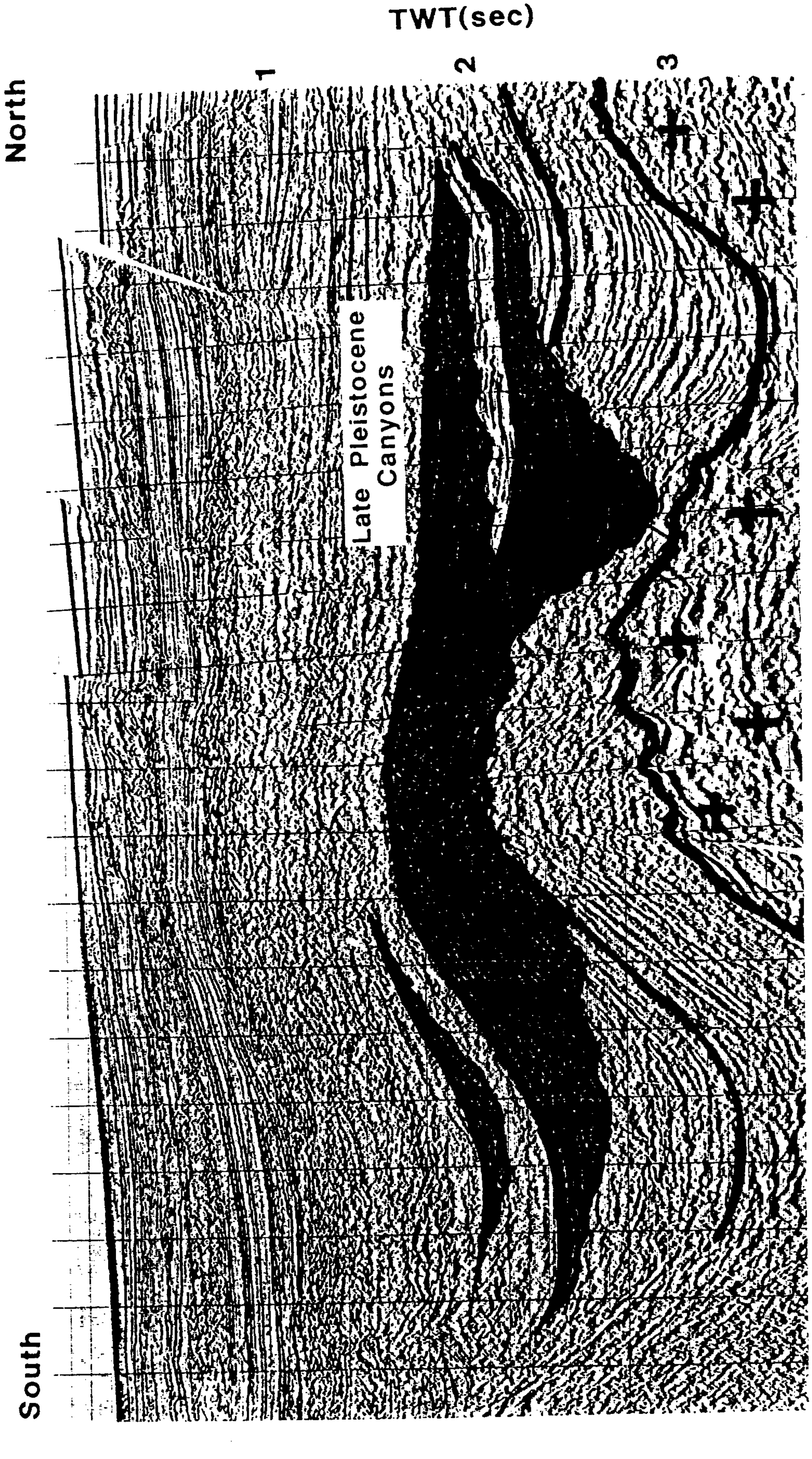

Figure 3—Continued.

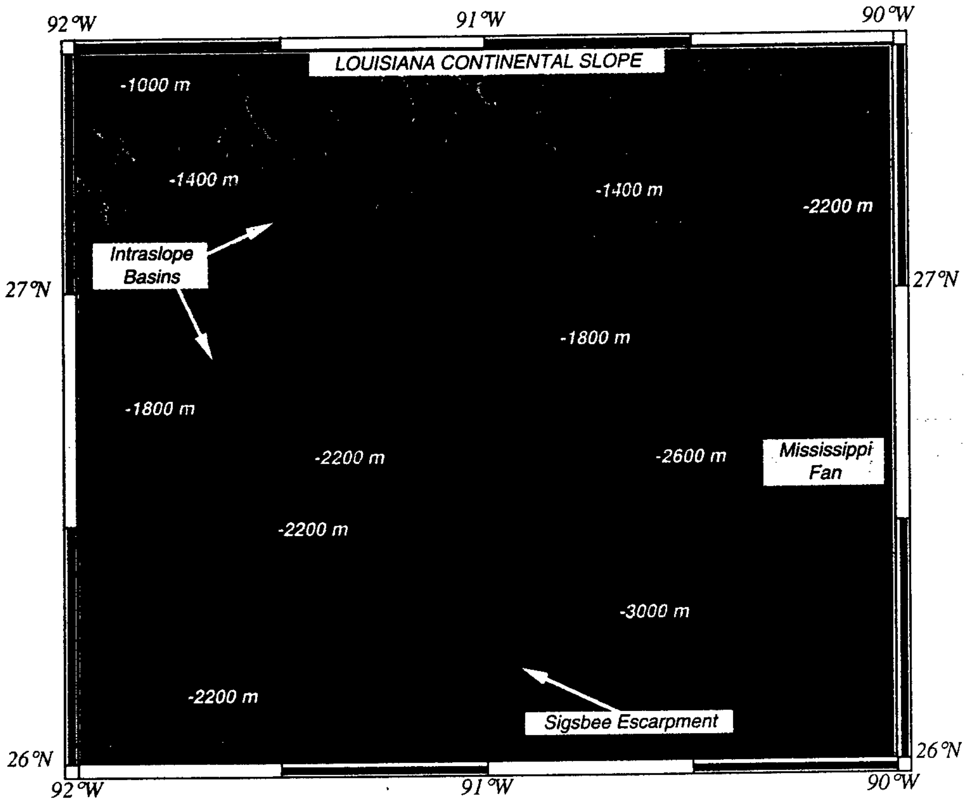

Figure 4—Sun-shaded (illumination from west) image of the NOAA gridded bathymetry within the study area. Grid cell spacing is 250 m. Study area encompasses the lower portion of the eastern Louisiana continental slope, a segment of the Sigsbee Escarpment, and the western part of the Mississippi Fan. Intraslope basins are the numerous depressions that pockmark the slope surface.

of intraslope basin morphology are identified, their distributions across the study area fail to form any downslope linkages that might be attributed to former slope channelways. However, the analyses provide a geologically recent perspective on how depositional infilling of the intraslope basins is offset by basin subsidence caused by the interplay of sediment loading and salt withdrawal.

STUDY AREA

Geologic Setting

The study area (Figures 1, 3) encompasses a large portion of the Louisiana continental slope, a segment of the Sigsbee Escarpment, and part of the western Mississippi Fan. It is located in the offshore slope areas of Green Canyon and Walker Ridge. Water depths range from 670 m in the northwest corner of the study area to 3400 m in the southeast corner.

The portion of the slope covered by the study area is part of a complex terrain created by the deformation of the buried Louann Salt. The Louann Salt was deposited in the northern and northwestern region of the Gulf of Mexico in the Middle to Late Jurassic during the opening of the Gulf of Mexico when sea-floor spreading separated North America from Africa and South America (Salvador, 1987). During the Tertiary, rapid loading of deltaic sediments along the Texas-Louisiana coast led allochthonous appendages of the salt to be emplaced in the overlying strata often seaward of their original site of deposition (Humphris, 1978, 1979). Emplacement of this allochthonous salt has occurred as a variety of structures—salt pillows, stocks, bulbs, tongues, etc. (Jackson and Talbot, 1986, 1989)—that underlie and complicate the surface of the gentle (<1°) southward-dipping slope plateau. This plateau runs from Texas to Louisiana, extends up to 250 km seaward of the shelf break, and ranges from 200 to 2200 m in water depth (Figure 1). The seaward front of the plateau is the Sigsbee Escarpment (Figure 4), which drops 600 to 800 m at an angle of 15 to 22° down to the Mississippi Fan at a water depth of 3000 m.

NOAA Bathymetry

Bathymetry of the study area was collected by NOAA using the SeaBeam swath mapping system, a hull-mounted, multibeam echo sounder (Renard and Allenou, 1979; de Moustier, 1988). The system emits a 12-kHz signal, which is beam formed to produce 16 equally spaced depth measures along a profile of the sea floor that is perpendicular to the survey direction and about 75% of the water depth in

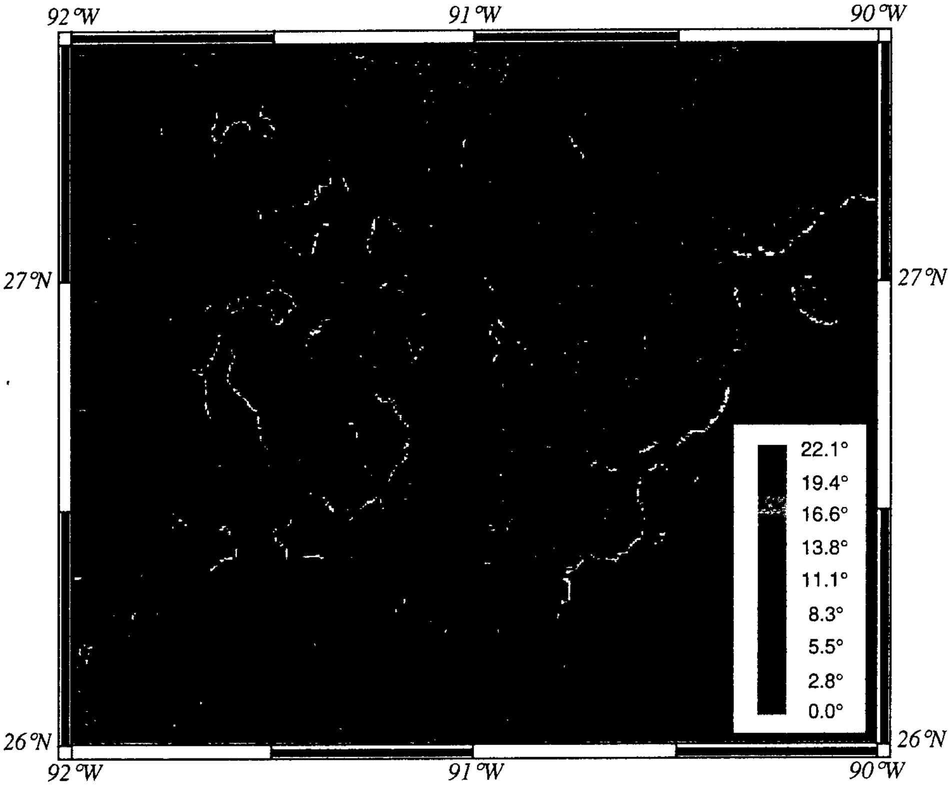

Figure 5—Local slope magnitudes. Scale at lower right is in degrees below the horizontal.

length. Each of the 16 depth measurements in the profile has a position accuracy of within 50 m and vertical accuracy of within 1% of actual water depth. The bathymetric profiles are recorded every few seconds and build a swath of sea-floor bathymetry centered along the track line followed by the survey ship. In the case of the NOAA bathymetry, the ship tracks were structured so that neighboring swaths overlapped at least 10%, resulting in complete sea-floor coverage of the study area (Grim, 1992).

The bathymetry was gridded by NOAA into six grids (NOAA, 1989a, b, c, d, e, f; Figure 1), each grid covering a map area measuring one degree of longitude by one-half degree of latitude. The individual grids are based on roughly 300,000 soundings selected from 5 to 10 million "raw soundings" (Grim, 1992). Grid projections are in Universal Transverse Mercator (UTM) coordinates, and grid node spacing is 250 meters. The six grids share a common central longitude, and adjacent grids overlap by 1 to 2 km, allowing construction of the composite grid shown in Figure 4.

Regional Slope Morphology

Despite the irregular morphology of the numerous intraslope basins and intervening slope highs, the regional dip of the continental slope is relatively uniform. A best-fit surface to the gridded slope bathymetry has a goodness-of-fit of 0.72 (or a multiple correlation coefficient of 0.85) and yields a mean slope gradient of approximately 0.5° dipping 170° from true north. Roughly the same goodness-of-fit, slope gradient, and dip direction are obtained for best-fit surfaces determined using only the depths of the floors of the intraslope basins (0.4° dipping 172° from true north with a goodness-of-fit of 0.74) and only the depths of the highs that separate the basins (0.5° dipping 170° from true north with a goodness-of-fit of 0.87). Although offset more than 200 m, these two latter best-fit surfaces essentially parallel one another, indicating that the intraslope basins do not become systematically deeper or shallower seaward of the shelf break.

Local slope gradients are extremely variable and can be quite steep. Figure 5 shows slope magnitudes determined by calculating the best-fit surface to a 3 × 3 cell window (an area 750 m × 750 m square) centered on each grid cell. The flattest areas occur within the floors of the intraslope basins and approach 0°. The steepest areas occur along the walls of the basins and along the Sigsbee Escarpment where slopes often exceed 15° and in some instances reach 22°.

Slope dip directions are shown in Figure 6. The directions are independent of slope magnitude and therefore reflect any directional change in slope dip. Dip directions within the intraslope basins change

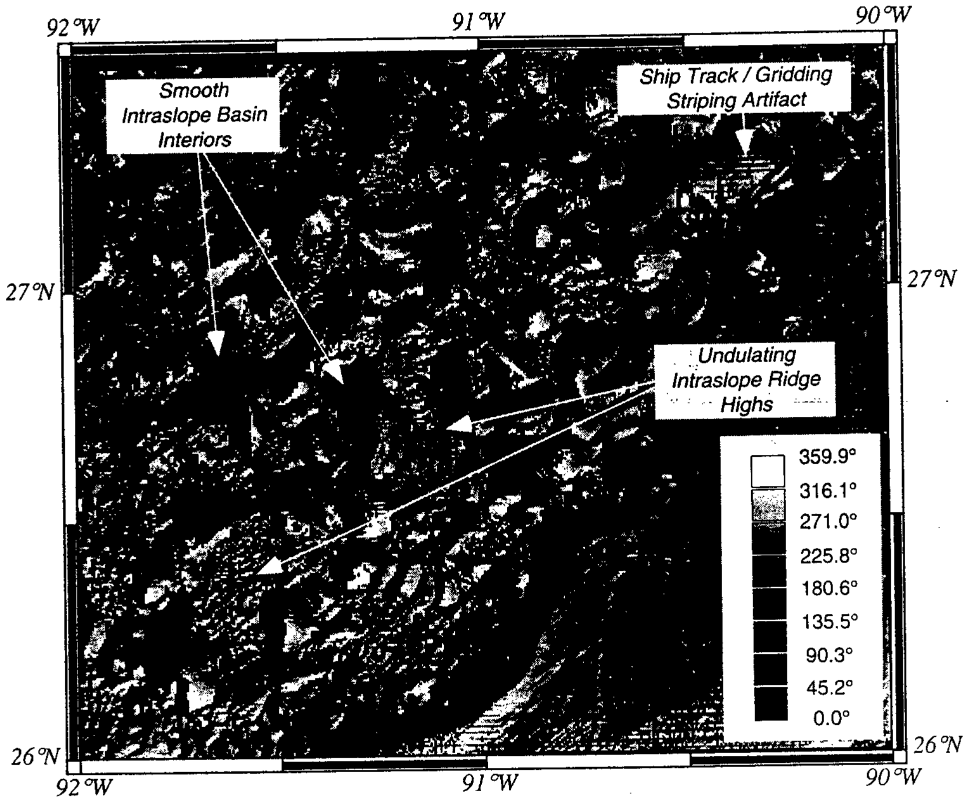

Figure 6—Local slope dip directions. Scale at lower right is in degrees from true north.

gradually, indicating that the basin interiors depicted at the grid cell spacing of 250 m are in general surprisingly smooth. Bathymetric evidence of mass wasting is rarely seen despite the steepness of the intraslope basin walls. Dip directions along the topographic highs that separate the intraslope basins are much more variable and often form a corrugated pattern (Figure 6). This pattern reflects a surface roughness that has a wavelength of approximately 5 to 10 km and a relief of 10 to 50 m. Its cause is unclear.

Spectral analysis indicates that the intraslope basins do not exhibit a periodicity to their occurrence or a preferred orientation. Slope bathymetry yields a red-noise power spectrum (Figure 7) in which statistically significant wavelengths relating to the spacing of intraslope basins are not seen. The circular shape of the power spectrum indicates that slope topography is isotropic, meaning that there is no preferred orientation to the slope highs and lows. Lacking in the bathymetry are any detectable trends, notably the downslope lineations of canyons and chutes seen along other continental slopes, which tend to produce elliptical 2-D power spectrums.

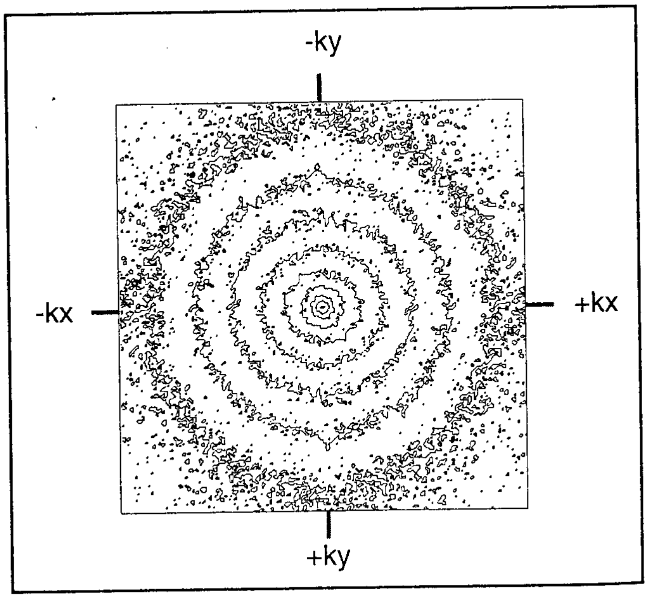

Figure 7—Contour map of a two-dimensional power spectrum in log coordinates derived from the NOAA gridded bathymetry of the continental slope. Black lines are contours for each magnitude change in power. The spectrum represents the average of eight tapered spectra that were calculated for a 256 × 256 cell window, which was moved across the slope bathymetry at half-window increments. Spectra were calculated using the 2-D fourier transform algorithm of Press et al. (1989).

MORPHOLOGY OF THE INTRASLOPE BASINS

The intraslope basins on the Texas-Louisiana continental slope have come to be recognized as mod-

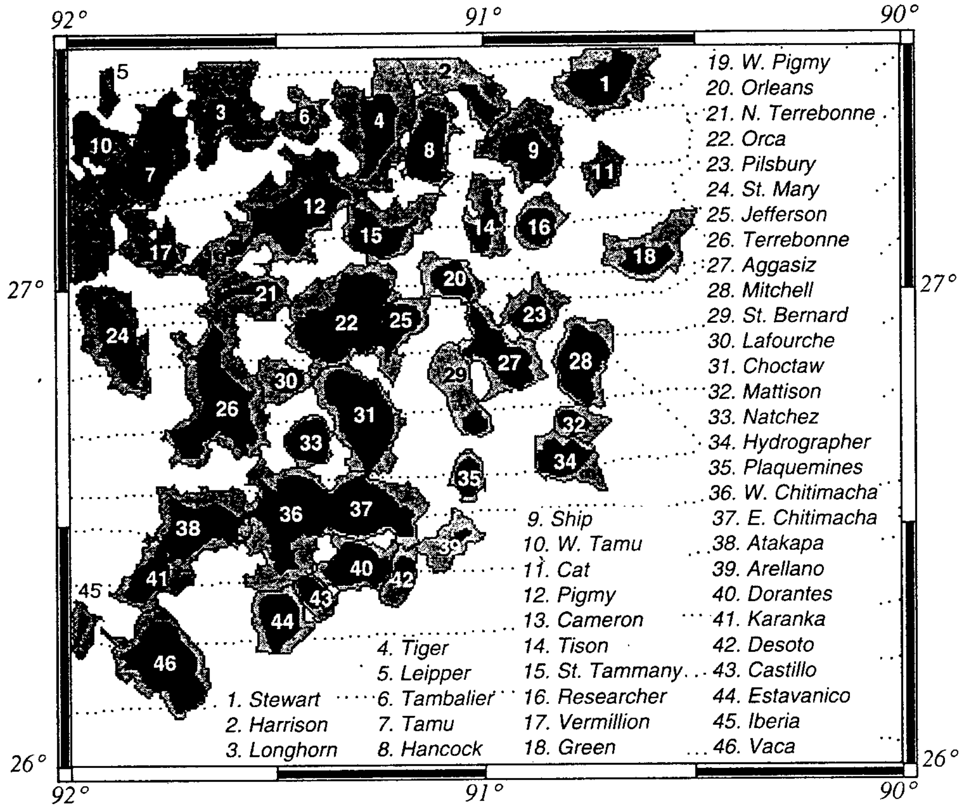

Figure 8—Map showing the locations and names of the 46 intraslope basins within the study area. The basins are delineated by two boundaries: outer boundaries are the basin rims; inner boundaries, which encircle the darker-gray areas, are all elevations within the basins that occur below the lowest (i.e., spillpoint) elevations along the basin rims. Dotted lines are track lines of SCS profiles collected by the USGS.

ern analogs for salt-shouldered basins buried beneath the Louisiana continental shelf (Pacht et al., 1990, 1992). These buried shelf basins are among the most prolific oil- and gas-charged basins in the Gulf of Mexico, and in some instances the most prolific in the world (e.g., Eugene Island Block 330; Holland et al., 1980, 1990). The dimensions of the buried shelf basins can be determined from closely spaced seismic reflection data. But their original form has undoubtedly been distorted by postburial sediment loading/compaction, salt movement, and faulting. A view of these basins prior to their burial is provided by the NOAA gridded bathymetry of intraslope basins on the eastern Louisiana continental slope. This bathymetry is used to compile measurements of the sizes and shapes of the 46 intraslope basins that occur in the study area.

Delineation of the Intraslope Basins

Measurement of the sizes and shapes of the intraslope basins first required delineation of the basins in the gridded bathymetry. This was done automatically using computer algorithms originally designed for extracting drainage information on river systems from digital elevation models of land topography (see Jenson and Dominique, 1988, and Pratson and Ryan, 1992, for details).

The intraslope basins were delineated by assigning each grid cell in the bathymetry a unit vector, or flow direction, that pointed to the one of eight neighboring grid cells that was steepest downslope. Grid cells at the bottoms of the intraslope basins had no lower neighboring grid cells, and so were flagged as having no flow directions. By grouping all surrounding grid cells with flow directions that led to these flagged cells, the interiors of the basins were mapped up to the basin rims, outlined by grid cells with flow directions that pointed away from the basins.

The rims of the intraslope basins are the outer boundaries of the light gray areas shown in Figure 8. The inner boundaries surrounding the dark gray areas encircle elevations that occur below the lowest elevation along the basin rims. This elevation is referred to as the basin "spillpoint" and is used as a proxy for the height to which each intraslope basin could be infilled before sediments would begin to bypass the basin (assuming no basin subsidence).

Intraslope Basin Dimensions

Table 1 lists the 46 intraslope basins, their geographic locations, and their dimensions as measured using each basin's spillpoint contour (inner boundaries, Figure 8). The measurements provide the exploration geologist with a reference as to the

Table 1. The Intraslope Basins Within the Study Area, Their Locations, and Their Dimensions Based on Each Basin's Spillpoint Contour*

Basin	Mean Latitude	Mean Longitude	Length (km)	Width (km)	Perimeter (km)	Area (km²)	Volume (km³)	Relief (m)	Stratal Geometry
Stewart	27° 27′ N	90° 42′ W	17.6	9.3	51.8	131.3	175.2	80	Bowl
Harrison	27° 25′ N	90° 59′ W	12.5	4.3	34.8	41.8	60.3	85	Bowl
Longhorn	27° 23′ N	91° 36′ W	16.7	6.3	54.0	93.9	142.7	227	Box
Tiger	27° 21′ N	91° 15′ W	21.6	8.3	55.6	120.2	207.1	159	Barrier
Leipper	27° 25′ N	91° 54′ W	4.0	1.8	9.9	5.5	5.6	75	•
Tambalier	27° 23′ N	91° 25′ W	7.2	3.8	21.4	24.5	35.0	155	Box
Tamu	27° 16′ N	91° 48′ W	17.2	9.8	50.4	125.0	188.6	166	Barrier
Hancock	27° 19′ N	91° 08′ W	17.5	9.3	51.8	131.3	209.8	346	Barrier
Ship	27° 17′ N	90° 53′ W	13.9	8.8	44.8	113.4	189.6	158	Barrier
West Tamu	27° 20′ N	91° 55′ W	8.3	4.3	24.2	27.9	39.2	78	Barrier
Cat	27° 15′ N	90° 42′ W	7.6	5.3	20.6	30.7	45.2	101	Bowl
Pigmy	27° 11′ N	91° 26′ W	28.7	9.8	86.3	226.1	452.7	521	Box
Cameron	27° 08′ N	91° 56′ W	5.0	3.3	14.5	12.3	20.0	53	Barrier
Tison	27° 09′ N	90° 59′ W	15.3	5.3	42.6	60.9	108.5	270	Box
Saint Tammany	27° 08′ N	91° 15′ W	17.6	8.3	55.5	109.9	210.8	305	Barrier
Researcher	27° 08′ N	90° 52′ W	9.1	8.3	28.5	61.2	105.7	174	Bowl
Vermillion	27° 06′ N	91° 47′ W	13.5	5.3	35.6	51.9	86.8	200	Bowl
Green	27° 04′ N	90° 37′ W	12.9	6.8	36.4	65.8	112.7	57	Bowl
West Pigmy	27° 07′ N	91° 36′ W	5.5	3.3	16.0	14.1	25.6	106	Box
Orleans	27° 02′ N	91° 04′ W	11.3	7.3	32.0	64.3	127.2	150	Barrier
North Terrebonne	27° 01′ N	91° 33′ W	16.3	5.3	44.6	56.2	119.5	247	Box
Orca	26° 57′ N	91° 20′ W	26.5	12.8	83.2	311.8	684.1	466	Box
Pilsbury	26° 57′ N	90° 53′ W	10.3	7.3	30.8	61.6	117.2	166	Bowl
Saint Mary	26° 55′ N	91° 53′ W	25.7	8.3	75.4	156.3	289.1	194	Bowl
Jefferson	26° 56′ N	91° 13′ W	14.9	7.3	44.3	80.4	165.8	228	Box
Terrebonne	26° 46′ N	91° 39′ W	33.3	11.3	114.4	295.0	626.1	281	Box
Aggasiz	26° 52′ N	90° 58′ W	23.7	8.3	66.9	146.3	299.5	301	Box
Mitchell	26° 50′ N	90° 46′W	19.2	9.8	53.2	148.5	289.3	216	Bowl
Saint Bernard	26° 43′ N	91° 01′ W	6.5	4.8	20.5	26.2	53.0	93	Barrier
Lafourche	26° 49′ N	91° 29′ W	8.1	6.3	23.0	38.2	70.9	51	•
Choctaw	26° 44′ N	91° 18′ W	25.5	12.8	68.6	242.7	550.5	443	Box
Mattison	26° 43′ N	90° 47′ W	7.8	5.8	21.8	33.3	68.1	75	•
Natchez	26° 41′ N	91° 41′ W	11.2	9.3	35.1	84.8	169.1	227	•
Hydrographer	26° 38′ N	90° 49′ W	13.8	7.3	38.9	85.4	192.1	212	Bowl
Plaquemines	26° 36′ N	91° 02′ W	9.6	6.3	26.4	45.0	93.2	75	Bowl
West Chitimacha	26° 32′ N	91° 28′ W	24.1	13.3	92.8	251.9	584.6	442	Box
East Chitimacha	26° 32′ N	91° 17′ W	23.7	13.3	68.2	214.5	495.5	282	Bowl
Atakapa	26° 30′ N	91° 41′ W	21.6	9.8	74.0	175.6	404.4	366	Box
Arellano	26° 28′ N	91° 05′ W	9.7	2.3	22.4	18.6	40.2	77	•
Dorantes	26° 25′ N	91° 19′ W	16.4	9.3	47.7	119.9	267.5	242	Barrier
Karanka	26° 24′ N	91° 49′ W	15.9	6.8	43.9	84.8	193.5	324	Barrier
Desoto	26° 25′ N	91° 12′ W	7.9	5.3	21.6	29.6	64.0	66	Bowl
Castillo	26° 22′ N	91° 25′ W	8.9	5.3	24.1	38.5	84.1	106	•
Estavanico	26° 18′ N	91° 30′ W	14.2	9.3	40.2	101.1	231.4	126	Bowl
Iberia	26° 17′ N	91° 59′ W	9.0	2.3	21.0	14.6	34.9	200	Box
Vaca	26° 13′ N	91° 47′ W	22.9	12.8	72.3	241.7	594.2	412	Bowl
Minimum			4.0	1.8	9.9	5.5	5.6	51	
Maximum			33.3	13.3	114.4	311.8	684.1	521	
Range			29.3	11.5	104.4	306.3	678.5	470	
Mean			15.0	7.4	44.4	100.3	202.8	204	
Standard Deviation			7.1	3.0	23.3	79.9	181.2	123.6	

*Length = diameter of smallest circle that encloses basin; width = diameter of largest circle enclosed by basin; perimeter = length of basin perimeter; area = surface area of basin interior; volume = volume of basin interior; relief = difference in elevation between basin spillpoint and deepest point within basin; • = USGS seismic survey did not cross basin.

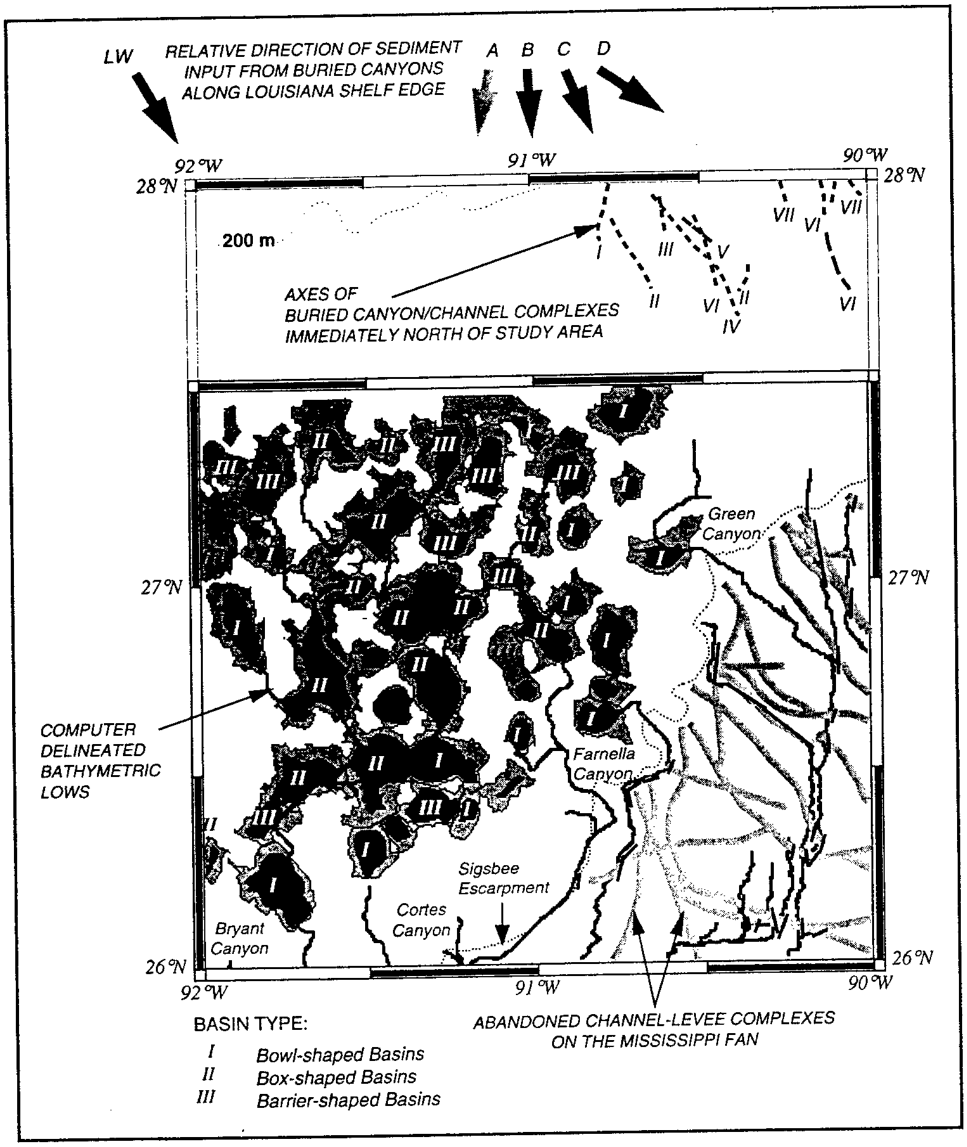

Figure 9—Distribution of regional bathymetric lows and the three types of intraslope basin morphologies identified in the study area. Thick black lines are bathymetric lows mapped using drainage extraction algorithms applied to NOAA bathymetric grids after infilling intraslope basins to their spillpoints. Also shown are the relative locations of Pleistocene submarine canyons buried along the shelf edge (Woodbury et al., 1978; Berryhill et al., 1987), canyon/channel axes mapped on the upper slope immediately to the north of the study area (modified from Mann et al., 1992), and the locations of channel-levee complexes abandoned at the foot of the Sigsbee Escarpment (modified from Weimer, 1989). The canyons mapped by Woodbury et al. (1978) (canyons A–D) and Mann et al. (1992) (canyons I–VII) are labeled according to age of burial (A and I being the oldest). The LW canyon mapped by Berryhill et al. (1987) is interpreted to be late Wisconsinian.

possible sizes of similar basins now buried beneath the Louisiana continental shelf. The intraslope basins within the study area range from 4 to 33 km in length, 2 to 13 km in width, and 6 to 312 km^2 in map area. Basin relief is cast in terms of depth below the spillpoint contour, and ranges from 51 to 521 m. As will be shown, these depths may vary over time as a result of the competing influences of sediment infilling and basin subsidence.

SEARCH FOR SURFICIAL EVIDENCE OF FORMER SLOPE SEDIMENT FAIRWAYS

Regional Bathymetric Lows as Potential Infilled Sediment Fairways

As noted above, submarine canyons are not readily identifiable in the NOAA bathymetry. Linear depressions resembling channels partially ring several of the intraslope basins (e.g., Cat, Researcher, St. Bernard, Choctaw, and Desoto, Figures 8 and 4), but shallow-penetration, single-channel seismic reflection profiles collected by the USGS in these areas show the depressions to be grabens or bottoms of scarps corresponding to basin-bounding faults that extend into the subsurface (Twichell and Delorey, in press).

Deeper-penetration seismic reflection profiles reveal buried canyons/channels that passed into intraslope basins immediately north of the study area (Figure 9; Mann et al., 1992). If these canyons extended into and across the study area, they might be overlain by regional bathymetric lows (e.g., Mississippi trough to the east, which overlies the buried Young Timbalier Canyon; Shipp, 1993). Delineation of such bathymetric lows is readily done with the drainage extraction algorithms used to map the intraslope basins. However, a present limitation in using the algorithms for this purpose is that depressions in an elevation grid first have to be "infilled." This is because the flow direction scheme employed by the algorithms identifies drainage routes as continuous paths of (monotonically) decreasing elevation. Once a chain of flow directions leading downslope across an elevation grid enters a depression, it dead-ends at the base of the depression. As a result, depressions, such as the intraslope basins, act to segment drainage routes extracted by the algorithms.

In order to map bathymetric lows in the study area that extend from the upper slope to the lower slope and out onto the Mississippi Fan, a depressionless version of the NOAA bathymetric grid was first generated by infilling each intraslope basin up to its spillpoint elevation. Flow directions for this depressionless version of the bathymetric grid were then determined, and were used to compute the total number of grid cells that occurred upslope of, and directed flow into, each grid cell. These totals represented the sea-floor area "drained" by each grid cell. Bathymetric ridges were delineated by grid cells with the lowest drainage areas, whereas bathymetric valleys were delineated by grid cells with the highest drainage areas. This characterization of the bathymetry allowed regional bathymetric lows to be mapped as those grid cells with sea-floor drainage areas greater than or equal to a user-defined threshold.

Figure 9 shows a map of regional bathymetric lows linking several series of intraslope basins across the study area. The lows are mapped as all grid cells draining sea-floor areas equal to or in excess of 5000 grid cells (1250 km^2). The lows are not mapped to the upslope edges of the grid where grid cell drainage areas are less than the threshold.

The mapped bathymetric lows occur seaward of buried submarine canyons on the continental shelf (Woodbury et al., 1978; Berryhill et al., 1987) and upper slope (Mann et al., 1992), and lead toward abandoned channels on the western Mississippi Fan (Weimer, 1989). Their occurrence represents one possibility as to the former routes of Pliocene-Pleistocene sediment fairways, and of the intraslope basins they crossed through on the mid to lower slope. Note, however, that because of salt deformation during the Quaternary, the bathymetric lows mapped in Figure 9 may have little to no relation to former sediment fairways now buried beneath the continental slope.

Basin Hypsometry

A second way of trying to locate buried sediment fairways using sea-floor bathymetry, and possibly to substantiate the computer-delineated sediment fairways in Figure 9, is to look for differences in the shapes of the intraslope basins that might be associated with infilling and/or bypassing of the basins by gravity-driven sediment flows. If such an association exists, former sediment fairways should be manifest in the spatial distribution of intraslope basins with distinctive basin morphologies.

The morphology of intraslope basins can be characterized in a variety of ways—e.g., circularity, elongation, and other form ratios such as those given by Davis (1986). Of the measures explored, the hypsometric curve was found to provide the most morphologic information, for it takes into account both the surface area and relief of the intraslope basins.

Hypsometric curves represent the relative proportion of the map area of a basin enclosed by each elevation contour within the basin. The curves are constructed by plotting a graph of basin elevation against the cumulative percentage of basin map area at or below each elevation (Strahler, 1952). The curves are read such that approximately 0% area occurs at the bottom of the basin, whereas 100% occurs at or below the highest point along the basin rim (outer boundaries of basins shown in Figure 7). The shapes of the curves between these two elevations depend on how the area of the basin increases with increasing elevation. For example, the hypsometric curve for a basin shaped like a half sphere is concave, because most of the basin area occurs at low elevations (Figure 10). The hypsometric curve for a basin shaped like a cone, on the other hand, is convex, because most of the basin area occurs at high elevations (Figure 10). Intermediate between the two is a basin shaped like a circular parabola (Figure 10). In this type of basin, there is a constant increase in basin area with elevation, and the resulting hypsometric curve is a straight line.

The unique shape of this last hypsometric curve is used here as a reference for distinguishing two types of hypsometric curves commonly exhibited by the intraslope basins. The first, type A, falls completely below the reference curve and generally resembles the hypsometric curve of a half sphere (e.g., Mitchell Basin, Figure 11A). The second, type B, crosses the reference curve and commonly has a bottom half that arcs above it and a top half that arcs below it (e.g., West Chitimacha Basin, Figure 11B).

Shallow Basin Stratigraphy

In order further to categorize the morphology of the intraslope basins, the hypsometric curves were related to the shallow stratigraphy (<1.5 seconds two-way travel time) within the basins imaged in single-channel seismic (SCS) reflection profiles. The SCS profiles available for this study were ana-

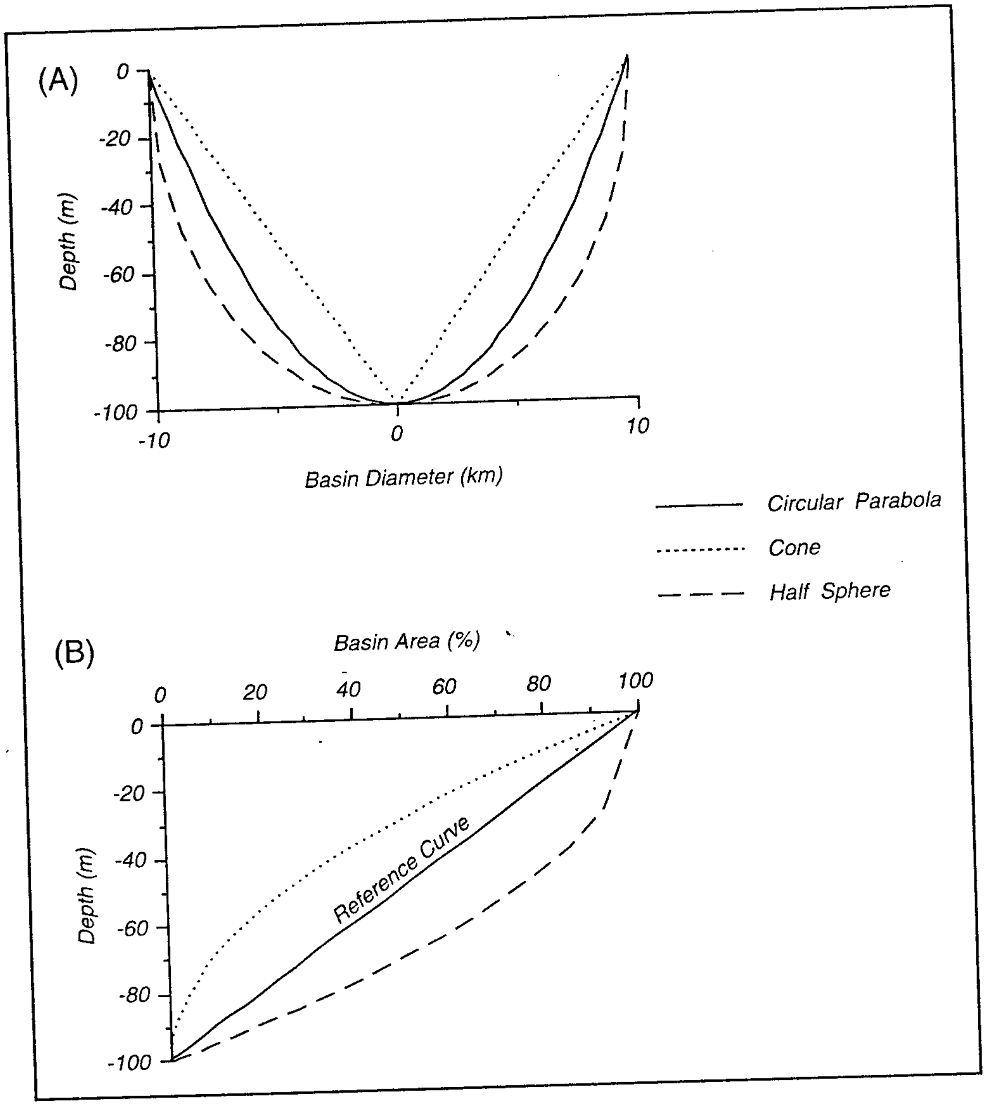

Figure 10—(A) Bathymetric profiles through hypothetical, circular basins with differing cross sections. (B) Corresponding hypsometric curves for the basins.

log profiles collected by the USGS using a small (160 in.^{3}) air gun and a two-channel hydrophone receiver (EEZ-SCAN Scientific Staff, 1987). The recorded data were filtered at 15 to 300 Hz. Data coverage is shown in Figure 8.

The SCS profiles show that the intraslope basins vary in terms of the stratal geometry of their shallow sediment fill. These differences are used to distinguish three types of intraslope basins. The first type of basin tends to have a bowl-shaped cross section and is referred to as a "bowl" basin (Figure 12A–D). The shallow fill in the basin appears in the SCS profiles as subparallel reflectors bounding units that thicken toward the basin's center. These reflectors also extend up the basin's walls and are clearly continuous with reflectors bounding units on the ridges surrounding the basin.

The second type of intraslope basin is referred to as a "box" basin, because a characteristically abrupt change in sea-floor slope at the basin floor/wall transition gives the basin a more box-shaped cross section (Figure 12I–L). The floor of this basin is commonly tilted, and in the SCS profiles, subbottom reflectors beneath the basin floor always diverge toward its deeper side. The shallow sediment fill within the basin is generally confined to the basin interior. Subbottom reflectors beneath the basin floor appear to end at the floor/wall transition, and cannot be traced separately up the walls to reflectors perched along the basin rim.

The third type of intraslope basin seems to be a transitional form between the bowl- and box-shaped basins (Figure 12E–H). Like the box basins, the floor of this transitional type of basin is tilted, and underlying subbottom reflectors diverge toward, and appear to terminate against, the wall bounding the basin's deeper side. On the opposite, shallower side of the basin, however, the subbottom reflectors can be

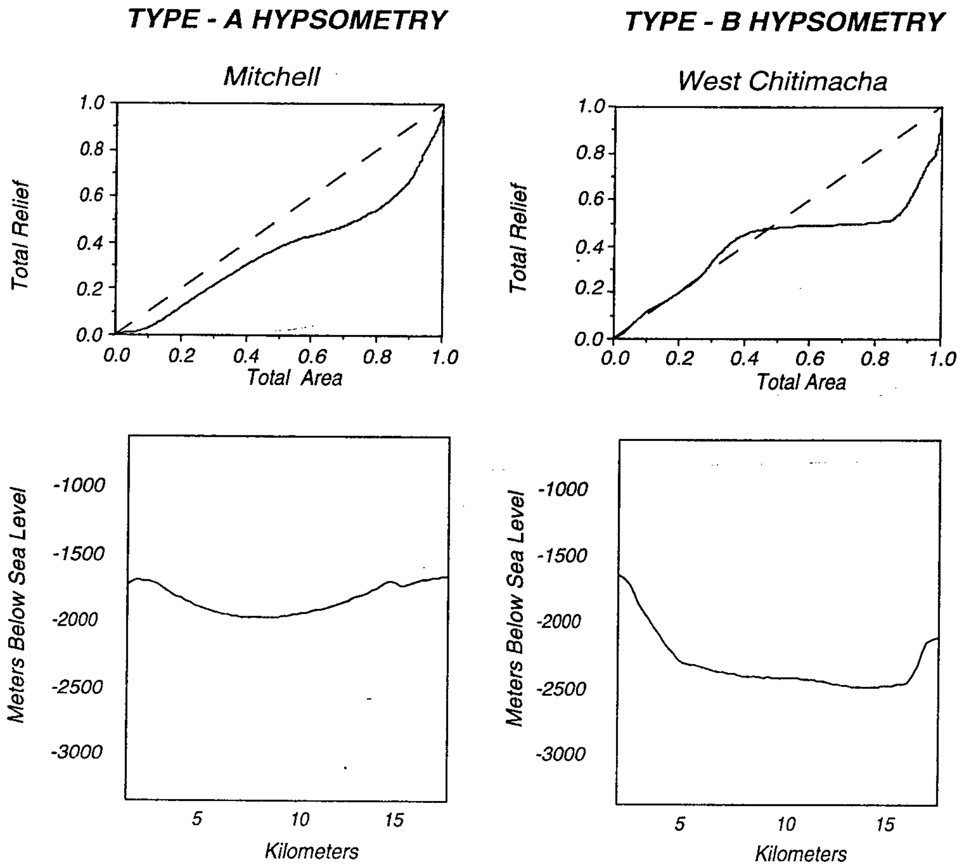

Figure 11—Examples of the two types of hypsometric curves commonly exhibited by the intraslope basins within the study area. Graphs at top are the type A hypsometric curve of Mitchell Basin and the type B hypsometric curve of West Chitimacha Basin vs. the straight, dashed reference hypsometric curve. Graphs at bottom are representative bathymetric profiles across the basins.

clearly traced up the basin wall to reflectors underlying the surrounding intraslope ridges—a characteristic common to the bowl basins. Because the wall along the deeper side of the basin appears as a bulwark to the basin's sediment fill, this type of intraslope basin is referred to as a "barrier" basin.

Relation Between Basin Hypsometry and Shallow Stratigraphy

A critical drawback to classifying the intraslope basins in terms of the three basin types described above is that the basin types are based on only one or two SCS profiles across each basin (Figure 8). Furthermore, almost all of these profiles are oriented in the same along-the-slope direction. As a result, the variation in shallow subbottom stratigraphy used to distinguish the different types of intraslope basins could be purely an artifact of limited and/or biased data coverage. A correspondence, however, is seen between the type of hypsometric curve exhibited by each intraslope basin and the stratal geometry of its upper sediment fill.

Figure 13 graphically depicts the relation between the hypsometric curves and the stratal geometries of the 40 (of 46) intraslope basins crossed by an SCS profile. Of the 14 intraslope basins identified as bowl basins, all but one exhibit type A hypsometric curves. Of the 13 intraslope basins identified as box basins, all but one exhibit type B hypsometric curves. And of the 11 intraslope basins identified as barrier basins, seven have type A hypsometric curves and four have type B hypsometric curves.

The relatively consistent association of type A hypsometric curves with bowl basins and of type B hypsometric curves with box basins supports the distinction made between these basins on the basis of the limited number of SCS profiles. The mixed association of type A and type B hypsometric curves with barrier basins also lends credence to the idea that these basins are a transitional form between bowl and box basins. Although evaluation of additional SCS profiles in the study area would better establish whether or not bowl, box, and barrier basins are truly distinct, these subdivisions are tentatively used here to classify the intraslope basins and examine their distribution across the study area.

Distribution of Intraslope Basin Types

Figure 9 shows the locations of bowl, box, and barrier basins in the study area. Only those basins

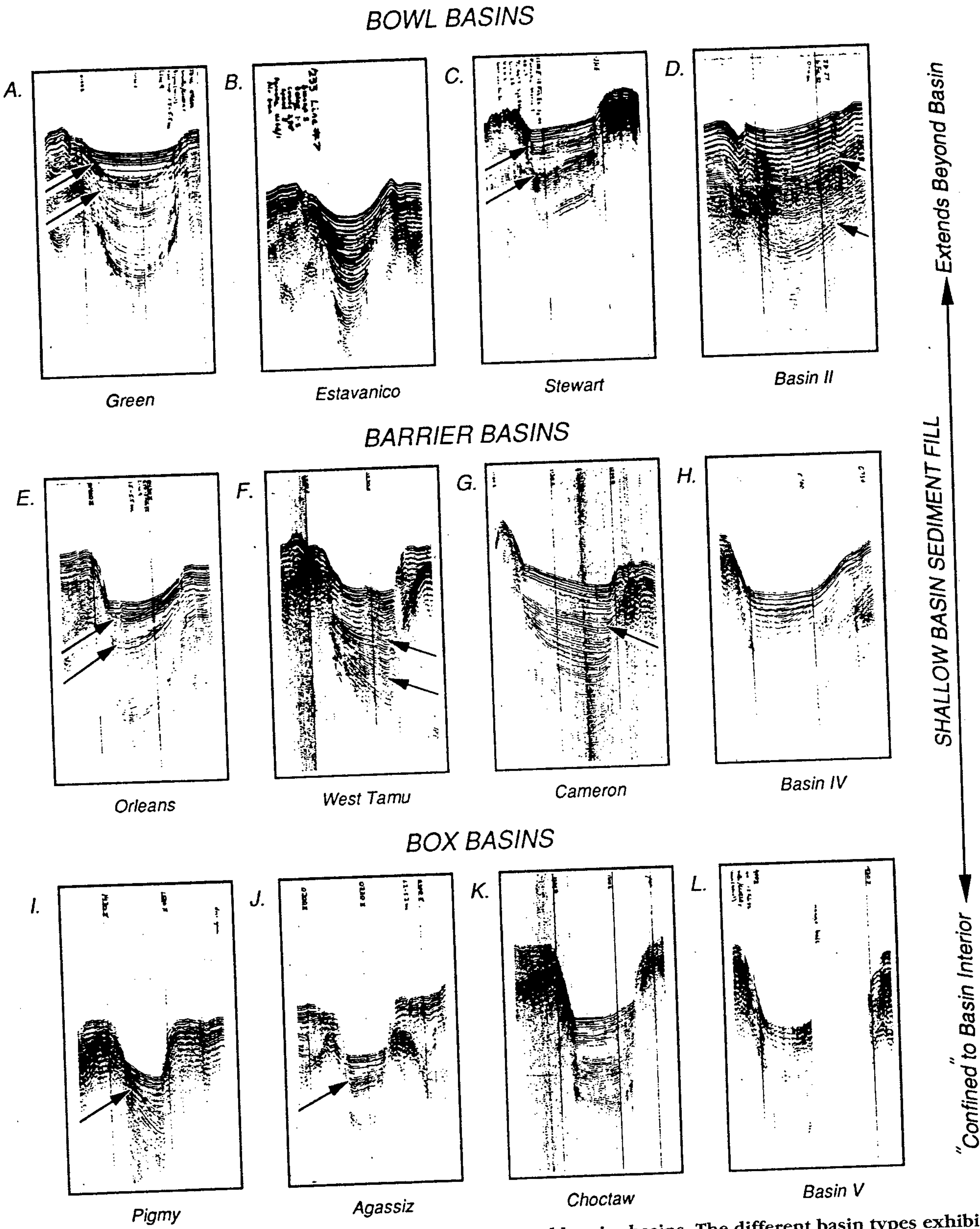

Figure 12—Examples of SCS profiles across bowl, box, and barrier basins. The different basin types exhibit distinguishable, but apparently transitional, differences in the stratal geometries of their upper sediment fills. Arrows point to surfaces of onlap that delineate seismic stratigraphic unconformities. Examples D, H, and L are the intraslope basins II, IV, and V of Satterfield and Behrens (1990).

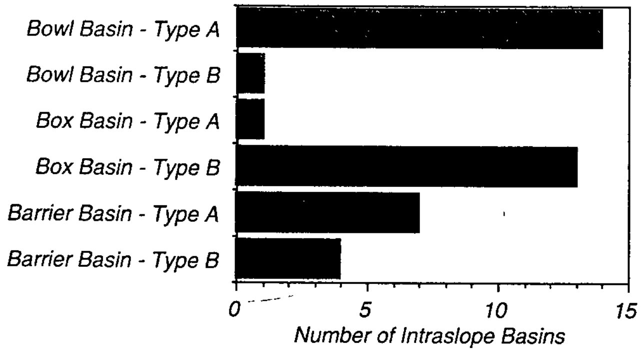

Figure 13—Bar graph showing the correspondence between the three types of stratal geometries used to distinguish among the intraslope basins and the two types of hypsometric curves exhibited by the intraslope basins.

crossed by an SCS profile are classified as one of the three basin morphologies. The different intraslope basin morphologies tend to form clusters. The box basins principally occur in the western half of the study area, distributed seaward across the mid-slope along or near the bathymetric lows mapped using the drainage extraction algorithms. The barrier basins are most common in the northern part of the study area, closest to the present-day shelf edge. And the bowl basins tend to occur around the perimeter of the study area, often farthest away from the present shelf edge.

Noticeably absent in the distribution of the intraslope basin types are any apparent linkages or downslope-trending patterns that could be interpreted to reflect the locations of former slope sediment fairways. The succession of box basins in the western part of the study area associated with the bathymetric lows mapped in this region is intriguing but not consistent. Several bowl and barrier basins also occur along these bathymetric lows, and randomly disrupt the sequence of box basins leading toward the Sigsbee Escarpment.

DISCUSSION

The categorization of the intraslope basins as bowl, box, and barrier basins fails to provide direct evidence as to the routes sediment flows once used to cross the Louisiana continental slope and reach the Mississippi Fan. There are at least three possible reasons why this is so. One is that no trace of the former sediment fairways remains on the present-day surface of the Louisiana continental slope, at least not at the 250-m resolution of the NOAA bathymetric grids. The second reason is that the morphologic-stratigraphic differences noted among the intraslope basins are the consequences of more than simply an association with slope sediment fairways. A third reason is that few (if any) direct sediment fairways were established across this region of the slope. Instead, there may have been a more dispersive, anastomosing, and/or temporally shifting system of slope sediment passages fostered by the changing shapes of the basins as they evolved in response to an interplay between sediment infilling and salt withdrawal.

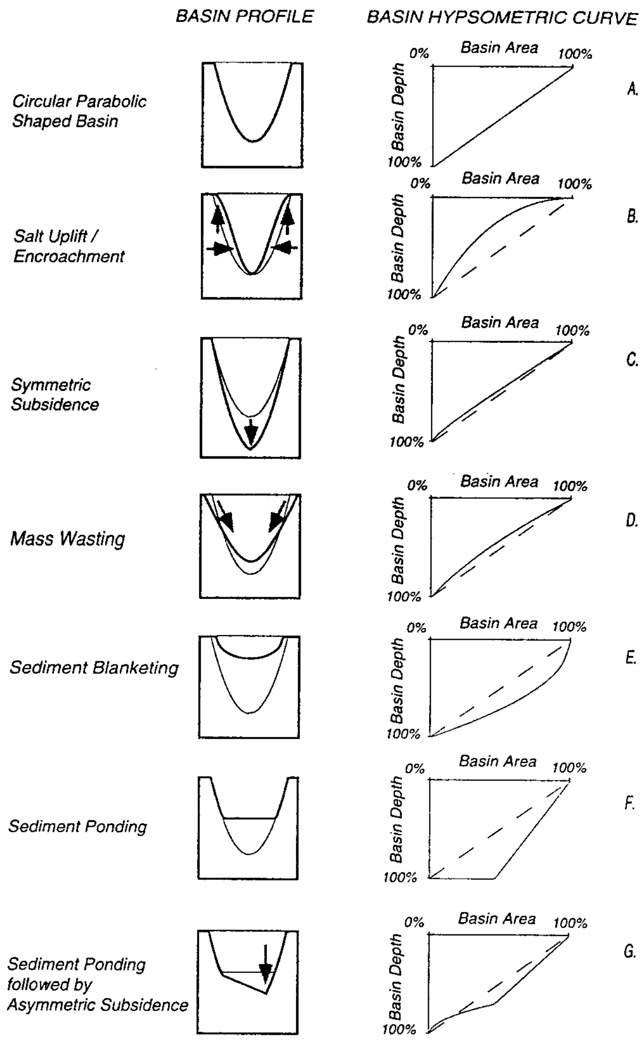

Figure 14—Illustration of how different basin-forming processes might affect the shape and hypsometric curve of a hypothetical basin that initially has a straight line for its hypsometric curve. See text for discussion.

Assessing the Influence of Salt Tectonics and Sedimentary Processes on Basin Hypsometry

The intraslope basins have been shaped by a variety of processes. These processes have included salt uplift, encroachment, and withdrawal, which have

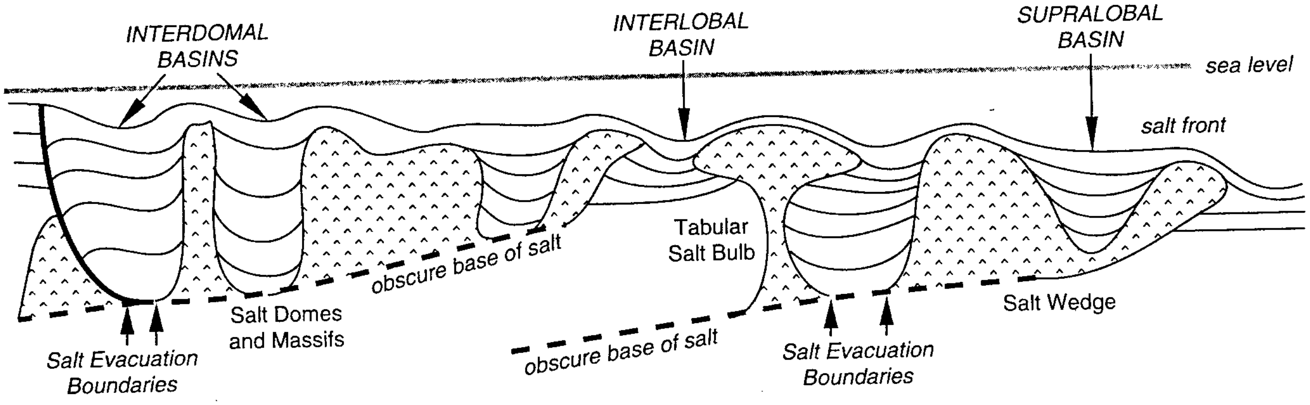

Figure 15—General illustration of the differences in salt body geometries surrounding interdomal, interlobal, and supralobal basins. Modified from Simmons (1992).

created the basins; and sedimentation and mass wasting, which have infilled the basins. Of interest is the relative influence each of these processes has had on the present-day form of the intraslope basins. One way of trying to determine this is by exploring how each of the processes might alter the shape of a hypothetical basin having the hypsometry of the reference curve (Figure 14A).

Individually, neither salt uplift nor salt encroachment appears capable of altering the form of an intraslope basin toward one with a hypsometric curve resembling those associated with the intraslope basins in the study area. Both salt uplift and salt encroachment presumably would bulge the walls of an intraslope basin inward (Figure 14B). In the case of the hypothetical basin, this would reduce the map area at or near the basin floor, resulting in a hypsometric curve that would arc above the reference curve. Of the intraslope basins in the study area, all but one (Leipper Basin) has a hypsometric curve that either arcs below or crosses the reference curve.

Similarly, the basin hypsometries observed in the study area also do not appear to be attributable to the individual effects of either salt withdrawal or mass wasting. Salt withdrawal associated with sediment loading is believed to be the principal mechanism by which the intraslope basins are deepened (Barton, 1933; Seni and Jackson, 1983; West, 1989). Deepening of the hypothetical basin would reduce the map area of the basin floor, which, like salt uplift or encroachment, would drive the basin's hypsometric curve to arc above the reference curve (Figure 14C). In opposition to salt withdrawal, mass wasting contributes to basin infilling through the transfer of materials from the basin walls to the basin floor (Figure 14D). However, while the floor of the basin is raised by deposition, the walls are regraded by erosion, and the increase in map area at or near the basin floor is more than offset by the increase in map area along the basin walls. Consequently, the hypsometric curve that would result from basin modification by mass wasting would also appear to arc above the reference curve (Figure 14D).

The examples above illustrate that in order for an intraslope basin to have a hypsometric curve that, like many of those in the study region, arcs below the reference curve, the map area encompassed by elevations in the lower half of the basin must be greater than the map area encompassed by elevations in the upper half of the basin. Of the major processes that act on the intraslope basins, infilling by sediments derived from outside the basin is one that clearly brings about such a redistribution in basin elevations. This infilling, however, cannot be uniform across both the walls and floor of a basin (e.g., strictly pelagic sedimentation), for although the basin will be infilled, its form will be preserved and its hypsometric curve unchanged. Instead, deposition must be greatest on the basin floor, which can be plainly seen in the SCS profiles. Such deposition is characteristic of gravity-driven sediment flows, suggesting that terrigenous materials represent the most significant component of intraslope basin fill. Recent drilling results support this interpretation (Boyd et al., 1993).

Infilling by gravity-driven sediment flows can alter the shape of an intraslope basin in one of two ways. The first is to make the basin more bowl shaped. Sediments are deposited throughout the basin, including the walls, but the thickest accumulation occurs in the deepest part of the basin (Figure 14E). As the basin infills, its hypsometric curve changes to one that arcs below the reference curve, much like the type A hypsometric curves of bowl basins (compare with the hypsometric curve of Mitchell Basin, Figure 11A).

The second way an intraslope basin's shape can be altered is if deposition is restricted to the basin floor (Figure 14F). In the case of the hypothetical basin, this would result in a box-shaped basin with a flat floor, but one with a hypsometric curve resembling neither of the curves (types A or B) observed in the study area. However, if the basin then were to undergo differential subsidence, say along a growth fault bounding the basin, the basin floor would be tilted, and its hypsometric curves would take on the form of the type B curves associated with box basins (Figure 14G); the lower half of the curve would arc above the reference curve, whereas the top half would arc below it (compare with the hypsometric curve of West Chitimacha Basin, Figure 11B).

Sediment Infilling and the Transition in Basin Type

Analysis of the hypsometric curves points to an interplay between sediment infilling and basin subsidence as the cause of the morphologic variations observed among the intraslope basins. An example of how this interplay may result in the transition of basin types tentatively identified in the SCS profiles can be seen in the shallow stratigraphy of five intraslope basins on the Texas continental slope (94–95°W). Satterfield and Behrens (1990) show that these basins were successively infilled downslope by turbidites from a submarine canyon that passed through the basins. In the USGS seismic reflection profiles, the three shallowest basins along the upper part of the canyon system are completely infilled, and have bowl basin stratal geometries (e.g., Basin II of Satterfield and Behrens, Figure 12D). The basin downslope along the midsection of the system is partially filled and has a barrier basin stratal geometry (Basin IV of Satterfield and Behrens, Figure 12H). And the fifth basin at the end of the system, although obscured by a data gap in the SCS profile, looks to be the deepest, and exhibits characteristics of a box basin (Basin V of Satterfield and Behrens, Figure 12L).

This downslope succession from bowl to barrier to box basins suggests that the different intraslope basin morphologies reflect progressive stages of infilling. Box basins would represent the early stages of infilling, when sediment input is relatively low and not sufficient to overcome the differential subsidence deepening the basins. Barrier basins would represent the mid-stages of infilling, when sediment input begins to outpace subsidence and the basins start to infill with materials that principally enter from one side of the basin. And bowl basins would represent the latter stages of infilling, when materials are deposited across the basin and onto the surrounding intraslope ridges as sediments begin to bypass the area.

Masking of Sediment Drainage by Salt Tectonics

Seismic stratigraphic unconformities identified within the shallow stratigraphy of the intraslope basins indicate that the rather simplistic sequence of basin infilling described above is complicated by basin subsidence, presumably caused by salt withdrawal. Surfaces of onlap within the fill of the intraslope basins suggest that, unless net sedimentation continues to exceed net subsidence, infilling may change to deepening and reverse the transition from box to bowl basins. The onlap surfaces are seen in all three types of intraslope basins (Figure 12), and were formed during intervals when the dipping floors of the basins were leveled by sedimentation. Subsidence then followed, probably by movement along a basin-bounding growth fault, and the floors of the basins were tilted once again. This recurring subsidence appears to have allowed the intraslope basins to continue capturing materials over the course of multiple phases of deep-sea sedimentation. It has also probably episodically altered the stratal geometry of the sediments filling the basins, possibly reverting bowl basins back to barrier basins, and barrier basins back to box basins.

Subsidence within the intraslope basins appears to have continued since the last great influx of terrigenous sediment to the study area. All of the intraslope basins examined are more than 50 m deep, and on average are more than 200 m deep. In the Green Canyon area, where several large Pliocene–Pleistocene oil and gas sand fields have been discovered [Jolliet field (Brannon et al., 1993); Bullwinkle field (McCarthy et al., 1993); Green Canyon Block 205 (Rafalowski and Bergeon, 1993)], intraslope basins in the southern part of the area (e.g., Green, Cat, Researcher, and Ship) average more than 100 m in depth below their spillpoints. Weimer (1989, 1990) interprets the youngest of the channel-levee systems on the Mississippi Fan seaward of this region (systems 8 and 9) to have formed more than 1.2 million years ago. Assuming that these basins were infilled to their spillpoints at that time, their present depths would require them to have subsided at a net average rate of roughly 10 cm/k.y. Whether this rate is less than or greater than the rate of basin subsidence caused by salt withdrawal is difficult to determine. The competing effects of basin fill compaction and continued slope sedimentation have also contributed to the intraslope basins' present relief.

The effect of basin subsidence on patterns of Pliocene–Pleistocene sediment drainage across the study area apparently has been profound. As discussed above, there is ample subsurface evidence, both in multichannel seismic reflection profiles and boreholes, that erosional canyons crossed the slope just north of the study area (Figures 1-3) and delivered thick sequences of clean turbidite sands to intraslope basins removed from the present-day shelf edge (Figure 2). The numerous abandoned channel-levee complexes mapped by Weimer (1989) at the foot of the Sigsbee Escarpment (Figure 9) imply that more than a few of these canyons made it all the way to the Mississippi Fan. Studies of ponded minislope basins on convergent margins (Thornburg and Kulm, 1987; Klaus and Taylor, 1991) and passive margins (Satterfield and Behrens, 1990) suggest that to cross the study area, submarine canyons on the eastern Louisiana slope would have first had to infill each intraslope basin they entered at least up to the basin's spillpoint before they could have extended farther downslope. Yet, in the study area, there are no trends in the bathymetry or in the form of the intraslope basins that can be clearly attributed to such a progressive downslope infilling of the basins.

One possible reason for the absence of such trends is that, because of the complex interplay of sedimentation and salt deformation (exhibited in the forms of the intraslope basins), the development of major sediment fairways to the Mississippi Fan was inhibited in this region. Salt movement triggered by sediment loading may have instead promoted a complex and dispersive system of canyons/channelways that entered/exited the intraslope basins at more than one location. Furthermore, these canyons/channelways may have changed position over time as the intraslope basins evolved in response to salt movement and the shifting location of sediment input from the shelf edge (Figure 9). An amalgamated history of sediment infilling within the basins, coupled with continued basin subsidence, is one possible reason why a pattern of downslope sediment transport is not readily discernable in the distribution of the differently shaped intraslope basins.

An important element missing in considering this distribution, however, is time. It appears from the analyses conducted here that the intraslope basins have assumed different forms at different stages of their infilling. If each of the basin shapes could be classified in terms of a specific time interval (something not possible with the database used in this study), a pattern of downslope sediment transport on the eastern Louisiana slope might emerge.

The Influence of Salt Structure on Basin Morphology

The focus of this study has been on aspects of intraslope basin morphology and shallow stratigraphy attributable to sediment infilling and basin subsidence. Beyond the paper's scope is the nature of the shallow salt structures surrounding and underlying the intraslope basins, which have also been an important influence on basin shape (i.e., size, planform shape, etc.). The relation of these structures to basin form is briefly considered here.

One of the most extensive studies of the salt structures underlying the study area is that of Simmons (1992). He identifies three types of intraslope basins (Figure 15): interdomal basins, which have formed between vertically intruded salt domes, ridges, and/or massifs; interlobal basins, which have formed between shallow, laterally intruded salt lobes spreading away from the tops of nearby salt domes; and supralobal basins, which have formed above, and are subsiding down into, laterally intruded salt lobes.

Although Simmons (1992) has not classified the structures of all the intraslope basins within the study area, there is a close correspondence between the basins he identifies as supralobal and interlobal basins, and the basins identified in this study as bowl- and box-shaped basins, respectively. For instance, the bowl-shaped basins Vaca and Estavanico have supralobal basin structures (Figure 26 on p. 49 in Simmons, 1992), whereas the box-shaped basins Pigmy (Figures 40, 41 on p. 68, 69 in Simmons, 1992) and North Terrebonne (Figure 47 on p. 77 in Simmons, 1992) have interlobal basin structures. Furthermore, the supralobal basins, which Simmons (1992) interprets to be in the youthful stage of intraslope basin formation, are most prevalent along the outer slope in the same areas where bowl basins are found. The interlobal basins, which may represent a more mature phase in intraslope basin development, are widespread across the middle slope in the region where box basins are common. The relation of barrier basins to subsurface salt structure, on the other hand, is uncertain. Both Dorantes Basin, which is a supralobal basin (Figure 30 on p. 53 in Simmons, 1992), and St. Tammany Basin, which is an interlobal/interdomal basin (Figure 45 on p. 74 in Simmons, 1992), have barrier basin morphologies. Regardless of this ambiguity, the distribution of intraslope basin morphologies (Figure 9) appears to exhibit a much clearer association with the structures of the salt bodies that surround the basins than with the possible locations of former slope sediment fairways.

SUMMARY

The intraslope basins on the Texas-Louisiana continental slope are modern analogs of basins rich in turbidite sands buried beneath the Louisiana continental shelf and on the upper slope (Holland et al., 1990; Mitchum et al., 1990; Pacht et al., 1990, 1992). The buried shelf basins formerly resided at the slope surface, but were prograded over by the Mississippi River depocenter during the Pliocene-Pleistocene. In order to give the exploration geologist a firmer understanding of the original dimensions of these buried basins, high-resolution gridded multibeam bathymetry is used to compile measurements of the sizes and shapes of modern-day intraslope basins on the eastern Louisiana slope. The bathymetry, along with SCS profiles, are also examined for surficial evidence of former sediment fairways in an effort to facilitate the search for sand reservoirs in this area.

Neither the overall morphology of the slope nor the morphologies of the individual intraslope basins provide any direct indication as to the locations of former sediment fairways. But the morphologies of the intraslope basins do provide insight into the complex interplay between the subsidence and sediment infilling that have shaped the basins. The principal findings of this study are as follows.

(1) No systematic variation in either the depths or the spacing of the intraslope basins is apparent in the gridded multibeam bathymetry.

(2) The interiors of the intraslope basins are notably smooth (at a grid cell resolution of 250 m), and show little bathymetric evidence of mass wasting despite the steepness of basin walls (5-22°).

(3) The intraslope basins average approximately 15 km in length, 10 km in width, 200 m in depth (below their spillpoint elevations), and 50 km^2 in map area, but these dimensions can vary up to an order of magnitude.

(4) Bathymetric lows delineated by computer algorithms connect several series of intraslope basins across the slope to the Mississippi Fan, but this study lacks subsurface evidence for confirming the presence of former and now buried sediment fairways beneath these lows.

(5) Two end members (bowl and box) and a third transitional intraslope basin shape (barrier) are tentatively identified on the basis of the hypsometry of the intraslope basins and the stratal geometry of their shallow sediment fill.

(6) The hypsometries of hypothetical intraslope basins modified individually by salt uplift, salt encroachment, salt withdrawal, mass wasting, and sediment infilling suggest that sediment infilling has been the last dominant process in forming bowl-shaped basins, whereas asymmetric basin subsidence, most likely by movement along a basin-bounding growth fault, has been the last dominant process in forming box-shaped basins.

(7) Seismic unconformities in the shallow stratigraphy beneath the floors of all three types of intraslope basins reflect the competing influences of infilling and subsidence on basin formation, indicating that subsidence has periodically staved off burial and allowed the basins to repeatedly capture new materials during cyclic phases of deep-sea sedimentation.

(8) The different types of intraslope basins may be related to routes used by sediments to bypass the slope to the Mississippi Fan during the Pliocene-Pleistocene, but there is no direct linkage of basin types across the slope that might be directly inferred to reflect the locations of former sediment fairways.

REFERENCES CITED

Barton, D. C., 1933, Mechanics of formation of salt domes, with special reference to Gulf Coast salt domes of Texas and Louisiana: AAPG Bulletin, v. 17, p. 1025-1083.

Berryhill, H. L. Jr., J. R. Suter, and N. S. Hardin, 1987, Late Quaternary facies and structure, northern Gulf of Mexico: AAPG Studies in Geology 23, 289 p.

Bouma, A. H., L. B. Smith, B. R. Snider, and T. R. McKee, 1978, Intraslope basin in northwest Gulf of Mexico, *in* A. H. Bouma, G. T. Moore, and J. M. Coleman, eds., Framework, facies, and oil-trapping characteristics of the upper continental margin: AAPG Studies in Geology 7, p. 289-302.

Bouma, A. H., H. H. Roberts, and J. M. Coleman, 1990, Acoustical and geological characteristics of near-surface sediments, upper continental slope of northern Gulf of Mexico: Geo-Marine Letters, v. 10, p. 200-208.

Boyd, J. D., M. J. Mayall, and C. A. Yeilding, 1993, Depositional models for intraslope basins: variability and controls (abs.): AAPG 1993 Annual Convention Program, p. 79.

Brannon, D., A. Chedburn, W. J. Schneider, and M. Sheedlo, 1993, Jolliet field revisited: producibility of upper slope turbidites in Green Canyon 184 (abs.): AAPG 1993 Annual Convention Program, p. 79.

Bryant, W. R., J. R. Bryant, M. H. Feeley, and G. R. Simmons, 1990, Physiographic and bathymetric characteristics of the continental slope, northwest Gulf of Mexico: Geo-Marine Letters, v. 10, p. 182-199.

Davis, J. C., 1986, Statistics and data analysis in geology: New York, John Wiley, 646 p.

de Moustier, 1988, State of the art in swath bathymetry survey systems: International Hydrographic Review, v. 65, p. 25-54.

EEZ-SCAN Scientific Staff, 1987, Atlas of the U.S. Exclusive Economic Zone, Gulf of Mexico and eastern Caribbean areas: U.S. Geological Survey, Miscellaneous Investigations Series I-1864-A,B, 164 p.

Grim, P., 1992, Dissemination of NOAA/NOS EEZ multibeam bathymetric data, *in* M. Lockwood and B. A. McGregor, eds., 1991 exclusive economic zone symposium; working together in the Pacific EEZ: U.S. Geological Survey Circular no. 1092, p. 102-109.

Holland, D. S., W. E. Nunan, D. R. Lammlein, and R. L. Woodhams, 1980, Eugene Island Block 330 field offshore Louisiana, *in* M. T. Halbouty, ed., Giant oil and gas fields of the decade 1968-1978: Tulsa, AAPG, p. 253-280.

Holland, D. S., J. B. Leedy, and D. R. Lammlein, 1990, Eugene Island Block 330 field—USA, offshore Louisiana, *in* E. A. Beaumont and N. H. Foster, eds., Structural traps III. Tectonic fold and fault traps: AAPG Treatise of Petroleum Geology, p. 103-143.

Humphris, C. C., 1978, Salt movement on continental slope, northern Gulf of Mexico, *in* A. H. Bouma, G. T. Moore, and J. M. Coleman, eds., Framework, facies, and oil-trapping characteristics of the upper continental margin: Tulsa, AAPG Studies in Geology 7, p. 69-86.

Humphris, C. C., 1979, Salt movement on continental slope, northern Gulf of Mexico: AAPG Bulletin, v. 63, p. 782-798.

Jackson, M. P. A., and C. J. Talbot, 1986, External shapes, strain rates, and dynamics of salt structures: Geological Society of America Bulletin, v. 97, p. 305-323.

Jackson, M. P. A., and C. J. Talbot, 1989, Salt canopies: SEPM Gulf Coast Section Tenth Annual Research Foundation Conference, Program and Abstracts, p. 72-78.

Jenson, S. K., and J. O. Dominique, 1988, Extracting topographic structure from digital elevation data for geographic information system analysis: Photogrammetric Engineering and Remote Sensing, v. 54, p. 1593-1600.

Klaus and Taylor, 1991, Submarine canyon development in the Izu-Bonin Forearc; a SeaMARC II and seismic survey of Aoga Shima Canyon: Marine Geophysical Researches, v. 13, p. 105-130.

Mann, R. G., W. R. Bryant, and P. D. Rabinowitz, 1992, Seismic facies interpretation of the northern Green Canyon area, Gulf of Mexico, *in* J. S. Watkins, F. Zhigiang, and K. J. McMillen, eds., Geology and geophysics of continental margins: AAPG Memoir 53, p. 343-360.

Mason, E. P., R. S. Barnard, and M. Kohli, 1993, The development of Plio-Pleistocene turbidite reservoirs at South Timbalier 295 field (abs.): AAPG 1993 Annual Convention Program, p. 147.

McCarthy, C. J., W. E. Holman, and M. Kohli, 1993, Bullwinkle (Green Canyon 65 field) development history (abs.): AAPG 1993 Annual Convention Program, p. 148.

McGee, D. T., P. W. Bilinski, P. S. Gary, D. S. Pfieffer, and J. L. Sheiman, 1993, Geologic models and reservoir geometries of Auger field, deepwater Gulf of Mexico (abs.): AAPG 1993 Annual Convention Program, p. 149.

Menke, W., P. Friberg, A. Lerner-Lam, D. Simpson, R. Bookbinder, and G. Karner, 1991, Sharing data over Internet with the Lamont View-Sharer system: EOS, Transactions, American Geophysical Union, v. 72, p. 409-414.

Mitchum, R. M. Jr., J. B. Sangree, P. R. Vail, and W. W. Wornardt, 1990, Sequence stratigraphy in Gulf Coast expanded sections, Gulf of Mexico: GCS-SEPM Eleventh Annual Research Conference, p. 237-256.

National Oceanic and Atmospheric Administration, 1989a, Pigmy Basin bathymetric grid, N275091W.

National Oceanic and Atmospheric Administration, 1989b, Researcher Basin bathymetric grid, N270090W.

National Oceanic and Atmospheric Administration, 1989c, Orca Basin bathymetric grid, N265091W.

National Oceanic and Atmospheric Administration, 1989d, Mitchell Basin bathymetric grid, N265090W.

National Oceanic and Atmospheric Administration, 1989e, Vaca Basin bathymetric grid, N260091W.

National Oceanic and Atmospheric Administration, 1989f, Farnella Canyon bathymetric grid, N260090W.

Pacht, J. A., B. E. Bowen, J. H. Beard, and B. L. Shaffer, 1990, Sequence stratigraphy of the Plio-Pleistocene depositional facies in the offshore Louisiana south additions: Transactions of the 40th Annual Meeting, Gulf Coast Association of Geological Societies, Lafayette, October 17-19, p. 643-659.

Pacht, J. A., B. Bowen, B. L. Shaffer, and W. R. Pottorf, 1992, Systems tracts, seismic facies, and attribute analysis within a sequence stratigraphic framework—example from the offshore Louisiana Gulf Coast, *in* E. G. Rhodes and T. F. Moslow, eds., Marine and clastic reservoirs: New York, Springer-Verlag, p. 21-38.

Pratson, L. F., and W. B. F. Ryan, 1992, Application of drainage extraction to NOAA gridded bathymetry of the U.S. continental margin, *in* M. Lockwood and B. A. McGregor, eds., 1991 Exclusive Economic Zone Symposium; working together in the Pacific EEZ, U.S. Geological Survey Circular 1092, p. 110-117.

Press, W. H., B. P. Flannery, S. A. Teukolsky, and W. T. Vetterling, 1989, Numerical recipes in C: the art of scientific computing: Cambridge, Cambridge University Press, 735 p.

Pulham, A. J., 1993, Variations in slope deposition, Pliocene-Pleistocene, offshore Louisiana, northeast Gulf of Mexico, *in* P. Weimer and H. W. Posamentier, eds., Siliciclastic sequence stratigraphy: recent developments and applications: AAPG Memoir 58, p. 199-233.

Rafalowski, J. W., and T. Bergeon, 1993, Green Canyon Block 205: a geologic and development overview (abs.): AAPG 1993 Annual Convention Program, p. 169.

Renard, V., and J. P. Allenou, 1979, SEABEAM, multibeam echo sounding on Jean Charcot: International Hydrographic Review, v. 56, p. 35-67.

Salvador, A., 1987, Late Triassic-Jurassic paleogeography and origin of Gulf of Mexico Basin: AAPG Bulletin, v. 71, p. 419-451.

Satterfield, W. M., and E. W. Behrens, 1990, A late Quaternary canyon/channel system, northwest Gulf of Mexico continental slope: Marine Geology, v. 92, p. 51-67.

Seni, S. J., and M. P. A. Jackson, 1983, Evolution of salt structures, east Texas diapir province: AAPG Bulletin, v. 67, p. 1219-1274.

Shipp, R. Craig, 1993, Late Pleistocene Mississippi River canyons: slope turbidites systems in Western Mississippi Canyon and Atwater, northern Gulf of Mexico (abs.): AAPG 1993 Annual Convention Program, p. 182.

Simmons, G. R., 1992, The regional distribution of salt in the northwestern Gulf of Mexico; styles of emplacement and implications for early tectonic history: Ph.D. thesis, Texas A&M University, College Station, Texas, 180 p.

Strahler, A. N., 1952, Hypsometric (area-altitude) analysis of erosional topography: Geological Society of America Bulletin, v. 63, p. 1117-1142.

Thornburg, T. M., and L. D. Kulm, 1987, Sedimentation in the Chile Trench: depositional morphologies, lithofacies, and stratigraphy: Geological Society of America Bulletin, v. 98, p. 33-52.

Twichell, D. C., and C. DeLorey, in press, Sedimentary processes in the salt deformation province of the Texas-Louisiana continental slope, *in* J. V. Gardner, M. Field, and D. C. Twichell, eds., Geology of the U.S. seafloor: the view from GLORIA: Cambridge, Cambridge University Press.

Weimer, P., 1989, Sequence stratigraphy of the Mississippi Fan (Plio-Pleistocene), Gulf of Mexico: Geo-Marine Letters, v. 9, p. 185-272.

Weimer, P., 1990, Sequence stratigraphy, facies geometry, and depositional history of the Mississippi Fan, Gulf of Mexico: AAPG Bulletin, v. 74, p. 425-445.

Weimer, P., and B. T. Dixon, in press, Regional setting of the Mississippi Fan complex: implications for the evolution of the northern Gulf of Mexico margin, *in* P. Weimer and A. H. Bouma, eds., Submarine fans and turbidite systems: sequence stratigraphy, reservoir architecture, and production characteristics—Gulf of Mexico and international: GSC-SEPM 15th Annual Research Conference Proceedings.

Wessel, P., and W. H. F. Smith, 1991, Free software helps map and display data: EOS, Transactions, American Geophysical Union, v. 72, p. 441-446.

West, D. B., 1989, Model for salt deformation on deep margin of central Gulf of Mexico Basin: AAPG Bulletin, v. 73, p. 1472-1482.

Woodbury, H. O., J. H. Spotts, and W. H. Akers, 1978, Gulf of Mexico continental-slope sediments and sedimentation, *in* A. H. Bouma, G. T. Moore, and J. M. Coleman, eds., Framework, facies, and oil-trapping characteristics of the upper continental margin: AAPG Studies in Geology 7, p. 117-137.

Worrall, D. M., and S. Snelson, 1989, Evolution of the northern Gulf of Mexico with emphasis on Cenozoic growth faulting and the role of salt, *in* A. W. Bally and A. R. Palmer, eds., The geology of North America—an overview: Boulder, Colorado, Geological Society of America, The Geology of North America, v. A, p. 97-138.

ABOUT THE AUTHORS

Lincoln F. Pratson

Lincoln F. Pratson is an associate research scientist at Lamont-Doherty Earth Observatory. His interests are the evolution of continental margin morphology, the dynamics of sedimentary and salt tectonic processes, and the formation of stratigraphic sequences. His work involves quantitative terrain analysis, time series analysis, and computer modeling of submarine erosion, sedimentation, and seascape development. His present research includes analysis of submarine slope stability, modeling clinoform formation, and the correlation of well logs to dated oxygen isotope records.

William B. F. Ryan

William B. F. Ryan is a Doherty senior scientist at Lamont-Doherty Earth Observatory. He teaches graduate-level courses in plate tectonics and marine geology in the Department of Geological Sciences at Columbia University. He is an active seagoing experimentalist and a developer of sea-floor mapping and imaging instrumentation. His current research includes investigations of the processes of crustal accretion at mid-ocean ridges and the formation of submarine canyons and deep-sea fans on continental margins.

Automated Drainage Extraction in Mapping the Monterey Submarine Drainage System, California Margin

LINCOLN F. PRATSON* and WILLIAM B. F. RYAN

Lamont-Doherty Earth Observatory of Columbia University, Palisades, NY 10964 U.S.A.
** Now at Institute of Arctic and Alpine Research, University of Colorado, Boulder, CO 80309 U.S.A.*

(Accepted 7 March 1996)

Key words: Multibeam bathymetry, submarine canyons, deep-sea channels, river networks, drainage areas

Abstract. Drainage-extraction algorithms traditionally used for extracting river networks and watersheds from gridded land topography are applied to gridded multibeam bathymetry of the mid-California margin. The algorithms are used to automatically map two regional tributary networks of submarine canyons and deep-sea channels draining Monterey Bay, the principal conduits of which are Acension and Monterey Canyons. The algorithms reliably map subaqueous drainage areas, but are prone to error in mapping the extent of submarine canyon and channel thalwegs due to operator subjectivity and algorithm limitations. A geomorphic comparison of the Acension and Monterey Canyon networks, with 12 river networks in the continental U.S., illustrates both the potential and weaknesses of using drainage extraction algorithms to analyze sediment pathways in gridded bathymetry.

Introduction

Early bathymetric maps of submarine canyons (e.g., Veatch and Smith, 1939) were the first to document the terrestrial attributes of seafloor features cut by sediment drainage along continental margins. Since then, extensive echo-sounding and swath-mapping surveys of continental margins have revealed canyon-cut terrains resembling semi-arid landscapes (Bellaiche *et al.*, 1983) and deep-sea channels with river-like morphologies (Damuth *et al.*, 1983). Such surveys have also led to the recent recognition of regional tributary networks of submarine canyons and deep-sea channels (Hesse, 1989; Schlee and Robb, 1991). In contrast to submarine fans, these networks act to collect sediment drainage rather than distribute it. Because of their similarity to large river networks on land, the networks have been termed submarine drainage systems (Hesse, 1989).

An example of a submarine drainage system is the network of submarine canyons and deep-sea channels draining Monterey Bay, California, which collect seaward into a central deep-sea channel that feeds the Monterey Fan. The system is referred to here as the Monterey Submarine Drainage System (MSDS), and is depicted in the National Oceanic and Atmospheric Administration's (NOAA, 1988a-g) gridded multibeam bathymetry of the mid-California margin (35.5°–37.5° N, 122°–124° W) (Figure 1). While the areal extent and detail of the NOAA grid is equivalent to that of a coarse digital elevation model (DEM) of land topography, it and similar multibeam bathymetric grids provide the most complete and accurate representations of deep-sea topography to date. These grids also permit seafloor features such as the MSDS to now be examined with computer techniques used by terrestrial geologists for analyzing landforms in DEMs.

The purpose of this paper is to demonstrate the potential of drainage extraction algorithms for mapping and quantifying the morphology of submarine canyons and deep-sea channels in gridded bathymetry. The algorithms were originally designed for automatically mapping river networks and watersheds in DEMs of land surfaces (e.g., O'Callaghan and Mark, 1984), but have been shown to be equally suited for mapping channel systems in DEMs of both Mars (Jenson, 1991) and the seafloor (Pratson and Ryan, 1992; Pratson and Ryan, 1994). In this study, we attempt to use drainage extraction algorithms as an objective means for extracting comparative geomorphic measures of the MSDS and twelve river networks in the continental U.S. The comparison is conducted in an effort to quantify the morphologic similarity between submarine and subaerial drainage systems noted above. As will be shown, results of the comparison prove inconclusive, in part because of inaccuracies in the extent of submarine canyons and channels mapped by the algorithms.

Marine Geophysical Researches **18:** 757–777, 1996.

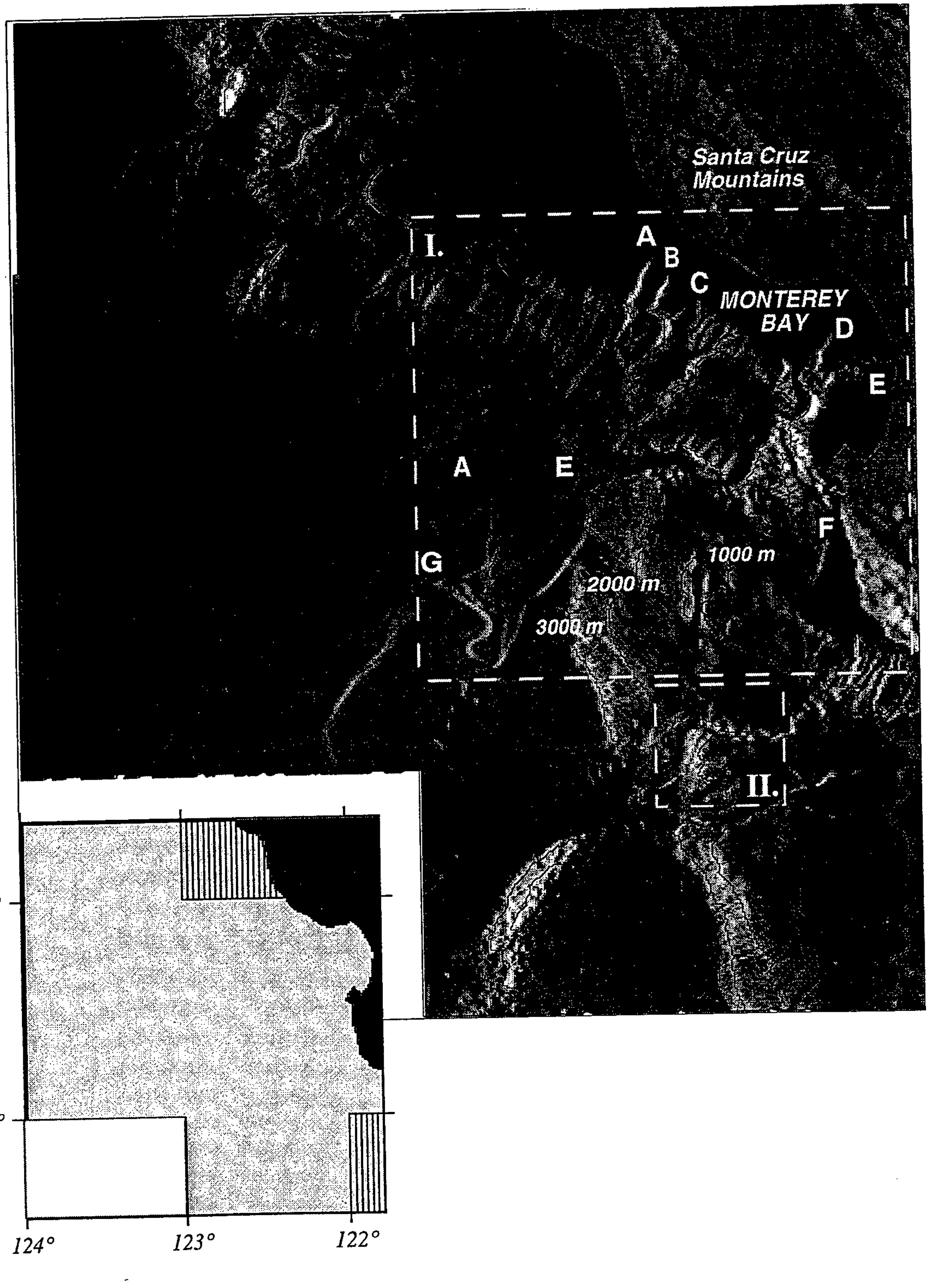

Fig. 1. Shaded image of NOAA bathymetry off Monterey, California (west illumination): A. Nuevo Canyon, B. Cabrillo Canyon, C. Acension Canyon, D. Soquel Canyon, E. Monterey Canyon, F. Carmel Canyon, G. Monterey-Acension Canyon confluence. Inset shows coverage of data used to create image: light grey area is NOAA bathymetry, vertical lined areas are bathymetry derived from Lamont-Doherty Earth Observatory's GeoBase (Menke *et al.*, 1991). Gridded using the surface routine of Smith and Wessel (1990). Dark area is NOAA 30 arc-second gridded topography of the U.S.

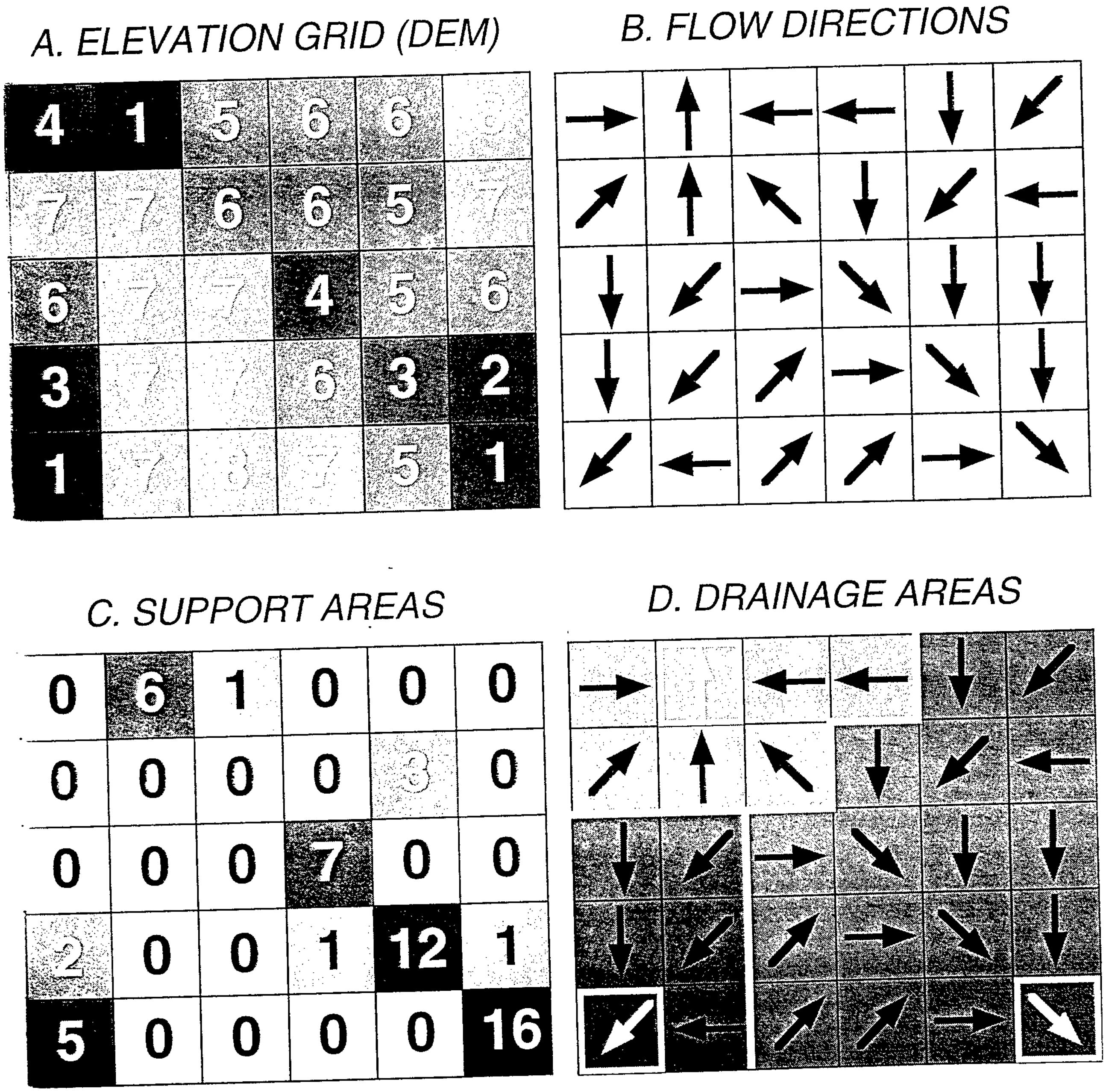

ig. 2. Illustration of how drainage extraction is accomplished. A. Example grid of elevations (numbers), or digital elevation model (DEM). Arrows indicate flow direction from each grid cell to its lowest neighboring cell. C. Support area, or number of grid cells that drain into ch grid cell along paths defined by flow directions. D. Drainage areas, or regions within DEM that direct flow to a common outflow point (white boxes with white arrows). White lines are drainage divides. See text for detailed explanation.

he Monterey Submarine Drainage System

he MSDS is principally composed of two submarine nyons: Acension and Monterey (Figure 1). Into these ed a number of tributary canyons including Nuevo nd Cabrillo which enter Acension Canyon, and Soquel and Carmel, which enter Monterey Canyon (Figure 1A-F). Acension and Monterey join at approximately 3200 m water depth (Figure 1G) to form the main channel that feeds the Monterey Fan. Together, these two canyon networks drain roughly 6500 km^2 of seafloor.

Fig. 3A.

The source of sediments to the MSDS has been the California coastal highlands surrounding Monterey Bay. Materials have been delivered to the MSDS by rivers and shallow marine currents, which because of the region's narrow continental shelf (≤ 15 km), continue to transport sediments to the upper reaches of the drainage system despite the present sea level highstand (McHugh *et al.*, 1992). Build-ups of these sediments have been redistributed within and out of the drainage system by sediment gravity flows (e.g., turbidity currents, debris flows, etc.), some of which appear to have been triggered by earthquakes along the San Andreas Fault Zone (Normark and Gutmacher, 1988). While the lower part of Acension Canyon is presently filled, turbidity currents have continued to pass through both Canyon networks during the Holocene (Hess and Normark, 1976).

Bathymetry

NOAA bathymetry of the MSDS (light grey area, inset, Figure 1) is primarily based on soundings collected in water depths greater than 600 m using the SeaBeam swath mapping system (Grim, 1992). In water depths less than 600 m, soundings are from pre-multibeam hydrographic surveys and surveys using a 36 kHz shallow-water multibeam echo sounder. Where multibeam systems were used, adjacent swaths overlapped 10%.

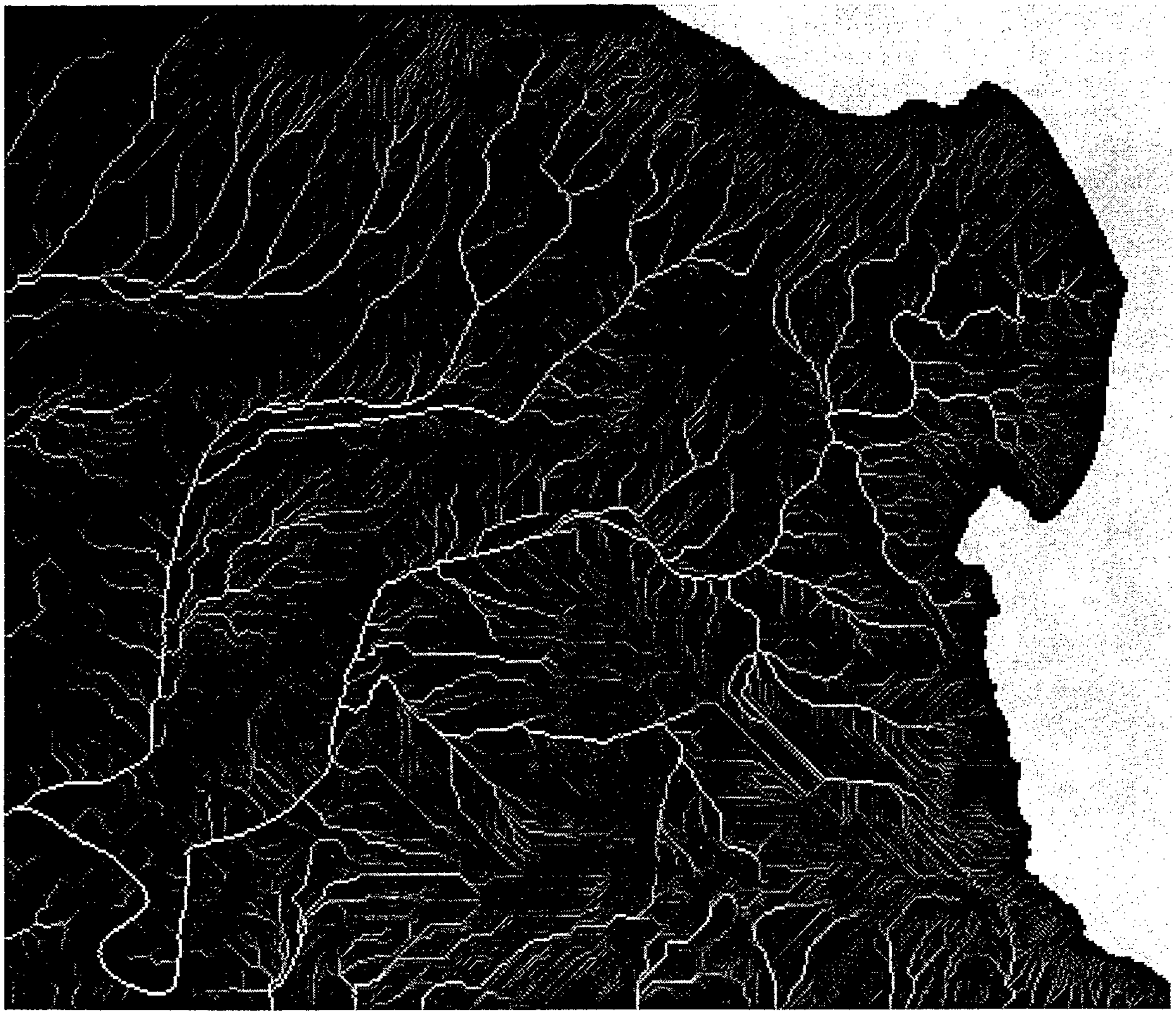

Fig. 3B.

Fig. 3 A. Flow directions for the gridded bathymetry of the MSDS in dashed box area I of Figure 1. Eight shades of grey represent the eight possible directions of flow, beginning with black which points towards the northeast, and proceeding clockwise at 45° increments to white which points to the north. B. Support areas for the same area computed from the flow directions in Figure 3A. Grid cell support areas increase from zero along interbasin ridges (displayed as black) to >100,000 grid cells at the downstream point of the MSDS in the image (displayed as white).

From the soundings, NOAA has constructed seven bathymetric grids (NOAA, 1988a-g), the composite of which is shown in Figure 1. This composite grid is based on roughly 1.8 million soundings selected from 30–60 million "raw soundings", each of which have a positional accuracy of within 50 m and depth accuracy of within 1% actual water depth (Grim, 1992). The grid projection is Universal Transverse Mercator (UTM) and cell spacing is 250 m.

Automated Drainage Extraction

Drainage information on the MSDS can be automatically extracted from the NOAA bathymetry using a sequence of computer algorithms that predict directions of gravity-driven fluid flow based on local slopes. A variety of such algorithms have been developed for extracting drainage information on fluvial systems from DEMs (see Moore *et al.*, 1991). The algorithms used in this study are based on the scheme proposed by Jenson and Dominique (1988), which incorporates a technique for mapping drainage pathways across grid depressions and plains; features that are common in gridded bathymetry. The general proceedure for automated drainage extraction is:

1. *Assign each grid cell a flow direction.* Flow directions define the paths fluid would flow from one grid cell to the next (Figure 2B), and are unit vectors that point from a grid cell towards the one of its eight nearest neighbors with the steepest descent in elevation (Figure 2A). Descents to lower neighboring cells are weighted as a function of distance from the center cell: east-west neighbors are weighted by the grid cell spacing in the x-direction (dx), north-south neighbors by the grid cell spacing in the y-direction (dy), and diagonal neighbors by $\sqrt{dx^2+dy^2}$. This study resolves cases in which two or more neighboring cells share the same distance weighted drop in elevation by selecting the one closest in line with the mean trend of flow directions pre-determined for the neighboring cells upslope of the center cell. Flow directions for the NOAA bathymetry of the MSDS (Box I, Figure 1) are shown in Figure 3A.
2. *Calculate the area drained by each grid cell.* This area is the summed area of all the grid cells upslope of a grid cell that lead flow into the grid cell. The area is commonly referred to as the cell's support area and is analogous to the amount of discharge the cell could potentially receive. Figure 2C shows the support areas determined for the hypothetical grid shown in Figure 1A. These support areas are determined by using the flow directions for the grid (Figure 2B) to count the number of upslope cells that direct flow into each grid cell. These numbers then represents the grid cells' support areas. The support areas for the MSDS, which are derived from the flow directions in Figure 3A, are shown in Figure 3B.
3. *Extract drainage networks.* Drainage networks are extracted by specifying a support area threshold. All grid cells having support areas equal to or greater than the threshold constitute part of the drainage network. Grid cells with support areas less than the threshold constitute the interfluves between channels in the network. If the support area threshold is high, the drainage network that is extracted is sparse. If the threshold is low, the drainage network is dense. Figure 4 shows the drainage network corresponding to the MSDS extracted from the support areas in Figure 3B using a threshold of 50 cells.
4. *Delineate network drainage areas.* Network drainage areas are delineated by grouping all grid cells with flow directions that direct flow to the outlet cell at the end of the network (Figure 2D). Those cells that do not direct flow to the outlet cell are considered to be outside the network's drainage area. Figure 4 shows the drainage areas of the Acension and Monterey Canyon networks.

Prior to the steps outlined above, a DEM is often preconditioned to infill all grid depressions up to their spill point, which is the lowest elevation along a depression's rim. If depressions are not infilled, local flow directions oppose one another on either side of the depressions. This breaks the downslope path of flow directions that mark the course of canyons and channels, resulting in the extraction of segmented drainage networks. Infilling of depressions prior to steps 1–4 ensures extraction of continuous drainage networks by approximating the natural behavior of fluid flows, which infill depressions up to their spill points before exiting downslope. The reader is referred to Jenson and Dominque (1988) and Pratson and Ryan (1992) for further details on preconditioning DEMs.

Representation of the Monterey Submarine Drainage System

Figure 4 shows drainage networks and drainage areas extracted from the NOAA bathymetry in the region surrounding the MSDS (Box I, Figure 1) using a support area threshold of 50 cells. The drainage networks in this figure correspond to the networks of the submarine canyons and canyon tributaries that form the MSDS. The canyons and most of the large canyon tributaries are shown to initiate near the shelf break. The canyons are mapped seaward into deep-sea channels on the Monterey Fan that are fed laterally by shorter tributaries corresponding to gullies incising the channel walls. The MSDS is clearly seen in the center of the figure as the regional tributary network formed by the collection of canyons, channels and gullies. The system can be subdivided into the Acension and Monterey Canyon systems, whose subaqueous drainage areas span the light and dark grey regions (respectively) in Figure 4.

Closer inspection reveals discrepancies between the extent of the canyons and channels mapped in Figure 4 and the NOAA bathymetry (Figure 1). An example is the small tributary network mapped on the northwestern levee of Acension Canyon (dashed box, mid-left, Figure 4). This network is not evident in the corresponding bathymetry.

The mapping of the tributary network highlights two important limitations associated with automatic drainage extraction. The first is that the drainage ex-

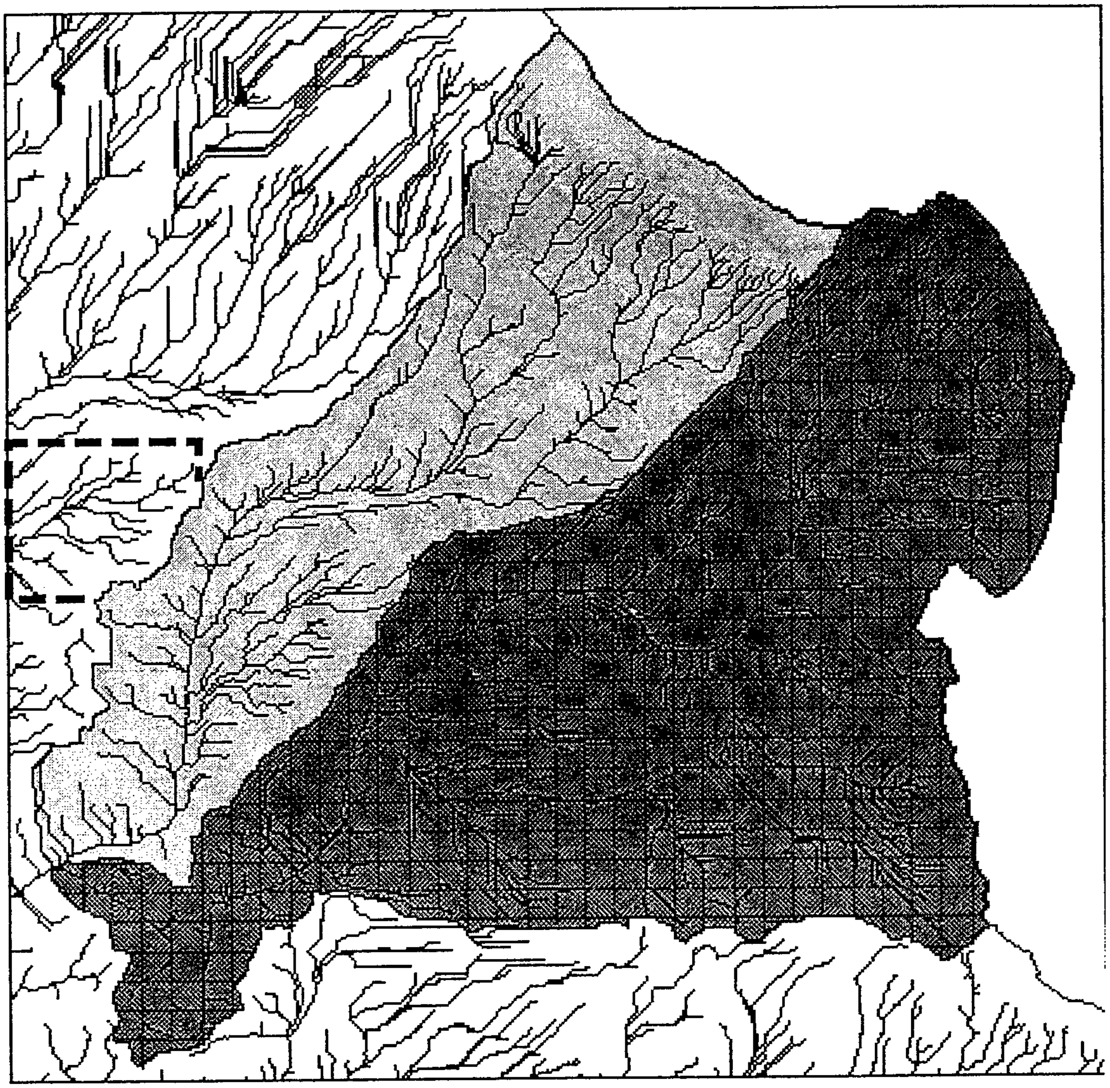

Fig. 4. MSDS canyon-channel networks extracted from the gridded bathymetry in dashed box area I of Figure 1 using a support area threshold of 50 grid cells. Shaded regions are the subaqueous drainage areas of the Acension (light grey) and Monterey (dark grey) Canyon networks.

traction algorithms assign each grid cell only one flow direction. As a result, the algorithms can only map parallel and tributary channel geometries. Distributary or braided channel geometries, which would require multiple flow directions, are not mapped. This presents a problem on the Monterey Fan levees where gradients are low and sediment waves form obstructions to turbidity current overbank flows, making distributary and/or braided sediment pathways more likely.

The second and more serious limitation is that the drainage extraction algorithms map channel pathways purely as a function of grid cell support area, a measure that is independent of whether a grid cell actually falls within an eroded channel or occurs on an uneroded slope. The tributary network extracted over the northwestern levee of Acension Canyon is composed of grid cells in troughs between depositional sediment waves with support areas that exceed 50 cells. Evidence that such a network actually exists is not seen in either the bathymetry or in side-scan sonar imagery of levees just to the south collected by the authors aboard the R/V *Point Sur* in September of 1990. Other artificial channels mapped by drainage extraction are commonly straight. Such channels are evident in Figure 4 and

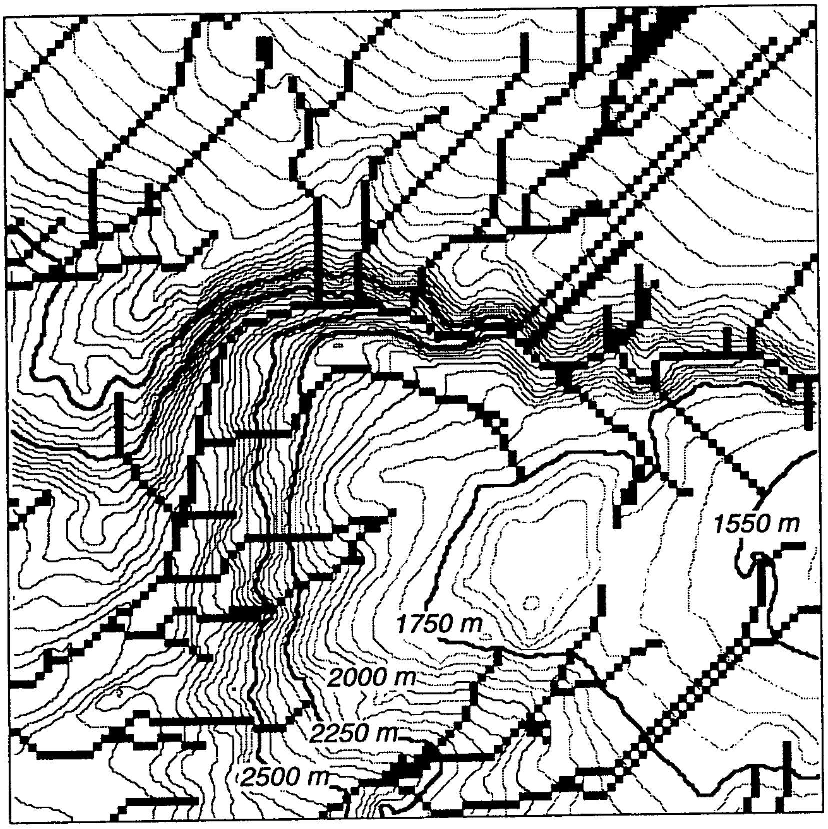

Fig. 5A.

are a consequence of using a support area threshold which is too low for regions in the DEM. Figure 5A shows the drainage network extracted for Sur Canyon to the south (Box II, Figure 1) using the same support area threshold of 50 cells. The network contains several straight channels on slopes leading into the canyon, which at the resolution of the grid (250 m) appear to be uneroded. When the support area threshold is raised to 500 cells, the artificial channels are absent. As a consequence of this high threshold, however, several real erosional channels are not mapped either (Figure 5B).

Figure 5 illustrates that the accuracy of drainage information extracted by the algorithms is influenced by two factors: the resolution of the DEM and the support area threshold used to map drainage networks. The effect of DEM resolution on the measurement of drainage area and channel length is demonstrated in Figures 6A and B. The figures show results from a sensitivity experiment in which the resolution of the NOAA bathymetry was degraded from its initial grid cell spacing of 250 m to a coarser grid cell spacing of 1 km. At each grid resolution, a constant support area threshold of 50 cells was used to extract channel networks within the Acension and Monterey Canyon basins (grey areas, Figure 4). Results show that with decreasing grid resolution, measurement of drainage area remains relatively constant (for both the Acension and Monterey Canyon basins, drainage area decreases at a rate of 0.1 km^2 with decreasing grid resolution, Figure 6A), but total channel length decreases rapidly (Figure 6B). This indicates grid resolution has a minor influence on the measurement of drainage area, but a significant influence on the measurement of channel length.

A second sensitivity experiment demonstrates how channel length is also effected by the support area threshold used to map channel networks (drainage area is independent of support area threshold). In this experiment, grid resolution was held constant at a grid cell spacing of 250 m, while the support area threshold for mapping channel networks in the Acension and Monterey basins, was reduced from 500 to 0 cells. Figure 6C shows that as the threshold is decreased, total channel length increases slowly and almost linearly until reaching a narrow range of transition

Fig. 5B.

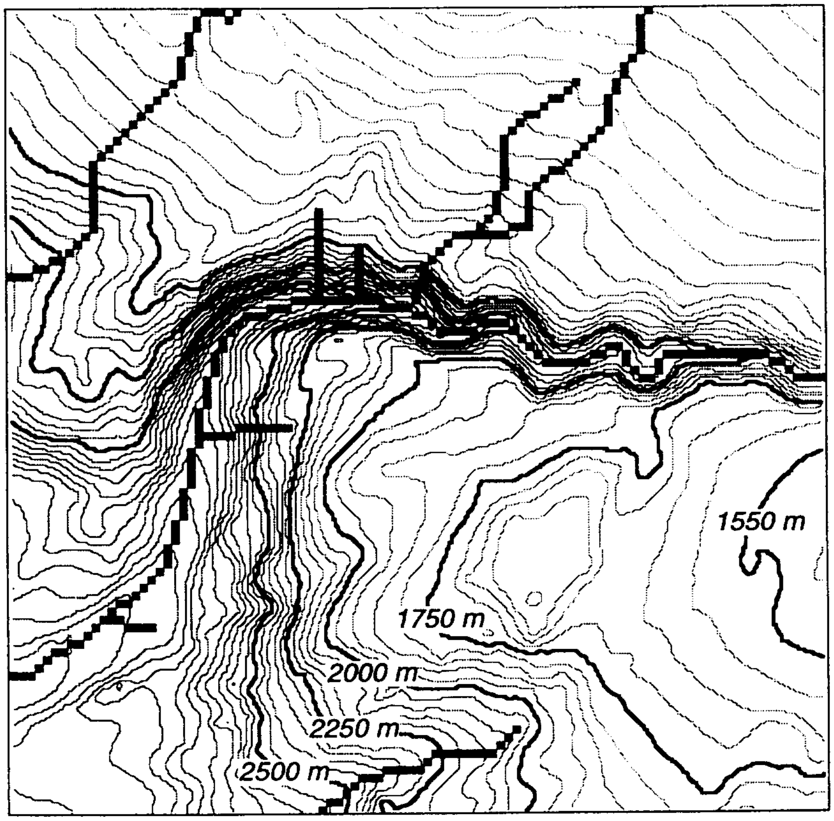

Fig. 5 A. Canyon-channel networks extracted from the gridded bathymetry of Big Sur Canyon south of the MSDS in dashed box area II of Figure 1 using a support area threshold of 50 cells. Note straight, "artificial" channels defined in regions where contours show no evidence of a channel. B. Canyon-channel networks extracted for the same area using a support area threshold of 500 cells. The higher threshold eliminates artificial channels, but prevents mapping of several real channels defined by contours.

thresholds below which channel length increases rapidly. The transition thresholds may represent basin-specific support area thresholds, over which extracted drainage paths change from principally conforming to eroded channels to occuring along both eroded channels and uneroded slopes.

Comparison to Subaerial Drainage Systems

Objective

In the first description of a submarine drainage system, Hesse (1989) noted that the regional organization of submarine canyons and channels feeding the Northwest Atlantic Mid-Ocean Channel was similar to that of the Mississippi River and its satellite tributaries. The regional organization of the MSDS is equally reminiscent of subaerial drainage systems and its Monterey Canyon has often been compared to Arizona's Grand Canyon (e.g., Shepard and Dill, 1966). An implication of these similarities is that aspects of continental margin evolution by gravity-driven sediment flows beneath the sea parallel topographic evolution by rivers on land. In contrast to subaerial drainage systems, the seafloor surfaces upon which submarine drainage systems form are essentially free of vegetation, have a relatively homogeneous surfacial lithology generally consisting of unconsolidated sediments, and are overlain by a marine climate that is comparatively uniform for long periods of time (months to tens of years vs. days). Given these differences, a quantitative geomorphic comparison of submarine and subaerial drainage morphology might illuminate some previously unrecognized erosional mechanism in either environment. In an attempt to address this issue, the geomorphology of the Acension and Monterey Canyon networks was compared with twelve river networks from the continental U.S. (Table I).

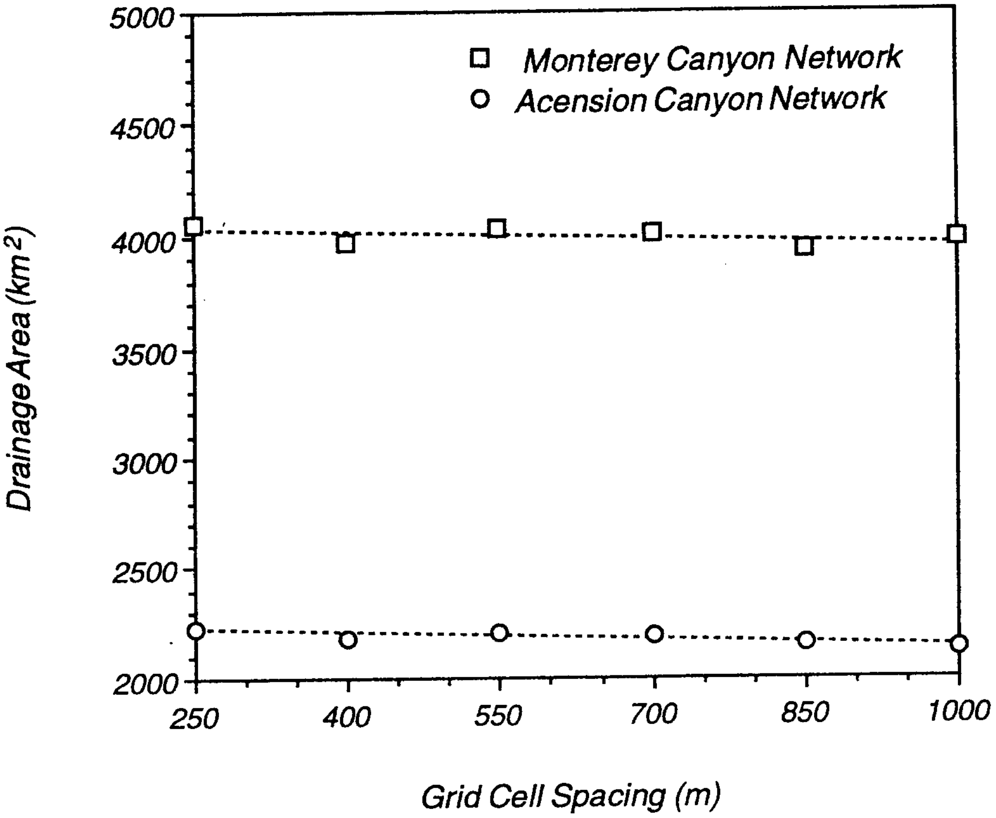
□ Monterey Canyon Network
○ Acension Canyon Network
Drainage Area (km^2)
5000
4500
4000
3500
3000
2500
2000
250
400
550
700
850
1000
Grid Cell Spacing (m)

Fig. 6A.

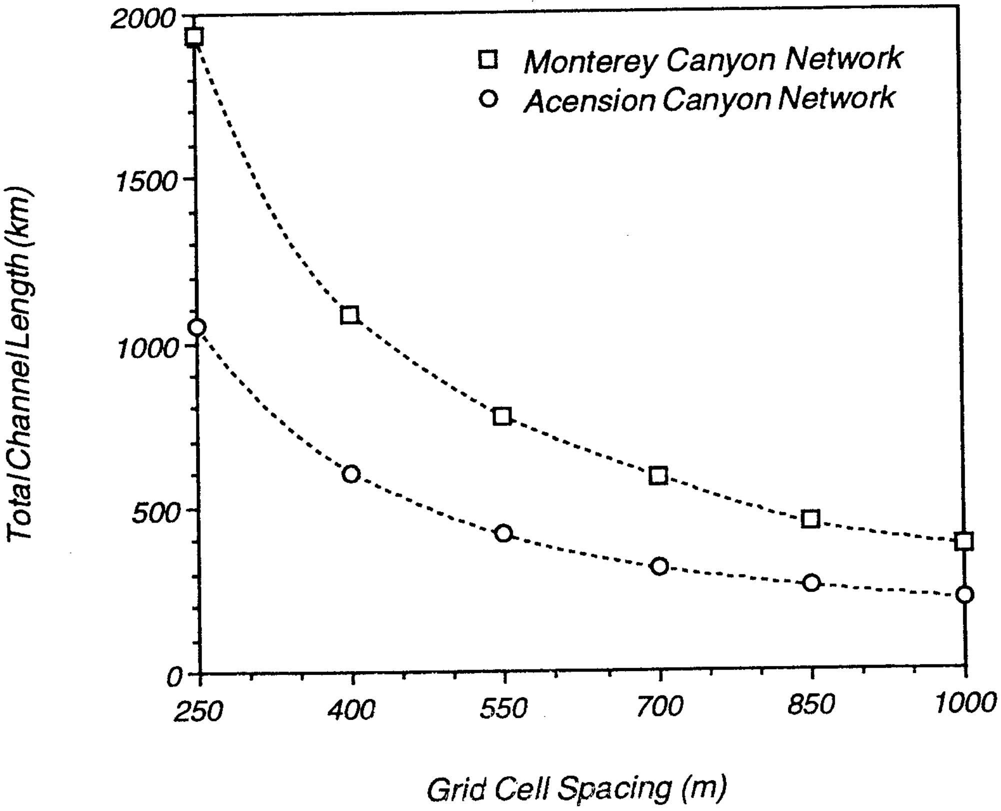
□ Monterey Canyon Network
○ Acension Canyon Network
Total Channel Length (km)
2000
1500
1000
500
0
250
400
550
700
850
1000
Grid Cell Spacing (m)

Fig. 6B.

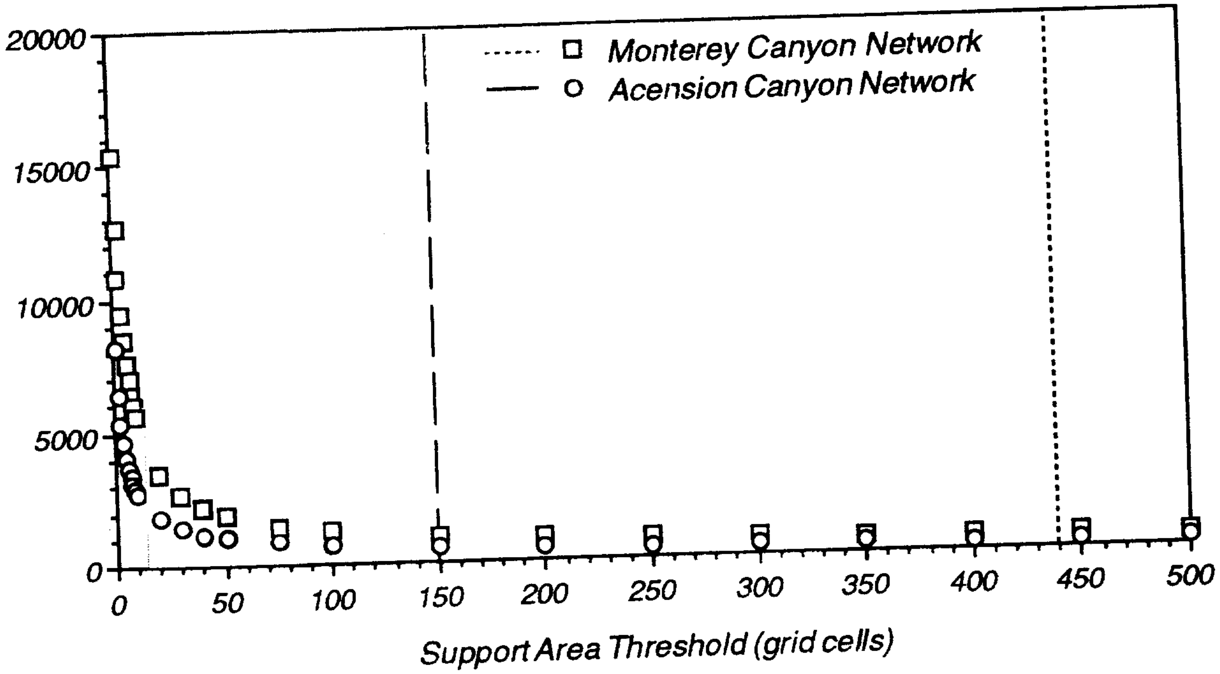

6C.

6. A. Plot of grid resolution versus drainage areas of the Acension and Monterey Canyon networks extracted from the gridded bathymetry.
lot of grid resolution versus total channel lengths extracted for the Acension and Monterey Canyon networks. C. Plot of support area
shold versus total channel lengths extracted for the Acension and Monterey Canyon networks. Grey area highlights transition thresholds
which measures of total channel length increase rapidly with decreasing support area threshold. Dashed and dotted lines mark minimum
ort area thresholds for extracting the Acension and Monterey Canyon networks from the NOAA bathymetry at a grid cell spacing of
250 m determined using the constant channel drop procedure of Tarboton *et al.* (1991)

thodology

e river networks selected for comparison to the Acen- n and Monterey Canyon networks come from four matically different regions representing a variety of hologies and vegetation, but having the same relief d general physiography as the California margin. e river networks were automatically extracted from NOAA 30 arc-second DEM of the continental S. (an available and comprehensive source of U.S. pography) after re-mapping it to an equivalent grid l spacing of 926 m in UTM projection. The Acen- n and Monterey Canyon networks were extracted the same resolution by first re-mapping the NOAA dded bathymetry to the 926 m grid cell spacing using bilinear interpolant.

To remove the subjectivity in selecting an appro- iate support area threshold while maximizing the apping of resolvable channels, the constant channel op procedure of Tarboton *et al.* (1991) was used in xtracting the channel networks from the individual rainage basins in the DEMs. The procedure required hat channel segments in both river and canyon networks be ordered according to the Strahler (1952a) scheme of channel hierarchy. In this scheme, headwater channels are first order channels, and higher order channels begin at the confluence between channels of equal order. Broscoe (1959) observed that when channels are ordered this way, the mean drop in elevation along channels of a given order is statistically the same from one channel order to the next. In the Tarboton *et al.* (1991) procedure, extraction of the highest resolution drainage network is accomplished by selecting the smallest support area threshold for which the constant channel-drop property still holds. This threshold is found by reducing the support area threshold until the mean drop in elevation between channels of successive orders is determined to be statistically different by a Student t test with a 95% confidence interval. As an example, support area thresholds determined by this technique for extracting the Acension and Monterey Canyon networks from the NOAA bathymetry at a grid cell spacing of 250 m are shown in Figure 6C. The support area thresholds determined for extracting the fourteen drainage net-

Table I

Location, support area threshold, and geomorphic measures of the twelve subaerial and two submarine drainage networks

Drainage Basin	Outlet		Support Area Threshold (cells)	Total Channel Length (km)	Drainage Area (km^2)	R_b	R_L	R_S	D_d (km^{-1})
	latitude	longitude							
Hudson River, NY			8	1310	5367	3.7	2.2	1.1	0.244
Hoosic River, NY, VM, NH	43°13′01″ N	73°34′48″ W	4	844	2551	3.7	1.9	1.5	0.331
Contoocoock River, NH	42°54′58″ N	73°39′24″ W	6	492	1728	4.6	2.4	1.3	0.285
Little Tennesee River, TN, NC, GA	43°16′04″ N	71°35′02″ W	9	1478	6638	5.9	3.3	2.0	0.223
French Broad River, TN, NC	35°45′18″ N	84°15′53″ W	30	1414	6677	3.9	2.3	1.6	0.131
Enoree River, SC	35°59′13″ N	83°10′46″ W	20	328	1935	5.0	3.8	1.2	0.170
Salmon River, ID	34°25′56″ N	81°25′58″ W	10	3834	16718	4.8	2.4	1.8	0.229
Middle Fork River, ID	45°17′31″ N	114°35′28″ W	7	1576	6556	4.0	2.1	1.7	0.240
South Fork Boise River, ID	45°17′01″ N	114°36′10″ W	20	527	3454	3.8	2.4	1.7	0.153
Cataract Creek, AZ	43°35′11″ N	115°50′09″ W	40	983	7779	3.9	2.1	1.2	0.126
Big Sandy River, AZ	36°17′36″ N	112°46′05″ W	60	651	7562	3.3	2.2	1.2	0.086
Chevelon Creek, AZ	34°13′52″ N	113°37′24″ W	20	292	1365	2.5	1.2	1.0	0.214
Acension Canyon (submarine), CA	34°56′33″ N	110°30′51″ W	20	362	2161	3.2	2.3	1.4	0.168
Monterey Canyon (submarine), CA	37°21′02″ N	122°56′42″ W	60	354	3811	4.1	3.9	2.4	0.093

Table II

Geomorphic measures

Drainage density:	$D_d = \Sigma L/A$
Bifurcation ratio:	$R_B = N_w/N_{w+1}$
Length ratio:	$R_L = L_w/L_{w+1}$
Slope ratio:	$R_S = S_w/S_{w+1}$

L = total channel length in a channel network
A = area drained by the channel network
N_w = number of channels in network of order w
L_w = mean length of channels in network of order w
S_w = mean slope of channels in network of order w

works at a grid cell spacing of 926 m are listed in Table I.

Once the river and canyon networks were extracted and ordered, four standard geomorphic measures defined in Table II were then made of network geometry: drainage density, bifurcation ratio, length ratio, and slope ratio. These measures are used to characterize channel patterns, variations in which are thought to reflect regional tectonics (Ollier, 1981; Cox, 1989; Burbank, 1992), geologic structure (Abrahams and Flint, 1983), erosional mechanisms (Dunne, 1980) and prevailing climate (Gregory, 1976; Daniel, 1981). Drainage density is the average length of channels per unit drainage area and represents the spacing of the channelways (Ritter, 1986). The latter three ratios, referred to as Horton ratios after Horton (1945), are dimensionless, hold over a range of length scales, and are designed to characterize the channel composition of a drainage net. The Horton ratios are derived empirically by plotting semilog plots of the number, mean length and mean slope of channels versus channel order. For river networks, these plots generally follow straight lines, the slopes of which equal the logarithm of the ratios. Such plots for the Ascension and Monterey Canyon networks exhibit the same linear trends (Figure 7).

Results

The geomorphic measures for the drainage networks are listed in Table I and are shown along with the regional means in bar graphs in Figure 8. The regional means suggest that on average, the Acension and Monterey Canyon networks have lower drainage densities and bifurcation ratios, and slightly higher length and slope ratios than the river networks. If true, this would imply that the Canyon networks tend to have lesser numbers of tributaries, which are proportionally shorter and steeper in relation to their main channels than subaerial networks. However, the regional means are based on few measures that vary in magnitude. The regional means for the Horton ratios are even somewhat less robust because of the errors in the linear regressions (goodness-of-fit > 85% in all cases) used to

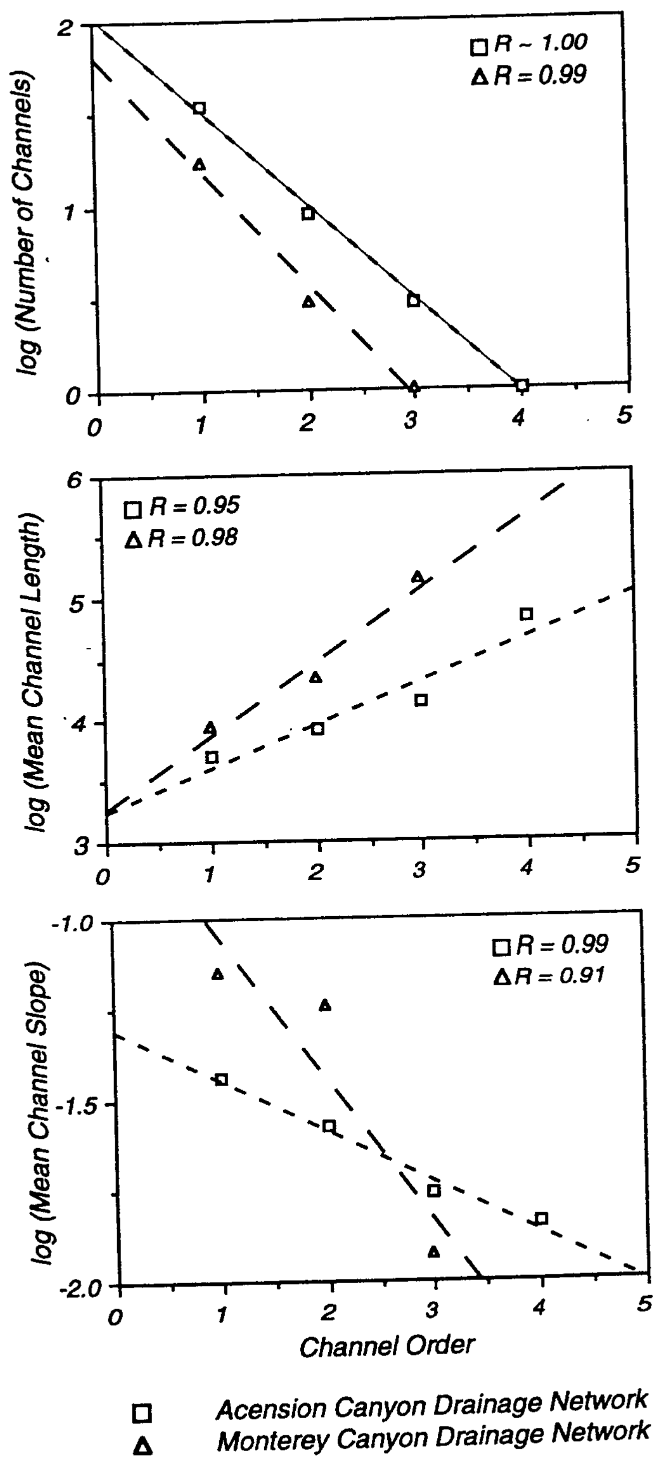

Fig. 7. Semilog plots of the bifurcation, length and slope ratios for the Acension and Monterey Canyon drainage networks extracted from the NOAA bathymetry at a grid cell spacing of 926 m using the support area thresholds listed in Table I. *R* is the correlation coefficient for the best-fit line through the individual plots (dashed lines).

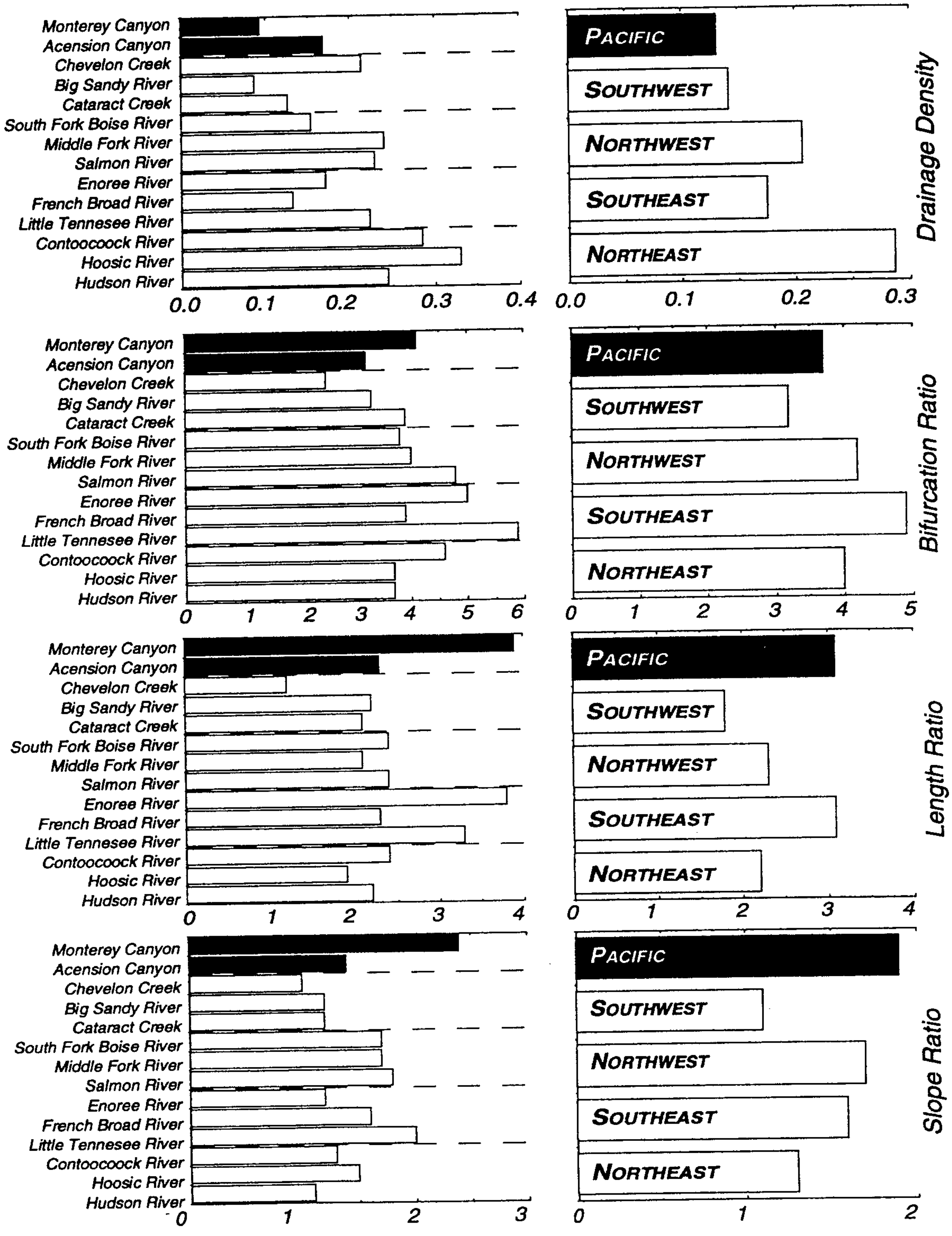

Fig. 8. Bar plots graphically depicting the geomorphic measures of the Acension and Monterey Canyon networks versus those for the twelve U.S. river networks listed in Table I. Bar plots to the left are of the measures for the individual drainage networks. Bar plots to the right are of the regional means.

culate the individual ratios. Given their uncertain-s, the only observation that can be made of the ults is that the drainage densities and Horton ratios :ermined for the Canyon networks by drainage ex-ction occur within the variability of those deter-ned for the 12 river networks at a DEM resolu-n ≈1 km.

cussion

e question that remains of the comparison is ether the similarity of the geomorphic measures nputed for the Canyon and river networks estab-es how closely the areal geometry of submarine inage systems approaches that of subaerial drain- systems. This question requires evaluation of the owing factors: the resolution of the DEMs used in comparison, the accuracy of the channel lengths d drainage areas derived from drainage extraction, d the robustness of the geomorphic measures used compare the drainage systems.

The first two factors have been addressed in part by aforementioned sensitivity experiments. Use in the nparison of DEMs with resolutions ≈1 km limits minimum observable width of erosional channels 5–10 km. On land, channels tend to extend into -scale valleys (Montgomery and Dietrich, 1988), l accurate representation of terrestrial channel net-ks can require DEMs with a grid cell spacing of little as 10 m, a vertical error of ±0.5 m and a izontal error of ±3 m (Dietrich *et al.*, 1993). Such h resolution DEMs are not yet available for deep-bathymetry. The maximum horizontal resolution a SeaBeam depth sounding in 1000 m of water is 0 m, while its vertical resolution ≈10 m (Tyce, 6). Horizontal resolution of gridded bathymetry the same water depths is worse due to interpolation ween grid points. As a result, multibeam bathy-ric grids probably cannot accurately resolve ero-al channels much less than 1/2 km in width and n in depth. By using such coarse resolution DEMs, comparison does not evaluate differences in net-k detail even at this scale. Further comparisons d to be done at higher resolutions and with addi-al submarine and subaerial drainage networks to ly establish the similitude of the two types of sys-s. The results presented here pertain only to the onal organization of the MSDS and its relation to e river networks at the same kilometer scale.

s Figure 5 shows, automated-drainage extraction npounds the problem of accurately mapping ero-al channel networks by introducing errors in chan- network extent. Since in deep water (>200 m) the nts of submarine erosion tend to be localized and because, at least seaward of the continental slope, the seafloor is largely a depositional surface, channel network extent may in fact be overestimated when the algorithms are applied to gridded bathymetry. Drainage extraction does define channels in the NOAA bathymetry where there is no observable channel morphology. However, several elements mitigate the effect of these inaccuracies in the comparison of the MSDS with the fluvial systems. First, the comparison is restricted to the Acension and Monterey Canyon networks (shaded areas, Figure 4), which the bathymetry clearly shows are erosional features. Second, drainage extraction of channels on uneroded slopes in these areas is partially compensated by the heads of channels not mapped using the support area threshold determined for each network (e.g., Figure 5B). Third, the river networks extracted from the gridded topography possess the same inaccuracies that mar the submarine canyon networks. And fourth, these inaccuracies are uniform among all the drainage networks compared, because an objective technique, the constant channel drop procedure of Tarboton *et al.* (1991), provided the support area thresholds used to extract each drainage network. In short, due to inaccurracies, the total channel lengths listed in Table I are not exact, but instead are estimates with some unknown degree of error. This unknown error prevents a quantitative assessment of the morphologic closeness of submarine and subaerial drainge systems.

Recognizing this fact, Pratson (1993) argues that because the measures for the submarine canyon networks occur within the variability of those for the river networks, the results could still be construed as a relative indication that the regional organization of submarine and subaerial drainage systems is morphologically similar. His argument is based on the reputation of the ratios listed in Table II as fundamental measures of drainage network structure, particularly the bifurcation, length and slope ratios. Horton (1945) devised the ratios as drainage network descriptors, and they have since been used by geomorphologists to compare channel networks among diverse landscapes (e.g., Strahler, 1952b; Schumm, 1956; Chorley, 1957; Morisawa, 1962). Because of this body of work, the Horton ratios have been termed "laws of drainage network composition" and are considered geomorphic principles in many textbooks (e.g., Chorley *et al.*, 1984; Press and Siever, 1986; Ritter, 1986; Judson and Kaufman, 1990; Summerfield, 1991; Easterbrook, 1993). However, in a study subsequent to that of Pratson (1993), Kirchner (1993) statistically confirms earlier, intuitive arguments (Bowden and Wallis, 1964; Milton, 1966; Smart, 1978) that Horton's laws

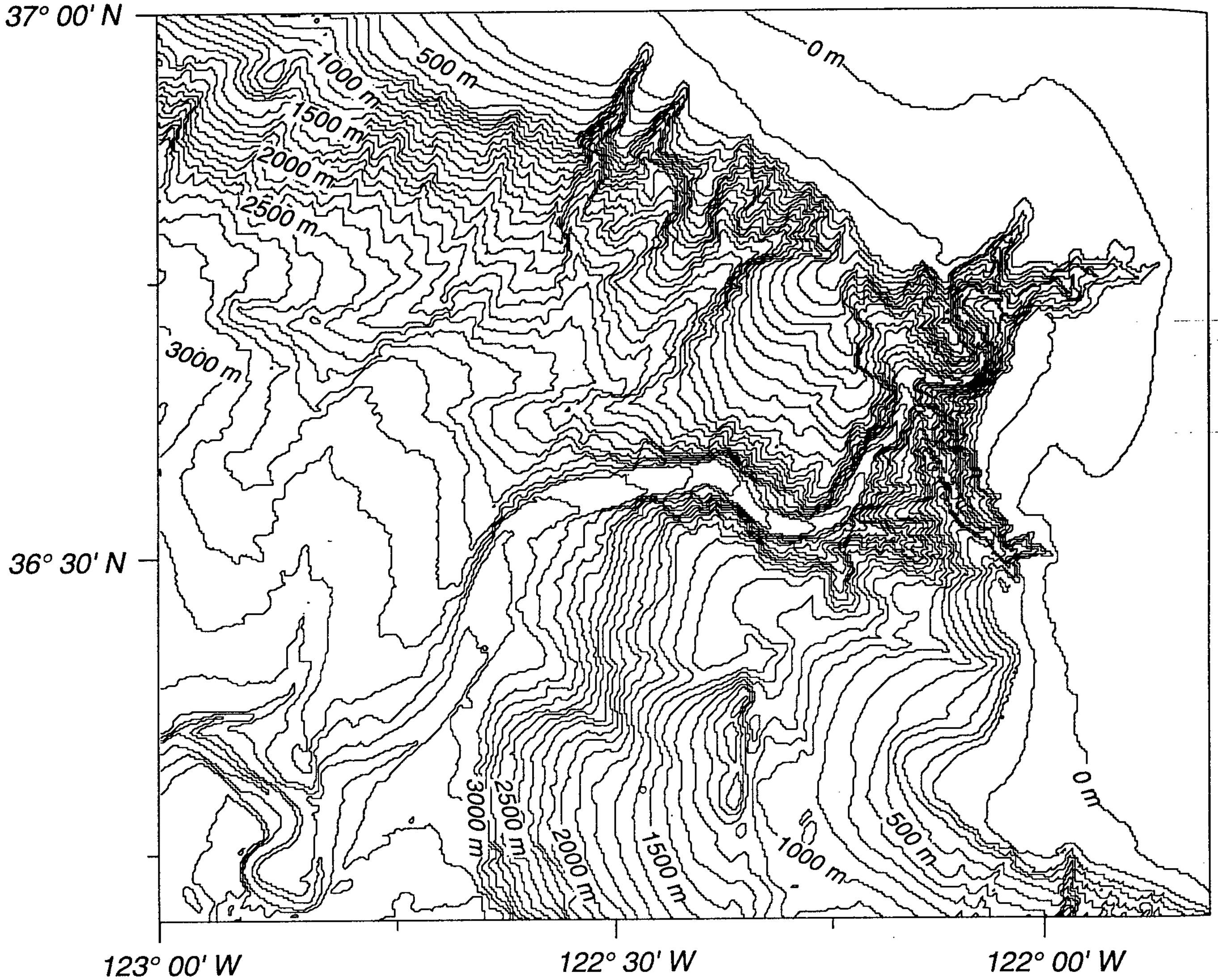

Fig. 9A.

are insensitive to pronounced differences in network structure. This analysis showed that the ratios do not provide distinctive geometric or topologic measures that can be used to contrast channel networks formed under different prevailing geologic and environmental conditions.

Kirchner's (1993) findings remove three benchmarks of "closeness" from the MSDS-fluvial comparison above. Since further investigation needs to be done to establish the error in total channel length resolved by drainage extraction, the drainage density values also cannot be compared without criticism. The geomorphic relation between the MSDS and its fluvial counterparts remains inconclusive.

While the MSDS is visually similar to terrestrial drainage systems, it is also different. For example, Figure 9 shows contour maps of the MSDS (Figure 9A) and the MacLeay River (Figure 9B), which incises the subaerial escarpment bordering the elevated New England Tableland in southeastern Australia. The MacLeay River has formed in a region where the New England Tableland plateau dips towards escarpment (Weissel *et al.*, 1992), approximating the regional form of the California continental shelf-slope-upper rise margin across which the MSDS has formed. In the map of the MacLeay River (Figure 9B), the density of contours is greatest in the dissected, rugged but regionally flat-lying terrain at the base of the escarpment. By contrast, the

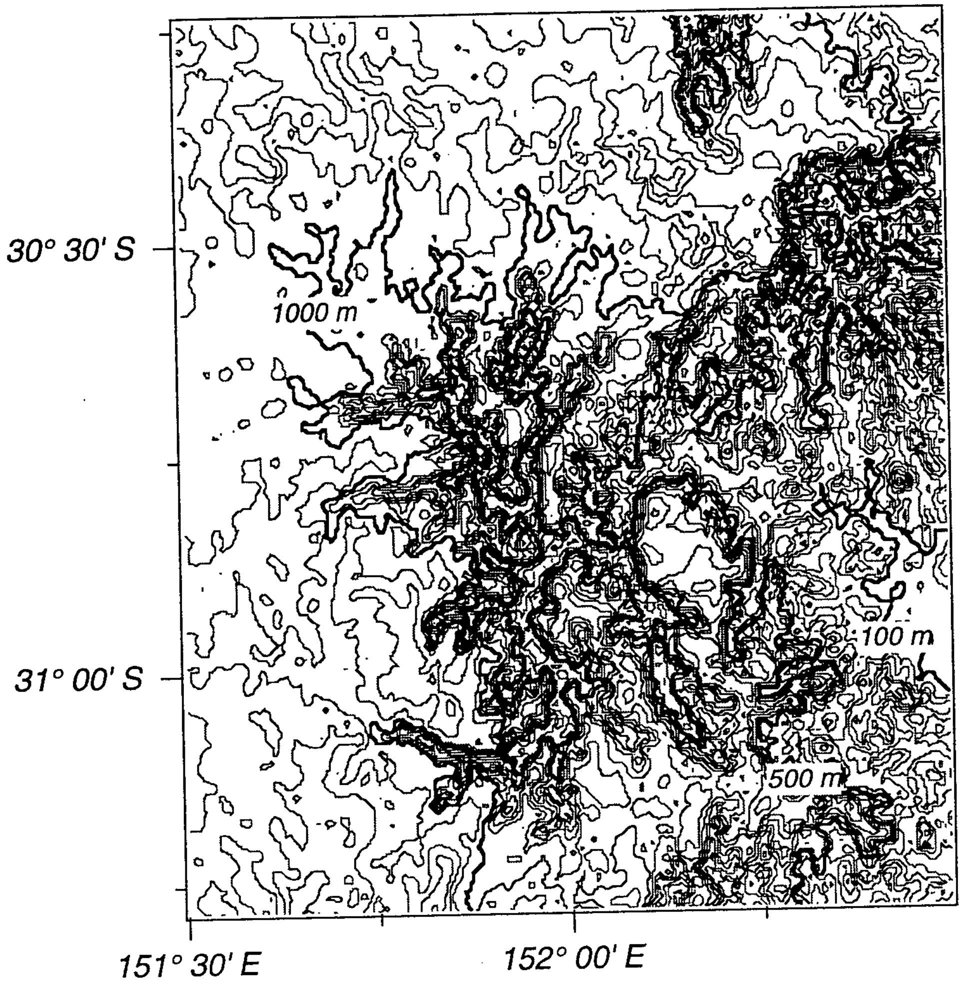

B.

A. Contour map of the MSDS in dashed box 1 of Figure 1. B. 1:250,000 scale contour map of the MacLeay River incising the ment along the Australian Tablelands, southeast Australia (vicinity of 30° S, 152° E). Both maps have a contour interval of 100 m, and approximately the same square kilometer area. But relief along the California margin is 3000 m, while that along the Tablelands escarpment is only 400–600 m.

ity of contours in the map of the MSDS is greatest the mid to upper continental slope, where the re- al seafloor gradient is steepest.

his distinction between the two types of drainage ms highlights a major difference between channel ation and drainage development in subaerial and marine environments. On land, channels are carved nning water, the erosive power of which is related scharge and controlled by drainage area (Howard, the more water, the greater the erosion of chan- Beneath the sea, channels are carved by failure- nced subaqueous sediment flows, which initiate and e their erosive power as a consequence of local e: the steeper the slope, the more likely slope fail- leading to sediment flows and the erosion of channels. Devising morphometric techniques to detect the type of drainage network differences seen between the MSDS and the MacLeay River remains a central problem in quantitative fluvial geomorphology (Kirchner, 1993). The same problem now confronts marine geologists attempting to gain insight on subaqueous sedimentary processes through quantitative studies of submarine canyon, channel and drainage system morphology using gridded multibeam bathymetry.

Applied Uses for Drainage Extraction

Keeping the limitations of drainage extraction in mind, there are a number of ways these algorithms can be

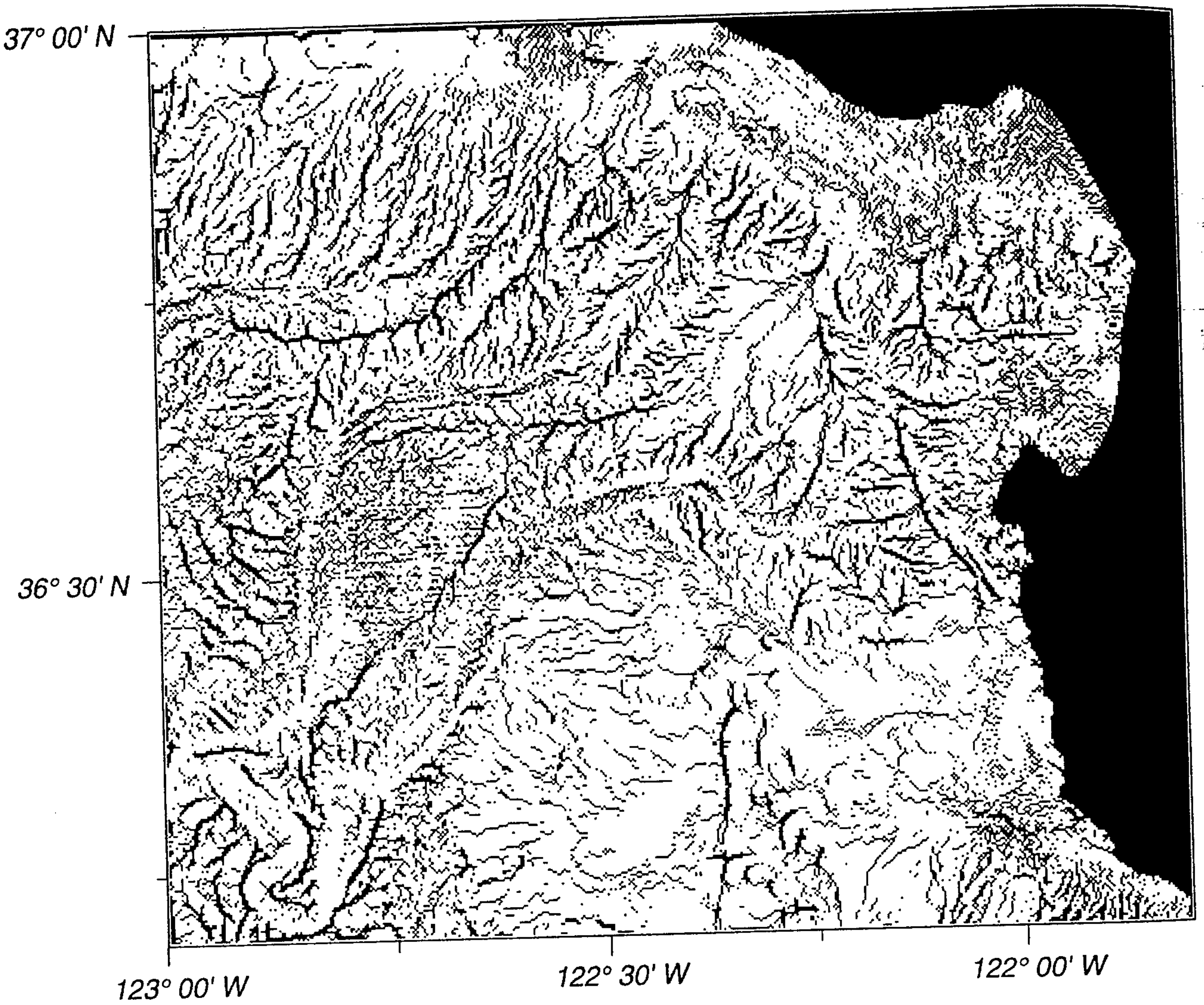

Fig. 10A.

used to analyze gridded bathymetry for both applied and academic interests in seafloor morphology. In terms of applied research, one of the benefits of drainage extraction is that in addition to mapping drainage networks, drainage divides can also be mapped. By setting the flow accumulation threshold equal to zero, it is possible to isolate all grid cells that do not receive input from other cells (Figure 10A). In other words, these cells are relative topographic highs. Such a map could be particularly useful in charting locations which minimize risks to offshore communication cables, hazardous waste disposal sites, or piping from marine oil production platforms.

The drainage extracted from gridded bathymetry can also be used to help interpret side-scan sonar imagery from the same region (Figure 10B). If drainage extracted from the bathymetry is overlain onto the side-scan sonar imagery, it's possible to map sediment pathways hard to detect in the side-scan imagery alone.

Finally by merging gridded bathymetry with gridded topography, drainage extraction algorithms can be used to map drainage areas and sediment pathways from land to sea. With such information, source areas of deep-sea depocenters, such as submarine fans, can be quantified. Additionally, if deep-sea sedimentation rates and denudation rates on land are known, it should be possible to estimate how erosion of a continental margin balances against the development of a submarine fan.

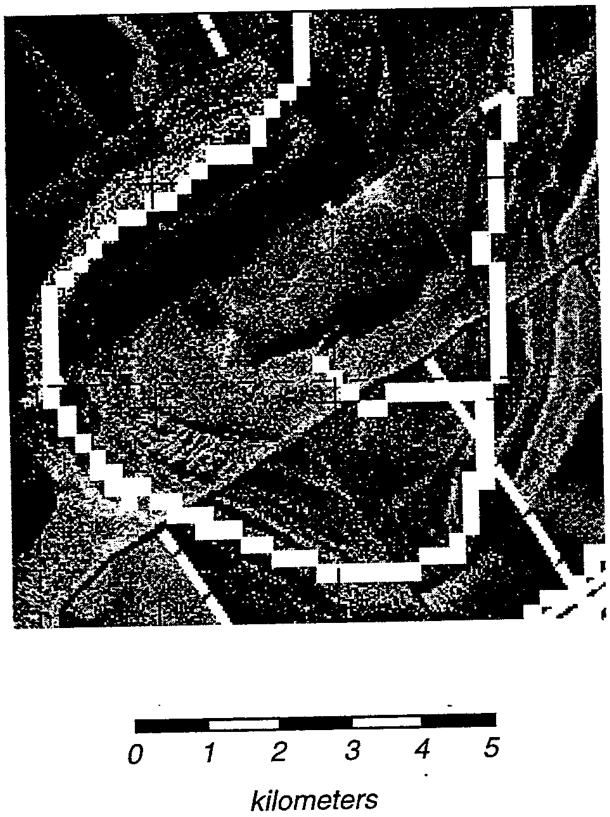

Fig. 10B.

Fig. 10. Examples of other uses for drainage extraction algorithms. A. Relative highs, or peaks and ridges (black areas within white region) extracted from the gridded bathymetry of the Monterey, California margin by setting the flow accumulation threshold to zero. B. Thalweg of the Shepard Meander in Monterey deep-sea channel (lower left in box I of Figure 1) extracted from the bathymetric grid and overlain on top of 30 kHz sidescan sonar imagery of the same region.

Conclusions

Although already frequently used in hydrologic and geomorphic studies of landscapes, automated drainage extraction algorithms represent a new tool for the analysis of submarine sediment pathways documented in gridded bathymetry. Using local seafloor slopes, the algorithms can rapidly define the paths of submarine canyons and deep-sea channels, and delineate the source areas from which they derive sediment.

The principal limitations of the algorithms are twofold: The first is that the algorithms assign all drainage in each grid cell to flow in the direction of steepest descent to a neighboring grid cell. This assignment excludes the possibility of flow divergence, preventing mapping of braided and distributary channel geometries. Recent experiments (e.g., Moglen *et al.*, 1993) suggest use of multiple flow directions, in which flow from each grid cell is partitioned among lower, neighboring cells as a function of slope, should help correct this inadequacy.

More problematic is the second limitation, which is that the algorithms map channelways based not on channel morphology, but on the area of the grid (i.e., support area) each cell "drains". Drainage area does appear to be an important factor in subaerial channel development (Hack, 1957), but slope failure by oversteepening may be more important in submarine channel development. As a consequence, submarine channel definition using a support area threshold can fail to map the heads of submarine channels with relatively small upslope areas, while erroneously mapping channels on uneroded seafloor slopes with relatively large upslope areas (Figure 5).

In the geomorphic comparison of the MSDS with fluvial drainage systems, an objective criteria meant to minimize these mapping errors is used to select support area thresholds appropriate for individual drainage basins depicted in DEMs. The comparison shows that inaccuracies in channel networks defined by automated drainage extraction are compounded by DEM resolution, which while only having a minor influence on the measurement of drainage area, limits the extent to which channels within a drainage area can be resolved. The comparison also illustrates, that even without inaccuracies, difficulty exists in quantifying submarine drainage morphology for lack of geomorphic measures that can characterize distinctive channel network attributes.

Despite their present limitations, drainage extraction algorithms have the potential to be a useful tool in seafloor mapping. They can already be used to isolate bathymetric ridges (grid cells with zero flow accumulation), a capability that would be helpful in determining seafloor locations where risks of hazards to offshore communication cables, waste disposal sites, and piping from offshore hydrocarbon production platforms are minimized. The future challenge lies in not only improving the mapping capabilities of drainage extraction, but in exploring new ways to gain geologic insight from the morphologic information the algorithms already provide.

Acknowledgements

The authors wish to thank R. Hesse and two anonymous reviewers for their reviews of the original manuscript, which led to its improvements. We also thank

M. Lockwood and P. Grim for providing us with the bathymetry used in this study. The study was supported by the Office of Naval Research (Contract Nos. N0014-87-K-0204 and 00014-93-1-0126) and the National Science Foundation (Grant No. OCE 89-12241). This is Lamont-Doherty Earth Observatory Publication No. 5475.

References

Abrahams, A. D. and Flint, J.-J., 1983, Geological Controls on the Topological Properties of Some Trellis Channel Networks, *Geol. Soc. Am. Bull.* **94**, 80–91.

Bellaiche, G., Orsolini, P., Petit-Perrin, B., Berthon, J.-L., Ravenne, C., Coutellier, V., Droz, L., Aloisi, J.-C., Got, H., Mear, Y., Monaco, A., Auzende, J.-M., Beuzart, P. and Monti, S., 1983, Morphologie au Sea-Beam de l'eventail sous-marin profound du Rhone (Rhone dep-sea fan) et de son canyon afferent: *Comptes Rendus Academie des Sciences de Paris*, serie II, **296**, 579–583.

Bowden, K. L. and Wallis, J. R., 1964, Effect of Stream-Ordering Technique on Horton's Laws of Drainage Composition, *Geol. Soc. Am. Bull.* **75**, 767–774.

Broscoe, A. J., 1959, Quantitative Analysis of Longitudinal Stream Profiles of Small Watersheds, *Office of Naval Research, Project NR 389-042, Technical Report No.* **18**, (Dept. Geol., Columbia University, New York).

Burbank, D. W., 1992, Causes of Recent Himalayan Uplift Deduced from Deposited Patterns in the Ganges Basin, *Nature* **357**, 680–683.

Chorley, R. J., 1957, Illustrating the Laws of Morphometry, *Geological Magazine* **94**, 140–150.

Chorley, R. J., Schumm, S. A. and Sugden, D. E., 1984, *Geomorphology* (Metheun, London, 605 pp.).

Cox, K. G., 1989, The Role of Mantle Plumes in the Development of Continental Drainage Patterns, *Nature* **342**, 873–877.

Damuth, J. E., Kolla, V., Flood, R. D., Kowsmann, R. O., Monteiro, M. C., Gorini, M. A., Palma, J. J. C. and Belderson, R. H., 1983, Distributary Channel Meandering and Bifurcation Patterns on the Amazon Deep-Sea Fan as Revealed by Long-Range Side-Scan Sonar (GLORIA), *Geology* **11**, 94–98.

Daniel, J. R. K., 1981, Drainage Density as an Index of Climatic Geomorphology, *J. Hydrol.* **50**, 147–154.

Dietrich, W. E., Wilson, C. J., Montgomery, D. R. and McKean, J., 1993, Analysis of Erosion Thresholds, Channel Networks, and Landscape Morphology Using a Digital Terrain Model, *J. Geol.* **101**, 259–278.

Dunne, T., 1980, Formation and Controls of Channel Networks, *Progress in Physical Geography* **4**, 211–239.

Easterbrook, D. J., 1993, *Surface Processes and Landforms* (Macmillan, New York, 520 pp.).

Gregory, K. J., 1976, Drainage Networks and Climate, in Derbyshire, E. (ed.), *Geomorphology and Climate* (John Wiley, New York, 520 pp.).

Grim, P., 1992, Dissemination of NOAA/NOS EEZ Multibeam Bathymetric Data, in Lockwood, M. (ed.), 1991 Exclusive Economic Zone Symposium; Working Together in the Pacific EEZ, Portland, Oregon, *Proceedings, U.S. Geol. Survey Circular No.* **1092**, 102–109.

Hack, J. T., 1957, Studies of Longitudinal Stream Profiles in Virginia and Maryland, *U.S. Geol. Survey Prof. Paper* **294-B**, 45–97.

Hess, R. and Normark, W. R., 1976, Holocene Sedimentation History of the Major Fan Valleys of Monterey Fan, *Mar. Geol.* **22**, 233–251.

Hesse, R., 1989, "Drainage Systems" Associated with Mid-Ocean Channels and Submarine Yazoos; Alternative to Submarine Fan Depositional Systems, *Geology* **17**, 1148–1151.

Horton, R. E., 1945, Erosional Development of Streams and Their Drainage Basins: Hydrophysical Approach to Quantitative Morphology, *Geol. Soc. Am. Bull.* **56**, 275–370.

Howard, A. D., 1980, Thresholds in River Regimes, in Coates, D. R. and Vitek, J. D. (eds.), *Thresholds in Geomorphology* (Allen and Unwin, Boston).

Jenson, S. K. and Dominique, J. O., 1988, Extracting Topographic Structure from Digital Elevation Data for Geographic Information System Analysis, *Photogrammetric Engineering and Remote Sensing* **54**, 1593–1600.

Jenson, S. K., 1991, Applications of Hydrologic Information Automatically Extracted from Digital Elevation Models, *Hydrologic Processes* **5**, 31–44.

Judson, S. and Kaufman, M. E., 1990, *Physical Geology* (Prentice-Hall, Englewood Cliffs, 534 pp.).

Kirchner, J. W., 1993, Statistical Inevitability of Horton's Laws and the Apparent Randomness of Stream Channel Networks, *Geology* **21**, 591–594.

McHugh, C. M., Ryan, W. B. F. and Hecker, B., 1992, Contemporary Sedimentary Processes in the Monterey Canyon-Fan System, *Mar. Geol.* **107**, 35–50.

Menke, W., Friberg, P., Lerner-Lam, A., Simpson, D., Bookbinder, R. and Karner, G., 1991, Sharing Data Over Internet with the Lamont View-Sharer System, *EOS, Trans. Am. Geophys. Union* **72**, 409–414.

Milton, L. E., 1966, The Geomorphic Irrelevance of Some Drainage Net Laws, *Australian Geographical Studies* **4**, 89–95.

Moglen, G. E., Bras, R. L. and Ijjasz-Vasquez, E. J., 1993, Modelling Hillslope Evolution Within a Basin – Evidence for Using Multiple Flow Directions and Erosion Thresholds (abs.), *EOS, Trans. Am. Geophys. Union* **74**, 152.

Montgomery, D. R. and Dietrich, W. E., 1988, Where Do Channels Begin? *Nature* **336**, 232–234.

Moore, I. S., Grayson, R. B. and Ladson, A. R., 1991, Digital Terrain Modeling; A Review of Hydrological, Geomorphological and Biological Applications, *Hydrological Processes* **5**, 3–30.

Morisawa, M. E., 1962, Quantitative Geomorphology of Some Watersheds in the Appalachian Plateau, *Geol. Soc. Am. Bull.* **73**, 1025–1046.

NOAA, 1988a, Pioneer Canyon Bathymetric Grid, N370123W.

NOAA, 1988b, Guide Seamount Bathymetric Grid, N365123W.

NOAA, 1988c, Monterey Canyon Bathymetric Grid, N365121W.

NOAA, 1988d, Monterey Fan Bathymetric Grid, N360123W.

NOAA, 1988e, Shepard Meander Bathymetric Grid, N360122W.

NOAA, 1988f, Point Sur Bathymetric Grid, N360121W.

NOAA, 1988g, Davidson Seamount Bathymetric Grid, N355122W.

Normark, W. R. and Gutmacher, C. E., 1988, Sur Submarine Slide, Monterey Fan, Central California, *Sedimentology* **35**, 629–647.

O'Callaghan, J. F. and Mark, D. M., 1984, The Extraction of Drainage Networks from Digital Elevation Data, *Computer Vision, Graphics and Image Processing* **28**, 323–344.

Ollier, C., 1981, *Tectonics and Landforms* (Longman, London, 324 pp.).

Pratson, L. F. and Ryan, W. B. F., 1992, Application of Drainage Extraction to NOAA Gridded Bathymetry of the U.S. Continental

Margin, in Lockwood, M. (ed.), 1991 Exclusive Economic Zone Symposium; Working Together in the Pacific EEZ, Portland, Oregon, *Proceedings, U.S. Geol. Survey Circular No.* **1092**, 110–117.

atson, L. F., 1993, *Morphologic Studies of Submarine Sediment Drainage* (Ph.D. Dissertation, Columbia University, New York, 107 pp.).

atson, L. F. and Ryan, W. B. F., 1994, Infilling and Subsidence of Intraslope Basins Offshore Lousiana; Overprinting of Sediment Drainage by Salt Tectonics, *Am. Assoc. Pet. Geol. Bull.* **78**, 1483–1506.

ess, F. and Siever, R., 1986, *Earth* (W. H. Freeman, San Francisco, 656 pp.).

tter, D. F., 1986, *Process Geomorphology* (W. C. Brown, Dubuque, 579 pp.).

hlee, J. S. and Robb, J. M., 1991, Submarine Processes of the Middle Atlantic Continental Rise Based on GLORIA Imagery, *Geol. Soc. Am. Bull.* **103**, 1090–1103.

humm, S. A., 1956, Evolution of Drainage Systems and Slopes in Badlands at Perth Amboy, New Jersey, *Geol. Soc. Am. Bull.* **67**, 597–646.

epard, F. P. and Dill, R. F., 1966, *Submarine Canyons and Other Sea Valleys* (Rand McNally, Chicago, 381 pp.).

Smart, J. S., 1978, The Analysis of Drainage Network Composition, *Earth Surface Processes* **3**, 129–170.

Smith, W. H. F. and Wessel, P., 1990, Gridding with Continuous Curvature Splines in Tension, *Geophysics* **55**, 293–305.

Strahler, A. N., 1952a, Dynamic Basis of Geomorphology, *Geol. Soc. Am. Bull.* **63**, 923–938.

Strahler, A. N., 1952b, Hypsometric (Area-Altitude) Analysis of Erosional Topography, *Geol. Soc. Am. Bull.* **63**, 1117–1142.

Summerfield, M. A., 1991, *Global Geomorphology* (John Wiley & Sons, New York, 537 pp.).

Tarboton, D. G., Bras, R. L. and Rodriguez-Iturbe, I., 1991, On the Extraction of Channel Networks from Digital Elevation Data, *Hydrological Processes* **5**, 81–100.

Tyce, R., 1986, Deep Seafloor Mapping Systems – A Review, *Mar. Tech. Soc. J.* **20**, 4–16.

Veatch, A. C. and Smith, P. A., 1939, Atlantic Submarine Valleys of the United States and the Congo Submarine Valley, *Geol. Soc. Am. Special Paper* **7**, 101 pp.

Weissel, J. K., Karner, G. D., Malinverno, A. and Harding, D. J., 1992, Tectonics and Erosion: Topographic Evolution of Rift Flanks and Rifted Continental Margins (abs.), Chapman Conference on Tectonics and Topography, Aug. 31–Sept. 4, Snowbird, Utah, Am. Geophys. Union, p. 31.

Introduction to Advances in Seafloor Mapping Using Sidescan Sonar and Multibeam Bathymetry Data

LINCOLN F. PRATSON[1]* and MARGO H. EDWARDS[2]

Lamont-Doherty Earth Observatory of Columbia University, Palisades, NY 10964 U.S.A.
Hawai'i Institute of Geophysics and Planetology, University of Hawai'i, Honolulu, HI 96822 U.S.A.
* *Now at the Institute of Arctic and Alpine Research, University of Colorado, Boulder, CO 80309 U.S.A.*

(Accepted 7 March 1996)

A Historical Perspective of Seafloor Mapping

Throughout history, humans have attempted to ascertain the shape and composition of the ocean floors (Emery and Uchupi, 1984). The vast size and depth of the oceans have hindered this endeavor, and it is only in the past 150 years that comprehensive maps of the seafloor and its major features, including mid-ocean ridges, seamounts, deep-sea trenches, and submarine canyons, have been generated (Maury, 1855; Heezen *et al.*, 1959).

This seafloor mapping has been undergoing a revolution driven by the invention and evolution of new imaging and navigation technologies for more than a quarter of a century now. Sidescan sonar, multibeam bathymetry, satellite altimetry and Global Positioning Satellite (GPS) navigation are at the forefront of an array of tools that enable the seafloor to be 'seen' at a greater level of detail than ever before. These technologies provide more than accurate and extensive measurements of seafloor depth; they also depict acoustic reflectance, key information for determining seafloor composition.

Vogt and Tucholke (1986) predicted that high resolution bathymetry and acoustic reflectance would be used in future seafloor mapping studies to: (1) quantify seafloor textures in different geomorphologic provinces; (2) detect and classify specific kinds of objects (e.g., fault scarps, lava fronts, etc.); (3) estimate acoustic properties and structures composing the shallow subbottom; and (4) search for temporal changes in bottom topography or texture as a result of bottom currents, slumping, or volcano-tectonic processes in dynamic areas such as plate boundaries and continental margins.

Well, the future is now, and the collection of papers assembled in this special issue of Marine Geophysical Researches on advances in seafloor mapping techniques exemplifies the research being conducted in these fields.

Advances in the Use of Sidescan Sonar and Multibeam Bathymetry

This special issue focuses on seafloor mapping and characterization using sidescan sonar and multibeam bathymetry data. Other technologies exist for mapping the seafloor, but sidescan sonar and multibeam bathymetry increasingly represent the most accurate, cost-effective, and consequently widely-used options for conducting regional-reconnaissance through high-resolution site surveys of the seafloor.

The subjects of how sidescan sonar and multibeam bathymetry systems work, their use in marine surveys, and techniques for data processing have been discussed in numerous scientific articles, including Grant and Schreiber (1990) and Searle *et al.* (1990), which appeared in an earlier special issue of *Marine Geophysical Researches* entitled 'Marine Geological Surveying and Sampling' (Hailwood and Kidd, 1990). Since the publication of these articles, new sonar systems have been introduced to the marine surveying community, including swath mapping systems that record both bathymetry and seafloor backscatter, such as the Simrad EM1000 discussed by Hughes-Clarke and others (this issue), and dual-frequency sidescan sonars, like the Klein system used in the study by Ryan and Flood (this issue). These new instruments represent important technological advances over original multibeam echo sounders and sidescan sonars. However, the emphasis of this issue of Marine Geophysical Researches is not on new instrumentation. Instead, the articles presented here describe new ways to create maps of the seafloor using both vintage and state-of-the-art sidescan sonar and multibeam bathymetry data.

Marine Geophysical Researches **18**: 601–605, 1996.

Data Processing and Enhancement

Most types of geophysical data require post-acquisition signal processing before they can be correctly interpreted; sidescan sonar and multibeam bathymetry data are no exception. Enhancement of sidescan sonar data is particularly critical, as geologic features depicted in the data will often remain obscured until they are revealed by processing techniques. Standard image processing algorithms such as contrast enhancement are an example but data processing is more than just image processing. It encompasses a spectrum of steps including corrections for environmental and instrument noise, merging data with navigation and other information, and display in various map and geometrical projections.

Hughes-Clarke *et al.* (this issue) describe aspects of data processing in a concise yet comprehensive review on the state-of-the-art use of shallow-water multibeam sonars to map the coastal zone and continental shelf – regions of increasing environmental and societal relevance. The authors discuss a variety of significant considerations when mapping in shallow water, including: instrument measurement resolution, the effect of positioning and ship-motion on depth measurement accuracy, water column effects (e.g., tides, fresh-salt water salinity and temperature gradients, etc.), and the quantitative derivation of acoustic backscatter measurements for use in seabed classification. They support their discussion with numerous illustrations, and conclude with examples of how multibeam sonars are being used in applied studies of the coastal environment.

For multibeam sonars used in deeper water, data processing has until recently been accomplished by the institutions responsible for operating the multibeam systems (e.g., Scripps Institution of Oceanography and the Northeast Consortium of Oceanographic Research at the University of Rhode Island). This has since changed with the introduction of a new, publicly available multibeam software package, *mbsystem*, written by Caress and Chayes (this issue). Their article on improved processing of Hydrosweep multibeam data on the R/V *Maurice Ewing* describes the *mbsystem* and shows how this software package empowers individual investigators with the tools (i) to process data from a variety of multibeam systems, (ii) to process the data to the level of their own needs, and (iii) to display the data in diverse ways, from its raw, individual-record form to a polished, processed grid.

Bird *et al.* (this issue) use multibeam bathymetry to enhance sidescan sonar imagery and improve its usefulness in geologic interpretations. All sidescan sonar systems suffer from signal over-saturation or 'clipping' in the nadir region due to the strong acoustic reverberation from the seafloor at vertical and near-vertical angles of incidence. This data loss is particularly acute in GLORIA sidescan sonar imagery because the width of the nadir region is so large (6–7 km) that it reduces the confidence with which geologic features can be correlated from one side of the swath to the other. Bird *et al.* (this issue) present a technique in which Hydrosweep multibeam bathymetry is used to construct pseudo-sidescan sonar imagery to replace the poor quality imagery in the GLORIA nadir band. They present an example where this integration technique proved an important aid in refining interpretations of the tectonic structure of an East Pacific Rise microplate.

Seabed Classification

One of the most active areas of research in the field of remote sensing is the development of automated techniques for classifying different terrains in remotely sensed data. The aim of this research is to have a computer segment an image into regions, or classes, that are distinct from one another. The potential benefits of automated terrain classification are attractive: it is objective, repeatable, fast, and quantitative. Yet in practice, the technique is difficult to implement. Along- and across-track variations in data quality, natural variations in the length-scales of the features being imaged, and ambiguities as to how image differences relate to real-world differences are among the factors that have challenged the development of robust terrain classification. Automated terrain classification remains an important goal in seafloor mapping, and the papers summarized below discuss three promising ways this goal may ultimately be achieved.

Keeton and Searle (this issue) build on work by Mitchell and Somers (1989) and Hughes-Clarke (1993, 1994), and examine variations in the level of seafloor backscatter strength to discriminate seabed differences. This approach departs from the often-attempted pattern recognition approach of segmenting a sidescan sonar image on the basis of statistical relations between neighborhoods of image elements (e.g., Pace and Gao, 1988; Reed and Hussong, 1989; Linnett *et al.*, 1993). Instead, Keeton and Searle (this issue) use co-registered bathymetry and sidescan sonar data to predict and remove from the sidescan imagery the backscatter component due to seafloor morphology. Ideally, the resulting imagery is a measurement of variations in acoustic backscatter strength as a function of incidence angle. This variation can be different for different bottom types, and thus can potentially be used to automatically classify compositional changes in the seabed, as Keeton and Searle (this issue) attempt using Simrad EM12 data of the Mid-Atlantic Ridge.

Another approach for identifying and mapping compositional changes in the seabed is to acquire sonar data at two acoustic frequencies (Ryan and Flood, this issue). The important advantage of this approach is that, if collected simultaneously and in an identical fashion (i.e., identical gain functions, etc.), all of the factors that influence one sonar frequency (attenuation, seafloor slope, bottom type, etc.) influence the other. This means that the relative acoustic backscatter strength of the imagery, rather than the absolute backscatter strength sought by Keeton and Searle (this issue), can be used to quantitatively detect changes in bottom type. That is, any differences in the imagery at the two frequencies are directly related to differences in the acoustic response of the seabed, which is often determined by bottom type. The satellite remote sensing community has exploited similar differences in the wavelengths of sunlight backscattered from the Earth's surface to distinguish vegetation type, soil type, and other terrain attributes (e.g., Sabins, 1978 and references therein). Ryan and Flood (this issue) demonstrate that multi-frequency sidescan sonar data may yield comparable successes in automatically distinguishing bottom sediment type in marine and fluvial environments.

Both of the above approaches to seabed classification exploit acoustic backscatter variations recorded in sidescan sonar imagery. A third approach, presented by Fox (this issue), characterizes seafloor terrains on the basis of topographic variations measured in multibeam bathymetry. Fox and Hayes (1985) were the first to document with power spectral methods that different types of seafloor terrains exhibit different roughness characteristics. They also recognized these differences could potentially be used to classify seafloor bottom types. Fox (this issue) extends his model for calculating power spectra of seafloor topography from one to two dimensions, and explores how measures of the critical parameters in the model (isotropic and anisotropic roughness, the orientation of the latter, and spectral roll-off) vary among two adjacent, visually-distinct mid-ocean ridge terrains. Fox (this issue) then demonstrates how different terrains can be defined and mapped on the basis of natural groupings of these measures determined using clustering algorithms. He concludes by exercising his classification scheme on a bathymetric grid of the variable terrain within the Juan de Fuca Ridge, comparing his results to existing geologic interpretations of the same area.

Seafloor Feature Extraction

The distinction between seafloor characterization and seafloor feature extraction is subtle but definite. As noted above, the aim of seafloor characterization is to subdivide an entire image into classes that possess unique sets of image attributes. The processing sequence for characterization is to define differences within an image, and then determine the geological significance of the differences. Contrastingly, the aim of seafloor feature extraction is to delineate specific features within an image. In this case, the processing sequence is reversed. First, an assumption is made as to how a certain feature (e.g., a fault) will appear in an image. Then, this assumption is used to isolate and extract only those parts of the image that meet the assumption criteria.

Mitchell (this issue) presents new processing and analysis techniques for working with Simrad EM1000 (shallow water) and EM12 (deep water) multibeam sonars. His analysis technique for computing measurements of seafloor slope, azimuth and particularly curvature from the bathymetric data lends itself to seafloor feature extraction. Mitchell (this issue) argues that many geologic features, such as abyssal hills, seamounts, and iceberg scours, have a curvature that is parabolic in shape. This curvature can be quantified by the coefficients of a paraboloid fit to circular groupings of soundings. The coefficients indicate whether the fitted paraboloid is concave upward or downward, to what degree it is elongated, and in what direction it is elongated. Mitchell (this issue) uses these coefficients to construct a simple geologic classification map from EM1000 data. He combines the coefficients with the other seafloor attributes measured by his analysis technique, including variations in acoustic backscattering strength, to produce from an example data set a map of sediment ponds, ridges, and troughs.

Little and Smith (this issue) present a direct application of feature extraction, the mapping of faults in mid-ocean ridge terrains. Studies of fault spacing, density, azimuth, length, and the direction in which faults face (towards or away from the ridge) have been used to understand processes of seafloor formation and modification at mid-ocean ridges, including the width of active fault formation, the generation of abyssal hills, plate kinematics, along-strike plate segmentation, and asymmetric ridge subsidence (e.g., Edwards *et al.*, 1991). The detailed and extensive mapping of faults required for these purposes can be exhausting when done by hand, and feature extraction offers a way of automating the task. Shaw (1992) and Shaw and Lin (1993) located fault scarps in Seabeam bathymetry data by fitting a quadratic surface to the data. Little and

Smith (this issue) develop a new approach for fault extraction that is based on wavelet theory and is capable of extracting faults from both multibeam bathymetry and sidescan sonar imagery. The authors use the technique to extract fault attributes from TOBI Sidescan sonar imagery and Seabeam bathymetry of the same seafloor swath, comparing their results to a human geologic interpretation of these data.

While seafloor feature extraction techniques have proved powerful aids in studies of mid-ocean ridges, they have not been used much in studies of continental margins. One reason for this may be the rarity of comprehensive sidescan sonar and bathymetry data sets available to adequately map features important in continental margin evolution, for example submarine canyons, which vary considerably in location, frequency, size and spacing. This situation has changed with the extensive sidescan sonar and multibeam bathymetry that has been collected of the U.S. Exclusive Economic Zone by the U.S. Geological Survey and the National Oceanic and Atmospheric Administration. Pratson and Ryan (this issue) take advantage of the NOAA multibeam bathymetry of Monterey Bay, California, to explore the utility of drainage extraction algorithms in automatically mapping submarine canyons, deep-sea channels, and their associated submarine drainage areas. These algorithms were originally developed by geomorphologists to aid in mapping terrestrial river networks and watersheds using gridded topography. Pratson and Ryan (this issue) test the mapping accuracy of the algorithms, and then attempt to use them in a morphologic comparison of the similitude between river networks and the networks of submarine canyons and deep-sea channels draining the floor of Monterey Bay.

Snapshot of a Rapidly Evolving Field

The papers assembled in this issue represent a snapshot of what can now be accomplished with sidescan sonar imagery and multibeam bathymetry to effectively strip away ocean waters and reveal the seabed. Like seafloor mapping instruments, the processing and analysis of sidescan sonar and multibeam bathymetry continues to evolve rapidly. At the time that this special issue becomes available, the subset of practitioners that contributed papers have moved beyond the work represented here. They and others are already engaged in developing new ways of enhancing and analyzing sidescan sonar and multibeam bathymetry data for the same purpose that drove our predecessors – to learn what lies beneath the seas.

Acknowledgements

We would like to express our sincere thanks to the authors for their significant contributions toward bringing this special issue to fruition, and their saintly patience in waiting to see their efforts in print. The participation of L. Pratson as an editor was made possible through funds from Office of Naval Research (ONR) contract 00014-93-1-0126. This is Lamont-Doherty Earth Observatory publication 5481.

References

Bird, R. T., Searle, R. C., Paskevich, V. and Twichell, D. C., 1996, Merged GLORIA Sidescan and Hydrosweep Psuedo-Sidescan Processing and Creation of Digital Mosaics, in Pratson, L. F. and Edwards, M. (eds.), *Advances in Seafloor Mapping Using Sidescan Sonar and Multibeam Bathymetry Data, Mar. Geophys. Res.* **18**, 651–661 (this issue).

Caress, D. W. and Chayes, D. N., 1996, Improved Processing of Hydrosweep DS Multibeam Data on the R/V *Maurice Ewing*, in Pratson, L. F. and Edwards, M. (eds.), *Advances in Seafloor Mapping using Sidescan Sonar and Multibeam Bathymetry Data, Mar. Geophys. Res.* **18**, 631–649 (this issue).

Edwards, M. H., Fornari, D. J., Malinverno, A., Ryan, W. B. F. and Madsen, J., 1991, The Regional Tectonic Fabric of the East Pacific Rise from 12°50′ N to 15°10′ N, *J. Geophys. Res.* **96**, 7995–8017.

Emery, K. O. and Uchupi, E., 1984, *The Geology of the Atlantic Ocean*, New York, Springer-Verlag, 1050 pp.

Fox, C. G. and Hayes, D. E., 1985, Quantitative Methods for Analyzing Roughness of the Seafloor, *Rev. of Geophys.* **23**, 1–48.

Fox, C. G., 1996, Objective Classification of Oceanic Ridge-Crest Terrains Using Two-Dimensional Spectral Models of Bathymetry: Application to the Juan de Fuca Ridge, in Pratson, L. F. and Edwards, M. (eds.), *Advances in Seafloor Mapping Using Sidescan Sonar and Multibeam Bathymetry Data, Mar. Geophys. Res.* **18**, 707–728 (this issue).

Grant, J. A. and Schreiber, R., 1990, Modern Swathe Sounding and Sub-Bottom Profiling Technology for Research Applications: The Atlas Hydrosweep and Parasound Systems, in Hailwood, E. A. and Kidd, R. B. (eds.), *Marine Geological Surveying and Sampling, Mar. Geophys. Res.* **12**, 9–19.

Hailwood, E. A. and Kidd, R. B., 1990, *Marine Geological Surveying and Sampling, Mar. Geophys. Res.* **12**, 168 pp.

Heezen, B. C., Tharp, M. and Ewing, M., 1959, *The Floors of the Oceans, I. The North Atlantic, Geol. Soc. Am. Spec. Paper* **65**, 122 pp.

Hughes Clarke, J. E., 1993, The Potential for Seabed Classification Using Backscatter from Shallow Water Multibeam Sonars, *Proc. Inst. Acoust., Acoustic Classification and Mapping of the Seabed* **15**, 381–388, Bath, U.K., April, 1993.

Hughes Clarke, J. E., Mayer, L. A. and Wells, D. E., 1996, Shallow-Water Imaging Multibeam Sonars: A New Tool for Investigating Seafloor Processes in the Coastal Zone and on the Continental Shelf, in Pratson, L. F. and Edwards, M. (eds.), *Advances in Seafloor Mapping using Sidescan Sonar and Multibeam Bathymetry Data, Mar. Geophys. Res.* **18**, 607–629 (this issue).

Keeton, J. A. and Searle, R. C., 1996, Analysis of Simrad EM12 Multibeam Bathymetry and Acoustic Backscatter Data for Seafloor Mapping, Exemplified at the Mid-Atlantic Ridge at 45° N, in Pratson, L. F. and Edwards, M. (eds.), *Advances in Seafloor Mapping Using Sidescan Sonar and Multibeam Bathymetry Data, Mar. Geophys. Res.* **18**, 663–688 (this issue).

Linnett, L. M., Clarke, S. J., Reid, C. St. J. and Tress, A. D., 1993, Monitoring of the Seabed Using Sidescan Sonar and Fractal Processing, *Proc. Inst. Acoust., Acoustic Classification and Mapping of the Seabed*, **15**, 381–388, Bath, U.K., April, 1993.

Little, S. A. and Smith, D. K., 1996, Fault Scarp Identification in Side-Scan Sonar and Bathymetry Images from the Mid-Atlantic Ridge Using Wavelet-Based Digital Filters, in Pratson, L. F. and Edwards, M. (eds.), *Advances in Seafloor Mapping Using Sidescan Sonar and Multibeam Bathymetry Data, Mar. Geophys. Res.* **18**, 741–755 (this issue).

Maury, M. F., 1855, *The Physical Geography of the Sea*, New York, Harper and Brothers, 287 pp.

Mitchell, N. C. and Somers, M., 1989, Quantitative Backscatter Measurements with a Long-Range Sidescan Sonar, *IEEE J. Ocean. Eng.* **14**, 368–374.

Mitchell, N. C., 1996, Processing and Analysis of Simrad Multibeam Sonar Data, in Pratson, L. F. and Edwards, M. (eds.), *Advances in Seafloor Mapping Using Sidescan Sonar and Multibeam Bathymetry Data, Mar. Geophys. Res.* **18**, 729–739 (this issue).

Pace, N. G. and Gao, H., 1988, Swathe Seabed Classification: *IEEE J. Ocean. Eng.* **13**, 83–90.

Pratson, L. F. and Ryan, W. B. F., 1996, Automated Drainage Extraction in Mapping the Monterey Submarine Drainage System, California Margin, in Pratson, L. F. and Edwards, M. (eds.), *Advances in Seafloor Mapping Using Sidescan Sonar and Multibeam Bathymetry Data, Mar. Geophys. Res.* **18**, 757–777 (this issue).

Reed, T. B. and Hussong, D., 1989, Digital Image Processing Techniques for Enhancement and Classification of SeaMARC II Side-scan Sonar Imagery, *J. Geophys. Res.* **94**, 7469–7490.

Ryan, W. B. F. and Flood, R. D., 1996, Side-Looking Sonar Backscatter Response at Dual Frequencies, in Pratson, L. F. and Edwards, M. (eds.), *Advances in Seafloor Mapping Using Sidescan Sonar and Multibeam Bathymetry Data, Mar. Geophys. Res.* **18**, 689–705 (this issue).

Sabins, F. F., 1978, *Remote Sensing: Principles and Interpretation*, W. H. Freeman and Company, San Francisco, 426 pp.

Searle, R. C., Le Bas, T. P., Mitchell, N. C., Somers, M. L., Parson, L. M. and Patriat, P. H., 1990, GLORIA Image Processing: The State of the Art, in Hailwood, E. A. and Kidd, R. B. (eds.), *Marine Geological Surveying and Sampling, Mar. Geophys. Res.* **12**, 21–39.

Shaw, P. R., 1992, Ridge Segmentation, Faulting, and Crustal Thickness in the Atlantic, *Nature* **358**, 490–494.

Shaw, P. R. and Lin, J., 1993, Causes and Consequences of Variations in Faulting Style at the Mid-Atlantic Ridge, *J. Geophys. Res.* **98**, 21,839–21,851.

Vogt, P. R. and Tucholke, B. E., 1986, Imaging the Ocean Floor; History and State of the Art, in *The Western North Atlantic Region, in the Collection, The Geology of North America*, Geol. Soc. Am., Boulder, 19–44.

Vhat is the slope of the U.S. continental slope?

ncoln F. Pratson
illiam F. Haxby
Lamont-Doherty Earth Observatory of Columbia University, Palisades, New York 10964

BSTRACT

Extensive high-resolution, multibeam bathymetry of five U.S. ntinental margins provides new, detailed information about the ngle of continental slopes in different sedimentary and tectonic ttings. The steepest continental slope examined is the passive-rbonate west Florida slope (4.4° regional slope and 12.0° mean cal slope). The steepest of the four clastic continental slopes is the assive New Jersey–Maryland slope (2.5° and 7.6°). Less steep, at oth regional and local scales, are the more rugged, tectonically ctive and probably unstable salt-tectonized Louisiana slope (0.5° nd 2.9°), strike-slip California slope (1.8° and 5.2°) and convergent regon slope (2.0° and 5.2°). Frequency grids of local slope magtude vs. depth and dip direction for the two passive continental opes reflect present-day morphology predominantly being shaped y lithology (west Florida), sedimentation (New Jersey–Maryland), nd downslope-directed erosion (New Jersey–Maryland, west Florida). The grids for the three tectonically active continental slopes eflect morphology partly (California) to predominantly (Louisiana, Oregon) being shaped by tectonics.

NTRODUCTION

Due to a historic lack of bathymetric data, variabilities in connental slope grade have never been thoroughly documented. As a esult, process-oriented (e.g., Parker et al., 1986), slope-stability .g., Delinger and Iverson, 1992), and educational (e.g., Kennett, 982; Press and Siever, 1986) literature has relied on miscellaneous, average" slope measurements largely made from seismic reflection rofiles when characterizing the angle of a continental slope.

Extensive multibeam bathymetric surveys have now mapped most of the New Jersey–Maryland, west Florida, Louisiana, Caliornia, and Oregon continental slopes (Fig. 1), detailing examples of ope morphology in passive-clastic, passive-carbonate, salt-tectonized, strike-slip, and convergent margin settings, respectively. We se these survey data to define the slope of these continental slopes t both local (<0.1 km^2) and regional (>1500 km^2 or whole study rea) scales, and to document variations in local slope angle with epth and dip direction. We then evaluate what these measurements reflect about the recent influence of sedimentation, erosion, lithology, and tectonism in shaping the various present-day ontinental slope morphologies.

DATA

The multibeam bathymetry data for the New Jersey, Maryland, nd west Florida margins were compiled by the Northeast Consorum for Oceanographic Research, and those for the Louisiana, Calornia, and Oregon margins were acquired by the National Oceanic nd Atmospheric Administration (NOAA). The data were collected sing the SeaBeam swath-mapping system (deMoustier, 1988), hich has a vertical resolution ≤1% water depth and, in the case of ne NOAA data, a position accuracy ≤50 m (Grim, 1992).

The survey data were used to construct bathymetric grids of the ve study areas (Fig. 1). The grids have a grid cell spacing of 100 m. Regional slope measures were calculated from the trend of the bestt plane to each grid (areas >1500 km^2). Local slope measures were alculated from the trend of the best-fit plane to each grid cell and s eight nearest neighbors (areas <0.1 km^2). Only depths between the shelf-slope break and the slope-rise break (i.e., depths on the continental slope) were used in the calculations.

RESULTS

Slope Histograms

Cumulative histograms show the total sea-floor area dipping at or *above* local slopes measured from each bathymetric grid (Fig. 2, col. I, A–E). The histograms exhibit a large primary peak and a small secondary peak. The secondary peaks are artifacts related to slight, inconsistent shoaling in the depth measurements at swath edges, caused by increased noise and/or minute errors in the sound-velocity correction (deMoustier, 1988). The artifacts, which increase the areal frequency of the local slope grades beneath the secondary peak 1%–3%, have no bearing on the results discussed below.

Excluding west Florida, the regional grades of the continental slopes (Fig. 2, I, A–E) are ≤2.5°, lower than the often cited "average" grade of 4° of Heezen et al. (1959). The histograms show local slopes to be strongly skewed toward low values. However, with the exception of the Louisiana slope, the cumulative histograms show that 50% of all local slopes are at least twice as steep as the regional slope. Mean local slopes are as much as six times steeper than the regional slope.

Slope-Depth Frequency Grids

Slope-depth frequency grids graph variations in local slope with increasing water depth (Fig. 2, II, A–E). Each grid is a vertical "waterfall" plot of histograms of local slope at 50 m depth intervals down the face of a continental slope. Each row in a grid is a single histogram of the local slopes within a 50 m depth interval. And each value in a histogram is the areal frequency of a local slope within that depth interval. For example, on the New Jersey–Maryland slope, ~10% of the study area between 450 and 500 m has a local slope of 7°–8°. Note that the slope-depth frequency grids exhibit distinctive trends in each continental slope setting.

Slope-Direction Frequency Grids

Slope-direction frequency grids graph variations in dip direction—ranging from upslope (0°) to downslope (180°)—with increasing local slope (Fig. 2, III, A–E). In this case, each grid is a horizontal "waterfall" plot of histograms of local slope dip direction at 1° intervals of slope angle. Each column in a grid is a histogram of the dip directions for a given angle. The dip directions are binned at 5° intervals. Each value in a histogram is the areal frequency a local slope dips within a 5° direction range. For example, on the New Jersey–Maryland slope, ~8% of the sea floor that is inclined downward at an angle of 25° dips along slope (90°–95°). Like the slope-depth frequency grids, the trend in each slope-direction frequency grid is distinctive.

DISCUSSION

The accuracy of slopes measured in this study is limited by (1) the resolution of the SeaBeam depth soundings (noted above); (2) the gridding, which interpolates depths between soundings; and (3) the horizontal length scales used in measuring the slopes, which limit the maximum computable slope for a set vertical change in elevation.

Despite these limitations, the slope measurements reveal mor-

Geology; January 1996; v. 24; no. 1; p. 3–6; 2 figures.

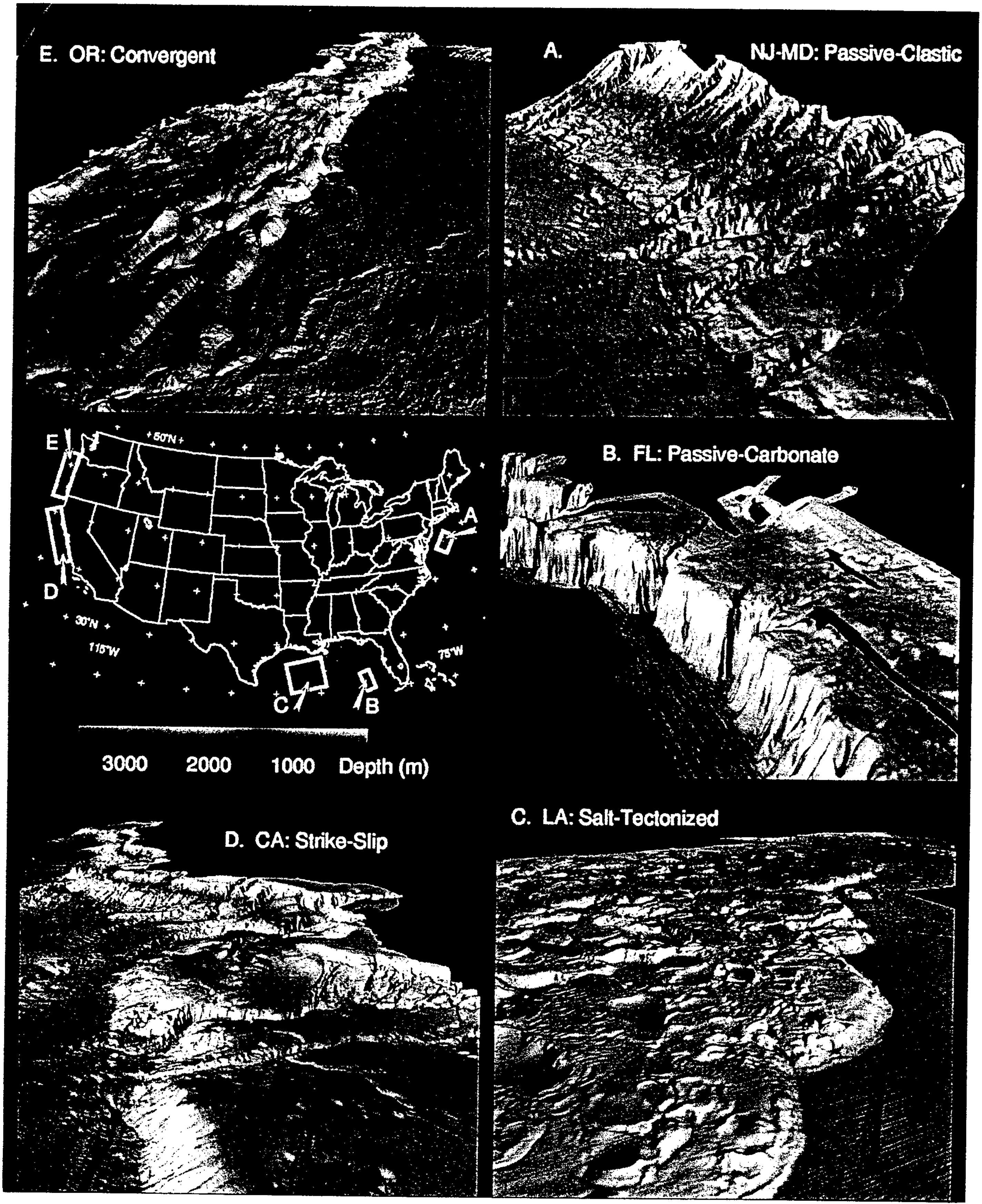

Figure 1. Center left: Map of United States showing areas (white boxes) examined in paper. Red areas within white boxes are regions depicted in perspective images. Arrows indicate viewing direction. Color scale and vertical exaggeration of 4:1 apply to all images. A: New Jersey–Maryland (NJ–MD); B: Florida (FL); C: Louisiana (LA); D: California (CA); E: Oregon (Or).

phologic differences among the five continental slopes beyond that seen in the bathymetric grids. These differences can be attributed to differences in the recent influence of tectonism, sedimentation, erosion, and lithology on the developing morphology of each continental slope.

New Jersey–Maryland: A Passive-Clastic Continental Slope

At both regional and local scales, the passive New Jersey–Maryland slope is steeper than the tectonically active and visually more rugged Oregon, California, and Louisiana slopes (Fig. 2, I, A). The greater steepness of the New Jersey–Maryland slope may be due to the region's relative stability. The other three clastic continental slopes are prone to frequent seismicity or salt movement, which promote slope failure, and thus may inhibit sedimentation and erosion from building comparably steep slope grades.

The slope-depth frequency grid (Fig. 2, II, A) shows that local sea-floor slopes tend to be steepest on the upper (<1500 m depth) rather than the lower New Jersey–Maryland slope. On the lower slope, lithified Eocene chalk crops out at or just beneath the sea floor (Robb et al., 1981). The upper slope is composed of semilithified to unconsolidated Tertiary to Quaternary muds that overlie the chalk. It is these more weakly lithified muds that tend to be steepest, suggesting this region may be predisposed to failure.

The slope-direction frequency (Fig. 2, III, A) grid reveals a transition from local slopes that are almost flat and tend to dip downslope, to steep slopes that tend to dip along slope. The former are predominantly in intercanyon areas, whereas the latter are predominantly along canyon walls, which dip perpendicular to the downslope strike of canyon floors. The slope-direction frequency grid thus reflects the region's lineated, canyon-intercanyon morphology formed by sedimentation and downslope-directed erosion.

West Florida: A Passive-Carbonate Continental Slope

Regional and local slopes are steepest on the west Florida slope (Fig. 2, I, B) due to its resistant carbonate lithology. The slope-depth frequency map (Fig. 2, II, B) shows that the west Florida slope is steepest below 1800 m, along the Florida Escarpment (mean incline ~31° over 470 km^2). However, with a mean regional grade of 2.9° (over 1050 km^2) the carbonate ramp above the escarpment is also steep.

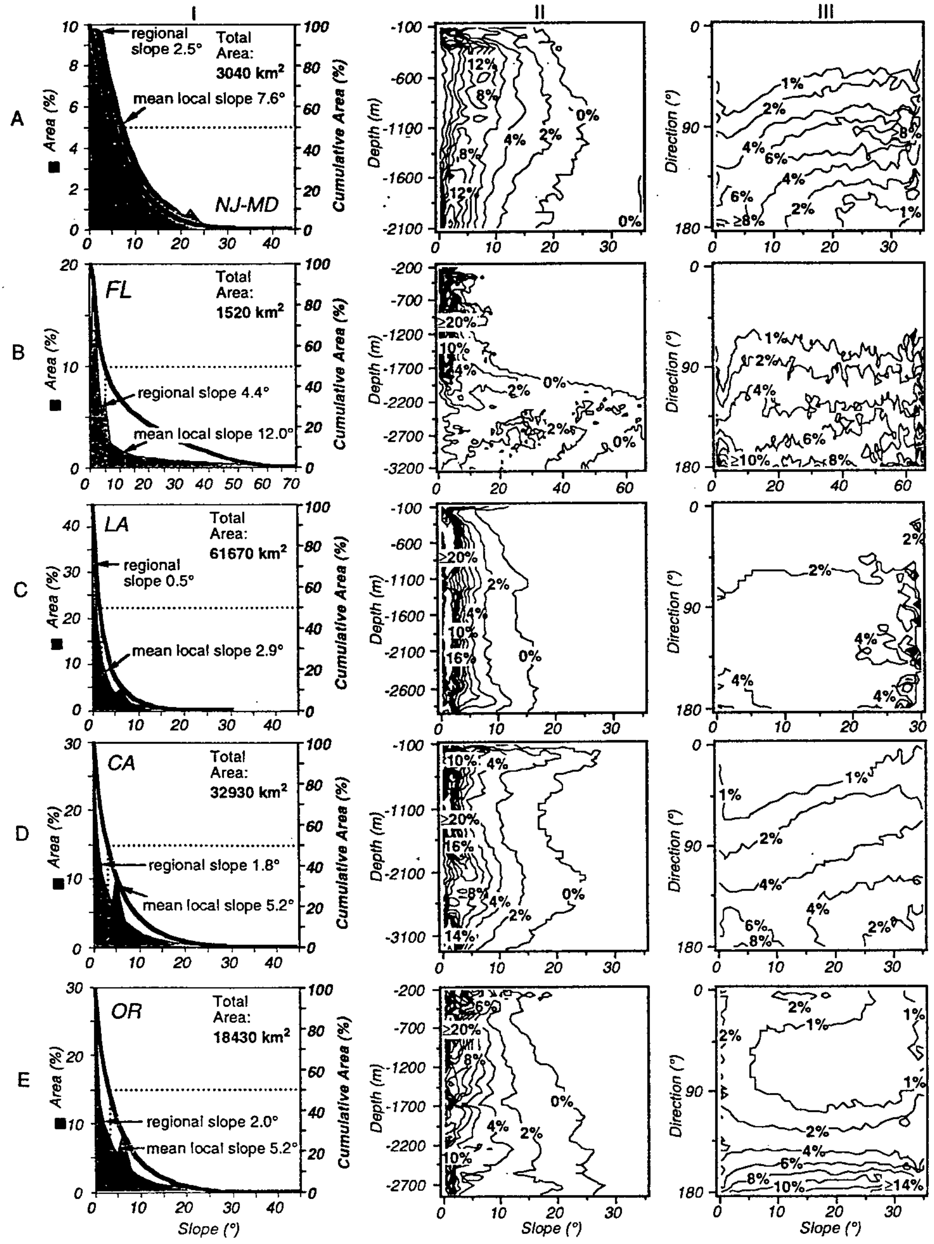

Figure 2. Slope measures of five study areas arranged in matrix. Rows: A—New Jersey-Maryland, B—west Florida, C—Louisiana, D—California, E—Oregon. Columns: I—slope histograms (gray) and cumulative histograms (black line); dashed lines are median local slopes; II—slope-depth frequency grids (see text for details); III—slope-direction frequency grids (see text for details).

The slope-direction frequency grid for the west Florida slope (Fig. 2, III, B) is highly variable. Although the greatest tendency of all local slopes is to dip downslope, they also commonly range in dip up to along-slope. This variability is caused by the many submarine canyons and chutes that gully the face and crest of the Florida Escarpment. The spacing of these features is apparently such that there is no clear transition between intercanyon and canyon wall areas, as there is in the New Jersey–Maryland slope-direction frequency grid (Fig. 2, III, A). This difference between the two passive continental slopes is in part due to lithology, but it also reflects differing degrees and styles of erosion. The west Florida slope has been undergoing net erosion, largely by slope failure (Paull et al., 1990). On the New Jersey–Maryland slope, erosion by both slope failures and sediment flows has been offset by deposition (Pratson et al., 1994).

Louisiana: A Salt-Tectonized Continental Slope

Regional and local slopes are lowest on the Louisiana slope (Fig. 2, I, C) despite a rugged terrain of numerous intraslope basins formed between, and often above, shallow to deeply buried allochthonous salt structures (Worral and Snelson, 1989). The seaward limit of these salt structures is marked by the 600–800 m drop at the edge of the Louisiana slope known as the Sigsbee Escarpment. Local slopes along both the escarpment and the intraslope basin walls can exceed 20°. However, on average, local slopes are about two or more times lower than on the other continental slopes.

The low grade of the Louisiana slope is undoubtedly tied to the allochthonous salt that underlies the region. The salt may not be competent enough to support steep sea-floor slopes, and/or being mobile, may frequently trigger slope readjustment through failure. Evidence for the latter is the numerous debris aprons at the base of the Sigsbee Escarpment (Twichell and DeLorey, 1995), where underlying allochthonous salt is thrusting basinward (Worral and Snelson, 1989).

Irregular salt movement is also a probable cause for the lack of any trend in the slope-direction frequency grid (Fig. 2, III, C), which indicates that unlike the other continental slopes, there is no directional bias to the Louisiana slope bathymetry. Salt tectonics appears to have randomized the seafloor.

California: A Strike-Slip Continental Slope

The California slope exhibits a mixture of New Jersey–Maryland and Oregon slope characteristics. The regional and mean local slopes for California (Fig. 2, I, D) are similar to those for Oregon (Fig. 2, I, E), as are the local slope histograms. The slope-direction frequency grid (Fig. 2, II, D) resembles that for the New Jersey–Maryland slope (Fig. 2, III, A). The trend, however, is more diffuse, with a broader range of slope grades tending to dip directly downslope. The slope-depth frequency grid (Fig. 2, II, D) shows that the upper California slope steepens like the New Jersey–Maryland slope (Fig. 2, II, A), but over only half the water depth. An additional, broader cycle of steepening occurs on the lower California slope, similar to Oregon (Fig. 2, II, E).

These characteristics suggest that the California slope has an intermediate morphology between that of the New Jersey–Maryland and Oregon slopes. Like the New Jersey–Maryland slope, the relatively oversteepened upper slope and downslope-lineated morphology indicated in the California slope-direction frequency grid reflect the influence of sedimentation and erosion. However, California's low regional and mean local slopes, and the apparent "bulging" of its lower continental slope (detected in the slope-depth frequency grid), are attributes shared by the Oregon slope, and appear to be tectonically induced.

Oregon: A Convergent Continental Slope

The similarities in the regional and local slopes (Fig. 2, I, D and E) between the strike-slip California slope and the convergent Oregon slope suggest a commonalty that spans the change in tectonic regime north across the Mendicino Fracture Zone (Atwater, 1970). A potential cause for the equally low grades of these continental slopes may be seismicity, which is an important trigger for failure and slope readjustment along the entire western U.S. margin (Schwab et al., 1993).

The Oregon slope is a compound, terraced slope of stacked compressional folds formed by the convergence of the North American and Juan de Fuca plates (Goldfinger et al., 1992). The folding is reflected in the Oregon slope-depth frequency grid (Fig. 2, II, E) as four to five cycles of local sea-floor flattening (fold crests) and steepening (fold flanks) with increasing water depth. In the slope-direction frequency grid, all local sea-floor slopes tend to dip seaward, and to some degree in the reverse direction landward, across the fold flanks, highlighting the strong along-slope bias to the region's bathymetry. This contrasts with the New Jersey–Maryland, California, and even west Florida slope-direction trends (Fig. 2, III, A, D, and B), which reflect bathymetry with a strong downslope bias, largely due to submarine canyons. There are submarine canyons on the Oregon slope, but their presence is not indicated in its slope-direction frequency grid. The compressional folding dominates the bathymetry.

ACKNOWLEDGMENTS

Supported by Office of Naval Research (ONR) contract 00014-93-1-0126. The New Jersey bathymetry survey was funded by National Science Foundation (NSF) grant OCE 88-17563. The Florida bathymetry survey was funded by NSF grants OCE 85-16268 and OCE 85-15975. National Oceanic and Atmospheric Administration bathymetry was purchased from the National Geophysical Data Center with funds from the ONR contract and Department of Energy Project DE-FC22-93BC1496. We thank W. B. F. Ryan, C. Angevine, and R. Sheridan for their helpful reviews of the manuscript. Lamont-Doherty Earth Observatory publication 5404.

REFERENCES CITED

Atwater, T., 1970, Implications of plate tectonics for the Cenozoic evolution of western North America: Geological Society of America Bulletin, v. 81, p. 3513–3536.

Delinger, R. P., and Iverson, R. M., 1992, Limiting equilibrium and liquefaction potential in infinite submarine slopes: Marine Geotechnology, v. 9, p. 299–312.

deMoustier, C., 1988, State of the art in swath bathymetry survey systems: International Hydrographic Review, v. 65, p. 25–54.

Goldfinger, C., Kulm, L. D., Yeats, R. S., Applegate, B., MacKay, M. E., and Moore, G. F., 1992, Transverse structural trends along the Oregon convergent margin: Implications for Cascadia earthquake potential and crustal rotations: Geology, v. 20, p. 141–144.

Grim, P., 1992, Dissemination of NOAA/NOS EEZ multibeam bathymetric data, *in* Lockwood, M., and McGregor, B. A., eds., 1991 Exclusive Economic Zone Symposium; Working Together in the Pacific EEZ Proceedings: U.S. Geological Survey Circular 1092, p. 102–109.

Heezen, B. C., Tharp, M., and Ewing, M., 1959, The floors of the oceans, I. The North Atlantic: Geological Society of America Special Paper 65, 122 p.

Kennett, J. P., 1982, Marine geology: Englewood Cliffs, New Jersey, Prentice-Hall, 813 p.

Parker, G., Fukushima, Y., and Pantin, H. M., 1986, Self-accelerating turbidity currents: Journal of Fluid Mechanics, v. 171, p. 145–181.

Paull, C. K., Spiess, F. N., Curray, J. R., and Twichell, D. C., 1990, Origin of Florida Canyon and the role of spring sapping on the formation of submarine box canyons: Geological Society of America Bulletin, v. 102, p. 502–515.

Pratson, L. F., Ryan, W. B. F., Mountain, G. S., and Twichell, D. C., 1994, Submarine canyon initiation by downslope-eroding sediment flows: Evidence in late Cenozoic strata on the New Jersey continental slope: Geological Society of America Bulletin, v. 106, p. 395–412.

Press, F., and Siever, R., 1986, Earth: New York, W.H. Freeman, 656 p.

Robb, J. M., Hampson, J. C., Kirby, J. R., and Twichell, D. C., 1981, Geology and potential hazards of the continental slope between Lindenkohl and South Toms canyons, offshore mid-Atlantic states: U.S. Geological Survey Open-File Report 81-600, p. 1–33.

Schwab, W. C., Lee, H. J., and Twichell, D. C., 1993, Submarine landslides: Selected studies in the U.S. Exclusive Economic Zone: U.S. Geological Survey Bulletin 2002, 204 p.

Twichell, D. C., and DeLorey, C., 1995, Sedimentary processes in the salt deformation province of the Texas-Louisiana continental slope, *in* Gardner, J. V., et al., eds., Geology of the U.S. sea-floor: The view from GLORIA: Cambridge, United Kingdom, Cambridge University Press.

Worrall, D. M., and Snelson, S., 1989, Evolution of the northern Gulf of Mexico with emphasis on Cenozoic growth faulting and the role of salt, *in* Bally, A. W., and Palmer, A. R., eds., The geology of North America—An overview: Boulder, Colorado, Geological Society of America, Geology of North America, v. A, p. 97–138.

Manuscript received May 22, 1995
Revised manuscript received September 22, 1995
Manuscript accepted October 9, 1995

A model for the headward erosion of submarine canyons induced by downslope-eroding sediment flows

Lincoln F. Pratson
Bernard J. Coakley } *Lamont-Doherty Earth Observatory, Columbia University, Palisades, New York 10964*

ABSTRACT

A simple, physically based computer model of continental slope evolution is used to investigate the sequence of submarine canyon formation. The model simulates submarine canyons as evolving under the influence of sedimentation, slope failure, sediment flow erosion, and topography. Interactions between these factors are modeled as being governed by local sea-floor slope, which in the model determines the extent of sea-floor failures, directs the downslope path of sediment flows triggered by the failures, and scales the amount of sea-floor erosion caused by the sediment flows. Based on these interactions, the model simulates a three-stage sequence for submarine canyon formation: (1) the erosion of pre-canyon rills by sediment flows initiated at sites on the upper slope oversteepened by sedimentation; (2) localized slope failure of the walls and/or floor of the rills at one or more mid- to lower-slope sites destabilized by sediment flow erosion; and (3) evolution of the failure into a headward-eroding canyon that advances upslope along the rills by sediment-flow-driven retrogressive failure. Through this sequence, the model simulates canyon and intercanyon morphology that successfully reproduces crosscutting relations observed between Lindenkohl Canyon and adjacent erosional slope rills on the passive-margin New Jersey continental slope, and between slope failures and long, narrow dendritic tributaries that enter into the Aoga Shima Canyon on the convergent-margin Izu-Bonin fore arc. These results suggest that the model may be applicable in explaining submarine canyon formation along a variety of continental margins. More significantly, in illustrating how sediment flows might repeatedly trigger retrogressive failures, the model presents a new explanation for submarine canyon formation that reconciles morphologic evidence for headward canyon erosion by mass wasting with the stratigraphic evidence for canyon inception by downslope-eroding sediment flows.

INTRODUCTION

In one of the first regional studies of a continental slope using GLORIA side-scan sonar imagery, Twichell and Roberts (1982) pointed out that two general populations of submarine canyons occur along the mideast U.S. margin: a relatively few, large, often sinuous canyons with heads that indent the shelf break, and a much greater number of smaller, more linear canyons with heads hundreds of meters below the shelf break on the continental slope. They suggested that the slope-confined canyons had initiated on the continental slope, and that the shelf-indenting canyons had evolved from slope-confined canyons and thus were older.

This same idea was independently reached by Farre et al. (1983) after studying the morphology of a number of submarine canyons on the New Jersey and Maryland continental slopes imaged in higher-resolution SeaMARC I side-scan sonar imagery. They went a step further than Twichell and Roberts (1982) and hypothesized a scenario for the evolution from "youthful" to "mature" canyon morphology. Farre et al. (1983) proposed that the youthful stage of submarine canyon evolution begins with slope failure. Retrogressive mass wasting of the continental slope sediments along the failure headwall leads to the formation and upslope extension of a relatively straight, steep-walled chute. If this headward-migrating chute breaches the shelf break, the canyon taps into a new sediment source of outer shelf sands and enters into a mature phase of canyon evolution. Failure of shelf sediments in the vicinity of the canyon head initiates coarse-grained turbidity currents, which become an important agent in canyon erosion by downcutting the canyon and carving a sinuous thalweg.

The differences between shelf-indenting and slope-confined canyons first noted along the mideast U.S. continental slope by Twichell and Roberts (1982) and Farre et al. (1983) have subsequently been observed along other continental slopes throughout the world (e.g., McGregor, 1985; Dingle and Robson, 1985; Nelson and Maldonado, 1988; Klaus and Taylor, 1991). Their idea that slope-confined and shelf-indenting submarine canyons represent different stages of canyon evolution has provided a framework for interpreting the relative ages of canyons on a continental slope. Furthermore, the Farre et al. (1983) theory has provided an explanation for why slope-confined and shelf-indenting canyons co-exist.

Aspects of the Farre et al. (1983) theory have recently been called into question. Using multibeam bathymetry, seismic reflection profiles, and borehole data, Pratson et al. (1994) identified and mapped a number of buried canyons in an area of the New Jersey Slope investigated by both Farre et al. (1983) and Twichell and Roberts (1982). Pratson et al. (1994) found that at least several of the larger, "slope-confined" canyons in the area have buried, upslope extensions that may once have indented the shelf break but now are infilled and cannot be discerned in side-scan sonar imagery. They also found that a number of existing canyons exploited the lower slope reaches of the older, buried canyons, suggesting that the existing canyons were initiated by downslope-eroding sediment flows rather than upslope-eroding retrogressive failures.

To explain the formation of these canyons, Pratson et al. (1994) combined ideas of Farre et al. (1983) with those of Daly (1936), who was the first to suggest that submarine canyons are eroded by turbidity currents. Pratson et al. (1994) proposed that canyon initiation began with depositional over-

GSA Bulletin; February 1996; v. 108; no. 2; p. 225–234; 8 figures; 1 table.

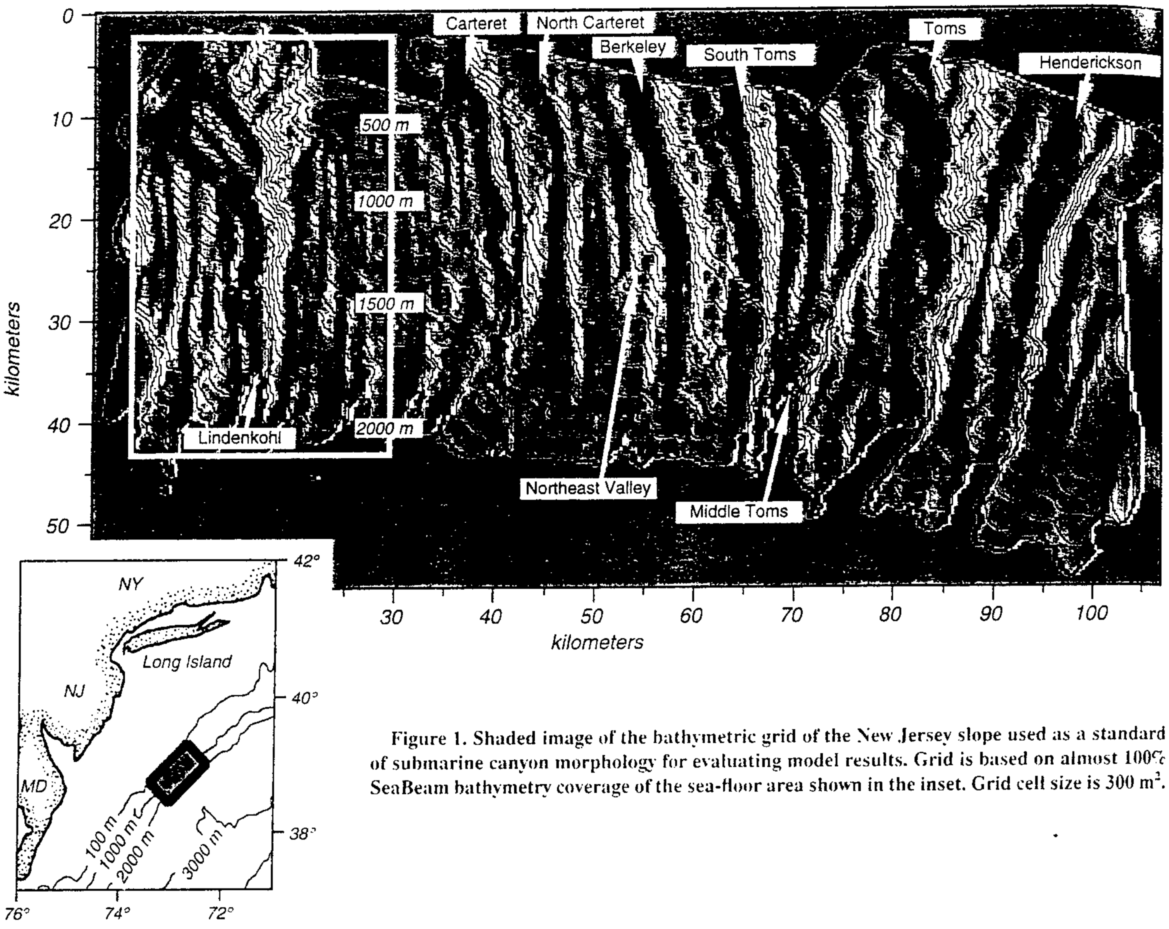

Figure 1. Shaded image of the bathymetric grid of the New Jersey slope used as a standard of submarine canyon morphology for evaluating model results. Grid is based on almost 100% SeaBeam bathymetry coverage of the sea-floor area shown in the inset. Grid cell size is 300 m^2.

steepening and localized failure of the upper continental slope. The failures ignited erosive sediment flows, which were routed downslope through preexisting bathymetric lows, including sea-floor troughs that overlie the buried canyons on the middle to lower slope where they become only partially infilled. The erosion caused by these flows established passages along which canyon development ensued. Subsequent sediment flows deepened the evolving canyons and oversteepened their walls, leading to a corresponding widening of the canyons through retrogressive canyon-wall failure.

Pratson et al. (1994) used their hypothesis to explain the initiation of a number of large, slope-crossing canyons that incise the Miocene through Quaternary muds that form the upper New Jersey Slope (Robb et al., 1981). They did not apply their hypothesis to the formation of smaller submarine canyons on the New Jersey Slope, which are confined to water depths ≥1500 m and cut into areas of shallow-buried and exposed Eocene chalk. McHugh et al. (1993) have shown that the formation of these canyons was controlled by diagenetically induced fracturing of the chalk. But the events that triggered this fracturing remain speculative.

We show in this study how the formation of these lower slope canyons could have been triggered by the same sediment flow erosion that appears to have ultimately led to the formation of larger slope-crossing canyons within the area. In so doing, we also show how downslope-directed sediment flow erosion could induce the type of headward canyon erosion conceived of by Twichell and Roberts (1982) and Farre et al. (1983). We demonstrate these possibilities through a new computer model of submarine canyon evolution that simulates the interaction between slope failure, sediment flow erosion, and topography as conceptualized by Pratson et al. (1994). The model results are contrasted to the morphology of the New Jersey continental slope in the vicinity of Lindenkohl Canyon (box, Fig. 1), a well-mapped subregion of the area where Twichell and Roberts (1982), Farre et al. (1983), and Pratson et al. (1994) have all suggested that submarine canyons in different stages of evolution are represented. The applicability of the model to canyon formation in other continental margin settings is then discussed in a comparison of the results to the morphology of the Aoga Shima Canyon on the Izu-Bonin fore arc off Japan.

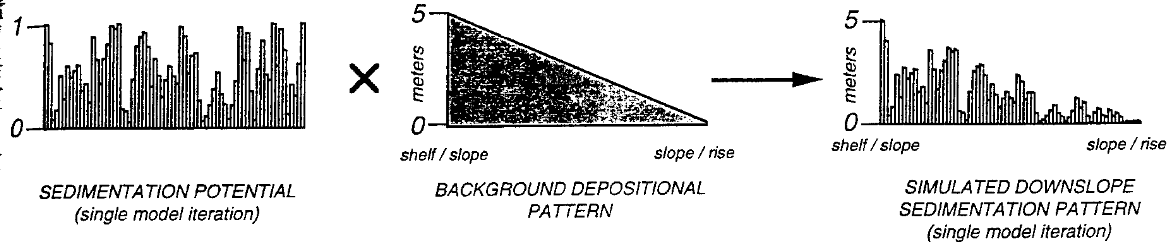

Figure 2. Schematic illustrating the downslope pattern of sedimentation simulated by the model. This pattern was uniform along the model slope.

THE MODEL

Few studies have simulated the formation of submarine canyons. Tetzlaugh and Harbaugh (1989) used their SEDSIM3 model to simulate the formation of Simpson Canyon, an ancient submarine canyon buried beneath Alaska's Arctic coast. More recently, Cao and Lerche (1994) have simulated the formation of a generic canyon with their MOSED3D model. The principal focus of these studies was not modeling submarine canyon formation, but the erosion, sediment transport, and deposition caused by gravity-driven sediment flows. The submarine canyons were modeled as being eroded by turbidity currents initiated at predefined model locations.

In this study, we present a new "seascape" evolution model for simulating the morphologic evolution of a passive, clastic continental slope. The model simulates sedimentation, slope failure, and sediment flow erosion by discrete grid cell interactions. The parameterizations for these processes are simple, but physically founded. They emulate the fundamental mechanics of each process but, in this study, not the rate at which the processes occur. A factor common to all of the parameterizations is local sea-floor slope. In the model, local slope governs the location and extent of sea-floor failure, directs the downslope path of the sediment flow triggered by the failure, and scales the amount of sea-floor erosion the sediment flow can cause.

Initial Model Surface. The initial model surface is a rectangular grid of sea-floor elevations. For this study, a smooth, dipping elevation grid covering an area 30 km × 30 km is used. The grid cells are 300 m on a side. The grid ranges in water depth from 100 to 2100 m and has a gradient of ~4°, which is similar to the New Jersey continental slope between Lindenkohl and Carteret Canyon. In this study, variations in the type and strength of the sediments composing the slope are not modeled.

Sedimentation. Sedimentation is simulated by raising the elevation of each grid cell on the continental slope a small amount during every model iteration. This amount varies randomly from one grid cell to the next (i.e., spatially) and with each model iteration (i.e., "temporally") but is scaled by a background depositional pattern that determines the maximum amount of sediment a grid cell can receive during a single iteration (Fig. 2). In this study, the depositional pattern reflects the accumulation of Quaternary sediments along the New Jersey Slope. These are thickest on the upper continental slope and thin seaward, suggesting they were input from a shelf-edge line source (Pratson et al., 1994). For simplicity, this source is approximated using a background depositional pattern that decreases linearly from a maximum of 5 m per iteration at the shelf edge to a minimum of 0 m per iteration at the slope base.

Slope Failure. Slope failure occurs in the model when sedimentation raises the elevation of a grid cell above the elevation of its neighbors such that the slope between the grid cell and its lowest neighbor exceeds a maximum slope threshold (Fig. 3A). This maximum slope threshold is the single free parameter that can be varied from one model run to the next. It represents the maximum angle of repose for the continental slope sediments and reflects the limit of their material strength or stability. When a grid cell exceeds the maximum slope threshold and fails, its elevation is reduced by an amount that brings the grid cell 5% below the maximum slope threshold. If the failure of the grid cell oversteepens any of its immediate neighbors, these fail too (Fig. 3C). This chain reaction of failures continues until the failure headwall is regraded below the maximum slope threshold. Thus, in the model, the extent of a slope failure is determined by the steepness of the surrounding continental slope area.

Sediment Flow Erosion. Sediment flow erosion is initiated in the model at a grid cell that fails. The failed sediment is removed from the grid cell as a sediment flow that is one grid cell in areal extent (0.09 km^2). The unit size sediment flow, or "floxel" (Fig. 3B), follows the steepest topographic descent downslope. As it moves, the floxel erodes the slope surface beneath it by reducing the elevation of each grid cell it passes over. This amount is equal to the square root of the local slope gradient times the volume of sediment the floxel is already transporting. This parameterization represents a non-time dependent linearization of the equation by Komar (1977) for the body flow of a turbidity current. Importantly, the influence of other hydrodynamic factors in sediment flow erosion, such as friction, water entrainment, and flow density (Parker et al., 1986), is not considered here.

In the case that the failure of a grid cell causes neighboring grid cells to retrogressively fail, each of these generates its own floxel (Fig. 3C). The individual floxels independently move down the continental slope and erode the sea floor as they are initiated; however, the downslope path each floxel follows is influenced by the eroded topography left by the floxel that immediately preceded it. Likewise, as it erodes the sea floor, a floxel influences the path of any following floxel. This dynamic feedback between erosion and surface evolution leads the individual floxels to converge and form a multigrid cell sediment flow train (Fig. 3C). The larger the retrogressive failure, the larger the resulting sediment flow train.

When a floxel or sediment flow train reaches the base of the continental slope, it exits the model. The model then iteratively

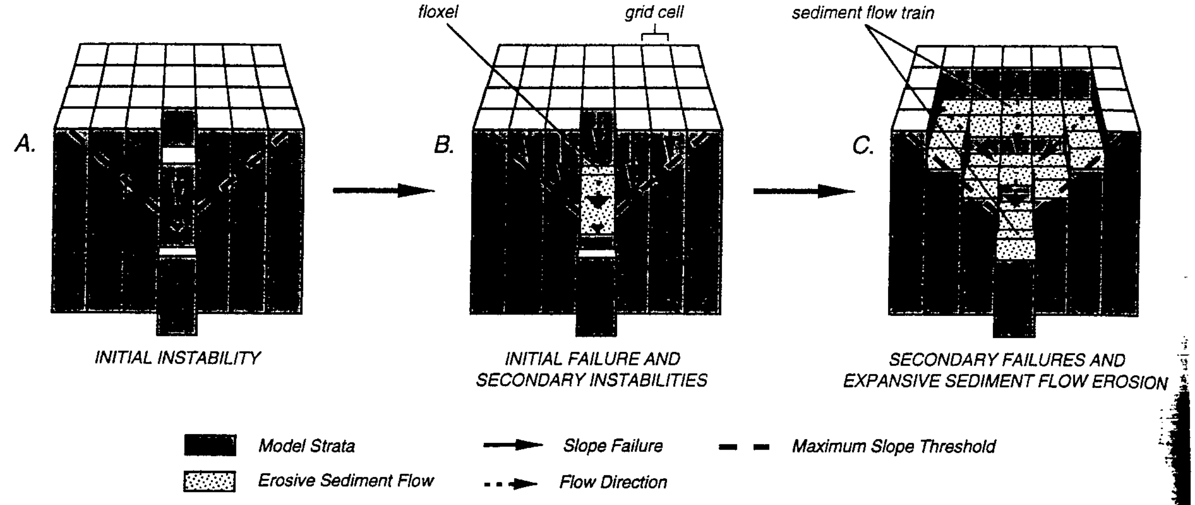

Figure 3. Schematic illustrating the possible sequence of slope failure and sediment flow erosion simulated by the model at sites on the model slope oversteepened by sedimentation.

adds sediment upon the new continental slope surface until another slope failure is initiated, and the sequence is repeated.

RESULTS

The style of submarine canyon evolution simulated by the model is illustrated with two model runs made with different maximum slope thresholds. In one, a maximum slope threshold of 12° is used, which approximates the mean gradient of the walls of submarine canyons on the New Jersey continental slope as measured from gridded multibeam bathymetry of the area (Fig. 1). In the other, a maximum slope threshold of 30° is used, which approaches the steepest gradient for the walls of these canyons.

The sequence of canyon evolution in both model runs is the same. Sedimentation in the model gradually oversteepens the upper continental slope, and grid cells begin to fail. At first, the failures involve only single grid cells. These initiate floxels that cut narrow, shallow rills to the base of the continental slope (Fig. 4A). Subsequent floxels moving downslope through topographic lows nearby are directed into the rills where their walls become steeper than the adjacent slope surface. The floxels then follow the rills to the base of the slope, eroding and deepening the rills before they are infilled by sedimentation.

With time, some of the rills are deepened to the point that portions of their walls are oversteepened and fail (Fig. 4B). The failures occur within these rills where the frequency of floxel capture and wall erosion is greatest. Eventually, these failures become large enough that they trigger a chain reaction of retrogressive slope failures (Fig. 4C). These retrogressive failures radiate from the initial failure site, regrading, expanding, and altering the form of the rill into a canyon-like excavation (Fig. 4D). Floxels of failed sediments join to form sediment flow trains that erode pinnate gullies into the walls of the simulated canyon as they are funneled into its emerging thalweg (Fig. 4D). There they converge with other sediment flow trains to form a "catastrophic" erosional event that excavates the downslope reach of the simulated canyon to the base of the model slope.

Once the walls of the simulated canyon are established, they become focal points for further slope failure for they already recline near the maximum slope threshold. Continued sedimentation along the canyon wall rims and downcutting within the canyon by sediment flow erosion steepen the canyon walls beyond this limit, and thus they fail more frequently than the surrounding slope. These failures are most common along the headwalls of the canyon toward the upper slope where sedimentation rates and the introduction of floxels are greatest. These failures lead to the headward growth of the simulated canyon (Fig. 5). At the same time, they initiate sediment flow erosion within the canyon, which deepens the thalweg and undercuts the walls. This in turn leads to a corresponding widening of the canyon by side-wall failures farther down the slope.

A consequence of this pattern of erosion, which was unanticipated during model development, is that the simulated canyons are mostly excavated by a few, large, retrogressive slope failures (Fig. 5). When the walls of a floxel-cut rill begin to fail, the volume of sediments removed by these failures increases orders of magnitude within a moderate number of failure events (Fig. 5). The magnitude of the slope failures then plateaus in size for about the same number of failure events. It is during this phase of the model that the most significant changes in simulated canyon morphology occur. Each big, retrogressive slope failure advances the head of the evolving canyon up the continental slope, forms new canyon tributaries, and widens the canyon (Fig. 5). The big retrogressive failures then diminish in frequency once the head of the canyon approaches the top of the continental slope in the model.

The headward canyon erosion simulated by the model is strikingly similar to the youthful, mass-wasting phase of submarine canyon evolution envisioned by Farre et al. (1983). However, the model simulation departs from the Farre et al. (1983) theory in several important ways. First, although Farre et al. (1983) proposed that localized failure on the continental slope begins headward canyon erosion, they did not speculate as to the possible causes for such a failure. In the model, the onset of headward canyon

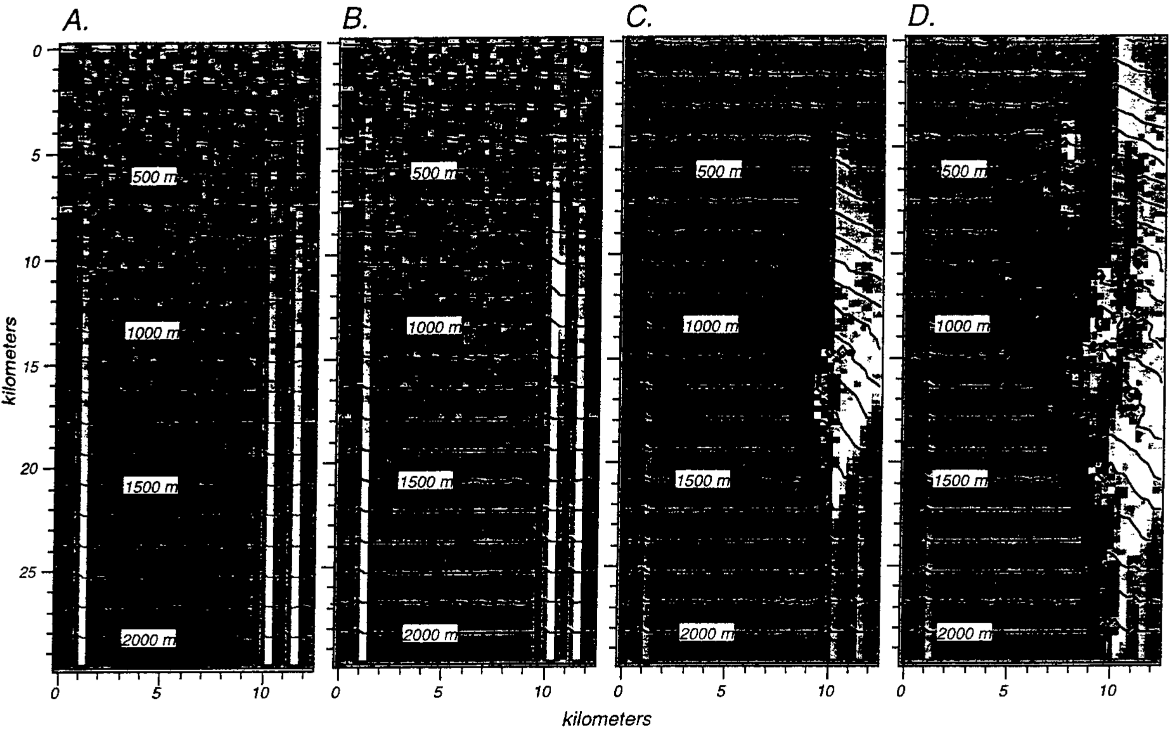

Figure 4. Simulations showing the sequence of submarine canyon evolution generated by the model.

erosion begins when repeated sediment flow downcutting in an area oversteepens the sea floor and triggers failure.

Second, Farre et al. (1983) proposed that sediment flows become an important factor in canyon erosion only after the head of a canyon breaches the shelf break. Prior to that point, other, continental slope–based mechanisms cause the retrogressive failures that advance the canyon upslope. By contrast, the model results predict that sediment flows trigger the retrogressive failures where they enter into the canyon and/or undercut its walls. Thus, in the model, sediment flows initiated upslope of a canyon are an important factor driving the headward erosion of the canyon throughout its evolution.

A third difference is that Farre et al. (1983) proposed that after the head of a canyon breaches the shelf break, downcutting by sediment flows leads to the development of a meandering thalweg. In the model, canyons develop meandering thalwegs through the slope failures that advance the canyon headwall up the slope.

Although this sequence of canyon formation simulated by the model is insensitive to the value of the maximum slope threshold, the canyon morphology produced by the model is not (Figs. 6 and 7). The canyon simulated using a maximum slope threshold of 12° is characterized by a wide canyon floor and a broad, flowering headwall. The canyon simulated using a maximum slope threshold of 30° has a deeper canyon floor and a narrower headwall. The results show that the maximum slope threshold influences the width and relief of the submarine canyons simulated by the model.

The two simulations are also compared to a bathymetric grid of Lindenkohl Canyon constructed from near-complete SeaBeam multibeam bathymetry of the New Jersey continental slope (Figs. 6 and 7). The grid has a grid cell spacing of 100 m and covers the same area as represented in the two simulations. Visually, the form and width of the simulated canyon produced using a maximum slope limit of 30° come closest to approximating the morphology of Lindenkohl Canyon (Figs. 6 and 7). The simulated canyon produced using a maximum slope limit of 12°, however, is more like Lindenkohl Canyon in its thalweg profile (Fig. 7; Table 1). Both simulated canyons are much larger than Lindenkohl Canyon (Table 1) and have wider canyon floors that are broader nearer to the base of the continental slope (Figs. 6 and 7).

DISCUSSION

The model results predict that the bulk of canyon formation is carried out by a few large-scale retrogressive failures (Fig. 5). Some submarine canyons, like the Mississippi, show morphologic and stratigraphic evidence of having undergone this type of catastrophic formation (Goodwin and Prior, 1989). But others, such as Oceanographer off Georges Bank, exhibit evidence of cyclic erosion and infilling dating as far back as the Cretaceous (Ryan et al., 1978). The latter observations suggest that many submarine canyons evolve over long time periods from repeated erosional events, presumably of varying magnitude and due to multiple causes (Shepard, 1981). This more gradual and varied form of canyon evolution is not addressed by the present model. It is biased

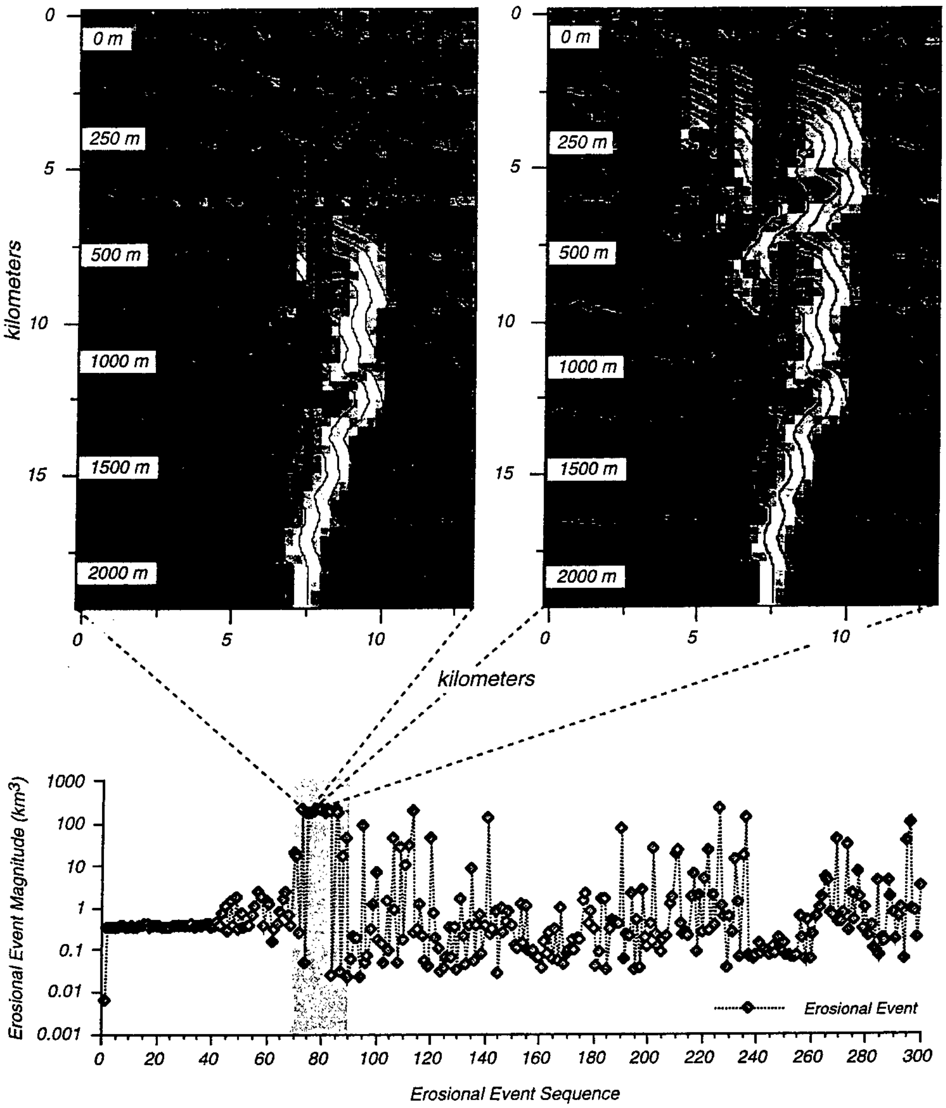

Figure 5. Time series showing sequential variations in the magnitude of erosion generated during a model run. Selected simulations demonstrate the significant growth and headward erosion that occur in the simulated canyons during a relatively few, large-volume retrogressive failures (gray area).

in its predictions toward canyon formation by catastrophic erosion.

This bias is attributable to at least two model simplifications. One is the use of a single maximum slope threshold, which implies all slope sediments are of uniform strength. A floxel in the model can downcut canyon floor sediments exhumed from depth the same amount as newly deposited sediments on the open slope. In reality, buried sediments should be less erodible, for they generally have undergone compaction and have been hardened by consolidation (Karig and Hou, 1992). As they are exhumed, consolidated sediments should be able to sustain greater angles of repose than can surface sediments and be more resistant to slope failure and sediment flow erosion. This resistance would slow canyon evolution. It is also the likely cause for many canyons having V-shaped cross sections, rather than the U-shaped cross section predicted by the model (Fig. 7).

A second simplification in the model is that sediment flow erosion is simulated without factoring in the influence of flow acceleration and related flow hydrodynamics (bed friction, water entrainment, flow density, etc.). Using the parameterization in the model, a simulated canyon develops a thal-

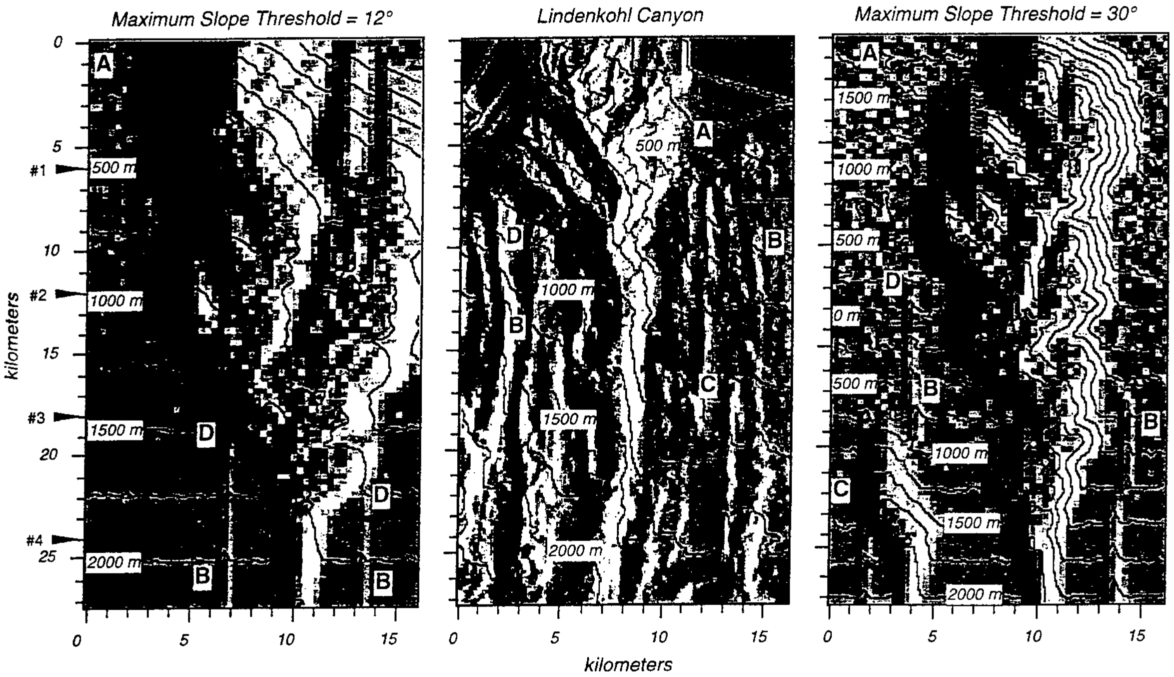

Figure 6. Examples of simulations generated with the model using two maximum slope thresholds and their comparison to Lindenkohl Canyon. Letters in all three images correspond to analogous morphologies: A, upper slope sediment buildup; B, narrow erosional rills; C, lower slope failure excavations; and D, heads of erosional rills truncated by canyon sidewalls and tributaries. Note that in the simulation using a maximum slope threshold of 30°, sedimentation in the model raised the elevation of the upper continental slope above sea level. This was because no process other than downslope erosion was simulated to offset sediment aggradation, such as subsidence or shallow water current and wave erosion. Although unrealistic, this consequence is not considered to have bearing on the results discussed in the text.

weg grade that reflects the volume and frequency of floxels that pass through it. However, the magnitude of erosion a sediment flow can cause, and the amount of sediment it can entrain, is dependent on the acceleration of the flow (Parker et al., 1986; Normark and Piper, 1991). The present model requires a more physically based parameterization of sediment flow behavior to assess the role of sediment flow acceleration on submarine canyon formation.

Variable sediment strength, sediment flow acceleration, and other improvements are being incorporated into a new version of the model. The version discussed in this study, however, already succeeds in reproducing several fundamental elements of canyon and intercanyon morphology in the vicinity of Lindenkohl Canyon on the New Jersey continental slope. This success suggests that, despite its biases and simplicity, the model may be correctly simulating the general sequence of events that led to the formation of submarine canyons within this area. This sequence of events is as follows: (1) erosion of precanyon rills by sediment flows initiated at sites on the upper slope due to depositional oversteepening (Fig. 4A); (2) slope failure along the rills at one or more mid- to lower-slope sites destabilized by sediment flow erosion (Fig. 4B); and (3) evolution of the failure into a headward-eroding canyon that advances upslope along the chute(s) by sediment-flow-driven retrogressive failure (Figs. 4C–4D and 5).

The intercanyon area surrounding Lindenkohl Canyon is incised by a series of relatively closely spaced slope rills (Fig. 6B) with headwalls that cut into a steepened section of the upper slope (Fig. 6A). Pratson et al. (1994) interpreted these slope rills to have been eroded by failure-induced sediment flows, triggered by depositional oversteepening of the upper slope. These slope rills may thus be a natural analog for the precanyon rills generated in the initial stages of the model results (Fig. 4A).

When followed downslope, the rills coalesce and enter three to four amphitheater-shaped failure scars on the middle to lower slope (Fig. 6C). Each of these scars constitutes one of the slope-confined canyons that incise an Eocene chalk, the surface of which is generally covered by a thin veneer of Pliocene-Pleistocene siliciclastic sediments (Farre and Ryan, 1987). The walls and floors of the slope-confined canyons follow fracture surfaces in the chalk that were initiated by pore-fluid expulsion during chalk diagenesis (McHugh et al., 1993). The fractures apparently expanded following the erosion of overburden above the chalk and, in exfoliating, fostered the slope failures that excavated the canyons.

What process could have removed late Cenozoic sediments from above the Eocene chalk is unknown. McHugh et al. (1993) presented several possibilities, including overburden removal by mass wasting. Our model results suggest to us that erosion by sediment flows passing over these areas is an

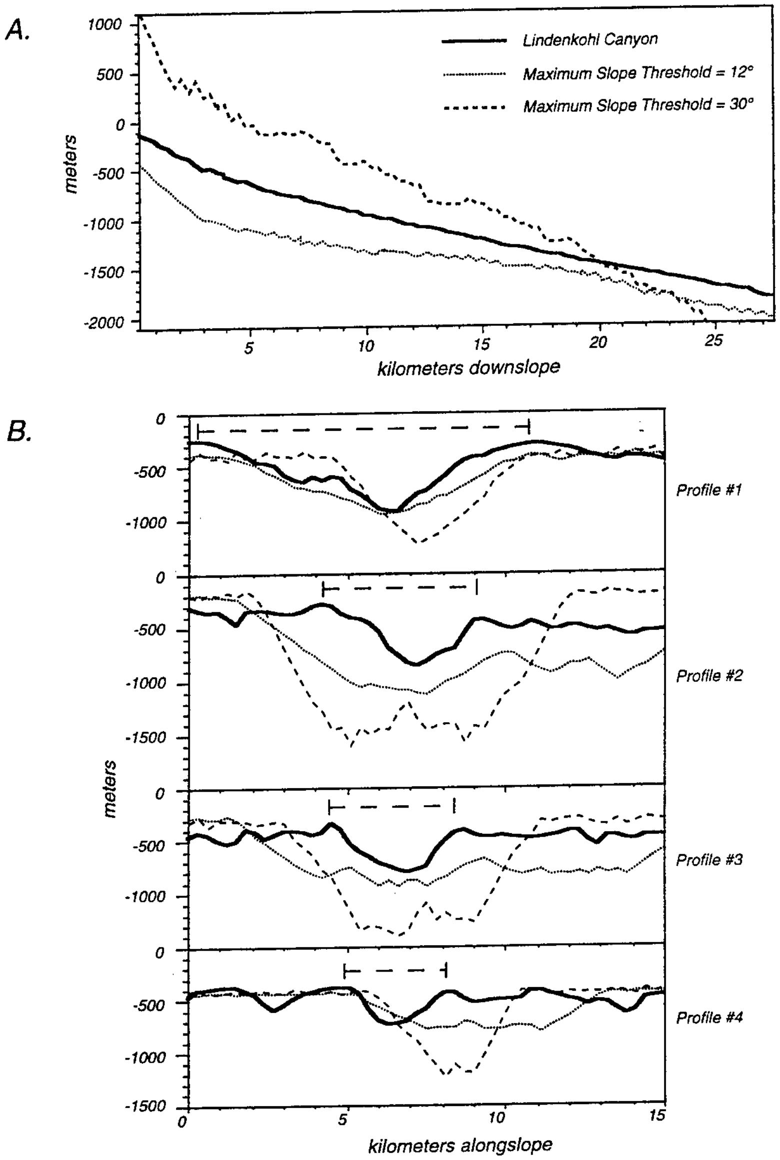

Figure 7. A. Bathymetric profiles down the thalwegs of Lindenkohl Canyon and the two simulated canyons shown in Figure 6. B. Four profiles across Lindenkohl Canyon and the two simulated canyons. The mean depth has been removed from these across-slope profiles to facilitate comparison of canyon widths and depths.

TABLE 1. AREA AND GRADE OF LINDENKOHL CANYON VERSUS SIMULATED CANYONS IN FIGURE 6

	Canyon area (km^2)	Mean canyon thalweg grade (°)
Lindekohl	153	3.1°
Maximum slope threshold = 12°	286	2.6°
Maximum slope threshold = 30°	230	6.1°

equally viable mechanism. In the model, failure-induced canyons are simulated as forming on the middle to lower slope by retrogressive failures. The mechanism that triggers these failures is oversteepening of the walls of the precanyon rills. The sediment flows that passed through the New Jersey Slope rills could have caused similar failures or simply downcut to a critical depth to trigger the exfoliation and subsequent failures that formed the lower slope canyons. Thus, we suggest the lower slope canyons may be representative of the early stage of headward canyon erosion simulated by the model (Fig. 6C).

Whether the lower slope canyons postdate the slope rills is uncertain and cannot be determined from the morphologic relation between these features. But the slope rills do appear to predate the present areal extent of Lindenkohl Canyon and Carteret Canyon to the northeast. The walls of these canyons cut into and terminate the heads of adjacent slope rills (Fig. 6D). This distinctive crosscutting relation is successfully reproduced by the model. As the headwall and sidewalls of simulated canyons advance up and across the slope by retrogressive failure, they erode into and terminate the upslope extensions of precanyon chutes formed earlier nearby (Fig. 4C). In so doing, the simulated canyons capture the upslope drainage area of the precanyon rills. This capture shadows the rills from further downslope sediment flow erosion, aborting their continued development. Growth of the intercanyon slope rills cut into by the walls of Lindenkohl and Carteret Canyons appears to have been suspended by similar circumstances (Fig. 6D).

The parallels between the model results and the slope morphology in the vicinity of Lindenkohl and Carteret Canyons (Fig. 6) suggest these canyons evolved first from slope rills, and possibly later from slope-confined canyons. The model shows how slope-confined and shelf-indenting canyons in this area can be related through a common evolution involving retrogressive slope failures induced by sediment flows initiated upslope of the failures. The model thus presents an explanation for the formation of submarine canyons on the New Jersey continental slope that reconciles the morphologic evidence for headward canyon erosion reported by Twichell and Roberts (1982) and Farre et al. (1983) with the stratigraphic evidence for canyon inception by downslope-eroding sediment flows presented by Pratson et al. (1994).

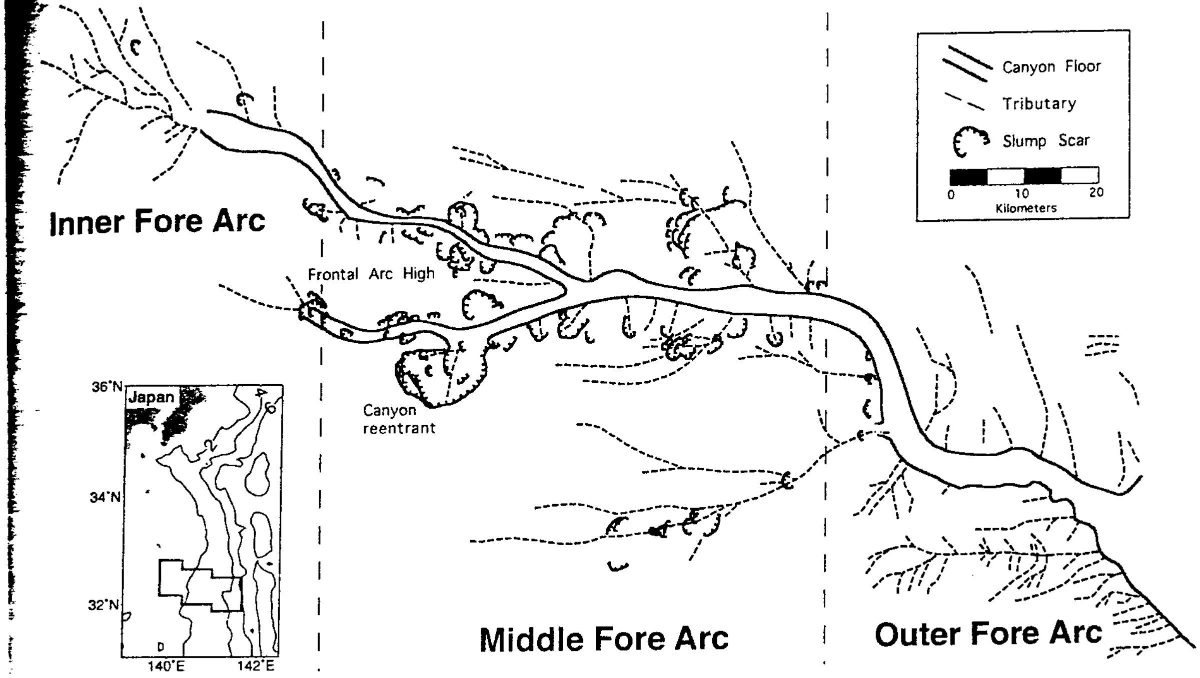

Figure 8. The Aoga Shima Canyon as interpreted from seismic reflection data and full-coverage SeaMARC II side-scan sonar imagery. Modified from Klaus and Taylor (1991).

Because our model of canyon formation is linked to sedimentation, it predicts that the process and pattern of canyon evolution is dependent upon when and where depositional oversteepening of the continental slope occurs. According to our model, canyon evolution should be most active when sediment influx to the slope is greatest. Offshore New Jersey, this would be during relative sea level lowstands. Studies of the activity of submarine canyons within this region support this notion (Prior et al., 1984; Stanley et al., 1984). Sediment flow source locations are also important, for their movement between sea-level cycles or within a single cycle could lead to the abandonment of one canyon head and the formation of another, or to the abandonment of the canyon altogether (Felix and Gorsline, 1971).

We recognize that all slope failures are not associated with depositional oversteepening and sediment flow erosion. Earthquakes, gas-hydrate decomposition, wave-loading, and a variety of other processes can cause slope failure as well (Schwab et al., 1993). We also recognize that there are regions where submarine canyons appear to have formed strictly from retrogressive failures. For instance, it does not seem likely that turbidity currents were involved in the formation of slope-confined canyons on the sheltered seaward flanks of accretionary ridges along the convergent Oregon margin (Orange and Breen, 1992).

Because many submarine canyons are not protected from sediment flow erosion, however, we believe that the model results presented here may be applicable in explaining the formation of a number of canyons in diverse continental margin settings. One candidate is the Aoga Shima Canyon on the central Izu-Bonin fore arc south of Japan (Fig. 1B), a region that is the tectonic opposite to the passive New Jersey margin. Klaus and Taylor (1991) have mapped the Aoga Shima Canyon using SeaMARC II side-scan sonar imagery and seismic reflection data. They show that the canyon is fed by a number of long, narrow, shallow dendritic tributaries (Fig. 8), similar to the slope rills offshore New Jersey. Those dendritic tributaries that enter into the canyon on the middle to outer fore arc are cut in their midsection by arcuate slumps (Fig. 8). Arcuate slumps also occur along the sidewalls of the canyon and at the headwalls of a slope-confined canyon re-entrant (Fig. 8).

The slumping along the Aoga Shima Canyon led Klaus and Taylor (1991) to infer that the canyon evolved from headward erosion by mass wasting as proposed by Farre et al. (1983). However, they noted that the dendritic tributaries that enter the head of the canyon on the inner fore arc (Fig. 8) are more likely to have been eroded by sediment flows than mass wasting. They also noted that aspects of the canyon drainage pattern, such as the bifurcation of the canyon around a frontal arc high (Fig. 8), are difficult to reconcile with headward canyon erosion strictly by mass wasting, for such canyon growth should follow the steepest slope gradients.

A number of the observations made by Klaus and Taylor (1991) can be explained in the context of our model results. As alluded to in the comparison to the New Jersey Slope rills above, the dendritic tributaries that feed into the Aoga Shima Canyon appear to have been eroded by sediment flows. The arcuate slumps that cut the midsections of these tributaries (Fig. 8) may have derived from where erosion by the sediment flows destabilized the sea floor. The most active tributaries would have fostered retrogressive slumping, leading to the formation and headward erosion of the canyon re-entrant and presumably the canyon itself. Importantly, the model results predict that this headward erosion would have occurred up the dendritic tributaries through which the failure-triggering sediment flows were being funneled. This prediction is consistent with the drainage pattern of the Aoga Shima Canyon (Fig. 8). The headwalls of both the canyon and its re-entrant connect to dendritic tributaries. The prediction is also consistent with the canyon re-entrant being cut around rather than up the frontal arc high, for sediment flows follow topographic lows, and this is the path along which a dendritic tributary would have been cut. Finally, the model results would predict that the arcuate slumps bordering the sidewalls of the Aoga Shima Canyon were widening the canyon in response to thalweg deepening by sediment flow erosion, which undercut the canyon walls.

CONCLUSIONS

On the basis of the results of our seascape evolution model, we propose that Lindenkohl Canyon, Carteret Canyon, the Aoga Shima Canyon, and other submarine canyons along other continental margins were formed from headward erosion driven by sediment flow downcutting. In this scenario, retrogressive failure of the headwall of a slope-confined submarine canyon does not fortuitously "capture" tributaries cut by sediment flows, as suggested by Farre et al. (1983). Instead, such tributaries are the precursors of a submarine canyon and establish the template along which submarine canyon formation ensues. The sediment flows that cut these passages promote slope failure and, if frequent enough, induce upslope erosion of the failure headwall along sediment flow passages toward their source. In so doing, the failure can evolve into a slope-confined canyon and ultimately a shelf-indenting canyon, which, depending on the process sourcing the sediment flows (fluvial/deltaic input, shelf-currents, etc.), may or may not connect with the mouth of a river on the continental shelf.

The results of our seascape evolution model are tested in this study against the morphology of existing submarine canyons. The model results can also be tested by examining the deposits at the base of slope-confined canyons. Our model results predict that these deposits should consist of a few, large slope failure deposits, such as debris flows, underlain by and interbedded with sediment flow deposits containing shallow-water materials from the upper continental slope and possibly outer continental shelf. A cursory review of Miocene-Pleistocene age sediments drilled on the New Jersey upper continental rise just seaward of several slope-confined canyons appears to support this prediction. Deep Sea Drilling Project Sites 604 (Shipboard Scientific Party, 1987a) and 613 (Shipboard Scientific Party, 1987b) were drilled ~10 km seaward of North Carteret Canyon and ~6 km seaward of Northeast Valley (respectively, Fig. 1), whereas Ocean Drilling Program Site 905 (Shipboard Scientific Party, 1994) was drilled ~35 km seaward of Berkeley Canyon (Fig. 1). The Miocene-Pleistocene sediments recovered in these boreholes consist of multiple and possibly thick (potentially >200 m at ODP Site 905) debris flow deposits composed of slope materials, and interbedded turbidites containing shallow-water sands and fauna. Further investigation is needed to determine how these deposits relate to the formation of the submarine canyons immediately upslope of the boreholes.

ACKNOWLEDGMENTS

This study was made possible through funds provided by the Office of Naval Research (ONR grant no. N00014-93-1-0126). The authors are grateful to David Piper, Gerard Middleton, and G. Parker, whose critical reviews greatly improved the manuscript. We also thank W. Ryan and C. Pirmez for their thoughts on submarine canyon formation and their constructive criticisms of the original manuscript. Preparation of the manuscript benefited from suggestions by J. Weissel and M. Steckler as well.

REFERENCES CITED

Cao, S., and Lerche, I., 1994, A quantitative model of dynamical sediment deposition and erosion in three dimensions: Computers & Geosciences, v. 20, p. 635–663.

Daly, R. A., 1936, Origin of submarine "canyons": American Journal of Science, ser. 5, v. 31, p. 401–420.

Dingle, R. V., and Robson, S., 1985, Slumps, canyons and related features on the continental margin off East London, SE Africa (SW Indian Ocean): Marine Geology, v. 67, p. 37–54.

Farre, J. A., and Ryan, W. B. F., 1987, Surficial geology of the continental margin offshore New Jersey in the vicinity of Deep Sea Drilling Project Sites 612 and 613, *in* Poag, C. W., and Watts, A. B., and others, Initial reports of the Deep Sea Drilling Project, Volume 95: Washington, D.C., U.S. Government Printing Office, p. 725–759.

Farre, J. A., McGregor, B. A., Ryan, W. B. F., and Robb, J. M., 1983, Breaching the shelfbreak; Passage from youthful to mature phase in submarine canyon evolution, *in* Stanley, D. J., and Moore, G. T., eds., The shelfbreak: Critical interface on continental margins: Society of Economic Paleontologists and Mineralogists Special Publication No. 33, p. 25–39.

Felix, D. W., and Gorsline, D. S., 1971, Newport submarine canyon, California: An example of the effects of shifting loci of sand supply upon canyon position: Marine Geology, v. 10, p. 177–198.

Goodwin, R. H., and Prior, D. B., 1989, Geometry and depositional sequences of the Mississippi Canyon, Gulf of Mexico: Journal of Sedimentary Petrology, v. 59, p. 318–329.

Karig, D. E., and Hou, G., 1992, High-stress consolidation experiments and their geologic implications: Journal of Geophysical Research, v. 97, p. 289–300.

Klaus, A., and Taylor, B., 1991, Submarine canyon development in the Izu-Bonin forearc: a SeaMARC II and seismic survey of Aoga Shima Canyon: Marine Geophysical Researches, v. 13, p. 105–130.

Komar, P. D., 1977, Computer simulation of turbidity current flow and the study of deep-sea channels and fan sedimentation, *in* Goldberg, E. D., McCave, I. N., O'Brien, J. J., and Steele, J. H., eds., The sea, Volume 6: New York, Wiley-Interscience, p. 603–621.

McGregor, B., 1985, Role of submarine canyons in shaping the rise between Lydonia and Oceanographer canyons, Georges Bank: Marine Geology, v. 62, p. 277–293.

McHugh, C. M., Ryan, W. B. F., and Schreiber, B. C., 1993, The role of diagenesis in exfoliation of submarine canyons: American Association of Petroleum Geologists Bulletin, v. 77, p. 145–172.

Nelson, C. H., and Maldonado, A., 1988, Factors controlling depositional patterns of Ebro turbidite systems, Mediterranean Sea: American Association of Petroleum Geologists Bulletin, v. 72, p. 698–716.

Normark, W. R., and Piper, D. J. W., 1991, Initiation processes and flow evolution of turbidity currents; implications for the depositional record, *in* Normark, W. R., and Piper, D. J. W., eds., From shoreline to abyss: Society of Economic Paleontologists and Mineralogists Special Publication No. 46, p. 207–230.

Orange, D. L., and Breen, N. A., 1992, The effects of fluid escape on accretionary wedges, 2. Seepage force, slope failure, headless submarine canyons, and vents: Journal of Geophysical Research, v. 97, p. 9277–9295.

Parker, G., Fukushima, Y., and Pantin, H. M., 1986, Self-accelerating turbidity currents: Journal of Fluid Mechanics, v. 171, p. 145–181.

Pratson, L. F., Ryan, W. B. F., Mountain, G. S., and Twichell, D. C., 1994, Submarine canyon initiation by downslope-eroding sediment flows: Evidence in late Cenozoic strata on the New Jersey continental slope: Geological Society of America Bulletin, v. 106, p. 395–412.

Prior, D. B., Coleman, J. M., and Doyle, E. H., 1984, Antiquity of the continental slope along the middle Atlantic margin of the United States: Science, v. 223, p. 926–928.

Robb, J. M., Hampson, J. C., Kirby, J. R., and Twichell, D. C., 1981, Geology and potential hazards of the continental slope between Lindenkohl and South Toms canyons, offshore mid-Atlantic states: U.S. Geological Survey Open-File Report 81-600, p. 1–33.

Ryan, W. B. F., Cia, M. B., Miller, E. L., Hanselman, D., Nesteroff, W. D., Hecker, B., and Nibbelink, M., 1978, Bedrock geology in New England submarine canyons: Oceanologica Acta, v. 1, p. 233–254.

Schwab, W. C., Lee, H. J., and Twichell, D. C., 1993, Submarine landslides: Selected studies in the U.S. Exclusive Economic Zone: U.S. Geological Survey Bulletin 2002, 204 p.

Shipboard Scientific Party, 1987a, Sites 604 and 605, *in* van Hinte, J. E., Wise, S. W., and others, Initial reports of the Deep Sea Drilling Project, Volume 93: Washington, D.C., U.S. Government Printing Office, p. 277–413.

Shipboard Scientific Party, 1987b, Site 613, *in* Poag, C. W., Watts, A. B., and others, Initial reports of the Deep Sea Drilling Project, Volume 95: Washington, D.C., U.S. Government Printing Office, p. 155–241.

Shipboard Scientific Party, 1994, Site 905, *in* Mountain, G. S., Miller, K. G., Blum, P., and others, Proceedings of the Ocean Drilling Program, Initial Reports: Washington, D.C., U.S. Government Printing Office, p. 255–308.

Shepard, F. P., 1981, Submarine canyons; multiple causes and long-time persistence: American Association of Petroleum Geologists Bulletin, v. 65, p. 1062–1077.

Stanley, D. J., Nelsen, T. A., and Stuckenrath, R., 1984, Recent sedimentation on the New Jersey slope and rise: Science, v. 226, p. 125–133.

Tetzlaff, D. M., and Harbaugh, J. W., 1989, Simulating clastic sedimentation: New York, Van Nostrand, 202 p.

Twichell, D. C., and Roberts, D. G., 1982, Morphology, distribution, and development of submarine canyons on the United States Atlantic continental slope between Hudson and Baltimore Canyons: Geology, v. 10, p. 408–412.

MANUSCRIPT RECEIVED BY THE SOCIETY AUGUST 12, 1994
REVISED MANUSCRIPT RECEIVED JULY 17, 1995
MANUSCRIPT ACCEPTED AUGUST 18, 1995
LAMONT-DOHERTY EARTH OBSERVATORY CONTRIBUTION NO. 5426

Printed in U.S.A.

The kinematics and pattern of escarpment retreat across the rifted continental margin of SE Australia

Michele A. Seidl,* Jeffrey K. Weissel and Lincoln F. Pratson
Lamont-Doherty Earth Observatory of Columbia University,
Route 9 W, Palisades, NY 10964, USA

ABSTRACT

Rifted continental margins generally display an interior, low-relief, highly weathered upland area and a deeply incised, high-relief coastal area. The boundary between the two zones is commonly demarcated by an abrupt, seaward-facing escarpment. We investigate the rate and pattern of escarpment erosion and landscape evolution along the passive margin of south-east Australia, in the region of the New England Tableland. The process of rifting is shown to initiate an escarpment across which rivers flow, resulting in an escarpment that takes the form of dramatic, elongated gorges. Using a mass balance approach, we estimate the volume/unit length of continental material eroded seaward of the escarpment to be between 41 and 68 km^2, approximately an order of magnitude less than the 339 km^2 of terrigenous sediments calculated to have been deposited offshore, but consistent with earlier denudation estimates based on apatite fission track data. On the bedrock rivers draining the New England Tableland region, the escarpment is manifested as a series of sharp knickpoints punctuating the river longitudinal profiles. The knickpoints are situated the same distance upstream along the different channels and uniform escarpment retreat rates on the order of 2 km Myr^{-1} are estimated, despite some differences in bedrock lithologies. Gorge head migration appears to be very important as a bedrock incision mechanism. Field observations indicate a coupling between escarpment retreat and knickpoint propagation, bedrock channel incision, and hillslope development.

INTRODUCTION

We advance the idea that the erosion of broad continental plateaus occurs by propagation of erosional 'fronts' laterally through the plateau mass over time. These fronts are often escarpments and escarpment propagation appears to happen regardless of the origin of the plateau topography, i.e. whether these broad elevated regions result from collisional plate tectonics (Fielding *et al.*, 1994; Masek *et al.*, 1994), rift flank uplift following extension (Ollier, 1985; Gilchrist & Summerfield, 1990; Weissel, 1990; Summerfield, 1991; Weissel *et al.*, 1995), or simply through a regional base-level fall.

Landscape evolution across passive continental margins provides a clear example of this dynamical picture of plateau erosion. Many passive margins are distinguished by an inland, relatively uneroded, low-relief, high-elevation plateau and a dissected, high-relief coastal zone. The boundary between the two zones is commonly demarcated by a seaward-facing escarpment. The main factors involved in the creation and maintenance of erosional escarpments at passive margins include (1) the geometry of rifting, particularly upper vs. lower plate margins and along-strike segmentation of rifts (e.g. Leeder & Gawthorpe, 1987; Lister *et al.*, 1992), (2) the gradients of extension (i.e. whether they are diffuse or concentrated), (3) the pre-rift topography (i.e. was it regionally high, and did pre-existing drainages flow across or away from the new margin) and (4) post-rift regional uplift or subsidence. The margins of the Red Sea and Gulf of Aden, southern Africa, eastern Australia, India, Madagascar and south-east Brazil are passive margins characterized by large-scale escarpments, despite wide differences in climate, dominant lithologies and age of rifting among them. Although not often acknowledged, an escarpment can also be seen on the eastern US passive margin. This escarpment runs from Georgia north into Virginia and is most clearly expressed in the Cumberland Plateau area and the Blue Ridge Mountains, as evident on the topographic image constructed by Thelin & Pike (1991).

Ollier (1982a, 1985) was the first to suggest that these escarpments initiate when rift flanks are elevated during rifting and propagate inland through the plateau over time. Long-term average propagation rates on the order of 1 km Ma^{-1} can be inferred for a number of passive

---

*Present address: Department of Geological Sciences, Wright-Rieman Laboratories, Rutgers University, New Brunswick, NJ 08903, USA.

margins by assuming that escarpment erosion initiated at the time of rifting, and that the seaward edge of the rift flank was originally located close to the present position of the coastline. Considering the length of passive margins worldwide and an average rift flank plateau height of several hundred metres, it is clear that sediment eroded from passive margins will be an important component of the mass flux from continents to oceans through geological time. The variability in escarpment retreat rates over the course of a given margin's evolution, however, remains unknown, as do the underlying geological and surficial processes responsible for the behaviour of propagating erosion fronts and escarpments. The main purpose of this paper is to explore these issues further using the escarpment along the south-east continental margin of Australia (Fig. 1) as a case study. Ultimately, understanding the geomorphic processes acting across passive margins will help improve geophysical models describing the erosional evolution of continental topography and perhaps shed light on the relationship between tectonics and topography.

Plateau-bounding escarpments in general exhibit two basic forms depending on the direction of surface water drainage on the plateau interior relative to the escarpment. Where surface water flows away from the escarpment, the escarpment takes the form of subdued embayments and promontories, such that its overall trend remains fairly straight as it evolves with time. Where upland streams flow across the escarpment, it takes the form of dramatic, narrow gorges whose heads appear to propagate up the plateau drainage systems as large-scale knickpoints. From now on we refer to these as the drainage divide and the gorge-like escarpment type, respectively. From work on the Colorado Plateau, Schmidt (1987) suggested that the two different escarpment forms are characterized by different propagation rates. In particular, Schmidt noted that the Colorado River is located much closer to the Grand Canyon's

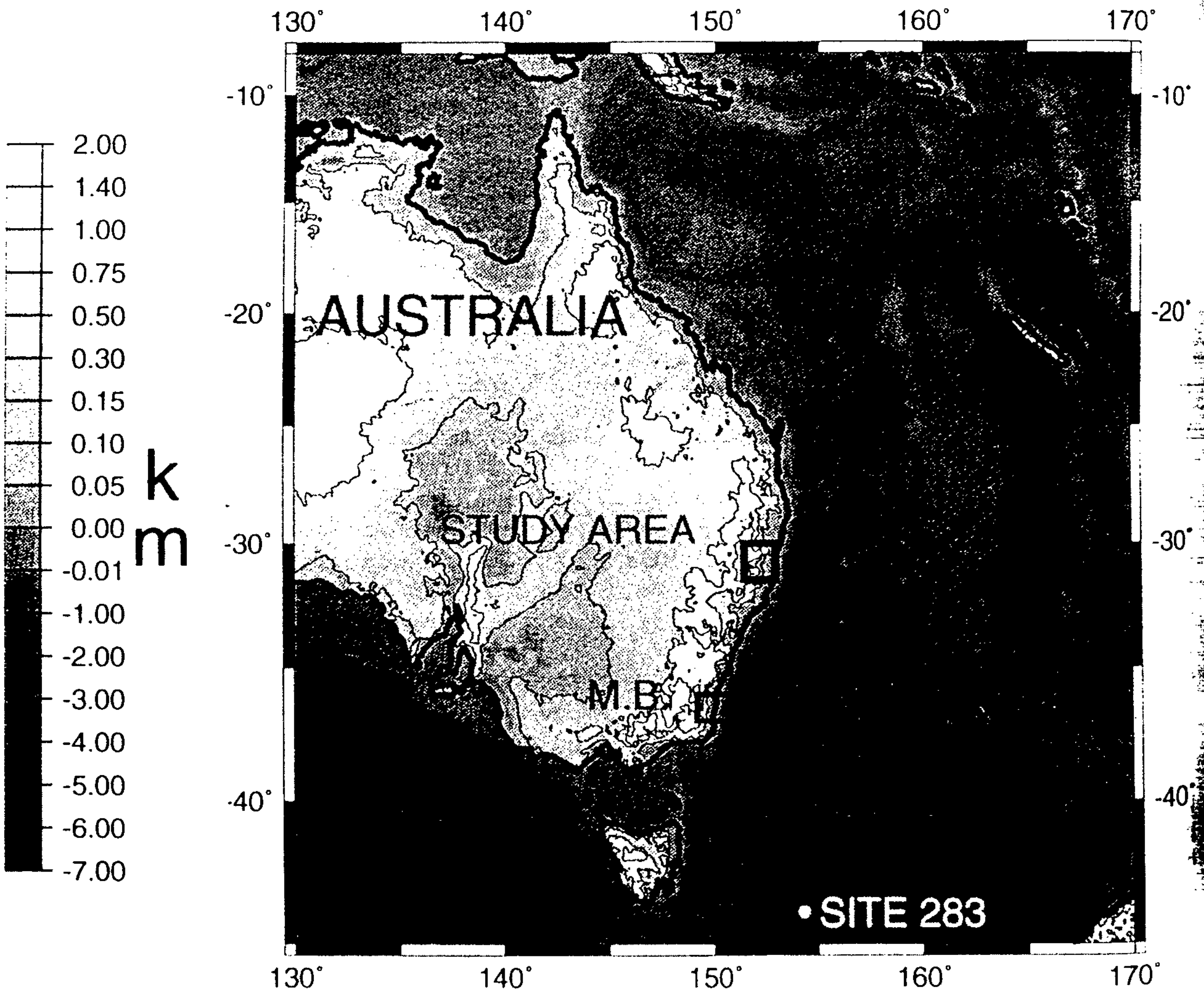

Fig. 1. Grey-scale image of topography of eastern Australia and the adjacent ocean basins. The 100-m, 400-m and 900-m height contours are shown in the continental areas. The New England section of the eastern Australia continental margin is located by the box. M.B. area locates the onshore erosion – offshore deposition mass balance calculation. The location of DSDP Site 283 in the southern Tasman Sea is also shown.

south rim, a drainage divide escarpment, than to the north rim, which is a gorge-like escarpment. The main implication is that the gorge-like form might be associated with higher long-term average erosion rates compared with the drainage divide escarpment type. The gorge-like form of the escarpment is a minority among passive margin escarpment forms. Observations along passive margin escarpments and models of their development show a preference for the drainage divide escarpment form. However, the gorge-like form of the escarpment is more easily explored in greater detail and, consequently, more easily understood because it occupies a more confined land area. Additionally, simple models for escarpment evolution (e.g. Stark, 1994) suggest that the degree of spatial focusing of processes is greater for the gorge-like escarpment form. What we learn from studying the gorge-like escarpments can then be applied to the drainage divide form of escarpment.

South-east Australian passive margin

We examine the link between escarpment propagation and landscape dissection on the south-east Australian passive margin (Fig. 1). Rifting between the Australian continent and the Lord Howe Rise terminated about 85 Ma with formation of the Tasman Sea in Late Cretaceous to Early Tertiary time (Hayes & Ringis, 1973; Weissel & Hayes, 1977). The continental-scale topography in Fig. 1 shows that a first-order correlation exists between the width of the submerged portion of the continental margin and the proximity of the eastern highlands to the coast, despite the differing lithostratigraphic units exposed along the length of the margin (Karner & Weissel, 1984). The highlands are high and narrow along the south-east margin where the continental shelf is very narrow. The highlands are lower in elevation and much wider along the north-east margin, where the continental margin is broad and marked by extensive submarine plateaus (Fig. 1). This correlation implies that the origin of the eastern highlands of Australia, and thus the initiation of the erosional escarpment along the seaward side of the highlands, is linked to the amount and geometry of extension that led to the formation of the adjacent ocean basin.

In common with other passive margins, eastern Australia is characterized by an escarpment located up to 200 km inland of the coast (Ollier, 1982a). The escarpment separates a western, highly weathered plateau from a deeply incised, high-relief coastal area to the east. Stable isotope studies indicate the extensive development of old, deep weathering profiles on the upland surface (Bird & Chivas, 1989, 1993). The preservation of Tertiary basalts on the upland surface similarly indicates an old age for the plateau (Young, 1983; Bishop *et al.*, 1985; Young & McDougall, 1993). The antiquity of the surface implies low erosion rates over the plateau surface compared with erosion rates seaward of the escarpment. Apatite fission track ages obtained from exposed early to mid-Palaeozoic granites of the Lachlan fold belt vary systematically across the south-east Australian continental margin, from relatively young (several tens of million years) ages at the coast to Late Palaeozoic ages over the interior plateau surface (Moore *et al.*, 1986; Dumitru *et al.*, 1991). The systematic variation in fission track ages provides a general picture of the thermal effects of erosional denudation across the margin: (a) the decrease in apparent age seaward of the escarpment suggests progressively larger amounts of denudation towards the coastline and (b) the older, less variable ages inland from the location of the escarpment suggest comparatively little erosion or a low erosion rate on the Tableland surface. Similar patterns have been found across the Arabian Red Sea margin (Bohannon *et al.*, 1989) and in south-eastern Brazil (Gallagher *et al.*, 1994).

New England Tableland region

The New England Tableland section of the south-east Australian margin (Fig. 1) offers an excellent opportunity for advancing our understanding of rates and mechanisms of inland propagation of erosional escarpments. It has: a well-known rifting and post-rift tectonic history, characteristic passive margin topography, clear expression in the landscape of the surficial processes attending escarpment retreat, available digital remote sensing and topographic data, and accessible field sites.

The aim of our study is to constrain rates of escarpment retreat, determine the form of the retreat, as expressed in the landscape, and, ultimately, understand the factors controlling the retreat. To this end, we document the kinematics and pattern of escarpment retreat at several spatial and temporal scales using offshore seismic reflection profiles, both cartographic and digital representations of topography, remote sensing imagery, and field observations. We focus here on the gorge-like form of escarpment because it appears (1) that the process rates are greatest here and (2) that the gorge-like form produces more sediment in the same amount of time than the surface water divide form. At the broadest scale, we employ a mass balance approach to assess continental scale dissection across the south-eastern Australian escarpment. At the intermediate scale, we construct a 500-m digital elevation model (DEM) to examine the pattern of erosion in the New England Tableland region of the Australian margin, in particular the Macleay river system. At the finest scale, we study hillslope and channel processes in the vicinity of the escarpment using field observations and 20-m SPOT-derived DEM data.

RIFTING PROCESSES AND ESCARPMENT INITIATION

Central to our study of escarpments is the assumption that these features form as a consequence of rifting. In order for the gorge-like escarpment form to develop, tectonic processes associated with rifting must produce a broad topographic surface that dips regionally toward the ocean basin. To test this idea we obtained almost 15 000 spot heights for the New England Tableland study area (Fig. 1) from the Australian Government's Land Information Group (AUSLIG). These are also used to produce a 500-m DEM for the study area shown later. For the present purpose we retained only those spot heights that are associated with remnant plateau surfaces. To do this we eliminated spot heights from areas seaward of the escarpment that are likely to have been eroded since rifting by inland propagation of the escarpment. We also eliminated those spot heights from Tertiary basalt flows (Wellman & McDougall, 1974) which have added extra height to the plateau surface. We were left with some 4700 elevation values from the remnant plateau surfaces, to which were added elevations hand digitized from the Comboyne and Bulga plateaus slightly to the south of the study area. Pain & Ollier (1986) recognized that these plateaus are seaward 'outliers' of the original, uneroded plateau surface isolated by inland advance of the escarpment.

Two-dimensional low-order polynomial surfaces were fit to the plateau surface spot heights by weighted least squares. Figure 2 shows the distribution of control points and contours of a best-fitting quadratic surface. The few elevations in the range 600–730 m from the Comboyne and Bulga plateaus were given a high weight of 10, the collection of spot heights from the eastern Dorrigo plateau ranging in elevation from 510 to 780 m were given weights of 1, while all other control points received weights of 0.9. It is necessary to give the outlier points a greater weight to ensure that the surface will conform to the elevations of these points. The main features of the quadratic trend surface are that it dips uniformly towards the ocean basin and that its height contours are almost parallel to the coastline (Fig. 2). The surface predicts that heights should be less than 500 m near the shoreline, in agreement with maximum spot height elevations on the 1 : 250 000 topographic sheets for the region. The weighting made little difference to the overall shape and seaward dip of the surface, but did make certain that the final surface contained the outlying elevations.

The main implication of the surface-fitting work is that we would expect the gorge-like escarpment form to develop along this section of the south-east Australian margin because the trend surface dips regionally toward the sea. The attitude of the sub-basalt surface of the early Miocene Ebor volcano (Ollier, 1982b) provides further evidence for a seaward regional dip of the Tableland surface at earlier times in the margin's history.

We suggest that post-rift flexural coupling between the rapidly subsiding oceanic lithosphere of the Tasman Basin and the buoyant, flanking continental margin (e.g. Turcotte *et al.*, 1977) might explain the inferred regional seaward dip of the plateau surface. To explore this we extracted a profile across the trend surface perpendicular to the coast (Fig. 2), and compared its shape with elevation profiles (Fig. 3) from a model for the time-dependent flexural coupling across the continental margin developed by Weissel & Karner (1989) and Karner & Driscoll (1993). Figure 3 also shows elevations along the same profile from a 500-m DEM constructed from the AUSLIG spot heights, as discussed below. Briefly, the model pertains to a continental lithosphere 125 km thick with a 37-km-thick crust, which is extended instantaneously over a width of 25 km to form a wide ocean basin. The present-day coastline is located at the 0-km abscissa, and the landward edge of the rift zone, which is located at the right-hand side of Fig. 3, coincides with the midpoint of the continental slope. As noted earlier the south-east continental margin of Australia is very narrow (Fig. 1). We have not tried to achieve a close match between the trend surface profile and either the 81- or the 100-Ma since rifting model profile because important tectonic processes affecting margin development, like erosional rebound and offshore sedimentation have not been included in the modelling. Rather, our intent is to show that flexural coupling across the continental margin since rifting provides a satisfactory explanation for the regional seaward dip of the remnant plateau surface and this, in turn, explains why the gorge-like form of erosional escarpment is predominant on the New England section of the south-east Australian margin.

MASS BALANCE APPROACH

The long-term denudation patterns of the Australian margin can been examined by combining knowledge of the margin's tectonic history with the offshore depositional record. First-order parity is expected between the amount eroded from the continent and that deposited offshore. The offshore sediment volume should be approximately equal to or greater than the volume of material removed onshore. Along the south-west African margin, Brown *et al.* (1990) and Rust & Summerfield (1990) compared the offshore sedimentary record with erosion across the continental landmass to evaluate the erosional history of the margin. Brown *et al.* (1990) utilized fission track data and borehole data to constrain erosion rates on the south-west African margin. The apatite fission track data suggested early Cretaceous cooling of the upper crust and they linked this cooling event to accelerated erosion onshore during early rifting (Brown *et al.*, 1990). Rust & Summerfield (1990) analysed isopach and borehole data offshore and compared these data to models of onshore drainage development. They integrated the isopach and borehole data (the two data sets must be combined; if used independently they give inconsistent results) and estimated the onshore catchment area draining to the ocean basin. They concluded that the sediment accumulation data are consistent with an erosion scenario in which denudation is spatially and temporally variable and is generally focused along a narrow zone bordering the margin. Their results also suggest significant isostatic uplift and flexural upwarping

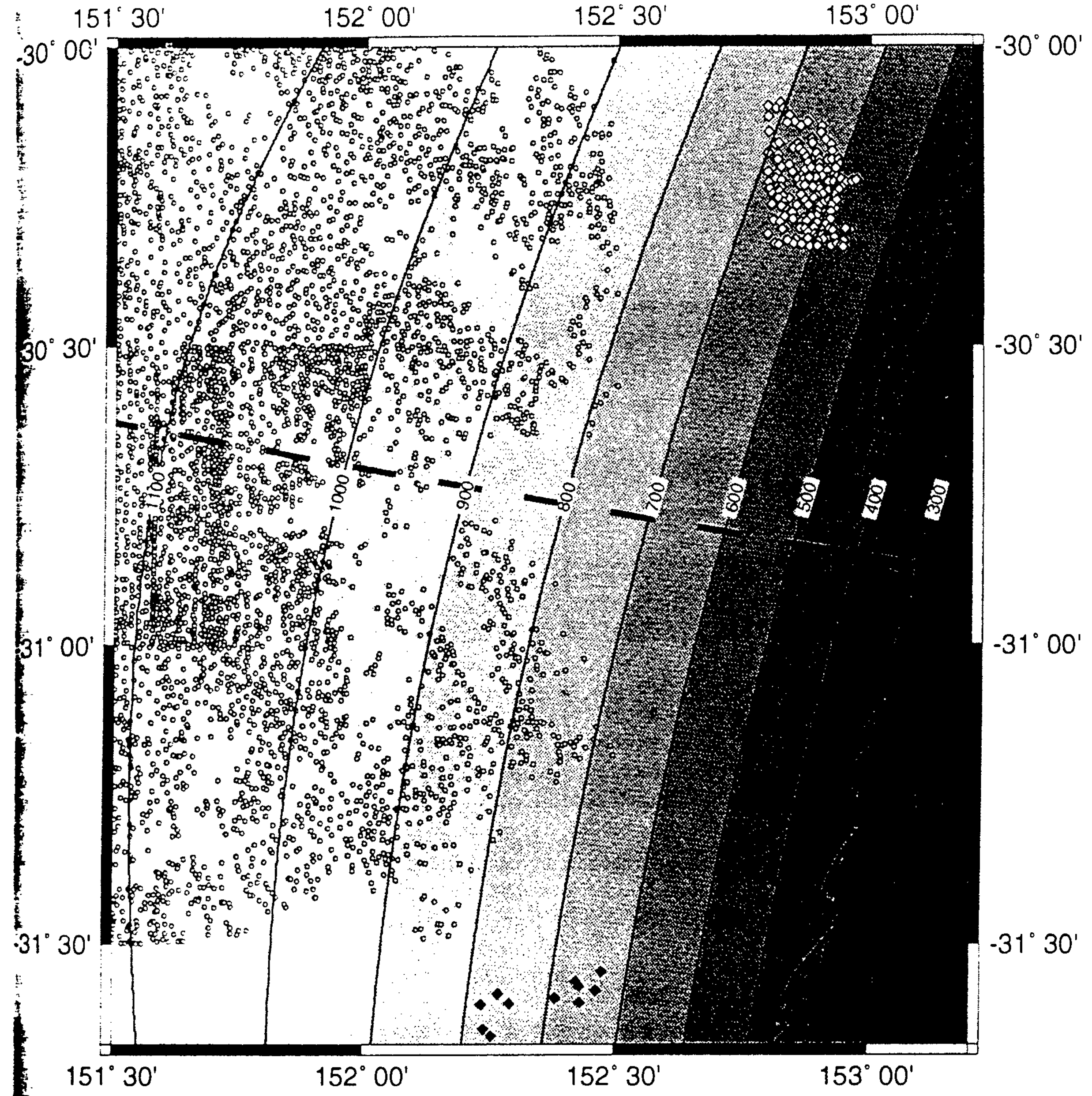

ig. 2. Best fitting two-dimensional quadratic surface to the spot heights from remnants of the New England Tableland surface. rface height is contoured every 100 m. The numerous, small open circles denote control points given a weighting of 0.9 in the ulation, the small white diamonds from the eastern part of the Dorrigo plateau in the north-east are weighted at 1.0, and the ll black diamonds from the Bulga and Comboyne plateaus in the far south have weights of 10.0. The present-day coastline is solid black curve. The bold broken line locates the profile of the trend surface shown in Fig. 3.

he margin has occurred since rifting. We performed imilar mass balance along the Australian margin ween 36° and 37°S latitude, using offshore sediment ckness estimates from seismic reflection profiles and stratigraphy from DSDP Site 283 (Figs 1 and 4), in mbination with estimates of onshore denudation based n assumed initial rift-flank plateau surface. This area selected because of the available detailed offshore iment accumulation data and because the amount and e of denudation has been estimated for this section of margin by modelling of apatite fission track data umitru *et al.*, 1991; van der Beek *et al.*, 1995).

Methods

Offshore, Tasman Sea abyssal plain sediments provide a record of the sediments eroded from the rift flank and delivered to the ocean basin over the last 80–100 Ma, assuming erosion proceeds after instantaneous development of an escarpment. To calculate the volume of clastic material deposited in the Tasman Basin, we used sediment thickness estimates made by Ringis (1972) from seismic profiles collected during cruise 47A of the USNS Eltanin (Fig. 5), tied to the stratigraphic section drilled at DSDP Leg 29, site 283 (Fig. 4; Kennett *et al.*, 1974).

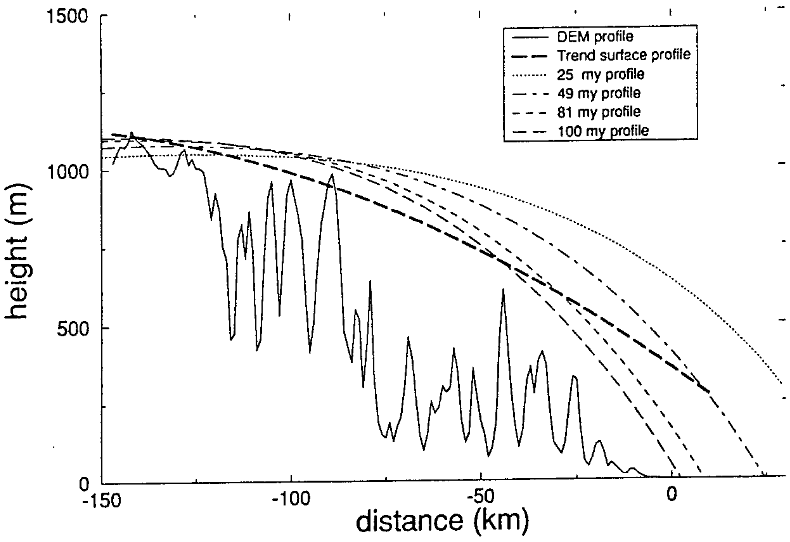

Fig. 3. The quadratic trend surfac profile from Fig. 2 is compared with flank topographic profiles for vario times since rifting generated from models for flexural coupling across th continental margin described in the text. Topography along the same pro extracted from the 500-m DEM in Fig. 7 is also shown.

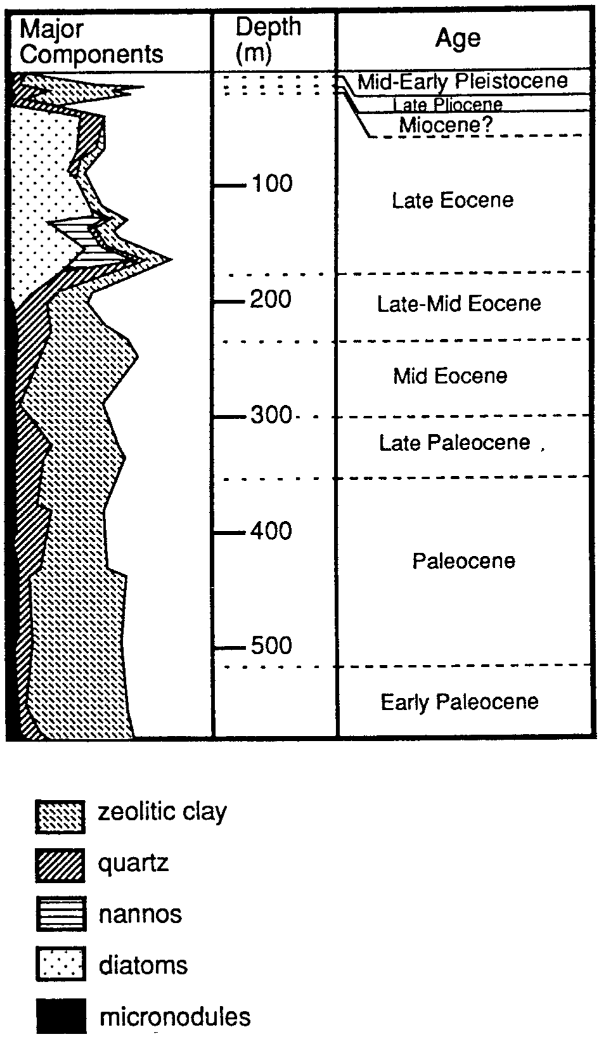

Fig. 4. Lithology, thickness and age of ocean basin sediments cored at DSDP Site 283 (modified from Kennett *et al.*, 1974). Location of the drill site is shown on Fig. 1.

Sediment isopachs indicate sediment thinning eastward to the centre of the basin at the location of the extinct spreading centre, and slight thickening further east toward the Lord Howe Rise (Ringis, 1972). Maxim two-way travel times of over 1.2 s are mapped just e of the base of the slope. The areal extent of the vario sedimentary units was determined using a planimete Although no deep-sea drilling has been done in th latitude band examined, the sedimentary section in th southern part of the Tasman Sea (Fig. 4) has been drilled at DSDP Site 283 (Fig. 1). The section at Site 28 includes five stratigraphic units: a thin late Pliocene t Pleistocene zeolitic clay unit separated by a major hiatu from late Eocene diatom ooze, which is underlain b mid-Eocene silty clay and Palaeocene claystone, restin on highly altered basalt (Fig. 4; Kennett *et al.*, 197 We extrapolated the lithological data recorded at Site 2 to the sedimentary sequences shown on the seism profiles (Fig. 5). In the western part of the basin, interpret the seismics to indicate a sequence of Neoge clastics (seismic unit I, Fig. 5) overlying a layer of diato ooze approximately 200 m thick (seismic unit II, ins Fig. 5), which was deposited over a second underlyin clastic layer (seismic unit III, Fig. 5). To the east, t top layer of clastics is missing, and the sequence consis only of the diatom ooze overlying a presumed clastic un (Fig. 5). The contact between the overlying ooze a underlying clastic layer can be clearly seen in Fig. 5.

We included *all* presumed clastic sediment from t deep Tasman Basin in our mass balance. The Lord Ho Rise is not considered to be a sediment source, as the is little evidence of subaerial erosion and the seismic d indicate sediments onlap the Rise. We decompacted t net sediment accumulation after subtracting the 200 thick diatom ooze layer and assuming an average 2 porosity for the entire clastic section. Some sedimen also stored on the continental shelf and slope, althou the continental shelf is narrow and the slope is steep. estimated this volume of material by using the isopac published in Colwell *et al.* (1993).

We calculated the amount of continental mate eroded seaward of the escarpment by digitizing top

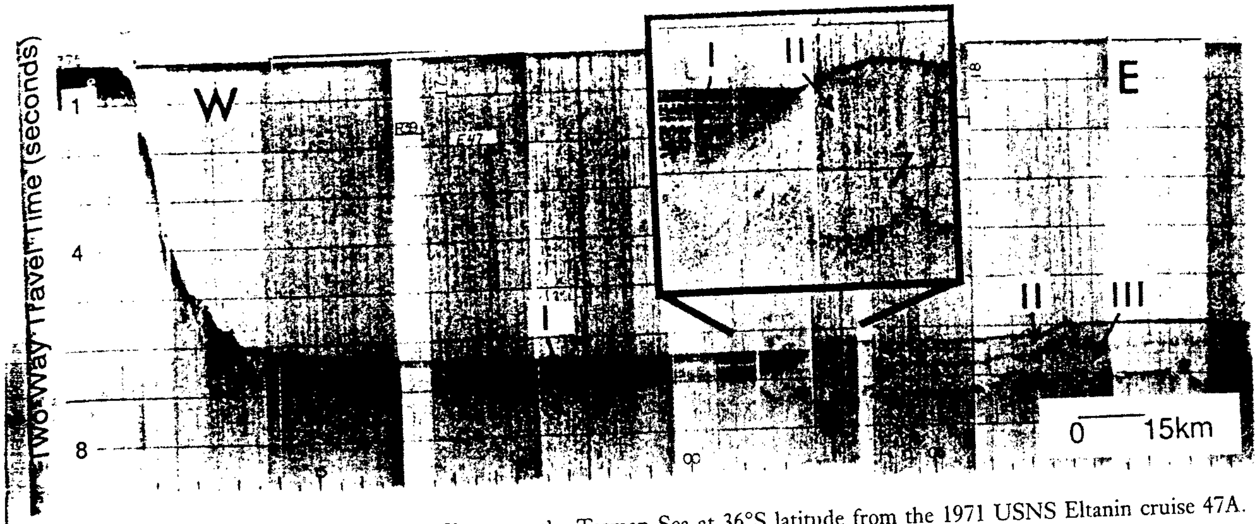

Fig. 5. Single-channel seismic reflection profile across the Tasman Sea at 36°S latitude from the 1971 USNS Eltanin cruise 47A.

graphic profiles 80–100 km in length across the escarpment and out to the coastline (Fig. 6). Five profiles, which were hand digitized from the Bega, Canberra and Ulladulla 1:250000 topography sheets, are spaced approximately every 10 minutes, at 36°7', 36°17', 36°28', 36°39', 36°50' south latitude. The western edge of all the profiles was located on the plateau surface at 149°13'E. Enough topography was digitized west of the escarpment to allow calculation of a mean elevation for the plateau surface on each profile (Fig. 6). The total amount of rock removed is estimated by subtracting the digitized elevations from the assumed plateau surface elevation for each of the profiles. We included all material eroded seaward of the escarpment out to the 200-m continental shelf break.

Results and discussion

Taken together, we estimate the amount of terrigenous material stored offshore averaged along strike to be 339 km^2. The calculated volume/unit length along strike of the margin of material removed by erosion for each profile from south to north are 41, 61, 68, 57 and 58 km^2, respectively, with the maximum occurring along the centre profile. Time-averaged erosion rates can be calculated by dividing the amount of eroded rock by the time since rifting (about 85 Myr). These rates range from 0.04 m Myr^{-1} on the ridge tops to 12 m Myr^{-1} in the valleys. This result is very similar to the average post-rifting erosion rate of 12 m Myr^{-1} estimated for the south-west African margin (Rust & Summerfield, 1990).

The amount of material eroded from the margin has been estimated from apatite fission track data by Dumitru *et al.* (1991) and van der Beek *et al.* (1995). Dumitru *et al.* (1991) calculated a maximum 150 km^2 and a minimum 85 km^2 of rock removed since mid-Cretaceous rifting averaged along strike of the south-east margin. The difference between the two estimates stems from assumptions made about upper crustal temperature gradients that prevailed during rifting. The larger estimate results when a 'normal' (i.e. low) geothermal gradient is assumed during rift and post-rift time. The smaller estimate results when elevated temperature gradients are produced in the rift flank by heat derived from the adjacent rift zone. Our estimates for the amount of erosion are closer to the minimum estimate of Dumitru *et al.* (1991).

Clearly, the amount of rock removed, as determined by subtracting observed topographic cross-sections from assumed initial plateau surfaces, is 5–10 smaller than that derived from analysis of the offshore record of sedimentation. The total volume of sediments stored in the Tasman Sea is likely to be a maximum, as all material below the Eocene diatom ooze was considered to be terrigenous, and the Lord Howe Rise was not considered to be a source of clastics. Conversely, the continental flux calculations are likely to be biased to the low side, as the plateau surface is modelled simply as a flat feature. The values determined by Dumitru *et al.* (1991) fall between our onshore erosion and offshore deposition estimates, with the minimum value based on the fission track data close to our erosion estimates. However, the erosion estimates derived from the fission track data depend on a number assumptions, whereas our estimates are strictly empirical. That the continental flux of material appears to have been lower over time relative to that accumulated in the adjacent ocean basin is an unexpected result that must be resolved in future work.

KINEMATICS OF SCARP RETREAT

Plateau regions are dissected and ultimately eroded by surficial processes occurring along their edges (e.g. Schmidt, 1987; Seidl & Weissel, 1994; Weissel & Seidl, 1994; Weissel *et al.*, 1995). Consequently, understanding the kinematics of scarp retreat (by kinematics, we refer to the speed or rate at which escarpments propagate through the continental landmass) is crucial to understanding erosional evolution of passive margins. As stated at the outset, long-term average migration rates on the

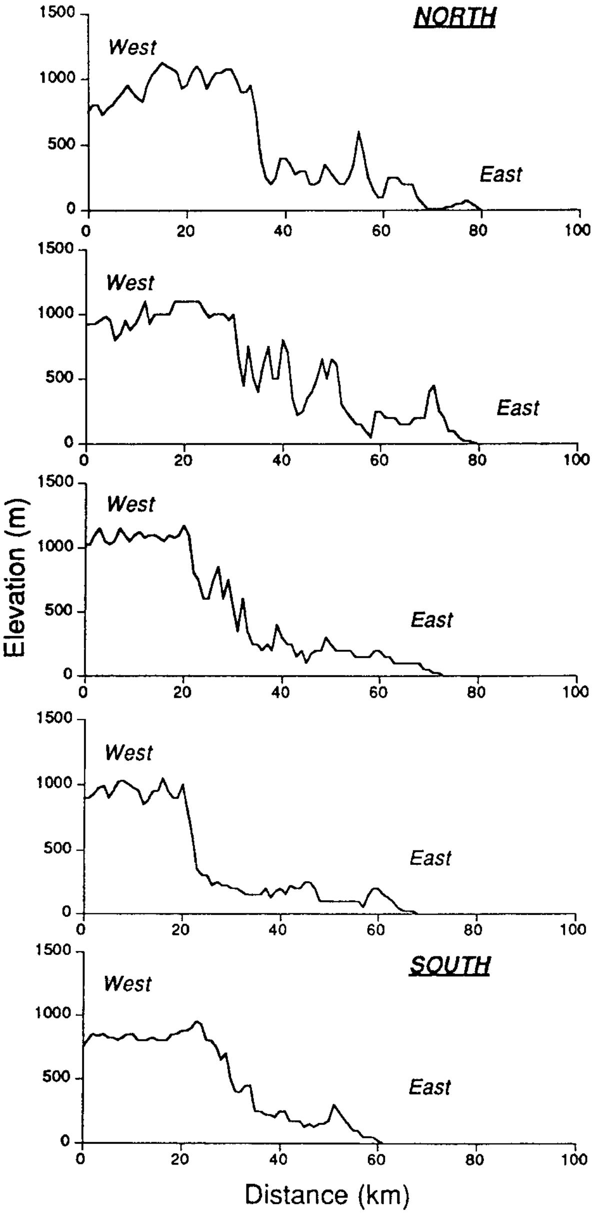

Fig. 6. Topographic cross-sections drawn across the escarpment and out to the coast. The profiles were spaced at 36°07', 36°17', 36°28', 36°39', 36°50' latitude; the western edge of all the profiles was located on the plateau surface at 149°13'.

order of 1 km Myr^{-1} have been estimated for many passive margins; we constrain escarpment retreat rates along the south-east Australia margin below.

Methods

Approximately 15 000 spot heights for the New England Tableland study area on the south-east Australian margin were supplied to us by AUSLIG. These were interpolated onto a 500-m grid using the tensioned spline algorithm of Smith & Wessel (1990). Figure 7 shows the 500-m DEM re-sampled onto a latitude–longitude grid. Drainage networks were extracted from the DEM following the methods of Pratson & Ryan (in press). Streams with more than 100 contributing 500 × 500-m areas are drawn on Fig. 7.

Results and discussion

We focus this study on the tributaries of the Macleay river system (labelled A–N in Fig. 7) which flow some 20–50 km across the gently undulating tableland surface from the continental divide to the west and cascade across the escarpment into narrow, dramatic gorges. Stream bed elevations as a function of distance from the mouth of the Macleay River are shown in Fig. 8. The jaggedness of the profiles shown in Fig. 8 is an artefact of filling 'pits' in the 500-m DEM (Fig. 7) to ensure continuity of drainage. These artefacts do not obscure the main point of our discussion. The position of the gorge head on the profiles, indicated in Fig. 8 as the top or 'lip' of the waterfall or cascade, is manifested as sharp and prominent knickpoints punctuating these profiles. The top of the knickpoint occurs at elevations between 900 and 1000 m for most of the rivers. The main feature of the stream bed elevation profiles for the Macleay river system is that the knickpoints, or gorge heads, for the various streams are all presently situated about 200 km from the coast. It is interesting to note that all knickpoints are located at about the same distance upstream, despite some differences in bedrock lithology traversed by those streams. Because the margin is about 100 Myr old, a long-term average retreat rate on the order of 2 km Myr^{-1} can be calculated from these profiles. This rate is similar those determined for escarpments on other passive continental margins (Ollier, 1985).

Recent modelling efforts have been constructed to explain escarpment retreat along passive margins (Gilchrist *et al.*, 1994; Masek *et al.*, 1994; Tucker & Slingerland, 1994). As pointed out by Tucker & Slingerland (1994), river incision into bedrock and concomitant escarpment retreat are likely to be the primary landscape-forming processes. Measurement of erosion rates, drainage areas and slopes on Hawaiian channels indicates that erosion along bedrock reaches is linearly related to stream power, the product of discharge (or equivalently, contributing area) and channel slope (Seidl *et al.*, 1994). As stated earlier, where the upland streams flow across the escarpment the scarp takes the form of narrow gorges headed by waterfalls, or stream channel knickpoints. River incision into bedrock is important in this context and, where upland streams flow across the escarpment, the scarp acts as a series of discrete channel knickpoints. Tucker & Slingerland (1994) indicate that one of the necessary and sufficient conditions for long-term scarp retreat is incising bedrock rivers along which the erosion rate increases with increasing drainage area. However, our knickpoint retreat rate results (Fig. 8) do not show a straightforward dependence on drainage area. Drainage areas upstream of the knickpoints on the studied channels range from 96 to 1110 km^2. Yet, although the drainage areas vary by an order of magnitude, all the

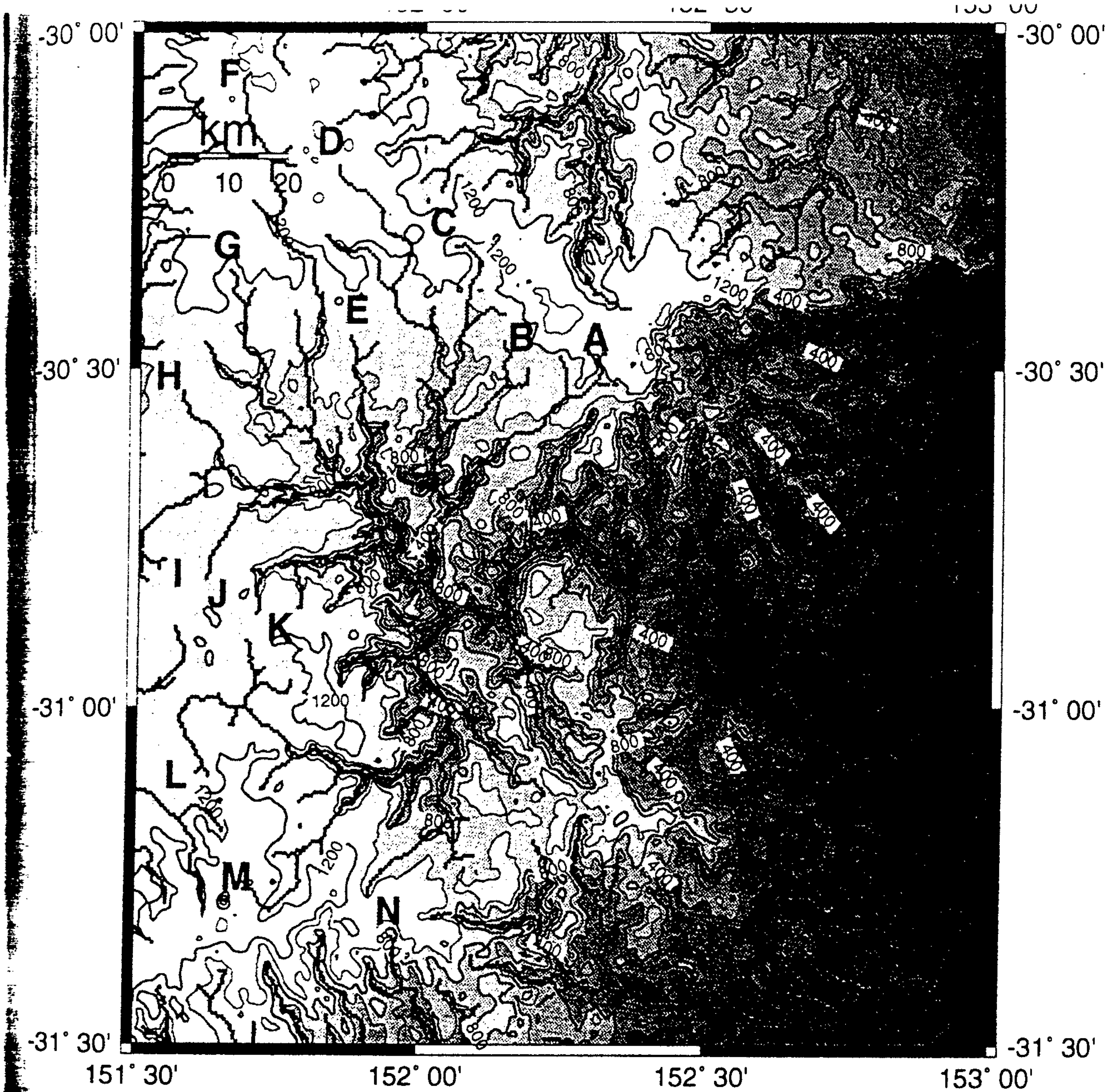

Fig. 7. Grey-scale image of the topography of the New England section of the south-east Australian continental margin (box in Fig. 1). Height values were interpolated at 500-m grid intervals from spot height values provided by AUSLIG. Heights are contoured at 200-m intervals and labels are affixed every 400 m. Fourteen rivers labelled A–N drain from the upland surface into the finger-like gorges and were extracted from the 500-m DEM. Longitudinal stream bed profiles for these rivers are shown in Fig. 8.

knickpoints are located approximately the same distance upstream (Fig. 8).

The propagation of the escarpment through the continental landmass can be viewed as the upstream migration of large-scale knickpoints in bedrock rivers. The problem, then, becomes one of understanding both the rate and process of river incision into bedrock and, equally importantly, the rates and processes associated with knickpoint propagation. Recent work on bedrock rivers has provided clues to the pattern and pace of river incision into bedrock (Bishop *et al.*, 1985; Seidl & Dietrich, 1992; Wohl, 1993; Merritts *et al.*, 1994; Seidl *et al.*, 1994; Wohl *et al.*, 1994; Personius, 1995; Burbank *et al.*, 1996). In Hawaii, knickpoints in basalt are estimated to propagate on the order of 0.5–2.0 mm yr^{-1} (Seidl *et al.*, 1994), similar to the 2 km Myr^{-1} rate estimated for the streams draining the New England Tableland. However, many of the former studies concentrated on basins ranging in size from one to several hundreds of square kilometres, whereas the landscape of SE Australia allows us to place these processes in a large-scale passive margin tectonic setting.

The notable similarity in escarpment retreat rates, both along different streams draining the New England

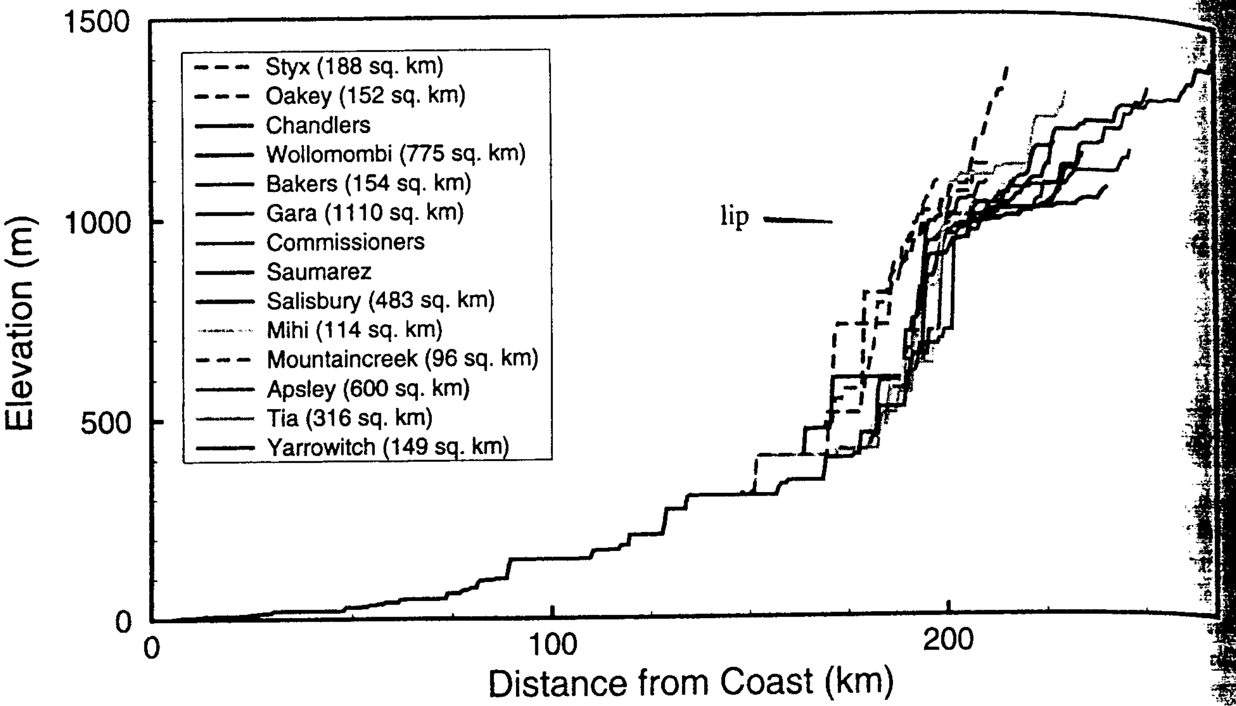

Fig. 8. Longitudinal profiles of rivers flowing into the upper Macleay gorges from the New England Tableland. See Fig. 7 for locations. Distance is given in kilometres from the mouth of the Macleay River. The position of the escarpment is denoted as 'lip'. Drainage areas extracted from the 500-m DEM are listed next to the river names and include only the contributing areas upstream of the knickpoints.

Tableland region and along passive margins worldwide, despite large differences in rock type and climate, suggests that the knickpoint retreat process is governed (to first order) less by surface water and groundwater processes than by rock strength and fracturing of steep rock slopes (Selby, 1993). Young (1985) stressed the need to understand (1) the morphology–stress relationship on waterfalls, (2) the effects of structure and lithology on waterfall form and retreat, and (3) the role water plays in knickpoint maintenance. The role of water is unclear; it may be important in undercutting the waterfall face by cavitation, the power of the water exerted on the lip of the waterfall may cause erosion, and it may reduce the strength of the face through saturation (Young, 1985). However, the knickpoints of the Macleay river system (Fig. 8) are frequently buttressed (Young, 1985), and plunge pools are generally absent. The waterfall crests are often incised but the amount of incision is much less than the height of the falls themselves. The loss of strength through saturation might be an important factor. The morphology of the eroded blocks may provide information about the nature of the retreat. Young (1985) indicated that the joint and fracture patterns determine the shape and size of blocks that will topple from the knickpoint face. A block will topple when $h/w > \cot\alpha$, where h/w is the ratio of height to thickness and α is the slope angle (Goodman & Bray, 1977), so that more failures, and perhaps a faster erosion rate, are to be expected in cases in which vertical fracturing is more extensive than horizontal.

PATTERN OF GORGE HEAD RETREAT

If the gorge heads propagate inland and erosion subsequent to the propagation is slow enough, the pattern of escarpment retreat should be clearly expressed in the south-east Australian landscape. In fact, if all gorge heads migrate according to similar processes, as is indicated by the general similarity in retreat rates (Fig. 8), the same sequence of landscape-forming events should be manifested in the various river valleys. To explore this possibility we looked in detail at the immediate gorge head morphologies of two of the gorges of the Macleay river system, Chandler's Creek – Wollomombi (C & D, Figs 7 and 8), and Baker's Creek (E, Figs 7 and 8).

Methods

We constructed a fine-scale (20-m) DEM for the area surrounding the Chandler's–Wollomombi and Baker's Creek gorges from a pair of SPOT multispectral stereo images. The construction method used is based on conventional stereo photogrammetrical techniques (e.g. Otto & Chau, 1989). As for the 500-m DEM, we extracted the network of streams, this time with support areas ≥ 4 km^2. Longitudinal stream profiles along the drainage lines were extracted from the SPOT-derived 20-m DEM. The Chandler's–Wollomombi and Baker's Creek gorges were visited in 1993 (Fig. 9), and photographs from the two gorges are shown in Figs 10 and 11, respectively.

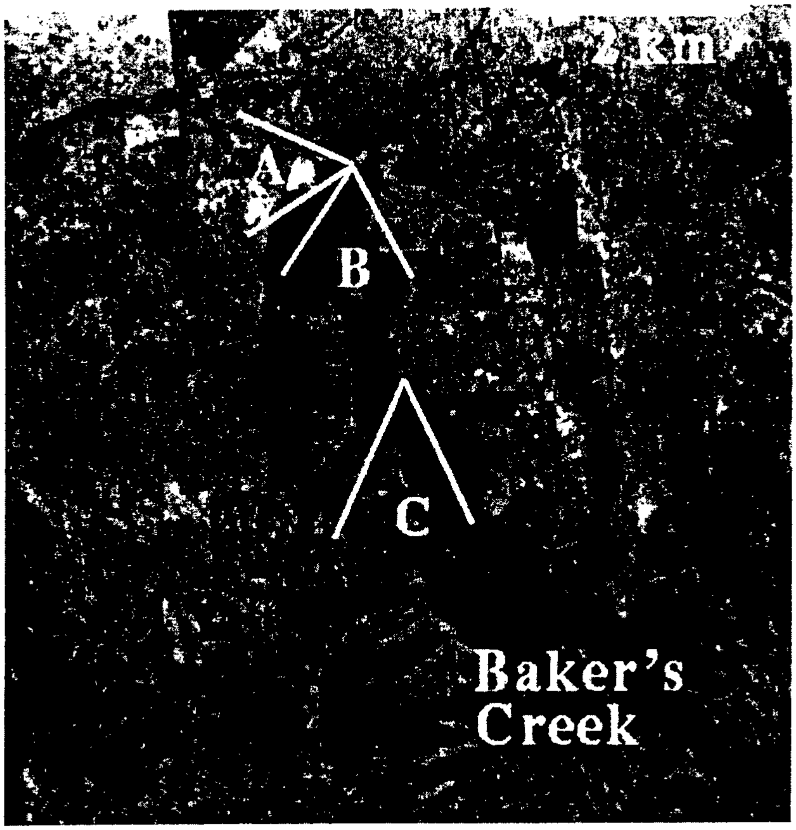

(a)

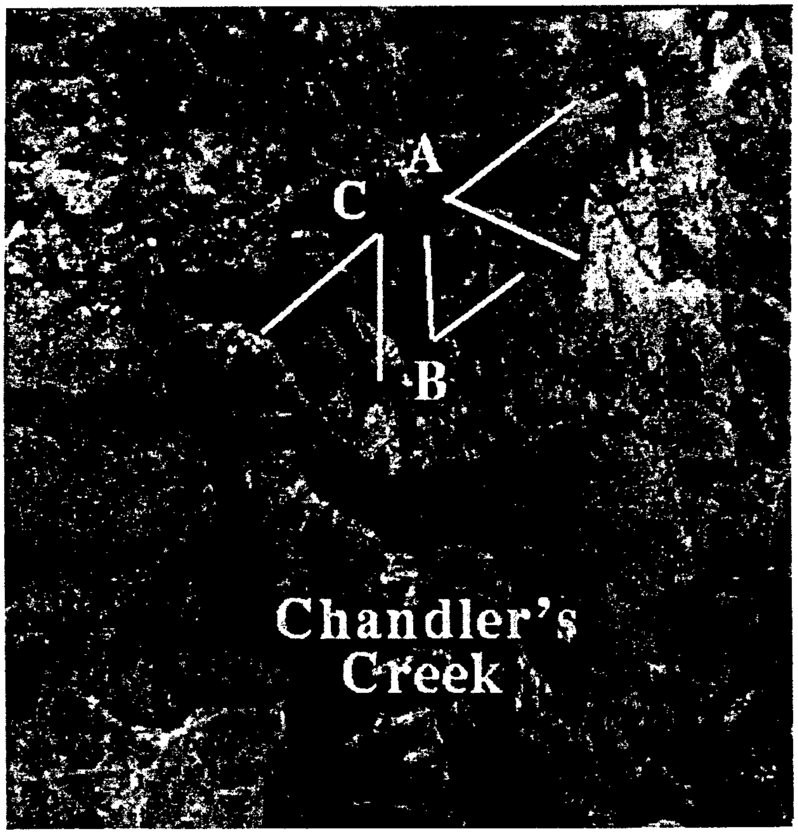

(b)

Fig. 9. Grey-scale rendering of SPOT multispectral imagery showing locations of the photographic views illustrated in Figs 10 and 11. (a) Baker's Creek (E in Figs 7 and 8), (b) Chandler's Creek – Wollomombi (C & D in Figs 7 and 8).

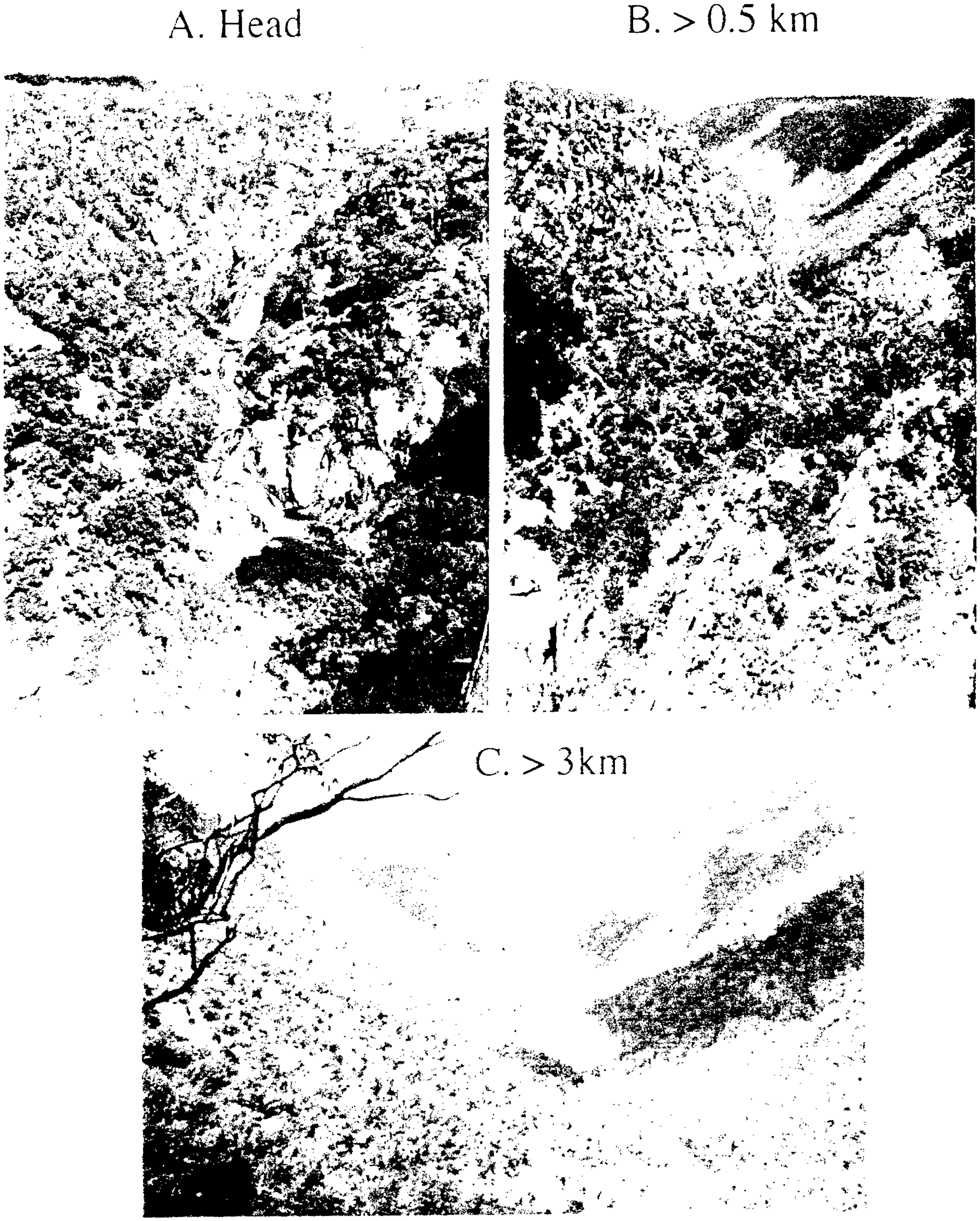

Fig. 10. Photographs of Baker's Creek gorge (E in Figs 7 and 8) showing systematic morphological changes (photographs A–C) in valley sidewall morphology with distance downstream from the gorge head. Photographs located and orientated on Fig. 9(a).

Bedrock lithologies

Most streams of the upper Macleay river system (Fig. 7) have eroded through upper Palaeozoic, fine-grained metasedimentary rocks of the Nambucca 'slate belt' (Binns *et al.*, 1967). The dominant lithologies are shales and silts and their metamorphic equivalents (up to amphibolite grade). Chandler's Creek – Wollomombi (Figs 9b and 11) is an example of a gorge cut into the metasediments. However, the Gara River (F in Figs 7 and 8) and Baker's Creek (Figs 9a and 10) have incised into rocks of the Hillgrove granite suite, probably for the past several million years. The Hillgrove granites, which are classed as adamellites on the 1 : 250 000-scale geological map of the area (Binns *et al.*, 1967), are exposed at several locations east of Armidale. A late Carboniferous

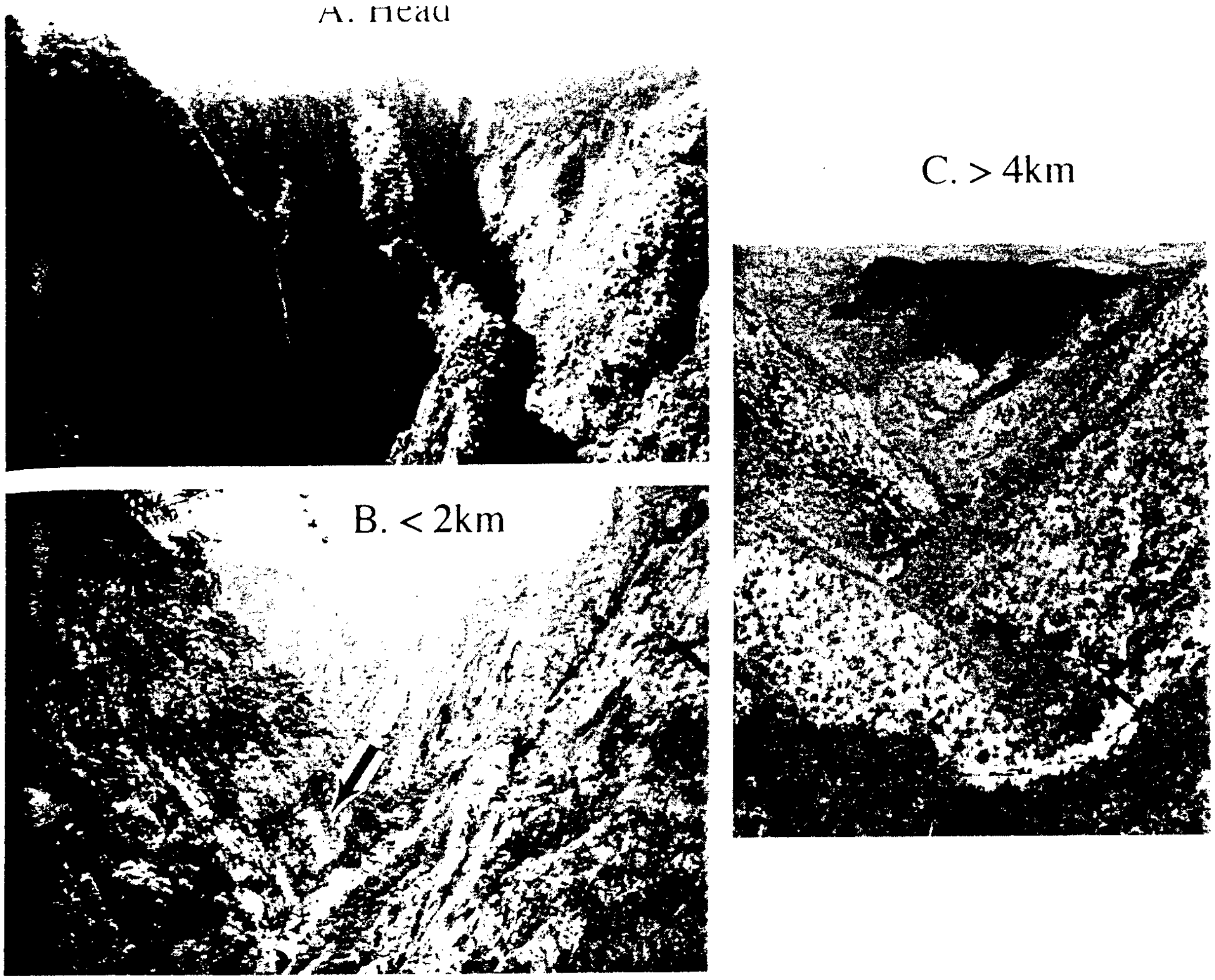

Fig. 11. Chandler's Creek – Wollomombi River gorge (C and D in Figs 7 and 8) showing changes in hillslope morphology (photographs A–C) with distance downstream from gorge head. In A, the Wollomombi River enters over the sidewall, while the gorge head on Chandler's Creek can be seen in the distance. Note the overall decline in sidewall slope as the valley deepens with increasing distance from the gorge head. Photographs located and orientated on Fig. 9(b).

cooling age of about 295 Ma has been obtained for the Hillgrove granite suite from Rb–Sr whole-rock dating (Flood & Shaw, 1977).

Evolution of stream channels and gorge sidewalls

On the Tableland the river longitudinal profiles are generally straight and are commonly punctuated by convexities. Downstream of the knickpoints, the channel profiles are generally concave up. The furthest upstream advance of the erosional escarpment is marked by the dramatic cascades across the gorge heads (Figs 10a and 11a). The gorges in the metasediments are marked by extremely abrupt, almost vertical headwalls, over which the upland streams cascade in vertical drops exceeding 150 m (e.g. Fig. 11a). Different characteristic waterfall morphologies are associated with different rock types: knickpoints formed in the granites have a stepped form (Fig. 10a), whereas those formed in the metasediments are sheer vertical drops buttressed at the base (Fig. 11a).

Close examination of gorge sidewall and channel morphology downstream of the gorge heads (Figs 10 and 11) suggests an evolutionary pattern repeated in most, if not all, of the Macleay river gorges, with minor variation related to bedrock lithology. Overall, the gorge sidewalls decline in slope and alluvial sediment size decreases as the valleys deepen and widen with distance downstream from the gorge head. The walls in the gorge head vicinity are very steep, exposing bare rock, and fresh rockfall scars are evident on the walls along with debris slide material below (Figs 10a and 11a). In the first few kilometres downstream the sidewalls are mainly bare rock and, although less steep, appear mechanically unstable, and large boulders mantle the channel bed (Figs 10b and 11b). Several kilometres downstream the slopes have declined sufficiently to allow development of soil profiles and vegetation on the hillslopes, although bedrock outcrops sporadically (Figs 10c and 11c).

These observations demonstrate a clear coupling between channel and hillslope processes following passage of the gorge head upstream. Assuming an initial condition similar to that demonstrated by the upstream channels, we observe the following sequence of events: (1) immediately after passage of the knickpoint, a deep, narrow gorge with steep valley sidewalls is formed directly downstream of the waterfall as the channel is incised to the depth of the knickpoint (Fig. 10a); (2) the increased sidewall gradient and surface area promotes mechanical instability of the hillslopes, and debris delivery to the channel is increased commensurately; (3) the introduction of increased sediment load into the channel causes a initially rapid channel incision and a narrow, steep-walled notch is cut into the channel (Fig. 10b); (4) with time, the supply and size of sediment delivered to the channel decreases, channel beds become mantled by alluvium and valley walls become soil-mantled (Figs 10c and 11c). We illustrate this pattern of landscape change with distance downstream schematically in Fig. 12, and suggest that the same sequence of geomorphic processes occurs in all the valleys of the Macleay river system of the south-east Australian margin.

This coupling between stream incision and hillslope development is not a new idea in geomorphology. Boundary conditions to one-dimensional numerical models of hillslope development commonly involve an aggrading or incising 'velocity' for an external stream as a driving mechanism for slope evolution (e.g. Kirkby, 1971, 1983; Carson & Kirkby, 1972; Ahnert, 1973, 1976; Fernandes, 1994). The Macleay River valleys provide remarkably clear field evidence that landscapes evolve through coupling between stream incision and hillslope mass-movement processes. The trigger for this development is the passage upstream of knickpoint or gorge head. However, the exact processes underlying knickpoint propagation still remain to be defined (e.g. Young, 1985; Seidl *et al.*, 1994).

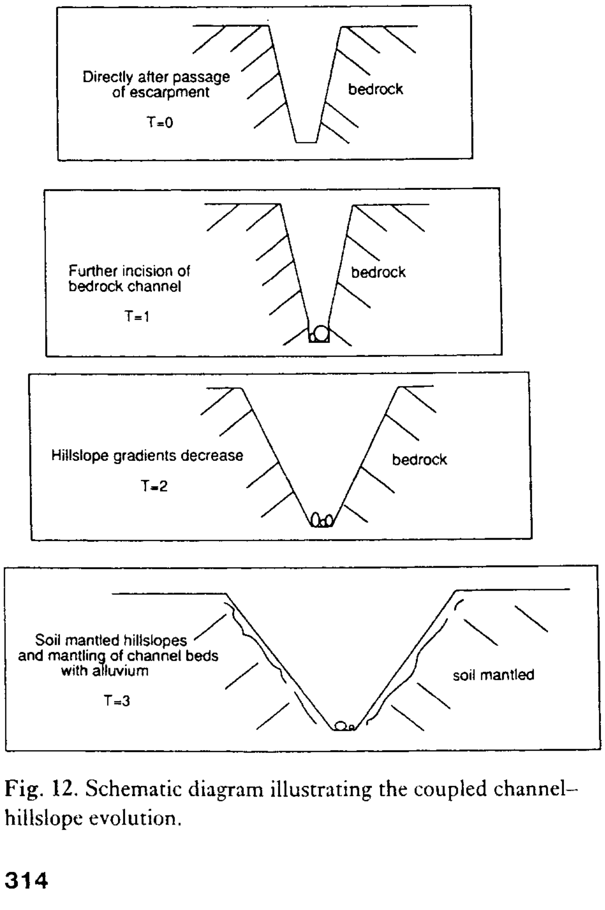

Fig. 12. Schematic diagram illustrating the coupled channel–hillslope evolution.

CONCLUSIONS

Field relations in the New England Tableland region clearly demonstrate the interrelationships among scarp retreat, bedrock channel incision, and hillslope form, which are likely to be applicable to other passive margins and to the general problem of knickpoint migration up bedrock rivers. Our study of the rate and pattern of escarpment propagation across the south-east Australian margin allows us to draw the following conclusions.

1 The remnant New England Tableland surface dips regionally toward the Tasman Sea; this explains why the gorge-like form of escarpment is prominent along the margin. Flexural coupling between the buoyant rift flank and the rapidly subsiding Tasman Sea Basin provides an explanation for the seaward dip of the Tableland surface.

2 Using a mass balance approach we have determined that the amount of clastic material stored offshore is greater than that estimated to have been eroded onshore and seaward of the escarpment. Our estimate of the material eroded is close to the Dumitru *et al.* (1991) estimate from fission track data. However, it is likely that our offshore estimate is a maximum because we have attributed all of the material stored across the entire width of the Tasman Sea to erosion of the south-east Australian margin.

3 Analysis of longitudinal profiles of rivers draining across the New England Tableland reveals that gorge head knickpoints are all located about 200 km upstream, despite different bedrock lithologies traversed by the channels. Based on the age of the south-east Australia margin, a long-term escarpment propagation rate of 2 km Myr^{-1} is estimated and this propagation rate is similar to that inferred for other passive margins.

4 Field-based observations made in several of the Macleay River gorges indicate a common and consistent evolutionary pattern of channel and hillslope development following passage of the knickpoint upstream.

ACKNOWLEDGEMENTS

We thank Neal Driscoll, Garry Karner, Jim McKean and Colin Stark for fruitful discussions and Kelin Whipple for his review. G.K. is thanked for help with the flexure modelling software. We thank the Australian Government's Land Information Group (AUSLIG) for providing the spot height data for the New England Tableland area. This work was supported by NASA grants NAGW-2114 and NAG5-2987. Lamont-Doherty Earth Observatory contribution no. 5471.

REFERENCES

AHNERT, F. (1973) COSLOP-2: a comprehensive model for simulating slope profile development. *Geocom. Programs*, **8**, 1–14.

AHNERT, F. (1987) Process-response models of denudation at different spatial scales. In: *Geomorphological Models–Theoretical and Empirical Aspects* (Ed. by F. Ahnert), *Catena Supplement*, **10**, 31–51.

VAN DER BEEK, P., ANDRIESSEN, P. & CLOETINGH, S. (1995) Morphotectonic evolution of rifted continental margins: inferences from a coupled tectonic-surface processes model and fission track thermochronology. *Tectonics*, **14**, 406–421.

BINNS, R.A. *et al.* (1967) *Geological map of New England, 1,250,000 – New England Tableland – southern part, with explanatory text*. University of New England, NSW.

BIRD, M.I. & CHIVAS, A.R. (1989) Stable-isotope geochronology of the Australian regolith. *Geochim. Cosmochim. Acta*, **53**, 3239–3256.

BIRD, M.I. & CHIVAS, A.R. (1993) Geomorphic and palaeoclimatic implications of an oxygen-isotope chronology for Australian deeply weathered profiles. *Aust. J. Earth Sci.*, **40**, 345–358.

BISHOP, P., YOUNG, R.W. & MCDOUGALL, I. (1985) Stream profile change and long term landscape evolution: Early Miocene and Modern rivers of the East Australian Highland Crest, Central New South Wales, Australia. *J. Geol.*, **93**, 455–474.

BOHANNON, R.G., NAESER, C.W., SCHMIDT, D.L. & ZIMMERMAN, R.A. (1989) The timing of uplift, volcanism and rifting peripheral to the Red Sea: a case for passive rifting? *J. geophys. Res.*, **94**, 1683–1701.

BROWN, R.W., RUST, D.J., SUMMERFIELD, M.A., GLEADOW, A.J. & DEWITT, M.C.J. (1990) An Early Cretaceous phase of accelerated erosion on the south-western margin of Africa: evidence from apatite fission track analysis and the offshore sedimentary record. *Nuclear Tracks Radiation Measurement*, 17, 339–350.

BURBANK, D.W., LELAND, J., FIELDING, E., ANDERSON, R.S., BROZOVIC, N., REID, M.R. & DUNCAN, C. (1996) Bedrock incision, rock uplift and threshold hillslopes in the northwestern Himalyas. *Nature*, **379**, 505–510.

CARSON, M.A. & KIRKBY, M.J. (1972) *Hillslope Form and Process*. Cambridge University Press, Cambridge.

COLWELL, J.B., COFFIN, M.F. & SPENCER, R.A. (1993) Structure of the southern New South Wales continental margin, southeastern Australia. *BMR J. Aust. Geol. Geophys.*, **13**, 333–343.

DUMITRU, T.A., HILL, K.C., COYLE, D.A., DUDDY, I.R., FOSTER, D.A., GLEADOW, A.J.W., GREEN, P.F., KOHN, B.P., LASLETT, G.M. & O'SULLIVAN, A.J. (1991) Fission track thermochronology: Application to continental rifting of south-eastern Australia. *APEA J.*, 31, 131–142.

FERNANDES, N.F. (1994) *Hillslope evolution by diffusive processes: the problem of equilibrium and the effects of climate and tectonic changes*. PhD thesis, University of California at Berkeley.

FIELDING, E.J., ISACKS, B.L, BARAZANGI, M., DUNCAN, C. (1994) How flat is Tibet? *Geology*, **22**, 163–167.

FLOOD, R.H. & SHAW, S.E. (1977) Two 'S-type' granite suites with low initial $^{87}Sr/^{86}Sr$ ratios from the New England batholith, Australia. *Contrib. Miner. Petrol.*, **61**, 163–173.

GALLAGHER, K., HAWKESWORTH, C.J. & MANTOVANI, M.S.M. (1994) The denudational history of the onshore continental margin of SE Brazil from apatite fission track data. *J. geophys. Res.*, 99, 18,117–18,145.

GILCHRIST, A.R., KOOI, H. & BEAUMONT, C. (1994) Post-Gondwana geomorphic evolution of southwestern Africa: implications for the controls on landscape development from observations and numerical experiments. *J. geophys. Res.*, **99**, 12,211-12,228.

GILCHRIST, A.R. & SUMMERFIELD, M.A. (1990) Differential denudation and flexural isostasy in the formation of rifted-margin upwarps. *Nature*, **346**, 739–742.

GOODMAN, N.M. & BRAY, J.W. (1977) *Rock Engineering for Foundations and Slopes*, pp. 201–234. American Society of Civil Engineering, New York.

HAYES, D.E. & RINGIS, J. (1973) Seafloor spreading in the Tasman Sea. *Nature*, **243**, 454–458.

KARNER, G.D. & DRISCOLL, N.W. (1993) Rift flank topography and extensional basin architecture: Formation of Broken Ridge, southeast Indian Ocean. *An. Acad. bras. Ci.*, **65** (Suppl. 2), 263–294.

KARNER, G.D. & WEISSEL, J.K. (1984) Thermally induced uplift and flexural readjustment of the eastern Australian highlands (abstract). *7th Australian Geological Convention, Geological Society of Australia*, pp. 293–294.

KENNETT, J.P., HOUTZ, R.E. *et al.* (1974) *Initial Reports of the Deep Sea Drilling Project*, 29, 365-402.

KIRKBY, M.J. (1971) Hillslope process-response models based on the continuity equation. In: *Slopes: Form and Process* (Ed. by D. Brunsden), *IBG Special Publication*, 3, 15–30.

KIRKBY, M.J. (1983) The continuity equation slope model and basal boundary conditions: a further comment. *Earth. Surf. Process. Landforms*, 8, 287–288.

LEEDER, M. & GAWTHORPE, R. (1987) Sedimentary models for extensional tilt-block/half-graben basins. In: *Continental Extensional Tectonics* (Ed. by M. P. Coward, J. F. Dewey and P. L. Hancock), *Spec. Pupl. Geol. Soc. Am.a*, 28, 139–152.

LISTER, G.S., ETHEERIDGE, M.A. & SYMONDS, P.A. (1992) Detachment models for the formaiton of passive continental margins. *Tectonics*, **10**, 1938–1064.

MASEK, J.G., ISACKS, B.L., GUBBELS, T.L. & FIELDING, E.J. (1994) Erosion and tectonics at the margins of continental plateaus. *J. geophys. Res.*, **99**, 13,941–13,956.

MERRITTS, D.J., VINCENT, K.R. & WOHL, E.E. (1994) Long river profiles, tectonism, and eustasy: a guide to interpreting fluvial terraces. *J. geophys. Res.*, **99**, 14,031-14,050.

MOORE, M.E., GLEADOW, A.J. & LOVERING, J.F. (1986) Thermal evolution of rifted continental margins: new evidence from fission tracks in basement apatites from southeastern Australia. *Earth planet. Sci. Lett.*, **78**, 255–270.

OLLIER, C.D. (1982a) The Great Escarpment of eastern Australia: tectonic and geomorphic significance. *J. Geol. Soc. Aust.*, **29**, 13–23.

OLLIER, C.D. (1982b) Geomorphology and tectonics of the Dorrigo Plateau, NSW. *J. Geol. Soc. Aust.*, **29**, 431–435.

OLLIER, C.D. (1985) Morphotectonics of passive continental margins: Introduction. *Z. Geomorphol., N.F.* Suppl. Bd., 54, 1–9.

OTTO, G.P. & CHAU, T.K.W. (1989) 'Region-growing' algorithm for matching of terrain images. *Image Vision Computing*, 7, 83–94.

PAIN, C.F. & OLLIER, C.D. (1986) The Comboyne and Bulga Plateaus and the evolution of the great escarpment in New South Wales. *J. Proc. Royal Soc. New South Wales*, **119**, 123–130.

Personius, S.F. (1995) Late Quaternary stream incision and uplift in the forearc of the Cascadia subduction zone, western Oregon. *J. geophys. Res.*, 100, 20,193–20,210.

Pratson, L.F. & Ryan, W.B.F. (in press) Automated drainage extraction applied to the Monterey Submarine Drainage System. In: *State of the Art in Seafloor Mapping* (Ed. by M. Edwards), *Marine Geophysical Research.*

Ringis, J. (1972) *The structure and history of the Tasman Sea and the Southeast Australian margin.* PhD thesis, University of New South Wales.

Rust, D.J. & Summerfield, M.A. (1990) Isopach and borehole data as indicators of rifted margin evolution in southwestern Africa. *Mar. Petrol. Geol.*, 7, 277–287.

Schmidt, K.-H. (1987) Factors influencing structural landform dynamics on the Colorado Plateaus and the necessity of calibrating theoretical models by empirical data. In: *Geomorphological Models – Theoretical and Empirical Aspects* (Ed. by F. Ahnert), *Catena Supplement*, **10**, 51–66.

Seidl, M.A. & Dietrich, W.E. (1992) The problem of channel erosion into bedrock. In: *Functional Geomorphology* (Ed. by K. -H. Schmidt and J. DePloey), *Catena Supplement*, **23**, 101–124.

Seidl, M.A., Dietrich, W.E. & Kirchner, J.W. (1994) Longitudinal profile development into bedrock: an analysis of Hawaiian channels. *J. Geol.*, **102**, 457–474.

Seidl, M.A. & Weissel, J.K. (1994) Erosion across a rifted continental margin: an example from SE Australia. *Geological Society of America Annual Meeting Abstracts with Programs*, 26, A241.

Selby, M.J. (1993) *Hillslope Materials and Processes.* Oxford University Press, Oxford.

Smith, W.H.F. & Wessel, P. (1990) Gridding with continuous curvature splines in tension. *Geophysics*, **55**, 293–305.

Stark, C.P. (1994) Cluster growth modeling of plateau erosion. *J. geophys. Res.*, **99**, 13957–13970.

Summerfield, M.A. (1991) *Global Geomorphology.* Longman, London.

Thelin, G.P. & Pike, R.J. (1991) Landforms of the conterminous United States – A digital shaded-relief portrayal. *USGS Miscellaneous Investigations Map*, **I-2206**, scale 1:3,500,000.

Tucker, G.E. & Slingerland, R.L. (1994) Erosional dynamics, flexural isostasy, and long-lived escarpments: a numerical modeling study. *J. geophys. Res.*, 99, 229–12, 243.

Turcotte, D.L., Ahern, J.L. & Bird, J.M. (1977) The state of stress at continental margins. *Tectonophysics*, 42, 1–28.

Weissel, J.K. (1990) Long-term erosional development of rifted continental margins: toward a quantitative understanding. *Proceedings of the Pacific Rim Congress* **90**, III, pp. 63–70. Austr. Inst. Min. & Metal., Parkville (Vic.) Australia.

Weissel, J.K. & Hayes, D.E. (1977) Evolution of the Tasman Sea reappraised. *Earth planet. Sci. Lett.*, 36, 77–84.

Weissel, J.K. & Karner, G.D. (1989) Flexural uplift of rift flanks due to mechanical unloading of the lithosphere during extension. *J. geophys. Res.*, **94**, 13919–13950.

Weissel, J.K., Malinverno, A., Harding, D.J. & Karner, G.D. (1995) Erosional development of the Ethiopian Plateau of Northeast Africa from a fractal analysis of topography. In: *Fractals in Petroleum Geology and Earth Processes* (Ed. by C. C. Barton and P. R. La Pointe), pp. 127–142. Plenum Press, New York.

Weissel, J.K. & Seidl, M.A. (1994) Geomorphic processes at erosional escarpments along passive continental margins: example from Eastern Australia. *Eos*, 75, 296.

Wellman, P. & McDougall, I. (1974) Potassium–argon dates on the Cainozoic volcanic rocks of New South Wales. *J. Geol. Soc. Aust.*, 21, 247–272.

Wohl, E.E. (1993) Bedrock channel incision along Piccaninny Creek, Australia. *J. Geol.*, 101, 749–761.

Wohl, E.E., Greenbaum, N., Schick, A.P. & Baker, V.R. (1994) Controls on bedrock channel incision along Nahal Paran, Israel. *Earth. Surf. Process. Landforms*, 19, 1–13.

Young, R.W. (1983) The tempo of geomorphologic change: evidence from southeastern Australia. *J. Geol.*, 91, 221–230.

Young, R.W. (1985) Waterfalls: form and process. *Z. Geomorphol., N.F.* Suppl. Bd, 55, 81–95.

Young, R.W. & McDougall, I. (1993) Long-term landscape evolution: early Miocene and Modern rivers in southern New South Wales, Australia. *J. Geol.*, 101, 35–49.

Received 25 July 1995; revision accepted 4 March 1996.

STUDIES OF MASS-MOVEMENT PROCESSES ON SUBMARINE SLOPES

By Lincoln F. Pratson, Homa J. Lee, Gary Parker, Marcelo H. Garcia, Bernard J. Coakley, David Mohrig, Jacques Locat, Ulisses Mello, Jeffrey D. Parsons, Sun-Uk Choi and Kenneth Isreal

THE OBJECTIVE OF THE STRATAFORM program of the Office of Naval Research (ONR) is to understand how the stratigraphy of continental shelves and continental slopes is created and preserved by the processes operative in these environments. On continental slopes, the dominant processes that affect the stratigraphic record are gravity driven and commonly involve mass movements of sediments by creep, slumps, slides, debris flows, and/or turbidity currents. Collectively these processes are a major force in sculpting continental slope morphology, creating such features as failure scars and submarine canyons. The processes are episodic and tend to be localized. Their occurrence dictates where sediment is preserved on continental slopes and where it is not. The unconformable surfaces they erode are complex, discontinuous and asynchronous, complicating the interpretation of continental slope stratigraphy, particularly as it relates to past environmental changes such as fluctuations in sea level. A goal of STRATAFORM is to develop models that can aid in predicting where and how mass movements could occur, and what role these events play in continental-slope evolution. To meet this goal, project members are pursuing several key objectives in studying the New Jersey and northern California continental slopes. These objectives are to:

On continental slopes, the dominant processes that affect the stratigraphic record are gravity driven . . .

- Quantify the causes of slope failure;
- Document the mechanics and progression of mass movements spawned by slope failure;
- Determine how mass movements link to slope morphology and stratigraphy.

Approach

Not enough is yet known about submarine slope failure and mass movements to reliably anticipate when, where, or how they may occur. Additionally, observation of these processes is hindered by the remoteness of the marine environment, and by the fact that the effect of mass movements on continental-margin evolution is cumulative, spanning geological rather than human time scales. To circumvent these difficulties, a three-pronged approach of field, laboratory, and modeling studies is being used to achieve the above objectives. The field studies are examining lithological, mechanical, morphological, and stratigraphic attributes of failed and unfailed seafloor sediments to determine the causes of submarine slope failures and to predict their future occurrence. The laboratory studies are using flumes to quantify the dynamic evolution of different types of mass movements spawned by slope failure. And the modeling studies are constructing computer algorithms that simulate how, over time, mass movements contribute to the formation of continental-slope morphology and stratigraphy. Preliminary accomplishments made by each of these studies are described in the following sections.

Field Studies

The field investigations of slope failure have focused on the continental slope within the northern California STRATAFORM study area, where many factors thought to induce slope failure are prevalent. Sediments from the Eel River are reaching the slope and accumulating at relatively rapid rates (1–4 mm y^{-1}) (Alexander, 1996), which can lead to excess pore pressures and seafloor destabilization (Terzaghi, 1956). The slope contains zones of buried gas hydrates (Syvitski *et al.*, 1996, this issue) and the seafloor in the northern part of the study area is pockmarked with small craters formed by seeping gas (Goff *et al.*, 1996, this issue), which can also destabilize the seafloor. And, due to the tectonic collision occurring between the North American

---

Lincoln F. Pratson, Institute of Arctic and Alpine Research, University of Colorado, Boulder, CO 80309, USA; Homa J. Lee, Kenneth Isreal, U.S. Geological Survey, Menlo Park, CA 94025, USA; Gary Parker, David Mohrig, Department of Geology & Geophysics, University of Minnesota, Minneapolis, MN 55455, USA; Marcelo H. Garcia, Jeffrey D. Parsons, Sun-Uk Choi, Department of Civil Engineering, University of Illinois, Urbana-Champagne, IL 61801, USA; Bernard J. Coakley, Lamont-Doherty Earth Observatory of Columbia University, Palisades, NY 10964, USA; Jacques Locat, Department of Civil Engineering, Lavelle University, Quebec, Canada; Ulisses Mello, IBM T.J. Watson Research Labs, Yorktown Heights, NY 10598, USA.

and Juan de Fuca plates in this region, the area is periodically subject to earthquakes.

A combination of these processes (earthquake and gas) could have caused the large Humboldt slide in the southern part of the study area (Lee *et al.*, 1981; Field and Barber, 1993). And new swath-mapping imagery and high-resolution seismic profiles suggest this slide actually formed by more than one type of mass movement process (for a detailed discussion of this data and of the Humboldt slide, see Goff *et al.*, 1996, this issue, and Syvitski *et al.*, 1996, this issue). Other parts of the slope may be prone to future failures.

A key goal of the field studies is to identify which types of measurements in this area (when mapped regionally) can be used to constrain where slope failures might occur, how large and deep-seated these failures would be, and what forms of mass movements they would produce. For example, sediment properties that can be rapidly measured and mapped in the field, such as wet-bulk density and Atterberg limits, are being tested as proxies for sediment shear strength. If successful, these proxies will then be compared with estimates of gravity-induced downslope shear stresses made from maps of seafloor slope to predict the minimum earthquake magnitude that could trigger slope failure.

To date, 120 box-core subsamples and 5 piston cores have been recovered from the study area. All the cores have been logged for wet-bulk density, sound velocity, and magnetic susceptibility at a resolution of 1 cm. The wet-bulk-density measurements, which have been corrected for depth in the cores, reflect the lithology and stress history of the sediments, and they will eventually be used to estimate variations in sediment shear strength. Figure 1 is a map of these density measurements. Comparison of this map with sediment accumulation rates determined from the cores (Syvitski *et al.*, 1996, this issue) indicates that sediments with low (<1.5–1.7 g cm^{-3}) wet bulk densities occur in the active depocenters on the slope (green and blue areas in Fig. 1). These sediments are fine-grained and are accumulating rapidly (1–4 mm y^{-1}) (Alexander, 1996). Sediments with higher wet-bulk densities (1.7 to >2.0 g cm^{-3}) occur along other portions of the slope (red and pink areas in Fig. 1). These sediments are coarser grained, but their higher densities may also reflect erosion of overburden.

Laboratory Studies

Whereas the field studies are focusing on the causes of submarine slope failure, the laboratory studies are focusing on the dynamics of mass movements spawned by slope failures. Unique flumes are being used to simulate and collect direct measurements of these processes. The measurements are in turn being used to develop and calibrate numerical models of the processes. So far, the flume experiments have centered on the dynamics of subaqueous debris flows and the propagation of turbidity currents.

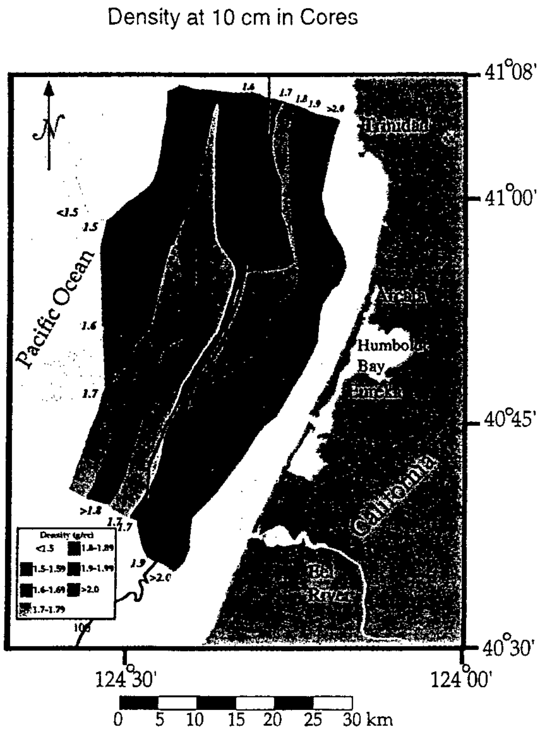

Fig. 1: Contoured seafloor wet-bulk densities as determined at 10 cm depth in 125 cores taken within the northern California STRATAFORM study area. On the portion of the continental slope investigated, areas of low (<1.5–1.7 g cm^{-3}) wet-bulk density (green and blue areas) occur where fine-grained sediments are actively accumulating. Areas of higher (1.7 to >2.0 g cm^{-3}) wet-bulk density (red and pink areas) occur where sediments are coarser grained, but also where overburden may have been eroded. Additional factors influence the bulk densities of sediments on the shelf.

. . . laboratory studies are focusing on the dynamics of mass movements spawned by slope failures.

The experimental program investigating the dynamics of debris flows is based at St. Anthony Falls Laboratory (SAFL) of the University of Minnesota. The lab has recently completed construction of a new type of flume containing a 0.2-m-wide channel with transparent walls that is suspended in a tank 10 m long, 3 m high, and 0.6 m wide. Flows initiated within the flume can be observed through a side wall and from above the flume along the entire length of the channel.

A major finding from one of the first sets of experiments run in the flume is an explanation for why the heads of subaqueous debris flows can move substantially faster and farther than those of subaerial debris flows (Mohrig *et al.*, 1995). The SAFL experiments indicate that under appropriate conditions the heads of the submarine debris flows hydroplane. In the flume, the heads of debris flows are observed to override a wedge of the water in front of them and detach from the flume channel floor (Fig. 2), significantly reducing the bed friction that would otherwise retard their movement.

This hydroplaning, which is directly analogous to the way tires hydroplane on wet roads (Horne and Joyner, 1965), offers one of the first physical explanations for the long run-out distances often observed for submarine debris flows deposited on seafloor slopes of <1° (Embley and Jacobi, 1986).

. . . to link individual models of different mass-movement processes . . . in order to correctly simulate . . . morphology and stratigraphy . . .

A second experimental program investigating the initiation, spatial development, and duration of turbidity currents, as well as the characteristics of the sedimentary deposits these flows generate is being led by the Department of Civil Engineering at the University of Illinois. In this program, turbidity currents are studied using a second flume that arrests the front of a turbidity current by generating a fresh water flow that moves in the opposite direction of the turbidity current with the same mean velocity as the current front. A conveyor belt is used to ensure that the speed of the bed equals that of the water flow so that the turbidity-current front remains stationary and can be studied in detail (Garcia and Parsons, 1996).

Measurements of dilute suspended-sediment flows (i.e., sediment concentrations <26.5 g l^{-1} or 0.0265 g cm^{-3}) made using this flume have contributed to the development of both one-dimensional and two-dimensional numerical models of how turbidity currents propagate. Results from the one-dimensional model, which predicts the evolution of turbidity-current height, velocity, and concentration with increasing distance from its source (Choi and Garcia, 1995), are shown in Figure 3. Other flume measurements indicate that in dilute turbidity currents, most of the mixing at the current front is due to billows (known as Kelvin-Helmholtz billows) that roll up above the front as the current moves downslope. This frontal mixing is quite different from the hydroplaning mechanism (above) that appears to facilitate the movement of denser debris flows (i.e., sediment concentrations of ~1,000 g l^{-1} or 1 g cm^{-3}), and may be an important reason for the differences between depositional structures in deposits formed by turbidity currents versus those formed by debris flows.

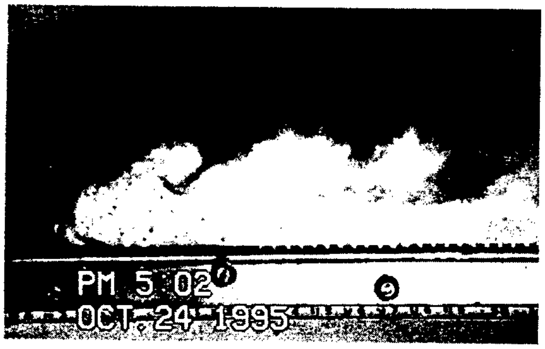

Fig. 2: Head of a subaqueous debris flow and overlying suspended-sediment cloud simulated within the flume at St. Anthony Falls Laboratory of the University of Minnesota. Note how the head of the debris flow is overriding the wedge of water in front of it and has detached from the grooved, dark-colored flume bed. This greatly reduces the bed friction that would otherwise retard the movement of the debris flow, allowing it to travel much farther downslope than it would under subaerial conditions. Image length is 49 cm.

Modeling Studies

Correctly scaling the flume measurements of mass-movement processes to the real world is one of the major goals of the computer modeling studies. Another is to link individual models of different mass-movement processes with models of other slope processes in order to correctly simulate how the morphology and stratigraphy of continental slopes evolve over geological time.

A first step toward the latter goal has been the development of a seascape evolution model (Pratson and Coakley, 1996). This model simulates continental-slope morphology that results from the interaction between sedimentation, slope failure, and sediment flow erosion. The processes are emulated by discrete interactions between cells in a grid of continental-slope topography that evolves over the course of a model run. The model predicts that submarine canyons evolve on continental

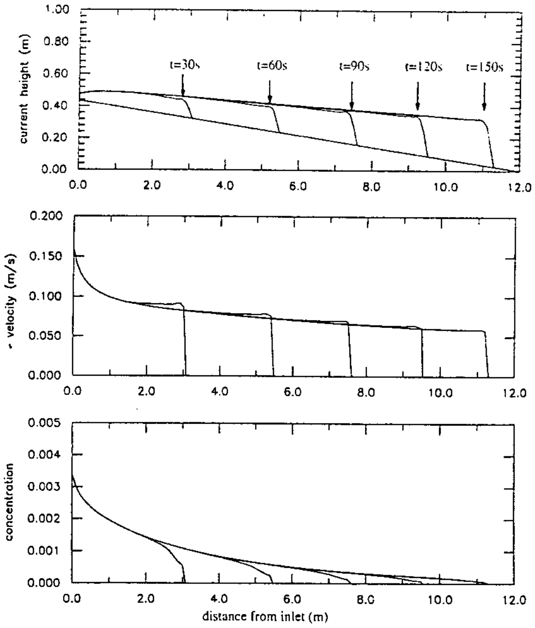

Fig. 3: Results from a one-dimensional model that predicts the evolution of a turbidity current as it propagates down a sloping channel. ***Top panel*** *shows that the height of the turbidity current will increase with increasing time and distance from its point of initiation due to the entrainment of ambient water. This entrainment, along with the deposition of sediment from the flow, causes corresponding decreases in the velocity (****middle panel****) and concentration (****bottom panel****) of the turbidity current.*

slopes in three stages: 1) where sedimentation oversteepens the upper continental slope and causes it to fail, sediment flows (e.g., turbidity currents) are triggered, and these cut relatively narrow gullies that extend to the base of the slope (Fig. 4A); 2) some of these slope gullies become pathways for subsequent sediment flows, and, as a consequence of the enhanced downcutting on the mid to lower slope, their walls fail (Fig. 4B); and 3) these mid- to lower-slope failures then evolve into headward-eroding submarine canyons that advance upslope along the gullies by further retrogressive failure, where sediment flows enter the canyons and undercut their headwalls (Fig. 4, C and D). This sequence for canyon evolution successfully replicates cross-cutting relations between intercanyon and canyon morphologies on the tectonically passive New Jersey continental slope and on the tectonically active Izu-Bonin fore arc off Japan.

A second, related model has been developed to simulate the progressive buildup of stratigraphic sequences deposited by sediment flows. Like the seascape evolution model, this model is rule-based and operates in map view. Sediment flow movement and deposition are linked to seafloor morphology, which dictates convergence or divergence of a sediment flow as it moves down slope. Figure 5 shows examples of how sediment is routed and deposited across the seafloor in the model. In these examples, a sequence of sediment flows across a sediment prism built by previous sediment flows earlier in the model run. From their entrance into the model at base of the continental slope, the flows produce continuous conduits analogous to channels. These conduits, which have a constant, "graded" slope, extend across the sediment prism and direct sediments to its seaward front. Successive flows cause the conduits to periodically switch and reorganize, particularly at their distal ends. This result is analogous to the channel switching and abandonment that occurs on submarine fans (see Weimer and Link, 1991 and papers therein). However, in contrast to the concave profile of submarine fans, the model forms a sediment prism with a table-top–like profile (i.e., the sediment prism aggrades to a certain thickness, and then grows basinward by the buildup of deposits along its distal front). This behavior results because sediment transport and deposition are parameterized in the model only in terms of seafloor slope. Other factors that determine where and how much a sediment flow deposits, such as its velocity, discharge, etc., now need to be considered as well.

Future Work

Research is already underway to expand on and integrate the investigations summarized above and in other articles in this issue. A major emphasis of this new work will be on using the laboratory and modeling techniques described above to help explain and correctly reproduce observations related to mass movement processes being compiled by the field investigations in the STRATAFORM study areas. When all the cores from the northern California study area are analyzed, the data will be coupled with the swath-mapping imagery, high-resolution seismic-reflection profiles, and other information (e.g., earthquake distributions and magnitudes) in a Geographic Information System (GIS). The GIS will facilitate correlations between these data, which in turn will be used to constrain the present stability of the area, and its relationship to the seafloor morphology and subsurface stratigraphy. This combination of data also will be used to constrain the types of mass-movement processes operative in the area and their regions of influence.

> . . . to help explain and correctly reproduce observations . . . being compiled by the field investigations . . .

Drawing on this information, the laboratory studies will attempt to simulate in flumes how mass-movement processes formed two key features on the northern California slope: the Humboldt slide and the gullies that incise the shelfbreak in the northern part of the study area (see Goff *et al.*, 1996, this issue). Flume experiments will examine the possibility that the Humboldt slide initiated a turbidity current, and if so, what percentage of the original sediment was removed from the study area by this process. The formation of the slope gullies will be studied in a new experimental tank containing a model continental shelf and slope surface.

The modeling studies will use the results from the flume experiments in three ways. One is to

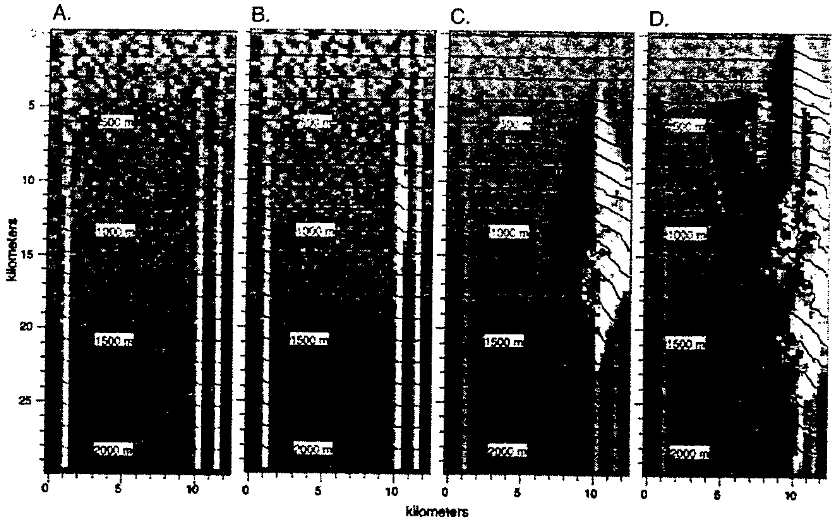

Fig. 4: The sequence of submarine-canyon evolution simulated by a first-version seascape-evolution model. (A) The sequence begins with turbidity currents, triggered by slope failures where the slope has been oversteepened by sedimentation, cutting narrow shallow gullies to the base of the slope (bottom of panels). (B) Repeated use of a gully by the turbidity currents oversteepens the gully wall and causes it to fail. (C) The initial failure triggers retrogressive failures that expand the gully into a canyon. (D) Additional turbidity currents enter the canyon and undercut the canyon walls, causing further retrogressive failures that expand the canyon and lead to the upslope migration of the canyon head. From Pratson and Coakley (1996).

. . . mass-movement processes formed two key features on the northern California slope: the Humboldt slide and the gullies . . .

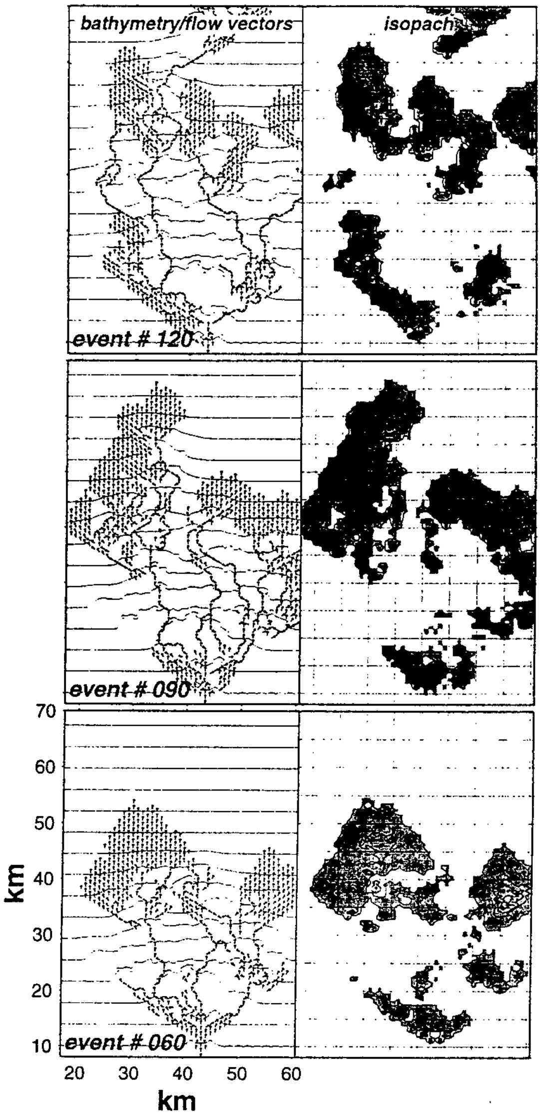

Fig. 5: Matrix of results from a map-view model that simulates the progressive buildup of stratigraphic sequences deposited by sediment flows. ***Bottom row*** *shows the results associated with the 60th sediment flow simulated by the model;* ***middle row*** *shows the results associated with the 90th sediment flow; and* ***top row*** *shows the results associated with the 120th sediment flow.* ***Left column*** *shows the preexisting bathymetry (contours) for the sediment flows, overlain by vectors that indicate the paths of the flows and how they diverged.* ***Right column*** *shows the areas over which sediments were deposited by each sediment flow.*

continue to develop numerical models of debris-flow and turbidity-current dynamics. These models will be extended to two dimensions and will include a new model that simulates the initiation of turbidity currents from debris flows. The second use of the flume experiments will be the incorporation of the turbidity-current "spreading laws" into the seascape evolution model. These formulations will improve how the model simulates the interaction between turbidity currents and other slope processes while maintaining a reasonable computation time. The third use of the flume experiments will be to calibrate the seascape evolution model. Selected flume experiments will be simulated with the model to determine how well it reproduces the experiment results and what aspects of the model need to be modified.

Acknowledgements

Funding for the generation of the manuscript and the research it highlights was provided by the Office of Naval Research, with special thanks to J. Kravitz, ONR program manager of STRATAFORM. We thank D. Prior, R. Bennett, C. Nittrouer, and J. Kravitz for their review of the original version of this manuscript.

References

Alexander, C.R., 1996: Slope sedimentation on the Eel River continental margin. *EOS Transactions of the AGU, 76,* OS 10.

Choi, S.U. and M.H. Garcia, 1995: Modeling of one-dimensional turbidity currents with a dissipative-Galerkin finite element method. *J. Hydraul. Res. IAHR, 33,* 623–648.

Embley, R.M. and R. Jacobi, 1986: Mass wasting in the western North Atlantic. In: *The Geology of North America, Vol. M, The Western North Atlantic Region.* P.R. Vogt and B.E. Tucholke. eds. *Geol. Soc. Am.,* 479–490.

Field, M.E. and J.H. Barber, Jr., 1993: A submarine landslide associated with shallow seafloor gas and gas hydrates off northern California. In: *Submarine Landslides: Selected Studies in the U.S. Exclusive Economic Zone.* W.C. Schwab, H.J. Lee and D.C. Twichell, eds. *U.S. Geol. Surv. Bull., 2002,* 151–157.

Garcia, M.H. and J.D. Parsons, 1996: Mixing at the front of gravity currents. *Dyn. Atm. Oc., 24,* 197–205.

Goff, J.A., L.A. Mayer, J. Hughes-Clarke and L.F. Pratson, 1996: Swath mapping on the continental shelf and slope: the Eel River Basin, northern California. *Oceanography, 9,* 178–182.

Horne, W.B. and U.T. Joyner, 1965: *SAE Technical Paper 970C,* 51 pp.

Lee, H.J., B.D. Edwards and M.E. Field, 1981: Geotechnical analysis of a submarine slump, Eureka, California. Proceedings, Offshore Technology Conference, Houston, 53–59.

Mohrig, D., G. Parker and K.X. Whipple, 1995: Hydroplaning of subaqueous debris flows. *EOS Transactions of the AGU, 76,* F277.

Pratson, L.F. and B.J. Coakley, 1996: A model for the headward erosion of submarine canyons induced by downslope eroding sediment flows. *Geol. Soc. Am. Bull., 108,* 225–234.

Syvitski, J.P., C.R. Alexander, M.E. Field, J.V. Gardner, D.L. Orange and J.W. Yun, 1996: Continental-slope sedimentation: the view from northern California. *Oceanography, 9,* 163–167.

Terzaghi, K., 1956: Varieties of submarine slope failures. Texas conference on Soil Mechanics and Foundation Engineering, 8th, *Proceedings, Texas University Bureau Engineering Research Special Publication 29,* 1–41.

Weimer, P. and M.H. Link, 1991: *Seismic Facies and Sedimentary Processes of Modern and Ancient Submarine Fans, Frontiers in Sedimentary Geology.* Springer-Verlag, New York, 349–363. ❑

SWATH MAPPING ON THE CONTINENTAL SHELF AND SLOPE: THE EEL RIVER BASIN, NORTHERN CALIFORNIA

By John A. Goff, Larry A. Mayer,
John Hughes-Clarke and Lincoln F. Pratson

. . . morphological structure of surficial features at a level of detail and coverage unavailable by any other means.

THE STRATAFORM program sponsored by the Office of Naval Research (Nittrouer and Kravitz, 1996, this issue) seeks to understand how sedimentary processes lead to the formation of the stratigraphic sequences on continental margins. A central challenge facing this effort is to understand the transport of sediments in shore-parallel as well as shore-perpendicular directions. Multidimensionality is necessary to describe, for example, the accumulation of sediments from river inputs, the distribution of gullies and canyons on the slope, the meandering of channels, and the structure of slumps and slides.

Acoustic swath mapping, which produces rapid, detailed, and complete aerial coverage of seabed bathymetry and backscatter, is a key component to investigating the multidimensionality of the continental-margin environment. Swath bathymetry provides data on the morphological structure of surficial features at a level of detail and coverage unavailable by any other means. Sidescan backscatter is responsive to both the composition and fine-scale roughness of surface sediments. Such information is complementary to other data sources, such as cores and seismic-reflection profiles that provide constraints on seafloor types and subseafloor structure. Collectively, these data will supply observational constraints for understanding and ultimately predicting sedimentary processes and strata formation on the shelf and slope within the STRATAFORM study areas.

The STRATAFORM program includes swath-mapping field work in two natural laboratories: the Eel River margin of northern California (Fig. 1), and the New Jersey margin (Austin *et al.*, 1996, this issue). The Eel margin was mapped using the Simrad EM1000 system in the summer of 1995 aboard the *R/V Pacific Hunter*. The New Jersey margin was mapped with the same system in the summer of 1996 aboard the Canadian Hydrographic Services vessel *F.G. Creed.* The EM1000 operates at 95 kHz (both bathymetry and sidescan), with bathymetric resolution generally better than ~50 cm. The New Jersey slope was previously mapped with the deeper-water, coarser-resolution Sea Beam system (Pratson *et al.*, 1994). These data abut the newly collected New Jersey EM1000 survey, and the combined data set will provide continuous coverage from ~20 m to ~2,500 m depth. The objective of this report is to examine the morphological data from the continental shelf and slope of the Eel margin and, in particular, its relevance to sedimentary transport processes operating in this area.

Geological Setting

The Eel margin is part of a larger active continental margin influenced both by the eastward subduction of the Gorda plate beneath North America and by the northward migration of the Mendocino Triple Junction (e.g., Clarke, 1987). The Little Salmon fault and anticline (Fig. 1) run NW-SE through the survey area and constitute an important tectonic and structural boundary in the subsurface. The Eel River (Fig. 1) is the primary source of sediments deposited within the survey area (e.g., Wheatcroft *et al.*, 1996, this issue), although there is also a significant contribution from the Mad River (Fig. 1). Figure 2 displays the sidescan and bathymetry data collected using the EM1000 during the Eel margin survey. Below we discuss the primary observations derived from this data set.

Shelf Morphology

The continental shelf of the Eel River Basin (depths less than ~120 m) is topographically very smooth (Fig. 2). What small-scale morphology does exist (ripples, bioturbation, etc.) is below the resolu-

---

John A. Goff, University of Texas Institute for Geophysics, 8701 N. MoPac Expressway, Austin, TX 78759, USA; Larry A. Mayer and John Hughes-Clarke, Ocean Mapping Group, Department of Geodesy & Geomatics Engineering, University of New Brunswick, Fredericton, N.B., E3B 5A3, Canada; Lincoln F. Pratson, Institute of Arctic and Alpine Research, University of Colorado, Boulder, CO 80309, USA.

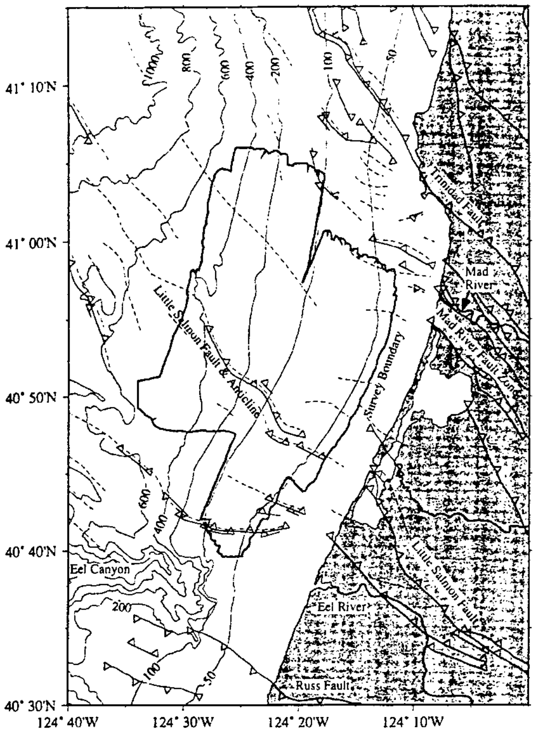

Fig. 1: Location of the Eel River Basin swath-mapping survey (bold lines). Bathymetric contours in meters. Thrust faults (triangles on upthrown block) and anticline axes (dashed lines) are digitized from Clarke (1987).

tion of the Simrad EM1000 instrument. The smoothness of the shelf is likely due to large input of fine terrigenous sediments from the Eel and Mad rivers and reworking by storms. The only bathymetric features on the shelf notable in Figure 2 are the shallows associated with the Eel River and Mad River sediment bulges and a dredge-spoil dump site.

The bathymetry of the shelf is not, however, entirely devoid of character. Subtle, longer-wavelength structures do exist but are difficult to see because they are small compared with the overall gradient of the shelf. Figure 3 displays contours of residual bathymetry on the shelf, where a regional shelf gradient has been subtracted from the bathymetry (see caption for details). Here the most dominating structures evident are the Eel River sediment bulge and an elongated secondary bulge that extends >20 km northward from the primary bulge, between ~55 m and 90 m water depth (Fig. 2) with ~1–6 m of relief. The location and strike of the secondary bulge correlates with the southern half of the flood deposit (see thickness contours overlain on Fig. 3) mapped by Wheatcroft *et al.* (1996, this issue) from coring work conducted in February, 1995. This observation suggests a possible connection between a long-term effect (the secondary bulge) and a short-term process (floods). Freshly deposited sediments are subject to resuspension and redistribution through physical and biological processes, so it is possible that flood deposits may not be retained and the correlation could be mere coincidence. However, in a study of earlier Eel River floods (Borgeld, 1996), it was found that a significant portion of sediments deposited during large (decadal scale) floods are usually preserved in the stratigraphic record for water depths >60 m. We therefore infer that the secondary Eel River sediment bulge is likely formed by enhanced long-term deposition on the shelf associated with repeated Eel River floods.

The southern side of the Mad River sediment bulge also exhibits an elongated secondary bulge. Unlike the Eel River secondary bulge described above, this one extends to the south ~8 km from the Mad River sediment bulge (Fig. 3) and lies between ~40 and 60 m water depth. It is unlikely that this secondary bulge can be attributed to flood deposits: studies indicate that sediment transport during flood events is generally northward (Wheatcroft *et al.,* 1996, this issue). One possibility is that this feature may be a remnant of when the Mad River mouth was ~4 km south of its current position, ~30 y ago (J. Borgeld, personal communication). Near the northern limit of the Eel River secondary bulge there exists a marked steepening to seaward, forming an indentation into the shelf (Fig. 3). This observation is discussed below.

Unlike the bathymetry, the sidescan image of the shallow (<70 m) shelf is quite varied over short length scales. Most noticeable are the low backscatter sandy deposits of the Eel River and Mad River sediment bulges. In the absence of strong local slope variations, backscatter intensity responds to bottom roughness and subbottom heterogeneity at scales less than the acoustic wavelength (~1.6 cm for EM1000). Bottom photographs and samples (Wiberg *et al.,* 1996, this issue) indicate that muddy bottoms and subbottoms are roughened at such scales by bioturbation. We therefore speculate that bioturbation may be an important factor in making muddy deposits acoustically brighter to the EM1000 acoustic wavelength than sandy deposits. More intriguing, however, are a series of subtle shore-normal striations ~0.2 to 1 km wide that appear to emanate northward from the Eel River sediment bulge (Fig. 2). These generally lie between ~50 and ~70 m depth, taper off from south to north, and disappear just south of the Mad River sediment bulge. They have no discernible topographic expression but lie along the shoreward side of the secondary Eel bulge noted above and in Figure 3. We therefore speculate that these striations are associated in some way with northward transport of Eel River sediments.

. . . a possible connection between a long-term effect (the secondary bulge) and a short-term process (floods).

Slope Morphology

The southern part of the continental slope within the survey area is dominated by the Humboldt slide (Fig. 2) (Field and Barber, 1993), a

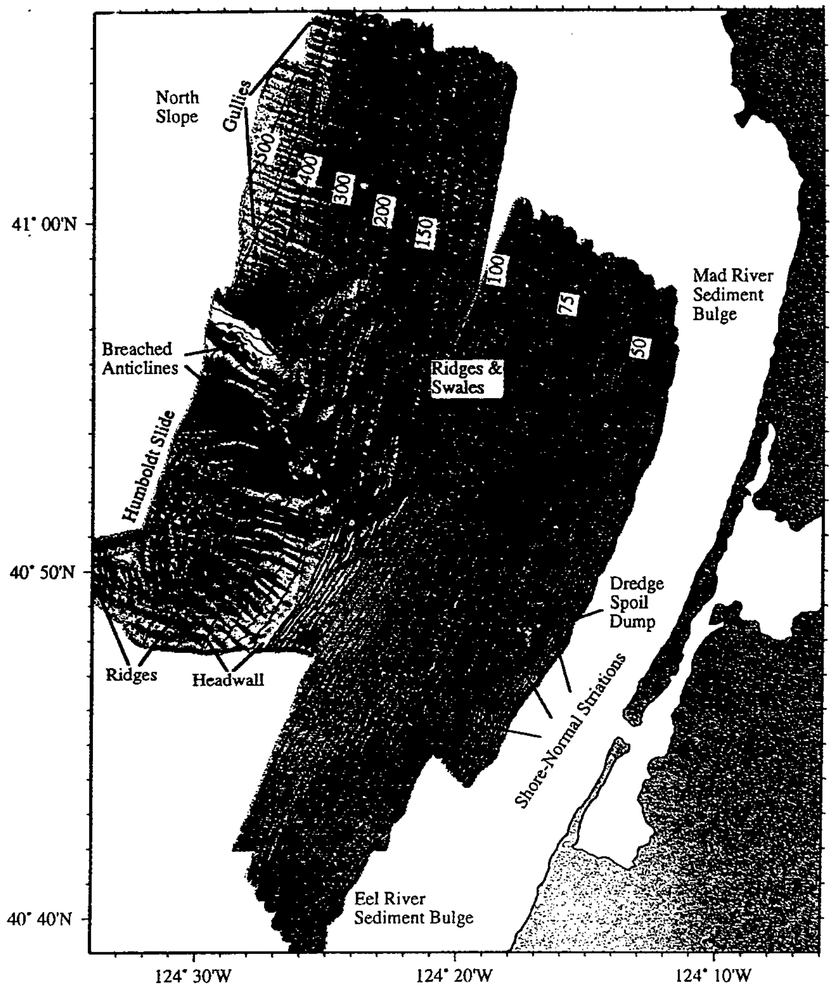

Fig. 2: Gridded sidescan and bathymetry data from the Eel River Basin swath-mapping survey. Colors are derived from side-scan backscatter data, with warmer colors (red and yellow) indicating high backscatter, and cooler colors (blue and purple) indicating low backscatter. Shading is derived from artificial sun illumination of bathymetry (azimuth N25°E). Contours are in meters. Principal features discussed in the text are identified.

. . . at the outlet of several . . . of the headwall gullies there is a small fan-like structure.

large failure scar with an amphitheater-shaped headwall incised by relatively deep gullies (~20 m relief). Below the headwall are a series of contour-parallel ridges (Fig. 2), interpreted as slump blocks grading downslope into pressure ridges (Syvitski *et al.*, 1996, this issue). The deep gullies on the headwall are indicative of a mature morphology, whereas ridges below the headwall, owing to the lack of infilling sediment (Syvitski *et al.*, 1996, this issue), appear to be more recent in origin. Hence these ridges likely did not originate as mass movement breaking away from the headwall, but rather originated in the sediments lying below it. The headwall in turn may have its origins in an earlier mass wasting event, now buried, or may be the product of a more gradual evolution. Above the headwall and along its upper slope (~300–120 m) lies a region of high backscatter (Fig. 2) which, in corroboration with seismic work (Syvitski *et al.*, 1996, this issue; Austin *et al.*, 1996, this issue), is interpreted to be outcrop of subsurface strata and evidence for erosion. The shallowest part of this high backscatter region extends to the shelf indentation noted in Figure 3.

Figure 4 displays a detailed view of the morphology for part of the Humboldt slide headwall and its base. Changes in the contour pattern from pointing upslope to downslope and a downslope-expanding crenulated pattern indicate that at the outlet of several (but not all) of the headwall gullies there is a small fan-like structure. The Humboldt slide

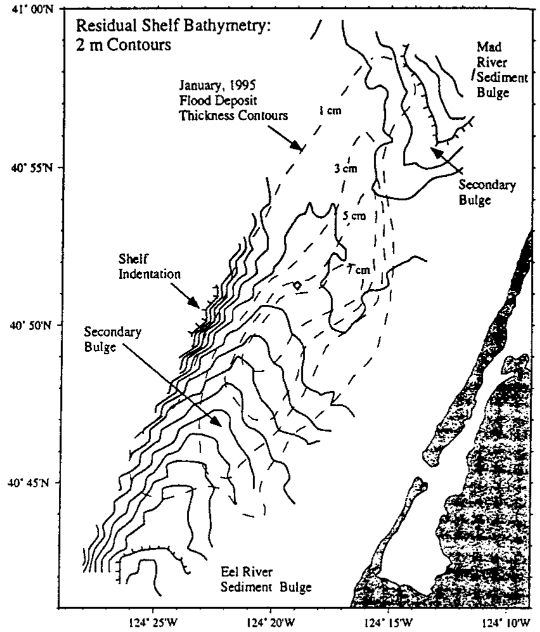

Fig. 3: Residual shelf bathymetry (depths <100 m), indicated with solid contours (2-m contour interval). Formulating residual bathymetry involved the following steps. 1) To prevent shore curvature from creating false anomalies, 18 shore-parallel profiles, from ~40 to 100 m depth, were sampled from the gridded data set. 2) Over most profiles, the minimum depth sampled along the profile was subtracted from the profile. This value, rather than the mean, was subtracted because the major anomalies on the shelf, the Eel and Mad River sediment bulges, are positive. 3) Over the deepest four profiles there is an evident large negative anomaly, so in these cases the depth subtracted was chosen from a location toward the northern end of the survey, where the outer shelf appears to be devoid of "anomalous" character. 4) The detrended profiles, sampled in geographical coordinates, were gridded and contoured at 2-m intervals. Overlain in thin dashed contours are measurements of flood-deposit thickness measured in February, 1995 (Wheatcroft et al., *1996, this issue). The southern half of the flood deposit correlates with a secondary bulge emanating northward from the Eel River sediment bulge.*

ridges lie downslope of the fan structures; there is no obvious connection between the two evident in the seafloor morphology, although a connection cannot be ruled out. We infer that the fan structures contain sediments that have deposited at the base of the headwall after flowing through the gullies, probably as turbidity flows, and that the previously noted high backscatter region (Fig. 2) and shelf indentation (Fig. 3) above the headwall are a source of these sediments. We suggest that turbidity flows have been a significant factor in the evolution of the headwall morphology.

Two breached anticlines (Clarke, 1987) bound the northern side of the Humboldt slide (Fig. 2). North and east of these lies a series of sinuous ridges and swales oriented roughly perpendicular to the breached anticlines (Fig. 2). The amplitude of these structures decreases from west (~20 m) to east (~1 m), and cross contours at ~45°. The ridges and swales are strongly correlated with changes in acoustic backscatter in the sidescan data: the seaward slopes exhibit high backscatter and the landward slopes exhibit low backscatter. Proximity to the breached anticlines suggests a causal relationship, but interpretation of these features must await analysis of high-resolution seismic-reflection data.

A series of seaward-trending linear slope gullies occurs along the north slope (Figs. 2 and 5). The shelf break here is ~60 m deeper and ~7 km farther from shore than the shelf break in the Humboldt slide region. The gullies on the north slope are an order of magnitude smaller (~2 m) than those incising the headwall of the Humboldt slide, although both sets have similar spacing (~100–1,000 m). The former are generally confined to depths greater than ~300 m, a depth that also marks the steepest part of this shelf terrace. In comparison, the Humboldt slide gullies rise to depths as shallow as 180 m.

Gullies similar to those on the north slope have been observed on the New Jersey continental slope between submarine canyons within the east coast STRATAFORM study area (Pratson *et al.*, 1994). However, the upslope termini of northern California gullies do not abruptly end in failure headwalls as on the New Jersey continental slope. Instead, they rise gradually to the elevation of the surrounding seafloor. Other similar gullies have been observed on the Arguello slope, California by Reynolds and Gorsline (1988), who interpreted them as erosional in nature.

How the slope gullies formed on the north slope remains uncertain. Reynolds and Gorsline (1988) discuss numerous possibilities for gully formation, and we refer the reader to that reference for a full discussion. One that we favor is that the gullies have been formed by turbidity flows composed of sediments introduced from the Eel and Mad Rivers. This scenario has parallels to early stages of submarine canyon formation predicted by the seascape-evolution model of Pratson and Coakley (1996). Initiation of flow may be induced by several mechanisms, including sediment oversteepening, fluid or gas seepage, and seismic triggering. However, the lack of a headwall scarp and minimum depth limitation suggest that these gullies are not growing by headward erosion, as appears to be the case on the New Jersey shelf.

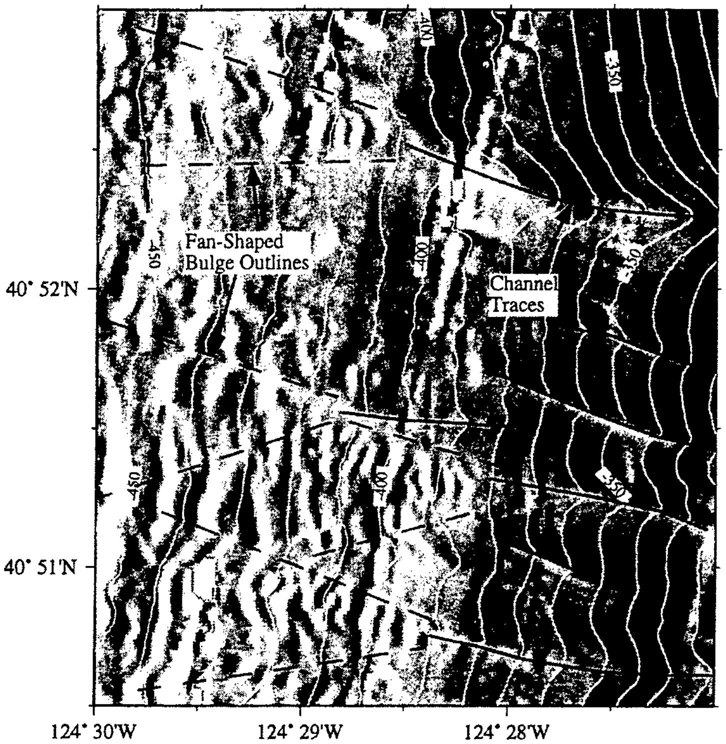

Fig. 4: Sun-illuminated image of the northern part of Humboldt slide headwall, with bathymetric contours in meters. Illumination is from the East. Image shows evidence of fan deposits (outlined, where present, with dashed lines) at the base of several channels (solid lines).

. . . turbidity flows have been a significant factor in the evolution of the headwall morphology.

The north slope also contains numerous small circular depressions, generally less than ~100 m in diameter (Fig. 5). Such features have been interpreted by others (e.g., Field and Barber, 1993) as craters formed by seeping gas. In the vicinity of the gullies, the depressions are often aligned within the gullies, especially at the northern limit of the survey. Elsewhere they appear randomly distributed. In the southern half of Figure 5, there are numerous gullies formed without any depressions in the vicinity. We conclude that gullies are affecting the position and formation of depressions, rather than vice versa.

Future Directions

One of the primary purposes of the swath-mapping work described here was to provide a geological and morphological context for the seismic, coring, sampling, and modeling investigations that are also part of STRATAFORM. In so doing we have raised many questions and generated many

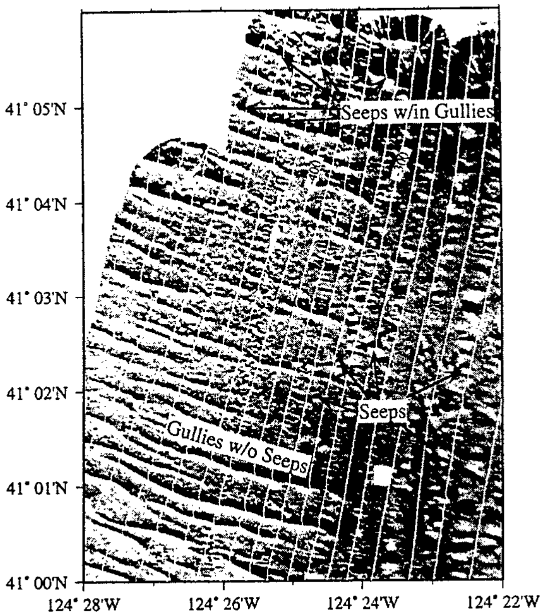

Fig. 5: Sun-illuminated image of the north slope region (Fig. 1), with bathymetric contours in meters. Illumination is from azimuth N20°E. Image shows small gullies incising lower half of terrace slope, and the presence of small circular depressions, interpreted as gas seeps, many of which are aligned within the gullies.

speculations that will need to be addressed in subsequent work. Perhaps the most important will be to ground truth many of the variations in sidescan intensity that we observe. Although high-resolution seismic data have already demonstrated that some of the high-backscatter anomalies are erosional unconformities, many other anomalies are of unknown origin. For example, on the shelf we are not certain (although we have speculated) why the Eel and Mad River sediment bulges have such low backscatter, nor what the origins of the shore-normal striations are. On the slope, we also are not certain why backscatter values generally increase with depth. These issues will be addressed within STRATAFORM; systematic coring will provide information on surface sediment types and volumetric heterogeneity in the immediate subbottom, and microtopography analysis will provide information on bottom roughness.

. . . some of the high-backscatter anomalies are erosional unconformities . . .

Seismic-reflection data, as we have already discussed, are also critical to our understanding of the features identified in the swath-map data. Although bathymetry and sidescan data provide exquisite detail and complete aerial coverage, seismic reflection penetrates into the internal architecture of features, which in many cases is essential to determine how they were formed. Features of particular interest to be investigated with seismic reflection include the Eel and Mad River primary and secondary sediment bulges, the Humboldt slide, the breached anticlines and nearby ridges and swales, and the gullies of the north slope and the Humboldt slide headwall.

Acknowledgements

This work was supported by the Office of Naval Research through grants N0014-95-1-0067 (J.A. Goff), N00014-95-1-0064 (L.A. Mayer), and N0014-93-1-0126 (L.F. Pratson). We thank Joe Kravitz, without whom STRATAFORM would not exist, and the captain and crew of the *R/V Pacific Hunter* and the personnel of C&C Technologies for their assistance and support during the swath-mapping field program. Reviews by C. Nittrouer, B. Carson, and D. Swift led to substantial improvements on an earlier draft. We appreciate constructive discussions with J. Austin, J. Borgeld, M. Field, C. Fulthorpe, J. Gardner, H. Lee, B. McAdoo, G. Mountain, D. Orange, and J. Yun. This is UTIG Contribution 1232.

References

Austin, J.A., C.S. Fulthorpe, G.S. Mountain, D.L. Orange and M.E. Field, 1996: Continental-margin seismic stratigraphy: assessing the preservation potential of heterogeneous geologic processes operating on continental shelves and slopes. *Oceanography, 9,* 173–177.

Borgeld, J.C., 1996: Preservation potential of strata deposited on the Eel River shelf during 1986 and 1989 flooding of the Eel River. *Eos Trans. AGU, 76,* OS10.

Clarke, S.H., Jr., 1987: Geology of the California continental margin north of Cape Mendocino. In: *Geology and Resource Potential of the Continental Margin of Western North America and Adjacent Ocean Basins—Beaufort Sea to Baja California.* D.W. Scholl, A. Grantz and J.G. Vedder, eds. Circum-Pacific Council for Energy and Mineral Resources, Earth Science Series, vol. 6, 337–351.

Field, M.E. and J.H. Barber, 1993: A submarine landslide associated with shallow sea-floor gas and gas hydrates off northern California. In: *Submarine Landslides: Selected Studies in the U.S. Exclusive Economic Zone.* W.C. Schwab, H.J. Lee and D.C. Twichell, eds. United States Geological Survey Bulletin 2002, 151–157.

Nittrouer, C.A. and J.H. Kravitz, 1996: STRATAFORM: a program to study the creation and interpretation of sedimentary strata on continental margins. *Oceanography, 9,* 146–152.

Pratson, L.F. and B.J. Coakley, 1996: A model for the headward erosion of submarine canyons induced by downslope eroding sediment flows. *Geol. Soc. Am. Bull., 108,* 225–234.

______, W.B.F. Ryan, G.S. Mountain and D.C. Twichell, 1994: Submarine canyon initiation by downslope-eroding sediment flows: evidence in late Cenozoic strata on the New Jersey continental slope. *Geol. Soc. Am. Bull., 106,* 395–412.

Reynolds, S. and D.S. Gorsline, 1988: Some enigmatic depressions of the Arguello slope, California. *Geo-Mar. Lett., 8,* 167–172.

Syvitski, J.P., C.R. Alexander, M.E. Field, J.V. Gardner, D.L. Orange and J.W. Yun, 1996: Continental-slope sedimentation: the view from northern California. *Oceanography, 9,* 163–167.

Wheatcroft, R.A., J.C. Borgeld, R.S. Born, D.E. Drake, E.L. Leithold, C.A. Nittrouer and C.K. Sommerfield, 1996: The anatomy of an oceanic flood deposit. *Oceanography, 9,* 158–162.

Wiberg, P.L., D.A. Cacchione, R.W. Sternberg and L.D. Wright, 1996: Linking sediment transport and stratigraphy on the continental shelf. *Oceanography, 9,* 153–157. ❑

LINCOLN F. PRATSON AND WILLIAM F. HAXBY

by Lincoln F. Pratson
and William F. Haxby

In 85 B.C. or thereabouts, a Greek named Posidonius set sail on a curious mission. He was not carrying freight or passengers, nor was he engaged in war. He simply wanted to answer an age-old question: How deep is the ocean? Halting his vessel in the middle of the Mediterranean Sea, Posidonius coaxed his ship's crew to let out nearly two kilometers of rope before a large stone attached to the end of the line finally hit bottom. He and his men must have been jubilant—at least until they realized that they then had to haul the great weight back on board.

For the next 2,000 years, naval surveyors and oceanographers continued to use exactly the same laborious line-and-sinker method to probe the ocean's depths. It is not surprising that they made scant progress. Then, during the 1920s, oceanographers developed the first echo sounders—instruments that could measure the water's depth by bouncing sound waves off the bottom. With the wealth of measurements these devices provided, scientists got their first glimmers of the true shape of the ocean basins.

In the past few decades engineers have constructed ever more sophisticated acoustic devices to speed the mapping of this hitherto hidden part of the earth. The major impetus for these developments initially came from concerns about national defense, but more recently economic considerations have taken precedence.

Beginning with the U.S. in 1981, the world's maritime nations declared the waters and seafloor within 200 miles of their shores to be "Exclusive Economic Zones." To help assess the value of the vast undersea expanse claimed by the U.S., the National Oceanic and Atmospheric Administration began surveying parts of the newly annexed area in 1983. That effort (which continued until 1993) mapped more than 200,000 square kilometers of the seafloor off the coasts of the Atlantic and Pacific oceans and the Gulf of Mexico.

Over this same period, the National Science Foundation funded two smaller sur-

Continued on page 86

COMPUTER-GENERATED IMAGES of the seafloor surrounding the U.S. show geologic features in great detail in regions where specialized sonar mapping has been done (*right of black line*).

Seafloor Mapping Tools

Our multibeam sonar images represent just one way scientists can visualize the seafloor. Other approaches are also used, and each has its peculiar advantages and shortcomings.

Satellites (*a*) cannot measure seafloor depth directly, but they can sense variations in the elevation of the water at the surface of the ocean. The U.S. Navy's Geosat satellite, for example, can measure the distance to the ocean surface to within five centimeters by bouncing radar pulses off the water below it. Because the precise position of the satellite is known, such determinations provide a measure of sea-surface height.

The ocean surface can vary in relief by as much as 200 meters. These undulations reflect minute differences in the earth's gravity from place to place that cause water to distribute itself unevenly. Most commonly, these gravitationally induced variations in the ocean surface are caused by rugged seafloor topography. For instance, a massive, submerged volcano that is 2,000 meters tall and 40 kilometers wide will pull water toward it, producing a bulge about two meters high in the ocean surface above it. But undersea features smaller than 10 kilometers across do not generally possess sufficient mass to affect the ocean surface and thus go undetected by satellite radars. What is more, gravity variations (particularly near continental margins) can reflect differences in the density of the underlying rock rather than topography. Still, satellites provide broad, if less than perfect, maps of regions not yet surveyed with ships.

SATELLITE RADAR IMAGE

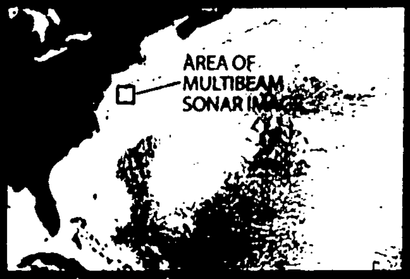

Multibeam sonar (*b*) bounces sound off the seafloor to gauge ocean depth. In contrast to simple echo sounders, this modern technique employs an array of sound sources and listening devices mounted on the hull of the survey vessel. Every few seconds the sources emit a burst that reaches only a slim strip of seafloor aligned perpendicularly to the direction the ship is moving. At the same time, the listening devices begin recording sounds reflected from the bottom. This equipment is arranged to detect sounds com-

MULTIBEAM SONAR IMAGE

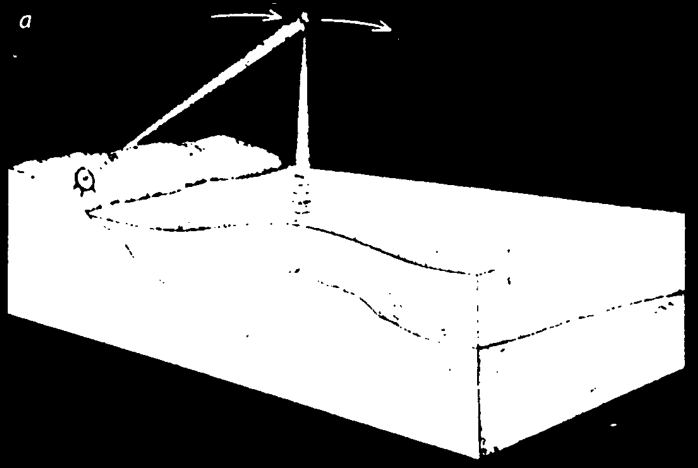

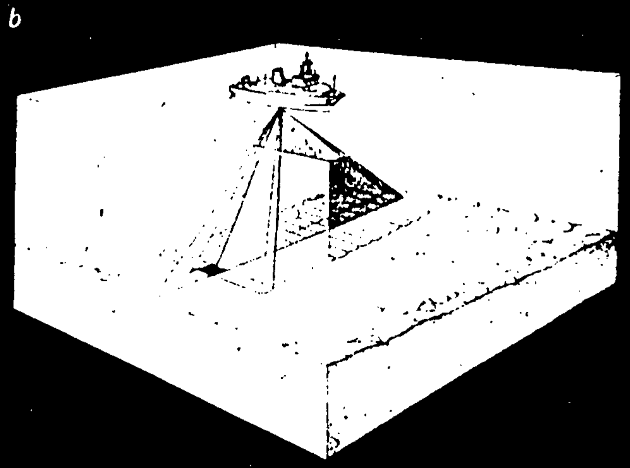

Continued from page 83

veys to study parts of the seafloor near the coasts of New Jersey and western Florida. All the vessels involved used multibeam sonars, the most modern form of instrumentation available for measuring the topography of the ocean bottom.

These surveys provide unprecedented views of the country's continental slope. Although no sunlight actually penetrates to these great depths, computers can render images of seafloor vistas as they would appear with the oceans drained. Such a perspective is particularly valuable in planning industrial activities offshore. For example, submarine cables increasingly carry international communications, and petroleum producers are moving drilling platforms into ever greater depths of water. These enterprises require maps of where the seafloor appears to be stable—not prone to subsea avalanches or violent currents. Disposal of waste at sea also demands this information, because currents running along the bottom can disturb the sites where waste settles. Bottom surveys further help geologists to locate offshore fault systems and to assess their risk of triggering earthquakes.

On a broader scientific level, undersea mapping is providing fundamental knowledge about the geologic forces that shape the ocean floor. Images such as those we have created offer scientists a way to take in vast stretches of undersea terrain in a glance—an ability they have long enjoyed while studying the surface of distant moons and planets. That perspective now offers some fascinating new insights into the marvelously complex evolution of the earth. ◻

ing only from within a series of narrow seafloor corridors that are aligned parallel to the ship's direction. Thus, the sound reflections received at the ship emanate from the regions where the slim strip of sound and the listening corridors intersect. The timing of these reflections provides a profile of seafloor depth. Such profiles are recorded every few seconds while the survey ship moves over the seafloor, and so successive observations build up a continuous swath of coverage along the ship's track. By running the ship in the same pattern one mows a lawn, scientists can produce a complete map of an area. With less than 200 vessels outfitted with the necessary equipment, however, charting the entire seafloor in this way would require hundreds of years.

Side scan sonar (*c*) provides yet a different perspective on what the seafloor looks like. The equipment is usually attached to a "sled" that is towed behind a ship. Two sonar units, affixed to either side of the sled, act as both sound sources and listening devices. These units emit bursts of sound outward, to either side. If the seafloor is flat and smooth, none of the energy emitted will be reflected back (as with a beam of light directed obliquely onto a mirror). But if the seafloor is rough, the sound hitting the bottom will be scattered in all directions, and some will return to the sonar sled (just as a beam of light illuminating ground glass will reflect in all directions). By equating the amplitude of the recorded echoes to different shades of gray and displaying the results to show the distance from the sled, scientists can obtain an image of the texture of the seafloor that looks similar to a black and white photograph. But like a single aerial photograph, a side scan sonar image does not indicate the heights of the surface below.

The most accurate and detailed view of the seafloor is provided by underwater photography (*d*), using either cameras towed along the bottom, piloted submersibles or remotely operated vehicles. Such camera carrying equipment gives researchers the opportunity to explore the seafloor up close. Yet because even the most intense illumination does not penetrate seawater effectively, photographic views obtained in this way are limited to the short distances that artificial beams of light can penetrate.

—L.F.P. and W.F.H.

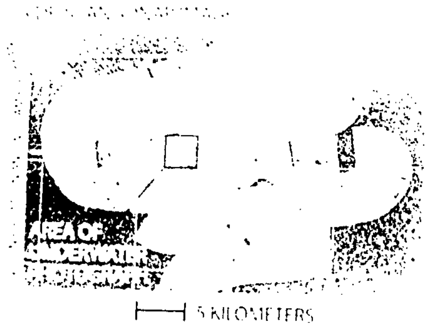

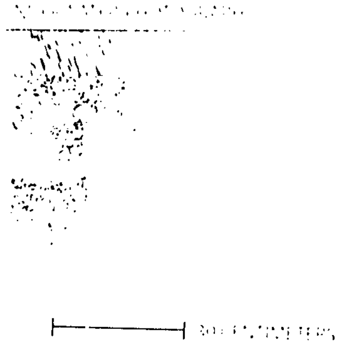

c

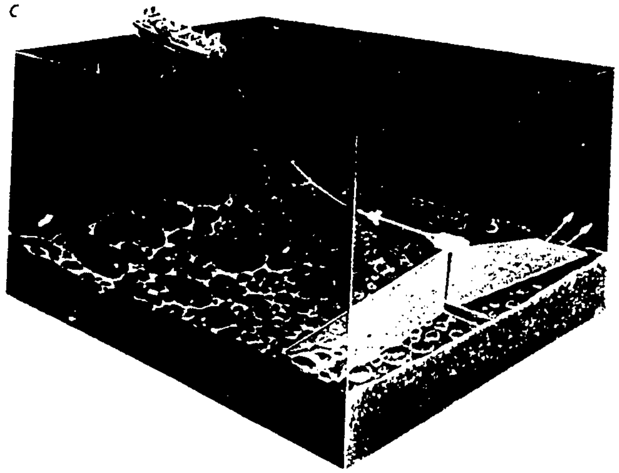

d

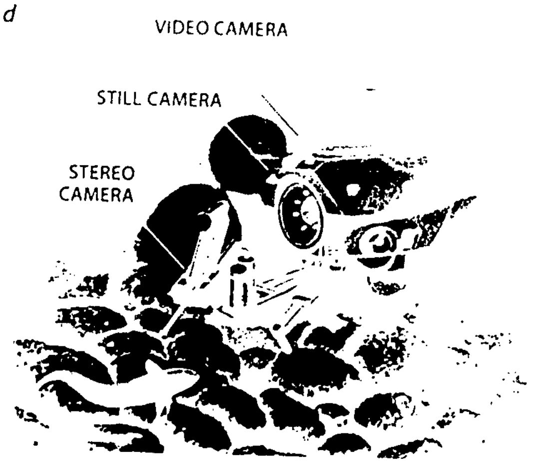

The Authors

LINCOLN F. PRATSON and WILLIAM F. HAXBY have worked together for two years probing the continental margins of the U.S. Pratson completed his Ph.D. in geological sciences at Columbia University in 1993. He then studied the topography of the seafloor for the Office of Naval Research at Columbia's Lamont-Doherty Earth Observatory. In 1996 he joined the Institute of Arctic and Alpine Research at the University of Colorado. Haxby earned his doctorate from Cornell University in 1978. Since then, he has conducted investigations of the ocean basins as a research scientist at Lamont-Doherty Earth Observatory.

Further Reading

SWATH BATHYMETRIC MAPPING. Special issue of *Journal of Geophysical Research*, Vol. 19, No. B3; March 10, 1986.

IMAGING THE OCEAN FLOOR: HISTORY AND STATE OF THE ART. Peter R. Vogt and Brian E. Tucholke in *Geology of North America*, Vol. M: *The Western North Atlantic Region*. Edited by P. R. Vogt and B. E. Tucholke. Geological Society of America, 1986.

WHAT IS THE SLOPE OF THE U.S. CONTINENTAL SLOPE? Lincoln F. Pratson and William F. Haxby in *Geology*, Vol. 24, No. 1, pages 3–6; January 1996.

National Geophysical Data Center World Wide Web site available at http://www.ngdc.noaa.gov/mgg/mggd.html

JOURNAL OF GEOPHYSICAL RESEARCH, VOL. 103, NO. B10, PAGES 24,141–24,157, OCTOBER 10, 1998

Clinoform development by advection-diffusion of suspended sediment: Modeling and comparison to natural systems

Carlos Pirmez[1]
Lamont-Doherty Earth Observatory of Columbia University, Palisades, New York

Lincoln F. Pratson
Institute of Arctic and Alpine Research, University of Colorado, Boulder

Michael S. Steckler
Lamont-Doherty Earth Observatory of Columbia University, Palisades, New York

Abstract. Clinoforms are the building blocks of prograding stratigraphic sequences. These sigmoid-shaped surfaces can be found forming today on modern deltas. Sedimentation rate profiles over the clinoform surface of these deltas show low rates of sediment accumulation on both topset and bottomset regions, with a maximum accumulation rate on the upper foreset region. We present a model for the formation of clinoforms that relies on the interpretation of modern clinoform sedimentation as a result of the distribution of shear stresses at the mouth of a river. Model clinoform surfaces are generated using an equation for the conservation of suspended sediment concentration, together with a conservation of fluid equation for simple time-averaged flow velocity fields. In the model, suspended sediment is advected horizontally into a basin, and gravitational settling of sediment particles is counteracted by vertical turbulent diffusion. In shallow water, shear stresses are too large to allow deposition, and sediment bypasses the topset region. With increasing water depth, near-bed shear stresses decrease, and sediment is allowed to deposit at the foreset region, with gradually decreasing rates toward deeper water. This sedimentation pattern leads to progradation of the clinoform surfaces through time. The clinoform surfaces produced by the model capture the fundamental morphological characteristics of natural clinoforms. These include the gradual slope rollover at the topset and bottomset, steeper foreset slopes with increased grain size, and an increase in foreset slope through time as clinoforms prograde into deeper water. Because the parameters controlling the model clinoforms have a direct relation to physical quantities that can be measured in natural systems, the model is an important step toward unraveling the physical processes associated with these deposits.

1. Introduction

The morphology and stratigraphy of deltaic deposits and their internal structure were first systematically investigated by *Gilbert* [1885, 1890], who identified the topset, foreset and bottomset beds of the deltaic deposits and their clinoform-shaped surfaces on the shores of Pleistocene Lake Bonneville. Clinoform-shaped deposits, however, extend beyond the Gilbert-type delta [*Bates* , 1953] and range in scale from deltaic deposits a few meters thick to continental shelf-slope deposits several hundreds of meters thick. The stacking of clinoform-shaped deposits makes up the bulk of stratigraphic sequences [*Mitchum et al.*, 1977], and, as such, clinoform surfaces can be thought of as the fundamental building blocks of the infill of sedimentary basins. Clinoforms are ubiquitous in the modern sedimentary record of continental margins, including carbonate platforms, siliciclastic shelves, and mixed siliciclastic-carbonate environments. The shape of their variable, basinward dipping profile is affected by the same factors that affect the sequences they comprise: relative sea level, sediment supply, depositional regime, and sediment type. However, what clinoforms indicate about these factors remains just partially understood, and only in qualitative terms.

The shape of clinoform surfaces is thought to indicate different depositional environments. *Sangree and Windmier* [1977] defined two basic clinoform shapes: sigmoid and oblique. Clinoforms surfaces characterized by aggradational topsets and gradual increase in slope from the topset to the foreset are termed sigmoid. Oblique clinoforms display abrupt change in slope from topset to foreset and a topset region characterized by little or no aggradation, suggesting sediment bypass and/or erosion. Sigmoidal clinoforms are generally interpreted to represent relatively low-energy deltaic environments. Oblique clinoforms commonly have steeper foresets (up to ~10°) and are interpreted to form in high-energy environments of shallow coastal waters [*Sangree and Windmier*, 1977]. These characteristics suggest that the dimensions, shape, and sediment type of clinoforms contain a record about the environment of deposition, including the energy of transport processes and grain size of the sediment particles. The interpretation of this record in terms of sea level changes, basin subsidence, and sediment supply has been one of the key

---

[1] Now at Exxon Production Research Co., Houston, Texas.

Paper number 98JB01516.
0148-0227/98/98JB-01516$09.00

elements in the sequence stratigraphic approach to investigating sedimentary sequences [*Vail et al.*, 1977; *Vail*, 1987; *Posamentier et al.*, 1988; *Van Wagoner et al.*, 1990].

While there is a general understanding of the factors that affect the stacking patterns of clinoform packages within sedimentary sequences and the evolution of the sequences themselves, we are still hampered in our ability to quantify the factors that influence the shapes of clinoform surfaces and their implications for estimating the depositional regime, sediment type, and sea level changes. Studies of modern clinoforms in deltaic depositional systems [e.g., *Kuehl et al.*, 1986, 1989; *Wright et al.*, 1988, 1990; *Alexander et al.*, 1991; *Nittrouer et al.*, 1995, 1996; *Nittrouer and DeMaster*, 1996] revealed that clinoform shape and growth patterns are determined to a large extent by the spatial and temporal distribution of energy in the water column. The hydrodynamic characteristics of the water column and the resulting sediment dispersal patterns ultimately determine the shape of the sedimentation rate profile across the clinoform surface. A maximum in the sedimentation rate profile in actively prograding modern clinoform systems occurs near the upper foreset, just below the clinoform break, or rollover point [*Kuehl et al.*, 1986; *Alexander et al.*, 1991]. Another important observation that is borne out from the studies of modern systems is that the clinoform rollover is, in general, located at variable distances from the shoreline and in variable water depths. Such a distinction may have important consequences for the characterization of depositional facies in ancient clinoforms as well as for estimating the magnitudes of sea level changes from shifts in the position of onlap within depositional sequences [*Greenlee and Moore*, 1988].

In this study we introduce a mathematical model to generate clinoform surfaces. The model uses conservation and sediment dispersion principles, including the interaction between fluid flow in the water column and changes in the basin morphology due to sediment accumulation. The model is an attempt to quantify the physical processes that control the characteristics of clinoforms and generate stratigraphic sequences, taking into account the observations on modern clinoform systems. Our model addresses three key points that have been either neglected or de-emphasized in previous modeling attempts: (1) quantification of the factors controlling the shape of clinoform surfaces and their significance to interpretation of sedimentary sequences; (2) the separation between the clinoform rollover point and the shoreline that is apparent in many observations of both the modern and ancient record; and (3) the integration of observations on modern clinoforms and the implications for the interpretation of the ancient sedimentary record. We begin by discussing key elements of existing models for clinoform formation and then summarize observations on selected modern and ancient clinoform systems. We then advance the basic equations that describe our model and how the model works through a series of runs that illustrate the model sensitivity to various parameters. Finally, we compare and contrast our model results with natural clinoform systems.

2. Background

2.1. Existing Models

Existing sedimentation models can be generally classified into geometric, diffusion-based, and process-based models. Many of the existing models have advantages and disadvantages which are only briefly discussed here. None of the existing models addresses the fundamental question of what factors control the shape of subaqueous clinoforms. Those that have been used to examine the shape and characteristics of subaqueous clinoforms follow a slope-driven diffusion of topography approach rather than a fluid-sediment interaction approach, contain the fundamental physical principles associated with fluid flow but do not generate clinoforms, or still are not suitable for a detailed analysis of the factors that control the characteristics of clinoform depositional surfaces.

Models that focus on the development of large-scale continental margin sequences often generate clinoforms by stacking sediment packages according to predefined geometric rules [e.g., *Jervey*, 1988; *Ross*, 1989; *Kendall et al.*, 1991; *Reynolds et al.*, 1991; *Thorne and Swift*, 1991; *Bowman and Vail*, 1993]. These models can be useful as a tool to understand the effects of sea level, sediment supply, and tectonics on the gross geometry of stratigraphic sequences, but they do not address the physical processes that are responsible for the formation of clinoform units, of which these sequences are composed.

Diffusion-based models of clinoform formation assume that sediment transport is a function of topographic slope [*Kenyon and Turcotte*, 1985; *Flemings and Jordan*, 1989; *Jordan and Flemings*, 1991; *Thorne*, 1995]. These models result in a clinoform geometry that resembles that in natural systems, but implicit in these models is the interpretation that sediment transport is a function of slope-driven processes, such as creep, sliding, and slumping [e.g., *Kenyon and Turcotte*, 1985]. While these processes certainly contribute to sediment distribution in modern clinoforms (e.g., Mississippi delta [*Coleman et al.*, 1983]), they are by no means the most significant process in many modern systems (e.g., Amazon delta [*Adams et al.*, 1986]). In addition, slope-driven mass-transport processes, by removing sediment from the steeper foreset slopes, may act as a retreating agent, counteracting the effects of clinoform progradation [*Ross et al.*, 1994; *Pratson and Coakley*, 1996; *Pratson and Haxby*, 1996]. Another shortcoming of slope-driven diffusion approaches is that only concave-up profiles are produced, which results in an active clinoform break that is coincident with the shoreline [*Flemings and Jordan*, 1989; *Kenyon and Turcotte*, 1985]. This shortcoming has been circumvented by introducing a water-depth dependent diffusion coefficient of *Kaufman et al.* [1991]. A different approach was used by *Thorne* [1995], who defined a mathematical sediment accumulation function, following the earlier work of *Thorne and Swift* [1991], and numerically computed a sigmoid clinoform shape using calculus of variations. The approach used here is similar in that sediment accumulation rates also are computed but differs in that it is based on the distribution of shear stresses within the water column above the basin floor.

Syvitski et al. [1988] advanced a new class of multiprocess models that includes sediment advection by fluid flow and gravity-driven sediment transport, in addition to slope-driven diffusion. This approach has proven to be a useful tool to understand the various sedimentary processes that affect the geometry of sedimentary basin infill and has been successfully applied to simulate specific depositional settings, in particular fjord basins [*Syvitski et al.*, 1988; *Syvitski and Daughney*, 1992; *Syvitski and Alcott*, 1993, 1995]. The usefulness of these models to investigate the formation of clinoform surfaces and the fundamental causes of their variable shape is limited because of the need to specify a large number of input parameters, including a detailed description of temporal fluctuations in water and sediment discharge through a model run. Our model approach differs in that we assume a small set of flow and sediment parameters that are thought to represent the time-averaged conditions for the formation of a model surface.

A few models have attempted to examine sedimentation processes through basic principles of fluid motion and sedimentation. Models such as those described by *Tezlaff and Harbaugh* [1989] can be efficiently used to simulate a specific basin setting or depositional system, but the large number of parameters makes it difficult to evaluate the fundamental effects of flow and sediment variability on the shape of the deposits. On the other hand, one can attempt to model the physical flow processes to a high degree of detail, but these computationally intensive and complex parameterizations of flow and sediment transport have not yet been applied to the generation of stratigraphy [e.g., *Jewell et al.*, 1993]. *Swift and Thorne* [1991], *Thorne and Swift* [1991] and *Thorne et al.* [1991] used basic physical principles of fluid motion under the effects of waves and currents, together with regional observations on continental shelves, to develop a sediment transport model based on the regime concept. One critical assumption embedded in their model is that the equilibrium shape of the coastal profile follows a power law function of distance from the coastline. The model has been used to successfully predict changes in the coastal morphology due to erosion and deposition [*Thorne et al.*, 1991], although only clinoforms constrained by an assumed equilibrium shape are generated by this model.

2.2. Natural Clinoform Systems

Modern clinoform surfaces are seen on the deltas of the Amazon, Colorado (in Lake Mead), Ganges, Mississippi, Rhine (in Lake Constance) and Yellow Rivers, among others (Figures 1–3). Ancient clinoform surfaces are common in the Miocene sedimentary sequences of many continental margins [*Bartek et al.*, 1991; *Steckler et al.*, 1993] (Figure 1a). The topographic profiles were digitized from figures published by several sources (Table 1). These depositional surfaces display significant variability of scales (Figures 1–3 and Table 1), and direct comparison between them (and model clinoforms) requires that the vertical and horizontal dimensions be normalized. We use the vertical dimension H as the scaling factor for the clinoform profiles, defined as the elevation difference between the toe and top of the clinoform surfaces. The toe elevation (zero) is determined at the point where the clinoform surface becomes horizontal or conformable (i.e., with the same gradient) with the underlying surface. The top is defined as the shallowest point at the mouth of the river or the topset surface of the clinoform where horizontal. The distance axis also was shifted for ease of comparison, with the origin placed at the point where slope reaches a maximum value, that is, at the clinoform face inflection point. The rollover point is defined as the point of highest curvature landward of the inflection point.

Examples of normalized clinoform surfaces are seen in Figures 2 and 3. Among the key elements that characterize these clinoform surfaces are the following:

1. All clinoform surfaces display a gently sloping topset. Depths of the clinoform rollover points investigated here vary significantly, being relatively shallow in low-energy lake environments such as Lake Mead (Figure 1a) and the Rhine deltas, and much deeper in open-shelf clinoforms and subaqueous deltas such as the New Jersey clinoforms (Figure 1a), or the Ganges and Amazon Rivers (see values in Table 1).

2. The maximum slope of clinoform foresets varies from less than 0.5° to 6.3° in the clinoforms analyzed here (Table 1). The total relief H of these clinoforms reaches in excess of 250 m for some of the Miocene surfaces. Presumably, there are several factors influencing the slope and height of clinoforms. To first order, the clinoform height probably is determined by the space available to accumulate sediment (basin depth) and the factors limiting vertical accumulation (such as sediment flux, sediment availability and water column energy). High-relief clinoforms generally are associated with steeper clinoform fronts (e.g., New Jersey and Lake Mead; see Table 1 and also *Steckler et al.* [1998]).

3. As clinoforms become steeper, the separation between rollover and inflection points tend to approach zero. It is important to note, however, that the distance never vanishes, since it would require an infinite curvature at the rollover. Many of the profiles display a very sharp rollover, with small separation from the foreset inflection point (e.g., Rhine and Mississippi, Figure 3). Two groups of clinoforms can be identified on the basis of slope distribution and relative elevation of the inflection point. In the first group, which includes the Lake Mead, Rhine, Mississippi, and New Jersey clinoforms, the surfaces are distinctly asymmetrical. The asymmetry is characterized by a rapid slope increase from the topset to the inflection point and by a more gentle slope decrease from the inflection point seaward (Figures 2b and 3a–3d). In the second group, which includes the large deltas of the Ganges, Amazon, and Yellow Rivers, slope distribution is nearly symmetric. The distinction between the two groups is clearly seen through the normalized elevation of the inflection point, y/H (Figure 2a). For the large subaqueous deltas, y/H<0.4, whereas for the smaller deltas, y/H is larger.

4. Studies of modern subaqueous deltas on continental shelves off major rivers indicate that modern, actively prograding clinoforms show a maximum sedimentation rate at the upper foreset, seaward of the clinoform rollover point [e.g., *Kuehl et al.*, 1986; *Alexander et al.*, 1991] (Figures 4a and 4b). Sedimentation rates are small at both the topset and bottomset portions of the clinoform. Similar sedimentation patterns appear to prevail over modern continental shelves, as indicated by both long-term and modern accumulation patterns. Seismic profiling and drilling results on the eastern U.S. margin show that preferential sediment accumulation occurred on the upper slope (foreset) during the Quaternary [*Hathaway et al.*, 1976; *Poag*, 1985; *Poag and Mountain*, 1987; *Pratson et al.*, 1994]. The present-day sediment distribution over the continental shelf surface shows a sand-mud transition region on the seafloor just below the shelf break, indicating bypass of muds over the sandy shelf [*Stanley et al.*, 1983; *Nittrouer and Wright*, 1994]. Modern sediment accumulation rates determined from sediment traps on the U.S. east coast are also enhanced on the upper slope (Figure 4c) [*Biscaye and Anderson*, 1994]. These observations suggest that continental shelf sedimentation rate profiles behave in a similar fashion to those observed for subaqueous deltas, and as suggested by *Thorne* [1995], shelves may be viewed as large-scale analogs of the deltaic clinoform surfaces observed at the mouth of rivers.

We interpret these observations to indicate that suspended sediment originating from the coastal areas or river source is prevented from being deposited on the topset region of clinoforms because of high near-bed shear stresses. As shear stresses decrease seaward because of increased water depth, sediment is allowed to deposit, and sedimentation rate increases, reaching a maximum at the foreset. As rates of deposition increase, less sediment remains in the water column, resulting in a decrease of the deposition rate farther seaward over the bottomset region of

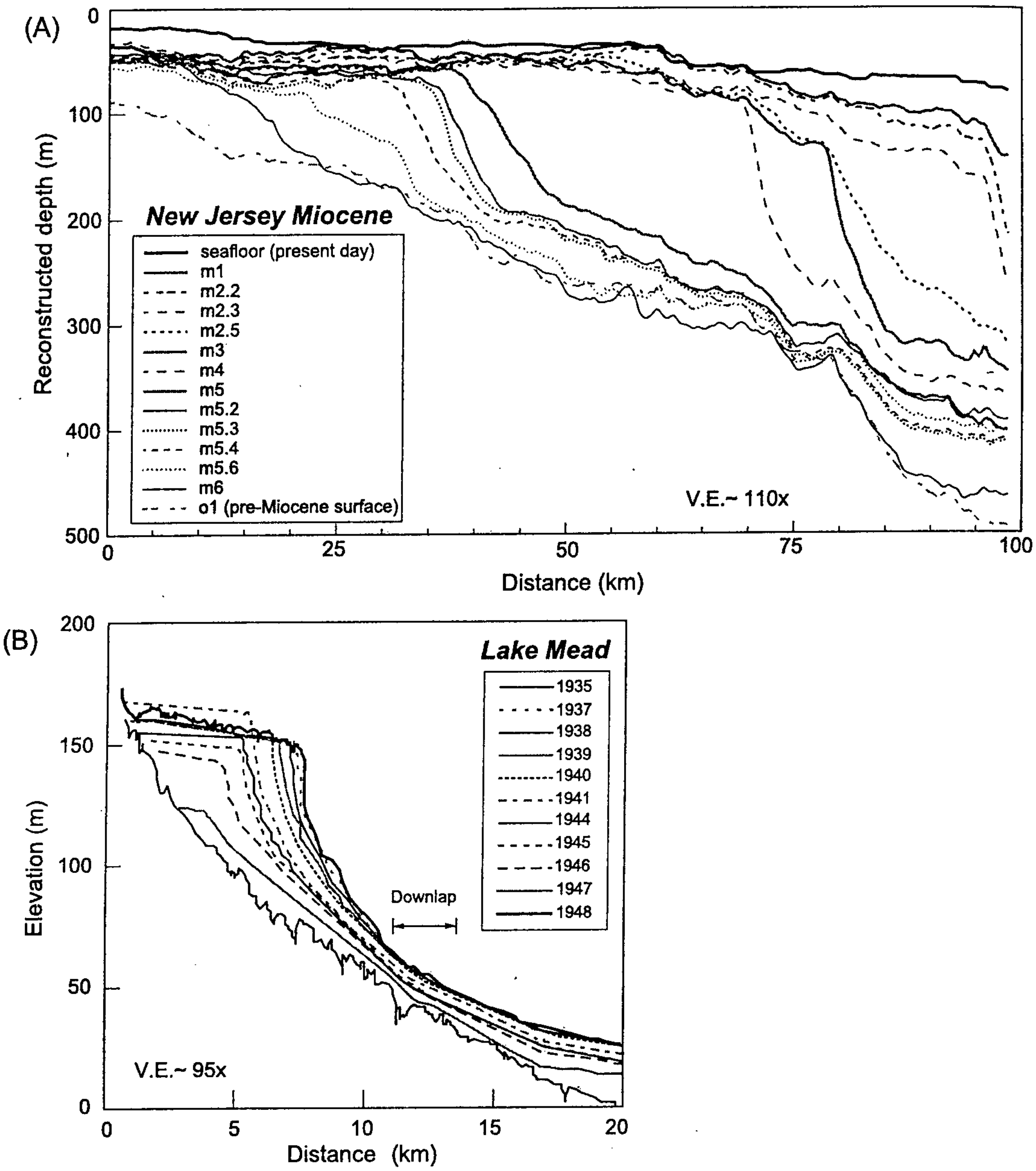

Figure 1. (a) Topographic profiles of natural clinoform surfaces from Miocene sedimentary sequences offshore New Jersey (surfaces and their respective names are sequence boundaries; see Table 1). Each surface represents the paleoelevation at the time of formation of each sequence boundary, reconstructed using two-dimensional backstripping (data from *Steckler et al.* [1998]). (b) Topographic profiles from Lake Mead. Each profile corresponds to a lake bottom survey during the period of lake filling after damming the Colorado River in 1935. Lake levels at each survey vary; depth of rollover for each profile is indicated in Table 1. Position of downlap of each profile occurs ~12 km from the river mouth, and flattening of profile beyond 12 km represents lake infill. Data digitized from *Smith et al.* [1954] (in Figure 12.16 of *Graf* [1984]).

the clinoform. Also, it is evident from the study of sedimentation on modern clinoforms that the peak in sediment accumulation often is detached from the shoreline, particularly in energetic shelf environments [*Nittrouer and Wright*, 1994]. The location of the clinoform break is therefore independent of the shoreline and is determined, to a large extent, by the distribution of shear stresses in the water column. These observations provide the foundation for our sediment dispersion model of clinoform development.

In summary, existing sedimentation models have not addressed key issues dealing with the formation of subaqueous clinoforms. No single model has combined the elements of water column energy distribution and sediment dispersal into the characterization of sedimentation accumulation profiles and how they affect the shape of clinoform surfaces. Our modeling approach starts from the basic observation of the characteristics and processes on modern clinoforms: their shape, sediments, overlying fluid flow characteristics, and sedimentation rate profiles. The present model is a step toward addressing the intermediate- to long-term formation of stratigraphic sequences and the factors that control the shape and sediment distribution on the clinoform surfaces that make up the sediment packages.

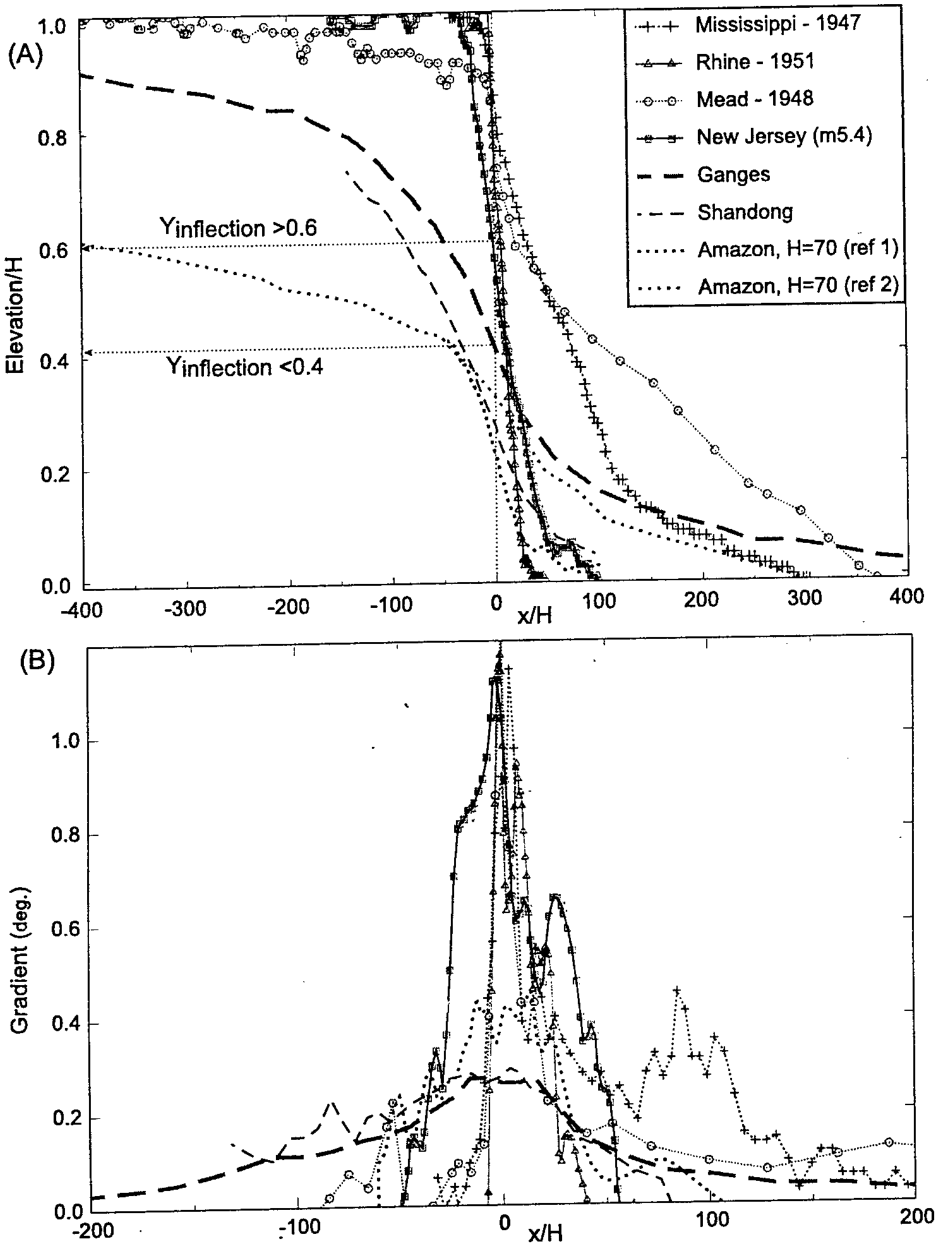

Figure 2. (a) Normalized topographic elevation profiles over several deltas (references from which profiles were digitized, and clinoform dimensions are in Table 1). Note low elevation of inflection point (x/H=0) for large deltas versus other clinoforms. (b) Bottom slope distribution of clinoform profiles.

3. Model Description

We model clinoform formation in two dimensions using the conservation equations for fluid and suspended sediment concentration and assuming steady state sediment input. In the model a sediment-laden river enters the basin with a mean velocity U and mean concentration C. It is assumed that river and basin waters are well mixed and that there are no external forces, such as waves, tides, or wind. Sediment grains are advected laterally at the same velocity as the fluid and deposit depending on the balance between the gravitational settling and uplifting vertical eddies of turbulence. The basic elements of the model are described below and illustrated in Figure 5. Symbols are given in the notation section.

3.1. Conservation of Sediment

The steady state equation for the conservation of sediment discharge is

$$\frac{\partial q_i}{\partial x_i} = 0 \tag{1}$$

where q_i is the sediment discharge in the x_i direction. Sediment discharge in the vertical,

$$q_z = (w + W_S)c - K_z \frac{\partial c}{\partial z} \tag{2a}$$

represents the balance between the vertical settling flux minus the resuspension flux, where K_z is the coefficient of vertical

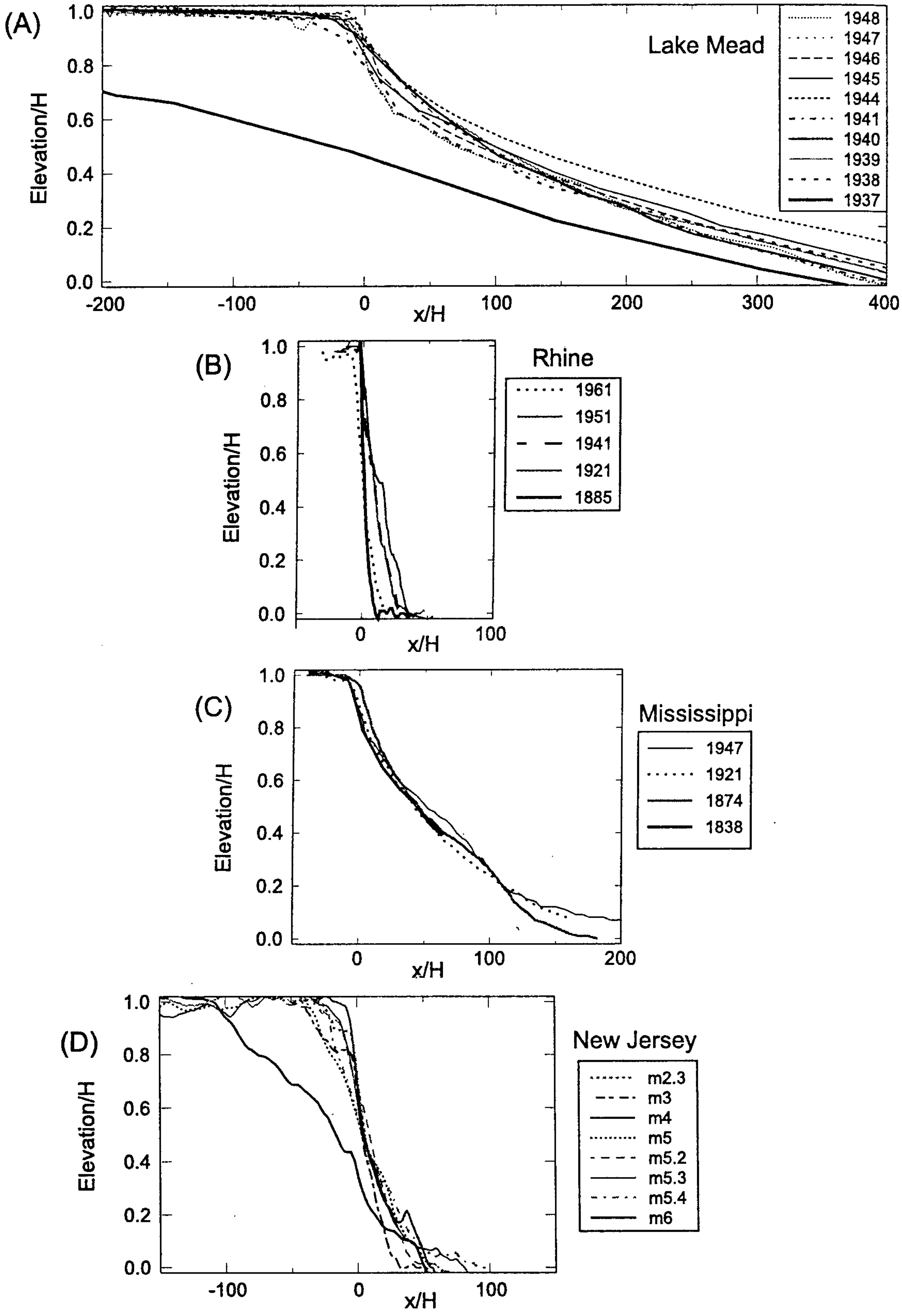

Figure 3. Normalized elevation profiles for clinoform surfaces surveyed at multiple instants during basin evolution on (a) Lake Mead (data from *Smith et al.* [1954]), (b) Rhine River delta (data digitized from *Kenyon and Turcotte* [1985, Figure 9]), (c) Mississippi River delta (data digitized from *Kenyon and Turcotte* [1985], Figure 12]), and (c) New Jersey Miocene clinoforms (data from *Steckler et al.* [1998]). Figures 3e–3h show the maximum clinoform front slope (slope at the inflection point) and seaward migration distance of the inflection point as a function of time.

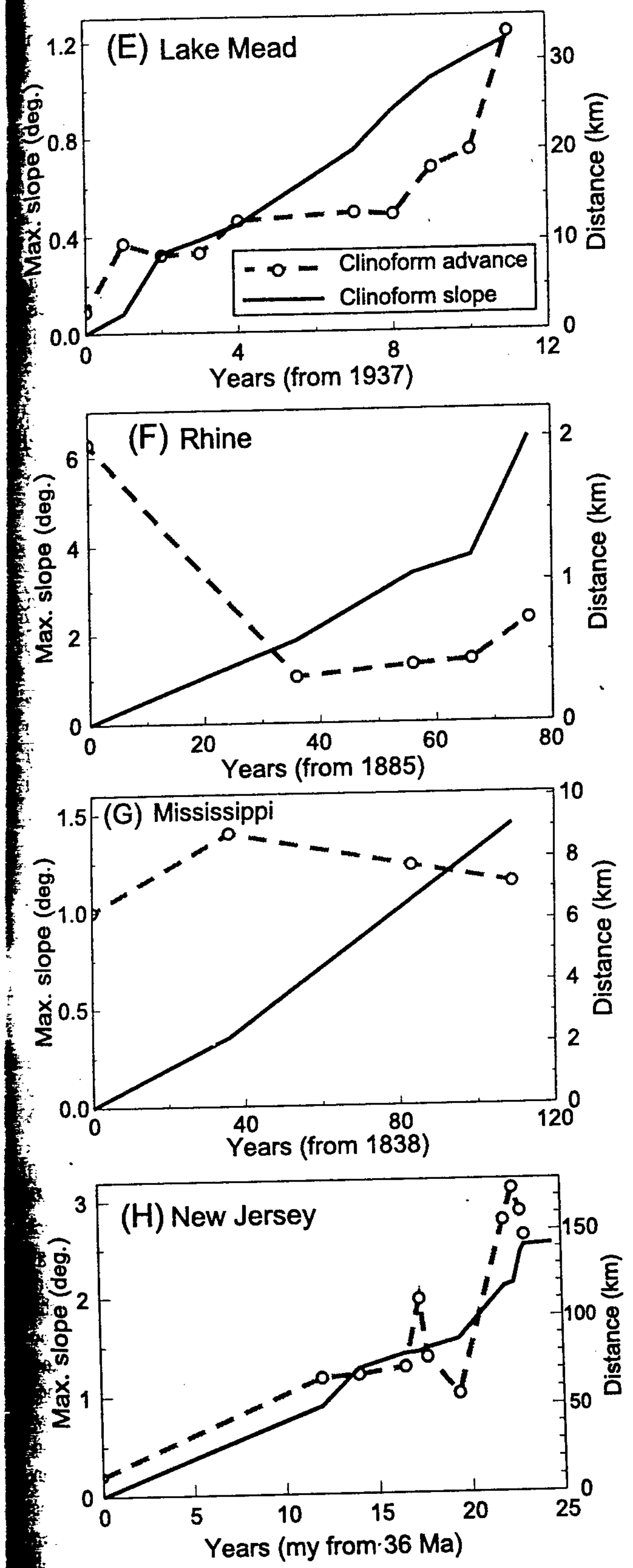

Figure 3. (continued)

turbulent diffusion. We assume that horizontal diffusion $(K_x \, \partial c / \partial x)$ is negligible such that lateral sediment dispersal is due solely to advection:

$$q_x = u\,c \tag{2b}$$

The solution of (1) with the discharge governed by equations (2a) and (2b) describes the suspended sediment concentration field, given appropriate boundary conditions and profiles for u, w, and K_z. In the current version of the model we use the layer-averaged conservation equations. The layer-averaged equation

Table 1. Scales of Natural Clinoforms

	H, m	Maximum slope, deg	Rollover depth, m
	New Jersey[a]		
o1 (Green-2, 36 Ma)[b]			
m6 (Pink-3, 24 Ma)	100	1.17	50
m5.6 (Blue-2, 22 Ma)	155	1.2	85
m5.4 (Sand, 19.5 Ma)	140	1.27	70
m5.3 (18.7 Ma)	137	1.96	68
m5.2 (Ochre, 18.3 Ma)	130	1.37	65
m5 (Green-1, 16.6 Ma)	119	1.0	60
m4 (Pink-2, 14.1 Ma)	216	2.77	87
m3 (13.6 Ma)	232	3.1	87
m2.3 (13.2 Ma)	202	2.86	138
	Lake Mead[c]		
1935[d]			
1937	24	0.09	15
1938	41	0.37	20
1939	59	0.32	12
1940	63	0.33	10
1941	82	0.46	10
1944	93	0.49	7
1945	88	0.48	7
1946	88	0.67	7
1947	84	0.74	8
1948	86	1.23	10
	Mississippi Delta[e]		
1838	106	1	5–10
1874	106	1.4	5–10
1921	99	1.23	5–10
1947	99	1.14	5–10
	Rhine Delta[e]		
1885	48	6.28	5
1921	69	1.04	2
1941	67	1.3	0
1951	67	1.4	0
1961	67	2.31	5
	Amazon Delta[f]		
Kuehl et al. [1986][g]	70	0.16	38
Alexander et al. [1991]	60	1.23	40
Nittrouer et al. [1996][h]	50	0.51	40
	Shandong Delta		
Alexander et al. [1991]	51	0.29	30
	Ganges Delta		
Kuehl et al. [1989]	100.4	0.27	25
	Model Examples		
Flat basin			
$D = 45$ µm	8.5	0.1	-
$D = 90$ µm	8.5	0.3	-
Sloping basin			
$t = 2$	17	0.25	-
$t = 10$	30	0.9	-
$t = 15$	35	1.2	-

[a] Names and ages of unconformities after *Steckler et al.* [1998].

[b] Basal surface, slope = 0.1° – 0.2°.

[c] Data from *Smith et al.* [1954], measured in Figure 12.16 of *Graf* [1984].

[d] Pre-dam river profile, mean slope = 0.02°.

[e] Data measured from profiles in *Kenyon and Turcotte* [1985].

[f] Data measured on different profiles published by several authors.

[g] Profile indicated as ref. 2 in Figure 2b

[h] Profile indicated as ref. 1 in Figure 2b

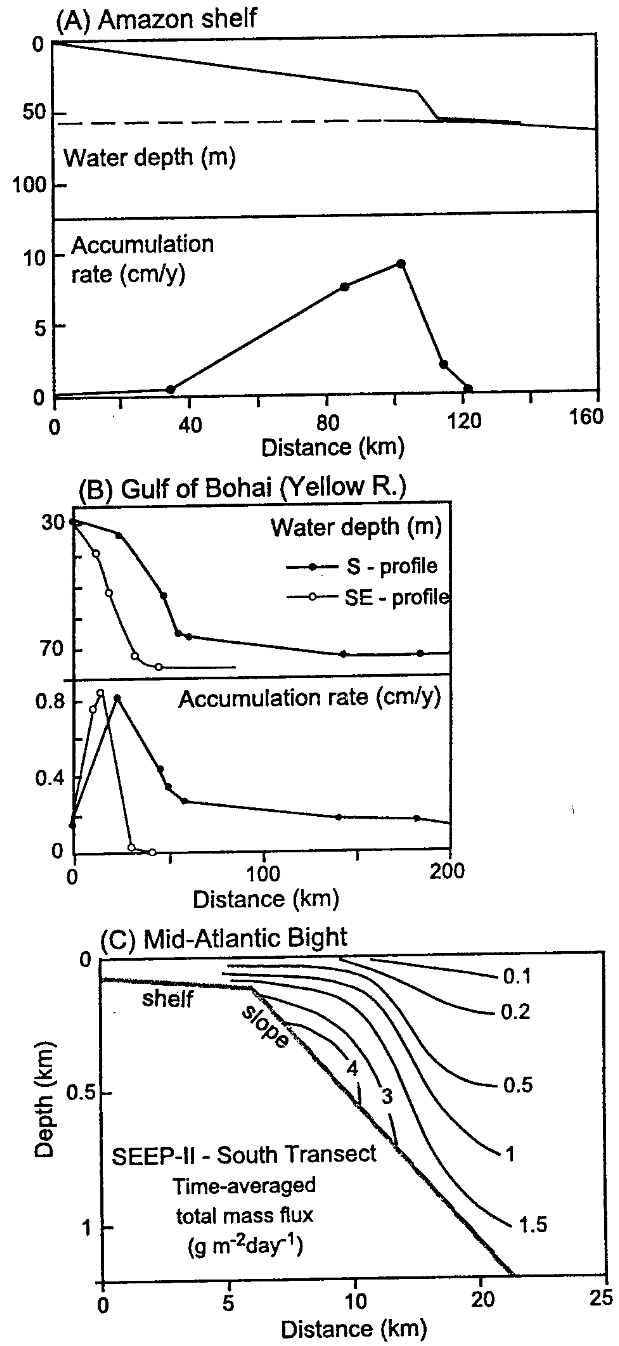

Figure 4. Sedimentation rate measured across modern clinoforms: (a) Amazon delta (based on ^{210}Pb data, modified from *Kuehl et al.* [1986]; (b) Shandong delta (based on ^{210}Pb data, modified from *Alexander et al.* [1991]); and (c) total sediment flux on the eastern U.S. shelf and slope measured with sediment traps (modified from *Biscaye and Anderson* [1994]), interpreted as a proxy for sedimentation rate.

for the conservation of suspended sediment is (for a full derivation, see, for instance, *Parker et al.* [1986]):

$$\frac{\partial UCh}{\partial x} = R(x) \qquad (3)$$

where UCh is the layer-averaged suspended sediment discharge and $R(x)$ is the net vertical flux of sediment at any point along the profile. Here we model $R(x)$ to represent the removal or addition of sediment from the water column by deposition or erosion, respectively.

We use the formulation of *McCave and Swift* [1976] for $R(x)$:

$$R(x) = W_S\, c_b \left(1 - \frac{\tau_b}{\tau_c}\right) p \qquad (4)$$

Equation (4) results from work on cohesive sediments [*Krone*, 1962, 1993]. The term $(1 - \tau_b/\tau_c)$ reflects the balance between floc aggregation as clays settle into zones of higher concentration, and floc disaggregation and resuspension by the flow turbulence. Where $\tau_b \geq \tau_c$, deposition does not occur, and the sediment is advected laterally; at present, erosion is not simulated in the model. Where $\tau_b < \tau_c$, deposition results from the net balance between the settling flux $W_S\, c_b$ and the upward directed resuspension flux determined by the ratio τ_b/τ_c. The value p represents the probability that a particle will remain at the bottom once deposited and is here assumed to be unity.

3.2. Basin Floor Evolution

Assuming the sediment has a bulk density ρ_B at the basin floor in the absence of sediment compaction and tectonic subsidence, the change in bottom topography with time is described by the one-dimensional Exner equation

$$\frac{dh}{dt} = \rho_B \left(\frac{\partial UCh}{\partial x}\right) \qquad (5)$$

which after substituting the right-hand side with (3) and (4) becomes

$$\frac{dh}{dt} = \rho_B \left[W_S\, c_b \left(1 - \frac{\tau_b}{\tau_c}\right)\right] \qquad (6)$$

The relation of c_b to C is determined by first assuming that the vertical distribution of suspended sediment concentration follows the open-channel Rouse profile [*Graf*, 1984, p. 173],

$$c(z) = C_{\text{ref}} \left[\left(\frac{z}{h - z}\right) \left(\frac{z_{\text{ref}}}{h - z_{\text{ref}}}\right) \right]^{\frac{W_S}{\kappa u_*}} \qquad (7)$$

and second, assuming that a constant factor, r_o, relates the near-bed and average concentrations:

$$c_b = r_o C \qquad (8)$$

Strictly, r_o depends on the flow conditions, in particular on the exponent in (7). For simplicity, we assume a constant value $r_o = 1.5$, which simplifies the calculations considerably and appears to be supported by experiments with open-channel suspensions described by *Garcia and Parker* [1987] and *Parker et al.* [1986]. Equation (8) allows the change in bed elevation described by (6) to be related to the layer-averaged conservation of sediment discharge described by (3).

3.3. Conservation of Fluid

The layer-averaged equation for conservation of fluid,

$$\frac{\partial Uh}{\partial x} = 0 \qquad (9)$$

determines the lateral variation of water discharge, with $h(x)$ representing the water depth and $U(x)$ representing the mean flow velocity.

The near bed shear-stress is

$$\tau_b = s\,\rho C_D u_{100}^2 \qquad (10)$$

where u_{100} is the flow velocity at a reference level 1 m above the bed and s is a dimensionless scaling factor. The flow velocity near the bed, u_{100}, is determined from the mean value U by assuming a logarithmic velocity profile,

$$u(x,z) = U\frac{\sqrt{C_D}}{\kappa}\ln\left(\frac{(h-z)+z_0}{z_0}\right) \qquad (11)$$

with the height above the bed, (h-z), set to 1 m.

Sediment deposition is controlled via a critical value for the near-bed shear stress, tc, using the suspension-bedload threshold [e.g., *Middleton*, 1976]

$$\tau_c = \rho\, u_{*c}^2 \qquad (12a)$$

$$u_{*c} = W_S \qquad (12b)$$

where u_{*c} is the critical shear velocity. In this paper, the settling velocity WS is reported through its Stokes-equivalent grain diameter for simplicity.

In order to provide for proper scaling in the model with respect to natural systems, that is, to relate model time to actual time, there is a need to introduce the scaling factor s in (10). The factor s equates to the ratio between the average magnitude of the instantaneous velocity field and the residual velocity:

$$s = \frac{\int_t |u|\,dt}{\int_t u\,dt} \qquad (13)$$

The residual advection velocity (denominator in (13)) in a specific basin is thought to be very small, although a net seaward flow probably can be assumed, given that a sedimentary deposit progrades outward from a river mouth. The average magnitude of the velocity (numerator in (13)) is primarily a function of the energy level of a particular environment. The factor s obviously depends on the time span considered in the integration and on the significance of extreme events, that is, on the magnitude-frequency distribution of the velocity. The value of s should be a characteristic of a particular environment and should be greater for high-energy environments. An estimate of the magnitude of s can be obtained for existing clinoform systems. For instance, on the Amazon delta a mean residual seaward flow of the order of 10^{-2} m/s over a tidal cycle is estimated from physical oceanographic models using tidal and shelf current measurements [*Geyer et al.*, 1996]. Time series of instantaneous currents indicate velocities of the order of 1 m/s near the bed, suggesting $s \sim 10$ [*Jewell et al.*, 1993; *Geyer et al.*, 1996]. The advective sediment and flow discharge modeled through (3) and (9), respectively, determines the rate at which sediment accumulates. In the model the same flow exerts a shear stress near the bed, calculated through (10) and (11), which, in turns, determines whether the sediment grains are kept in suspension or whether they are removed from the water column and become part of the substrate. Because the instantaneous velocity experienced by the sediment grains is, in general, higher than the residual velocity, the accumulation rates calculated in the model will also be higher than the long-term accumulation rates measured in a specific setting. Thus, at this stage we cannot perform direct comparisons of accumulation and progradation rates measured in natural systems with model clinoforms generated by the model. However, the model allows for the comparison of shapes between natural and model clinoform surfaces and the interpretation of variations in shape with regard to changes in basin physiography, grain size, and the spatial distribution of near-bed shear stresses. The effects of basin shape, sea level changes, and interaction between the velocity field and the evolving topography are also examined during model execution through simulated time stepping.

3.4. Model Execution

For a particular model run a set of initial parameters is specified, including the initial bathymetry, the initial mean sediment discharge (U_0, C_0 and h_0), and the grain settling velocity (or its Stokes-equivalent grain diameter). The critical shear stress is then calculated from (12a) (Figure 5). At any particular time step the mean flow velocity and near-bed shear stress are first determined from the discharge at the model entrance and using (9)–(11). The flow velocity distribution with depth, calculated from (11) and the sediment concentration profiles implied by (7), are shown in Figure 5a. The settling and resuspension fluxes (Figure 5b) are then calculated by computing the two terms in the right-hand side of (6). Their difference, scaled by ρ_B, is the sedimentation rate profile *dh*/*dt* (Figure 5c). The sedimentation rate profile leads to a sediment layer with thickness defined by an arbitrary time step (Figure 5d). The temporal evolution is simulated by recalculating the flow field with the newly formed basin bathymetry resulting from changes in elevation due to deposition during the previous time step and any changes in sea level height.

4. Results

Figures 6 and 7 illustrate the clinoform growth and progradation simulated by the model under several different conditions. In the simulations, discharge at the model entrance is kept constant, and the initial basin floor is linear, with or without a bottom slope. The maximum height of the clinoform, or the minimum water depth, is controlled by the near-bed shear stress at the model entrance and by the sediment grain size through τ_c (equation (5)). For simplicity, water depth at the model entrance is initially set to 10 m deeper than the depth of the critical shear stress for deposition for a given $u(x{=}0)$ and W_S in all model runs. Key results and comparisons to natural systems are described below.

4.1. Clinoform Growth

Clinoforms aggrade and prograde under a sedimentation-rate maximum that evolves with clinoform growth. Above an initially horizontal basin floor the near-bed shear stress is everywhere less than the critical shear stress. Sedimentation rate falls off from a maximum at the model entrance as a function of the sediment advection and settling velocities (Figures 6a and 6b). During this initial phase, clinoform growth is dominantly aggradational. As deposition raises the basin floor and water depth diminishes, flow velocity increases to maintain a constant discharge at the model entrance. As a result, near-bed shear stress increases to the critical stress, and sediments bypass the region. A sedimentation rate maximum forms over the evolving foreset slope, and clinoform growth reaches an equilibrium form, becoming dominantly progradational (Figures 6a and 6b). As clinoforms prograde, a composite topset surface is formed at a constant

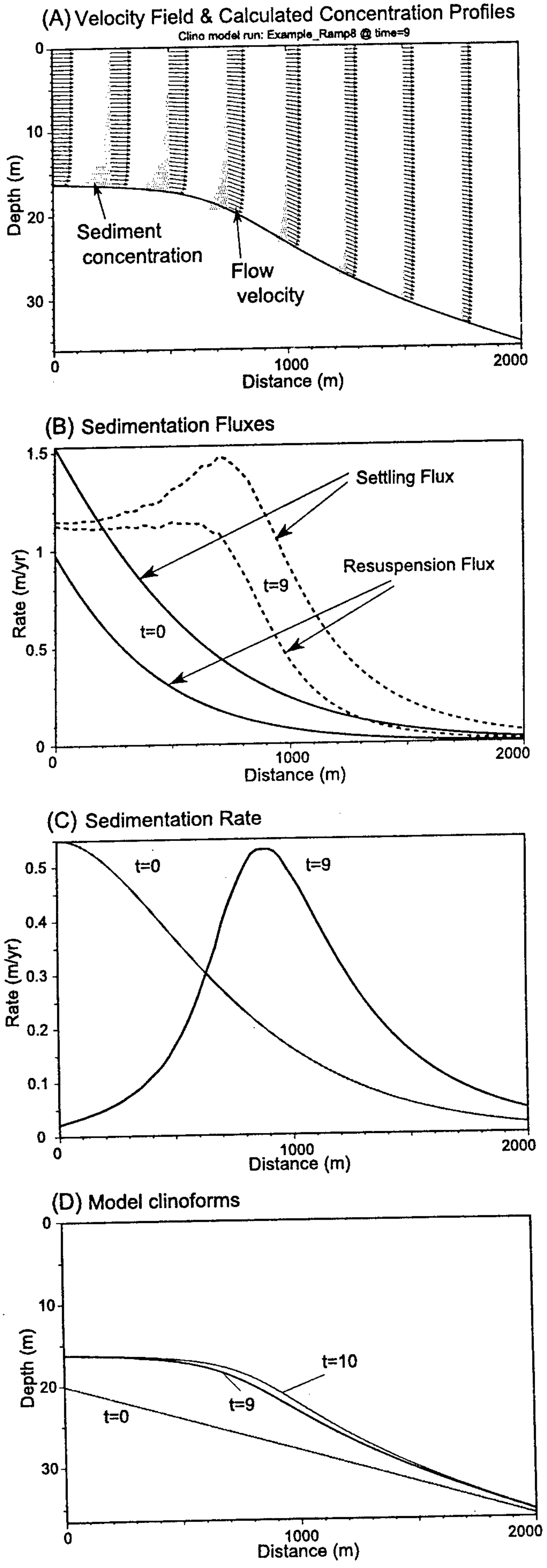

depth where $\tau_b = \tau_c$. These latter stages approximate the sediment accumulation rate profiles and clinoform geometries observed on modern deltas (e.g., Figure 4). The simulation over an initially flat surface provides a simple test of the present model, because it shows that clinoforms can be generated under physical conditions independent of preexisting topography, that is, solely as a result of gravitational settling under an advective flow field.

4.2. Clinoform Shape

Model clinoform surfaces exhibit the characteristic foreset-topset rollover and foreset-bottomset flattening observed in natural clinoforms. The rollover (e.g., Figure 6a, left-hand side) results in the model from the gradual increase in sedimentation rate as shear stresses diminish over the foreset. The flattening results from the gradual decrease in sedimentation rate over the bottomset as the water column is depleted of sediment. In all cases the clinoform shape is asymmetrical, that is, slope increases more rapidly across the rollover and decreases more slowly from the foreset to the bottomset (e.g., Figure 7a, right-hand side).

4.3. Grain Size Effects

Increasing grain size results in a steeper clinoform front with a more abrupt clinoform rollover and foreset-bottomset transition. Faster settling associated with larger grain sizes leads to narrower sedimentation rate profiles, with deposition increasingly focused on the upper foreset (compare Figures 6a and 6b). Relatively steep foreset slopes are observed, for instance, on Miocene clinoforms buried beneath the New Jersey continental shelf where sediments are predominantly sand (Figures 3d and 3h) [*Steckler et al.*, 1998]. Muddy clinoforms forming the Amazon delta, in contrast, display very gentle foreset slopes, of the order of 0.5° or less (Figure 2).

4.4. Basin Physiography

The shape of the receiving basin, in particular the initial slope, affects the evolution of the clinoform shape. An initially flat basin floor leads to the development of an equilibrium clinoform surface that is constant through time (Figures 6a and 6b). An initially sloping basin floor results in a foreset slope that increases with time (Figure 6c). The latter is the consequence of more rapid seaward expansion of the flow field as the relief between the topset and bottomset increases basinward. This type of foreset steepening is clearly observed in clinoforms of the Lake Mead delta (Figures 3a and 3e), where repeat surveys were carried out since the damming of the lake, showing progressively steeper clinoform fronts advancing over the Colorado River valley (mean gradient of 0.02°; Table 1).

Figure 5. (opposite) Example of model execution at a given time step. (a) Computed velocity and sediment concentration distributions. The vertical velocity distribution follows a logarithmic distribution (equation (11)). The concentration distribution is calculated using the Rouse distribution (equation (7)). The Rouse distribution is assumed and does not play a role in the model except in the definition of r_o in equation (8). (b) Computed settling flux and resuspension flux (terms in brackets, equation (6)). (c) Sedimentation rate, computed from the difference of the curves in Figure 5b. (d) Sediment layer resulting from the sedimentation rate curve.

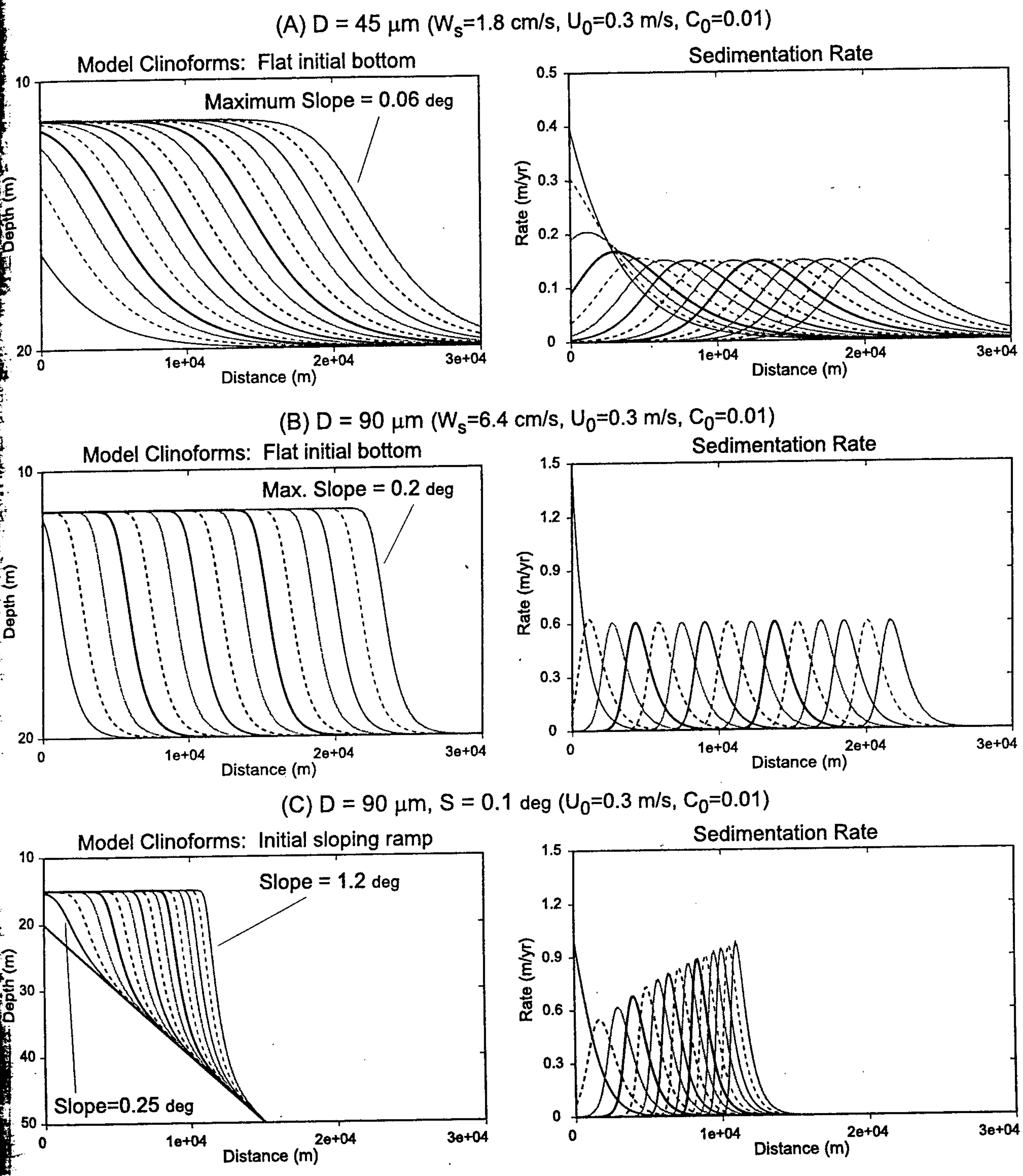

Figure 6. Model clinoforms produced under varying sediment grain size: (left) clinoform surfaces produced after 15 time steps and (right) corresponding sedimentation rate curves at each time step. Input parameters for each run are specified above each graph.

4.5. Sea Level Changes

The shapes of the model clinoforms and the stacking patterns of individual clinoform packages are clearly affected by changing sea level. Rising sea level progressively increases accommodation space above the topset, and clinoforms display simultaneous aggradation and progradation (Figure 7b). As sea level rises, sedimentation rate profiles narrow, with sedimentation focusing more sharply on the foreset. As a result, the foreset slope increases through time in a fashion similar to that displayed in the sloping basin floor model (Figure 6c). With falling sea level, model clinoforms prograde rapidly basinward as shoaling water depth leads to sediment bypassing of the topset (Figure 7c). In this instance, sedimentation rate profiles become broader, and the foreset slope decreases. In the case of falling sea level the composite topset surface ceases to be flat and dips

(A) Constant Sea Level, Initial Flat Bottom

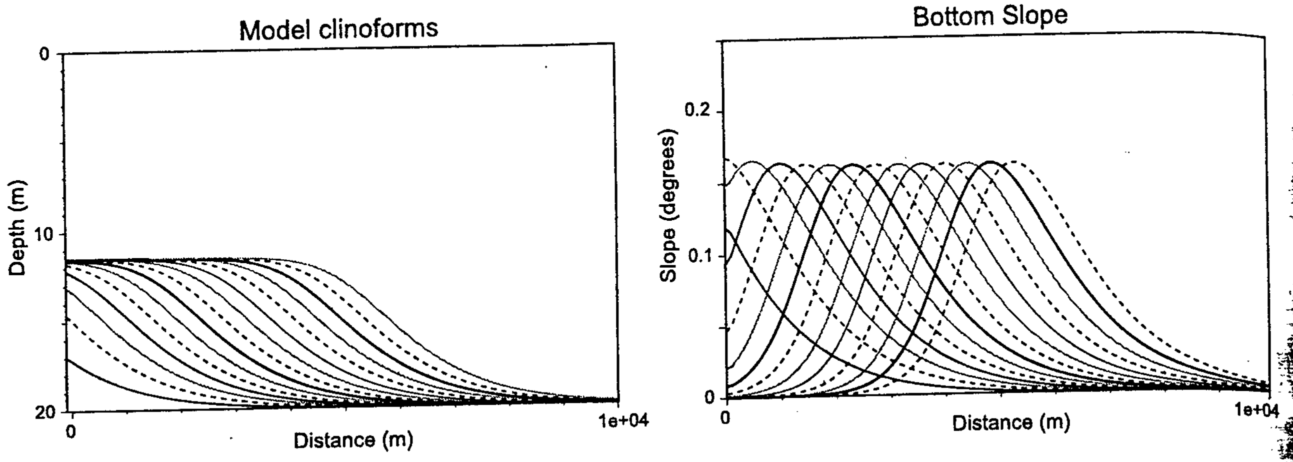

(B) Rising Sea Level, Initial Flat Bottom

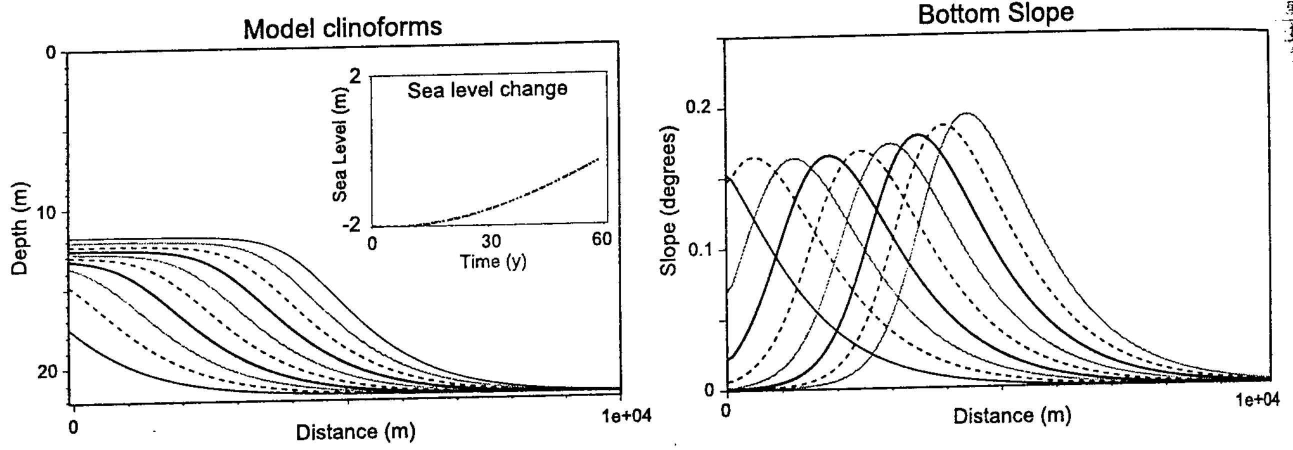

(C) Falling Sea Level, Initial Flat Bottom

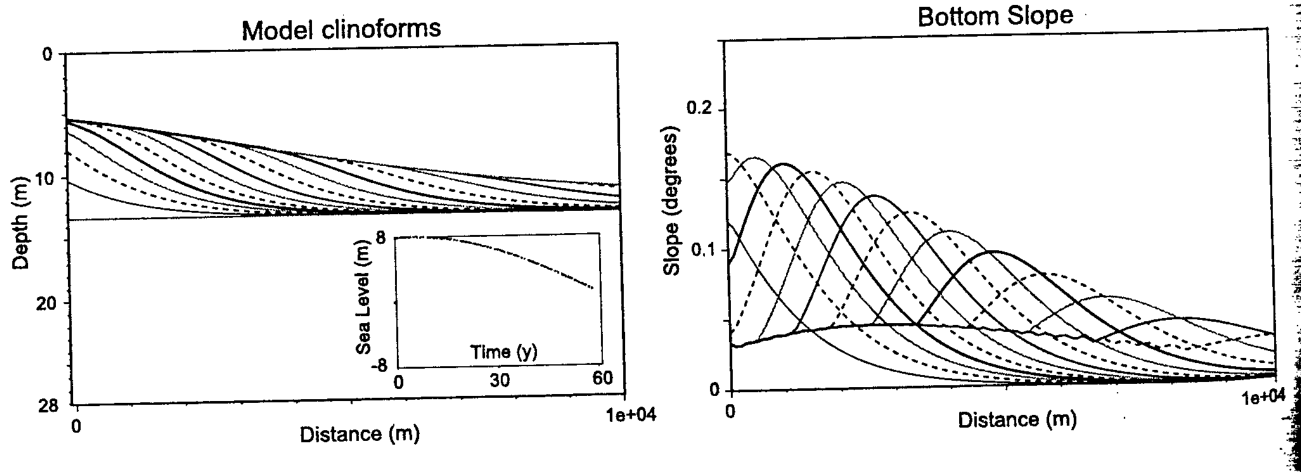

Figure 7. Model clinoforms produced under (a) constant sea level, (b) rising sea level, and (c) falling sea level. Insert shows the sea level curve applied during the model run (1/4 cycle for runs in Figures 7b and 7c). Right side panels show corresponding bottom slope curves at each time step. Input parameters common to all three runs are initial slope $S = 0$, $D = 45\mu\text{m}$, $U_0 = 0.1$ m/s and $C_0 = 0.02$.

gently basinward. During a sea level rise the aggradational topsets display a minor gradient that tends to become horizontal as the clinoforms prograde (Figure 7b). For the same rates of sea level change and sediment discharge at the model entrance, the composite topset surface atop the clinoform package is steeper during a relative sea level fall in comparison to that produced during a sea level rise. However, erosion which is not accounted for in this version of the model is likely to affect the profile shape significantly, particularly during the falling limb of the sea level curve.

5. Discussion

A basic feature of the current model is the feedback relationship between the evolving topography and the hydrodynamics of the water column. The flow field expansion in the model results in an overall decrease of near-bed shear stresses with increasing water depths. As sediment accumulation proceeds, so does the bottom configuration, which, in turn, affects the distribution of shear stresses. During the first execution step, when the basin floor has a constant gradient [$h(x) \sim Sx$], flow expansion determined through (9) leads to a decrease of mean flow velocity U proportionally to $1/x$, and, consequently, near-bed shear stress calculated through (10) falls off as $\sim 1/x^2$. As the basin floor evolves and ceases to be linear, the relationship between near-bed shear stress and distance becomes more complex and is solved numerically in the model.

The model velocity field is based on the concept of a river entering an enclosed basin, with discharge being kept constant. In natural systems, say over a continental shelf or enclosed lake basin, near-bed shear stresses generated by stirring waves and tides will also diminish with increasing water depth [*Nittrouer and Wright*, 1994; *Dyer*, 1989]. The net transport of sediment due to waves over a period of time can be negligible, but the important effect of wave motion stirring is that once in suspension, sediments will be advected by even very small lateral currents [*Grant and Madsen*, 1979]. In our model, the expansion of the flow field and consequent decrease of shear stresses with increasing water depth is intended to simulate the long-term average effects of waves, tides, and wind-driven currents. For comparison with our model the depth dependence of the wave-stirring effects on the near-bed shear stress can be estimated as follows. The horizontal orbital velocity due to waves near the sea bed is [e.g., *Allen*, 1985]:

$$U_{\text{orb}} = A\frac{2\pi\,\omega}{\sinh(k\,h)} \tag{14}$$

with the angular frequency ω defined by the dispersion relation $\omega^2 = g\,k \tanh(k\,z)$, where k is the wavenumber and A is the wave amplitude. The shear stress caused by wave orbital velocities can be computed using the same square law used here (equation (10)). This wave-induced shear stress decays with depth at a rate that is faster than in the present model and decreases to negligible values, that is, insufficient to suspend practically any sediment grains, below about 30-40 m for a wavelength of 50 m and amplitude of 1 m (Figure 8). Wave stirring is one component of the total shear stress occurring in natural systems, with the effects of tides and wind-driven currents further increasing the stress level and affecting the way stress varies with depth. The model distribution of shear stress as illustrated in Figure 8 has an important effect on the shape of the clinoform surfaces generated by the model. For instance, clinoform surfaces modeled with the wave-stirring stress distribution have a sharper rollover and shorter bottomset tail when compared to our model. While we do not include the effects of waves, currents, and tides explicitly, the model stress distribution used here can be interpreted as being caused by the integrated effects of all these factors. Clearly, more detailed modeling would be desired in order to determine the actual stress distribution in any particular environment and how it may affect sediment deposition and erosion. In our model we also assume a single grain size and neglect the effects of sediment compaction. These simplifications may be at the source of some of the features of natural clinoforms that are not captured by the current version of the model, such as the tendency for model clinoform packages to form a horizontal composite topset surface. Nevertheless, our model appears to capture several fundamental characteristics of natural clinoform surfaces that are not produced by previous modeling efforts. We now address some of the benefits of the model by comparing normalized model and natural clinoform surfaces.

In Figure 9 we plot normalized profiles of the Rhine, Mississippi, and Lake Mead clinoforms together with a sample of model clinoforms. Comparison between the surfaces in Figure 9 would suggest that the Rhine delta clinoforms are formed by coarser sediment than either the Lake Mead or Mississippi clinoforms. Given information on the basin physiography, the model could be used to quantitatively assess the differences in grain size and water column energy between these systems. Comparing clinoform surfaces within the same basin can also be facilitated through the model. For instance, the overall steepening of the Lake Mead clinoforms appears to result primarily from the progradation of the system over the sloping Colorado River valley rather than from a change in sediment grain size. On the other hand, the abrupt steepening of the clinoforms on the New Jersey margin seen at the middle Miocene (from the time of surface m5; Figures 1a and 3h) could be a result either of change in the gradient of the underlying surface or of an increase in the sediment grain size (and associated higher shear stress needed to carry the coarser material) or still a combination of both. Doubling the grain size (e.g., from 45 to 90 mm) represents an increase in settling velocity by a factor of about 3.5. In the model, given the same clinoform height (~9 m; Figure 6), this results in an increase of the maximum equilibrium foreset gradient by about the same factor (0.06° to 0.22°; Figures 6a and 6b). The slope increase for the middle Miocene New Jersey clinoforms is from about 1° to 3° (between surfaces m5 and m4; Table 1 and Figure 3). While the increase in sediment flux indicated by the rapid middle Miocene progradation (Figure 3h) would suggest that an increase in sediment grain size is a plausible source for the observed steepening, the model results would suggest that the steepening could also be accommodated by the increase in gradient of the underlying basin floor surface (Figures 1a and 6c).

The shapes of clinoforms over the large deltas of the Amazon, Shandong, and Ganges Rivers is characteristically different from the other clinoforms examined, with a broad, gently sloping topset and an inflection point occurring at low elevation with respect to the overall profile (Figure 2). The shape of these clinoform systems is reproduced only in generalized form in our model simulations. The simplified hydrodynamics over the model basin floor, and the sedimentation by simple advection and gravitational settling of a single grain size, cannot capture the complexity of these highly energetic clinoform systems. The lateral advective flux simulated in our model is an extreme simplification of the actual processes that transport sediment across continental shelves [*Nittrouer and Wright*, 1994]. In

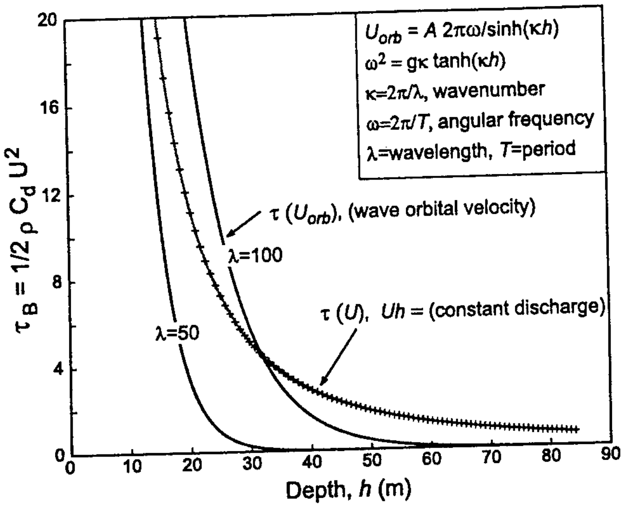

Figure 8. Near-bed shear stress distribution as a function of depth as calculated in our model versus that computed from a wave model. For our model, $h(x) = 5+Sx$, with $S = 0.004$. The wave-induced orbital velocity U_{orb} is calculated using equation (14), with $A = 1$. $U(x{=}0)$ is set equal to $U_{orb}(x = 0;\ \lambda = 100\text{ m})$ for this comparison. The near-bed shear stress was computed in both cases with the quadratic stress law (equation (10)).

particular, hyperpycnal flows, either directly from high sediment concentration rivers [e.g., *Wright et al.*, 1990] or after concentration of fluvially derived sediments over the topset as fluid-mud layers [*Kineke et al.*, 1996], have been shown to play an important role in the growth of these deltas. In the case of the Amazon, seaward advection of fluid muds from topset to foreset appears to occur at an approximately yearly cycle, with water column energy sufficiently strong to prevent incorporation of the fluid muds into the topset. The actual mechanisms of transport of these fluid muds are not yet well understood and cannot be simply characterized by either mass-movement or diffusive processes [*Nittrouer et al.*, 1996]. The advection of fluid muds appears to involve stirring and transport by waves and tidal currents, as well as transport due to excess density of the fluid muds downslope [*Kineke et al.*, 1996].

Our model presently simulates a fluvial source that remains fixed as clinoforms prograde basinward. The depth of the topset surface and clinoform rollover is dependent on the magnitude of the shear stress in the water column vis-à-vis the grain settling velocity. The model clinoforms, as in most natural clinoform surfaces, display a clinoform rollover at a water depth depending primarily on the energy conditions prevailing in the water column. In both modern and ancient clinoforms the shoreline and "offlap break," or subaqueous clinoform front [*Vail et al.*, 1991], can vary from being coincident to >100 km apart (e.g., Figures 1–3; *Molenaar and Baird*, [1992]). However, sequence stratigraphic concepts have not yet been fully modified to account for the possible variations in distance between these features, nor for the causes for these variations. The offlap break and the shoreline positions are critical, for they are used to interpret the extent of subaerial exposure of the shelf during sea level falls and to predict facies distributions. Natural clinoform surfaces investigated here commonly show that the topset surfaces dip at a small angle. In energetic shelf environments, such as in the Amazon and Ganges, the clinoform break can be widely separated from the coastline.

The results on clinoform geometry under varying sea level (Figure 7) are consistent with the clinoform stratal patterns inferred by the conceptual sequence stratigraphic model [*Posamentier et al.*, 1988]. In that model the geometry of clinoform surfaces depends primarily on the rate at which new space is produced for sediments to accumulate and on the influx of sediments. As relative sea level rises, during the lowstand systems tract, the addition of space at the top of the clinoforms would result in a progressive change from prograding to aggrading packages. Conversely, during a relative sea level fall, water depth remains constant or decreases above the foreset, resulting in sediment bypass and clinoform progradation. Whether differences in the geometry of clinoforms, such as the systematically different topset slope between lowstand and highstand clinoform packages (Figures 7b and 7c, respectively), are preserved in the geologic record remains to be tested against natural systems. In general, the topset surfaces of highstand clinoforms will be subject to erosion as sea level falls. However, these surfaces could be at least in part preserved where the change in water depth is relatively small, preventing marked erosion of the topsets.

Where clinoforms prograde across a dipping basin floor, the foreset slope steepens with time (Figure 6c). This occurs because, with a constant sediment input and advection velocity, sediment is allowed to fill the available space up to the water depth where tb equals tc. The model at present does not limit the foreset slope from attaining an unrealistic high gradient. Steepening foreset slopes of natural clinoforms would at some point fail. Presumably, mass wasting of the steep foresets would act to retreat the clinoform front, with the foreset returning to smaller, more stable slopes. Alternatively, the action of storm waves and currents could erode material from and/or induce mass-failures at the clinoform front. A possible example is seen on the Rhine delta clinoforms, which show a rapid decrease in gradient followed by a progressive increase through time (Figure 3f). Material removed from the clinoform front by mass wasting would deposit over the bottomset region, raising the seafloor and thus decreasing the relief between topset and bottomset regions of the clinoform. In the model this would result in spreading the sedimentation rate profile over a broader region. The model results suggest that mass wasting is likely to become more significant relatively late in the evolution of a clinoform package, as the system advances into deeper water and foreset slopes rise to some critical limit. The Lake Mead delta is a good example of a system that shows clinoform steepening during progradation over an inclined surface (the pre-dam Colorado River valley). Apparently, the Lake Mead delta sediments have largely been able to sustain clinoform front gradients up to 1.2° after 11 years of delta growth (Figure 3e). The early Miocene clinoforms off New Jersey show a rapid steepening of the middle Miocene clinoform fronts (Figure 3h), with clinoform height and foreset angle being directly related (Table 1; *Steckler et al.* [1998]). Patterns of increasing slope through time are detected internally within some of the early Miocene sequences, and significant steepening also is seen in the late Miocene to Pleistocene sequences off New Jersey [*Steckler et al.*, 1993; G. Mountain, personal communication, 1996]. *Ross et al.* [1994] observed a similar tendency of clinoform surfaces to steepen with time as they prograded into deeper water.

The model sensitivity tests performed thus far suggest that quantitative constraints on sediment grain size, relative sea level, sediment supply, and depositional environment might be obtained from clinoform geometry, particularly in instances

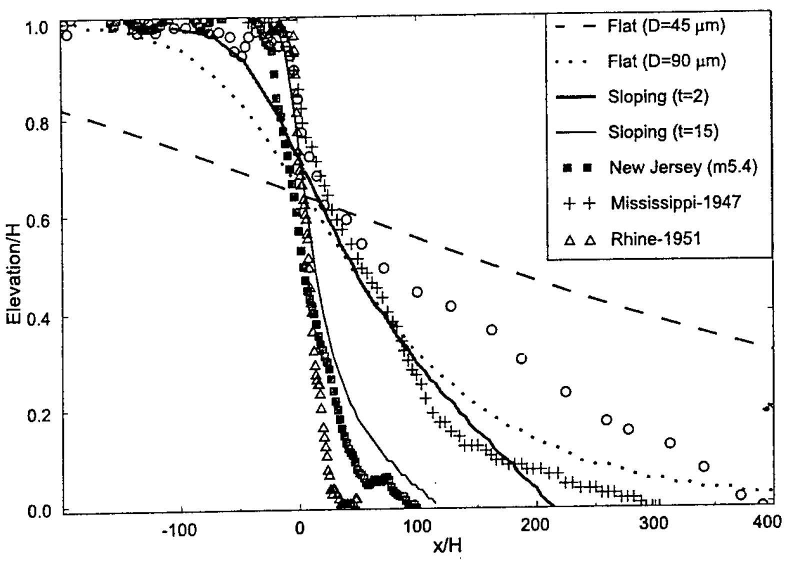

Figure 9. Comparison of normalized model clinoforms and selected natural clinoforms. Model clinoforms correspond to those shown in Figures 6a–6c. Natural clinoforms are taken from those shown in Figure 3.

where one or more of these factors are known (e.g., Figure 9). Geometric models suggest that stratigraphic sequences are a complex and possibly non unique combination of these factors plus subsidence [*Burton et al.*, 1987]. However, in assuming a predefined clinoform shape, these models forfeit formative constraints provided by clinoform geometries. Diffusion-based models suffer similar limitations. While it is a common observation that steeper clinoform fronts in siliciclastic systems tend to be associated with higher-energy environments and coarser grain sizes [*Sangree and Windmier*, 1977], there has been no attempt to quantify this important property of clinoform morphology in terms of grain size or facies. Diffusion models display steep fronts when the diffusion coefficient is small, that is, in situations where sediment transport is interpreted to be inefficient. In the present model the clinoform front slope will vary with time if the clinoform advances into deeper water or if sea level height changes. The equilibrium slope achieved under an initially flat basin, however, indicates that the maximum slope depends on a combination of parameters, in particular the settling velocity (grain size) and the near-bed shear stress, the latter depending on the flow velocity field. If information on sediment properties is available, say from samples or well logs, it may be possible to use the model in order to place constraints on the prevalent water column energy conditions during deposition.

6. Conclusions

We present a sediment dispersal model in which settling sediment grains are advected laterally or deposited according to the shear stress level near the bed. The model couples sedimentation with a fluid flow model that simulates a decrease in shear stress with increased water depth, thought to represent the variation of shear stresses in a basin due to the long-term averaged effects of waves, tides, and wind-driven currents. While the fluid flow model used here is extremely simple, the resulting model clinoforms reproduce some of the most fundamental characteristics of natural clinoform systems and provide the basis for some predictions that can be tested in the field and with further modeling. Among the characteristics of clinoforms reproduced here are (1) the gradual change in slope at the rollover between topset and foreset segments of a clinoform, as well as between the foreset and bottomset, resulting from the lateral variation in near-bed shear stresses affecting sediment accumulation rate; (2) the separation between the point of sediment input, or river mouth/coastline, and the rollover point is due to high shear stresses preventing deposition on the topset; (3) the equilibrium foreset slope increases with increasing grain size input to the system; (4) foreset slope increases progressively through time where clinoforms advance over a sloping basin floor (equilibrium foreset slope in these cases probably is limited by a combination of processes such as slope stability, sediment supply and accumulation rate, and erosion caused by storm events); and (5) temporal changes in clinoform morphology with varying space available for sediment accommodation, that is, relative sea level changes.

Perhaps most significantly, the model clinoform shapes result from a balance between sediment settling velocity, horizontal advection, and the turbulent energy that prevents deposition and keeps sediment in suspension. The linkage between the flow velocity field and basin physiography results in a feedback loop between sedimentation and the water column energy that is intrinsic to prograding clinoform systems.

Notation

b	subscript to indicate a near-bed quantity, $b << H$
C	mean sediment concentration in water layer.
c	suspended sediment concentration (by volume).
c_b	suspended sediment concentration near the bed.
C_D	Drag coefficient (set to 0.005).
h	layer thickness or total water depth.
H	height of clinoform.
κ	von Karman's constant (set to 0.4).
K_i	coefficient of turbulent diffusion.
λ	wavelength.
k	wavenumber, $2\pi/\lambda$.
p	probability of sediment particle "sticking" to bed (=1).
q_i	sediment discharge vector.
R	rate of sediment accumulation.
ρ	fluid density.
ρ_B	bulk-density of deposited layer (set to 1800 kg/m^3).
r_o	ratio of near-bed to layer-average sediment concentration.

s	scaling factor, ratio between u_{rms} and u_{residual}
S	bottom slope.
τ_b	near-bed shear stress.
τ_c	critical shear stress for deposition.
t	time.
U	mean horizontal fluid velocity in layer.
u	horizontal component of fluid velocity vector.
u_*	shear velocity [$u_* = \sqrt{(\tau_b / \rho)}$].
u_{*c}	critical shear velocity for deposition.
u_{100}	horizontal component of fluid velocity 1 m above bed.
W_s	grain settling velocity.
ω	wave angular frequency, 2π/period.
x	horizontal distance from sediment source.
z	depth below sea level.
z_0	Nikuradse roughness parameter (1/30th of grain diameter).

Acknowledgments. The authors thank the support of the National Science Foundation through grant NSF-EAR-92-05623. Coauthors L.F.P. and M.S.S. also acknowledge support from the Office of Naval Research through grants N00014-97-1-0016 and N00014-95-1-0076, respectively. Constructive discussions with Bill Ryan and Gary Karner were useful in improving our understanding of clinoform development. Chris Paola provided very constructive comments and criticisms that helped improve this paper. Christopher Kendall, John Carey, Don Swift, the Associate Editor Herbert Wang, and an anonymous reviewer are thanked for their thoughtful comments and constructive suggestions that helped improve the manuscript. This is L-DEO contribution 5797.

References

Adams, C.E., Jr., J.T. Wells, and J.M. Coleman, Transverse bedforms on the Amazon continental shelf, *Cont. Shelf Res.*, *6*, 175-187, 1986.

Alexander, C.R., D.J. DeMaster, and C.A. Nittrouer, Sediment accumulation in a modern epicontinental-shelf setting: The Yellow Sea, *Mar. Geol.*, *98*, 51-72, 1991.

Allen, J.R.L., *Principles of Physical Sedimentology*, 272 pp., Allen and Unwin, Winchester, Mass., 1985.

Bartek, L.R., P.R. Vail, J.B. Anderson, P.A. Emmet, and S. Wu, Effect of Cenozoic ice sheet fluctuations in Antarctica on the stratigraphic signature of the Neogene, *J. Geophys. Res.*, *96*, 6753-6778, 1991.

Bates, C.C., Rational theory of delta formation, *Am. Assoc. Pet. Geol. Bull.*, *37*, 2119-2162, 1953.

Biscaye, P.E., and R.F. Anderson, Fluxes of particulate matter on the slope of the southern Mid-Atlantic Bight: SEEP-II, *Deep Sea Res., Part II*, *41*, 459-509, 1994.

Bowman, S.A., and P.R. Vail, Carbonate sedimentation processes in PHIL, paper presented at *Am. Assoc. Pet. Geol. Annu. Conv.*, New Orleans, Louisiana, 1993.

Burton, R., C.G.S.C. Kendall, and I. Lerche, Out of our depth: On the impossibility of fathoming eustatic sea level from the stratigraphic record, *Earth Sci. Rev.*, *24*, 237-277, 1987.

Coleman, J.M., D.B. Prior, and J.F. Lindsay, Deltaic influences on shelf edge instability processes, in *The Shelfbreak: Critical Interface on Continental Margins*, edited by D.J. Stanley and G.T. Moore, pp. 121-137, Soc. for Sediment. Geol., Tulsa, Okla., 1983.

Dyer, K.R., Sediment processes in estuaries: Future research requirements, *J. Geophys. Res.*, *94*, 14,327-14,339, 1989.

Flemings, P.B., and T.E. Jordan, A synthetic stratigraphic model of foreland basin development, *J. Geophys. Res.*, *94*, 3851-3866, 1989.

Garcia, M., and G. Parker, On the numerical prediction of turbidity currents, in *Third International Symposium on River Sedimentation*, edited by S.T. Wang, H.W. Shen, and L.Z. Ding, pp. 1556-1565, Univ. of Miss. Press, St. Louis, 1987.

Geyer, W.R., R.C. Beardsley, S.J. Lentz, J. Candela, R. Limeburner, W.E. Johns, B.M. Castro, and I.D. Soares, Physical oceanography of the Amazon shelf, *Cont. Shelf Res.*, *16* (5/6), 575-616, 1996.

Gilbert, G.K., The topographic features of lake shores, *U.S. Geol. Surv. Annu. Rep.*, *5*, 104-108, 1885.

Gilbert, G.K., Lake Bonneville, *U.S. Geol. Surv. Monogr.*, *1*, 438 pp., 1890.

Graf, W.H., *Hydraulics of Sediment Transport*, Water Resour. Publ., Fort Collins, Colo., 1984.

Grant, W.D., and O.S. Madsen, Combined wave and current interaction with a rough bottom, *J. Geophys. Res.*, *84*, 1797-1808, 1979.

Greenlee, S.M., and T.C. Moore, Recognition and interpretation of depositional sequences and calculation of sea-level changes from stratigraphic data – offshore New Jersey and Alabama Tertiary, in *Sea-Level Changes: An Integrated Approach*, edited by C.K. Wilgus et al., pp. 329-353, Soc. for Sediment. Geol., Tulsa, Okla., 1988.

Hathaway, J.C. et al. , Preliminary summary of the 1976 Atlantic Margin Coring Project of the U.S. Geological Survey, *U.S. Geol. Surv. Open File Rep.*, *76-844*, 217 pp., 1976.

Jervey, M.T., Quantitative geological modeling of siliciclastic rock sequences and their seismic expression, in *Sea-Level Changes: An Integrated Approach*, edited by C.K. Wilgus et al, pp. 47-69, Soc. for Sediment. Geol., Tulsa, Okla., 1988.

Jewell, P.J., R.F. Stallard, and G.L. Mellor, Numerical studies of bottom shear stress and sediment distribution on the Amazon continental shelf, *J. Sediment. Petrol.*, *63*, 734-745, 1993.

Jordan, T.E., and P.B. Flemings, Large-scale stratigraphic architecture, eustatic variation, and unsteady tectonism: A theoretical evaluation, *J. of Geophys. Res.*, *96*, 6681-6699, 1991.

Kaufman, P., J.P. Grotzinger, and D.S. McCormick, Depth-dependent diffusion algorithm for simulation of sedimentation in shallow marine depositional systems, in *Sedimentary Modeling: Computer Simulations and Methods for Improved Parameter Definition*, edited by E.K. Franseen et al., pp. 490-508, Kansas Geol. Surv. Bull., Lawrence, 1991.

Kendall, C.G.S.C., P. Moore, J. Stroble, R. Cannon, M. Perlmutter, J. Bezdek, and G. Biswas, Simulation of the sedimentary fill of basins, in *Sedimentary Modeling: Computer Simulations and Methods for Improved Parameter Definition*, edited by E.K. Franseen et al., pp. 9-30, Kansas Geol. Surv. Bull., Lawrence, 1991.

Kenyon, P.M., and D.L. Turcotte, Morphology of a delta by bulk sediment transport, *Geol. Soc. Am. Bull.*, *96*, 1457-1465, 1985.

Kineke, G.C., R.W. Sternberg, J.H. Trowbridge, and W.R. Geyer, Fluid-mud processes on the Amazon continental shelf, *Cont. Shelf Res.*, *16*, 667-696, 1996.

Krone, R.B., *Flume Studies of the Transport of Sediment in Estuarial Shoaling Processes*, 110 pp., Univ. Hydraul. Eng. Lab., Berkeley, Calif., 1962.

Krone, R.B., Sedimentation revisited, in *Nearshore and Estuarine Cohesive Sediment Transport,Coastal and Estuarine Stud.*, vol. 42, edited by A.J. Mehta, pp. 108-125, AGU, Washington, D. C., 1993.

Kuehl, S.A., C.A. Nittrouer, and D.J. DeMaster, Nature of sediment accumulation on the Amazon Continental Shelf, *Cont. Shelf Res.*, *6*, 209-225, 1986.

Kuehl, S.A., T.M. Hariu, and W.S. Moore, Shelf sedimentation off the Ganges-Brahmaputra river system: Evidence for sediment by-passing to the Bengal Fan, *Geology*, *17*, 1132-1135, 1989.

McCave, I.N., and S.A. Swift, A physical model for the rate of deposition of fine-grained sediments in the deep sea, *Geol. Soc. Am. Bull.*, *87*, 541-546, 1976.

Middleton, G.V., Hydraulic interpretation of sand size distributions, *J. Geol.*, *84*, 405-426, 1976.

Mitchum, R.M., Jr., P.R. Vail, and S. Thompson III, Seismic stratigraphy and global changes in sea level, 2, The depositional sequence as a basic unit for stratigraphic analysis, in *Seismic Stratigraphy–Applications to Hydrocarbon Exploration*, edited by C.E. Payton, pp. 165-184, Am. Assoc. Pet. Geol., Tulsa, Okla., 1977.

Molenaar, C.M., and J.K. Baird, Regional stratigraphic cross sections of Upper Cretaceous rocks across the San Juan Basin, northwestern New Mexico and southwestern Colorado, *U.S. Geol. Surv. Open File Rep.*, *92-0257*, 3 sheets, 1992.

Nittrouer, C.A., and D.J. DeMaster, The Amazon shelf setting: tropical, energetic and influenced by a large river, *Cont. Shelf Res.*, *16*, 553-573, 1996.

Nittrouer, C.A., and L.D. Wright, Transport of particles across continental shelves, *Rev. Geophys.*, *32*, 85-113, 1994.

Nittrouer, C.A., S.A. Kuehl, R.W. Sternberg, A.G. Figueiredo Jr., and L.E.C. Faria, An introduction to the geological significance of sediment transport and accumulation on the Amazon continental shelf, *Mar. Geol.*, *125*, 177-192, 1995.

Nittrouer, C.A., S.A. Kuehl, A.G. Figueiredo Jr., M.A. Allison, C.K. Sommerfield, J.M. Rine, L.E.C. Faria, and O.M. Silveira, The geological record preserved by Amazon shelf sedimentation, *Cont. Shelf Res.*, *16*, 817-841, 1996.

Parker, G., Y. Fukushima, and H.M. Pantin, Self-accelerating turbidity currents, *J. Fluid Mech.*, *171*, 145-181, 1986.

Poag, C.W., Depositional history and stratigraphic reference section for the central Baltimore Canyon trough, in *Geologic Evolution of the*

United States Atlantic Margin, edited by C.W. Poag, pp. 217-264, Van Nostrand Reinhold, New York, 1985.

Poag, C.W., and G.S. Mountain, Late Cretaceous and Cenozoic evolution of the New Jersey continental slope and upper rise: An integration of borehole data with seismic reflection profiles, in *Initial Reports of the Deep Sea Drilling Project*, edited by C.W. Poag and A.B. Watts, pp. 673-724, U.S. Gov. Print. Off., Washington, D. C., 1987.

Posamentier, H.W., M.T. Jervey, and P.R. Vail, Eustatic controls on clastic deposition, I, Conceptual framework, in *Sea-Level Changes: An Integrated Approach*, edited by C.K. Wilgus et al., pp. 125-154, Soc. for Sediment. Geol., Tulsa, Okla., 1988.

Pratson, L.F., and B.J. Coakley, A model for the headward erosion of submarine canyons induced by downslope-eroding sediment flows, *Geol. Soc. Am. Bull.*, *108* , 225-234, 1996.

Pratson, L.F., and W. Haxby, What is the slope of the U.S. continental slope?, *Geology*, *24* , 3-6, 1996.

Pratson, L.F., W.B.F. Ryan, G.S. Mountain, and D.C. Twichell, Submarine canyon initiation by downslope eroding sediment flows: Evidence in Late Cenozoic strata on the New Jersey continental slope, *Geol. Soc. Am. Bull.*, *106*, 395-412, 1994.

Reynolds, D.J., M.S. Steckler, and B.J. Coakley, The role of the sediment load in sequence stratigraphy: the influence of flexural isostasy and compaction, *J. Geophys. Res.*, *96*, 6931-6949, 1991.

Ross, W.C., Modeling base-level dynamics as a control on basin-fill geometries and facies distribution: A conceptual framework, in *Quantitative Dynamic Stratigraphy*, edited by T.A. Cross, pp. 387-400, Prentice-Hall, Englewood Cliffs, N. J., 1989.

Ross, W.C., B.A. Halliwell, J.A. May, D.E. Watts, and J.P.M. Syvitski, Slope readjustment: A new model for the development of submarine fans and aprons, *Geology*, *22*, 511-514, 1994.

Sangree, J.B., and J.M. Windmier, Seismic stratigraphy and global changes in sea level, 9, Seismic interpretation of depositional facies, in *Seismic Stratigraphy: Applications to Hydrocarbon Exploration*, edited by C.E. Payton, pp. 165-184, Am. Assoc. Pet. Geol., Tulsa, Okla., 1977.

Smith, W.O., et al., Comprehensive survey of Lake Mead, *U.S. Geol. Surv. Prof. Pap.*, *295*, 1954.

Stanley, D.J., S.K. Addy, and E.W. Behrens, The mudline: Variability of its position relative to shelfbreak, in *The Shelf Break: Critical Interface on Continental Margins*, edited by D.J. Stanley and G.T. Moore, pp. 279-298, Soc. for Sediment. Geol., Tulsa, Okla., 1983.

Steckler, M.S., D.J. Reynolds, B.J. Coakley, B.A. Swift, and R.D. Jarrard, Modeling passive margin sequence stratigraphy, in *Sequence Stratigraphy and Facies Associations*, edited by H.W. Posamentier et al., pp. 19-41, Int. Assoc. Sediment., 1993.

Steckler, M.S., G.S. Mountain, K.G. Miller and N. Christie-Blick, Reconstruction of Tertiary progradation and clinoform development on the New Jersey margin by 2-D backstripping, *Mar. Geol.*, in press, 1998.

Swift, D.J.P., and J.A. Thorne, Sedimentation on continental margins, I, A general model for shelf sedimentation, in *Shelf Sands and Sandstone Bodies: Geometry, Facies and Distribution*, edited by D.J.P. Swift et al., pp. 3-31, Blackwell Sci., Cambridge, Mass., 1991.

Syvitski, J.P.M., and J.M. Alcott, GRAIN2: Predictions of particle size seaward of river mouths, *Comput. Geosci.*, *19* , 399-446, 1993.

Syvitski, J.P.M., and J.M. Alcott, RIVER3: Simulation of river discharge and sediment transport, *Comput. Geosci.*, *21*, 89-151, 1995.

Syvitski, J.P.M., and S. Daughney, DELTA2: Delta progradation and basin filling, *Comput. Geosci.*, *18* , 839-897, 1992.

Syvitski, J.P.M., J.N. Smith, E.A. Calabrese, and B.P. Boudreau, Basin sedimentation and the growth of prograding deltas, *J. Geophys. Res.*, *93*, 6895-6908, 1988.

Tezlaff, D.M., and J.W. Harbaugh, *Simulating Clastic Sedimentation*, 202 pp., Van Nostrand Reinhold, New York, 1989.

Thorne, J.A., On the scale independent shape of prograding stratigraphic units: Applications to sequence stratigraphy, in *Fractals in Petroleum Geology and Earth Processes*, edited by C.C. Barton and P.R. La Pointe, pp. 97-112, Plenum, New York, 1995.

Thorne, J.A., and D.J.P. Swift, Sedimentation on continental margins, II, Application of the regime concept, in *Shelf Sands and Sandstone Bodies: Geometry, Facies and Distribution*, edited by D.J.P. Swift et al., pp. 33-58, Blackwell Sci., Cambridge, Mass., 1991.

Thorne, J.A., E. Grace, D.J.P. Swift, and A. Niedoroda, Sedimentation on continental margins, III, The depositional fabric: An analytical approach to stratification and facies identification, in *Shelf Sands and Sandstone Bodies: Geometry, Facies and Distribution*, edited by D.J.P. Swift et al., pp. 59-87, Blackwell Sci., Cambridge, Mass., 1991.

Vail, P.R., Seismic stratigraphy interpretation using sequence stratigraphy, 1, Seismic stratigraphy interpretation procedure, in *Atlas of Seismic Stratigraphy*, edited by A.W. Bally, pp. 1-10, Am. Assoc. Pet. Geol., Tulsa, Okla., 1987.

Vail, P.R., J. Mitchum, R.M., R.G. Todd, J.M. Widmier, S. Thompson III, J.B. Sangree, J.N. Bubb, and W.G. Hatlelid, Seismic stratigraphy and global changes of sea level, in *Seismic Stratigraphy: Applications to Hydrocarbon Exploration*, edited by C.E. Clayton, pp. 49-212, Am. Assoc. Pet. Geol., Tulsa, Okla., 1977.

Vail, P.R., F. Audemard, S.A. Bowman, G. Einsele, and G. Perez-Cruz, The stratigraphic signatures of tectonics, eustacy and sedimentation, in *Cycles and Events in Stratigraphy*, edited by G. Einsele et al., pp. 617-659, Springer-Verlag, New York, 1991.

Van Wagoner, J.C., R.M. Mitchum, K.M. Campion, and V.D. Rahmanian, *Siliciclastic sequence stratigraphy in well logs, cores, and outcrops: Concepts for high-resolution correlation of time and facies*, 55 pp., Am. Assoc. Pet. Geol., Tulsa, Okla., 1990.

Wright, L.D., W.J. Wiseman, B.D. Bornhold, D.B. Prior, J.N. Suhayda, G.H. Keller, Z.-S. Yang, and Y.B. Fan, Marine dispersal and deposition of Yellow River silts by gravity-driven underflows, *Nature*, *332*, 629-632, 1988.

Wright, L.D., J. Wiseman, W.J., Z.-S. Yang, B.D. Bornhold, G.H. Keller, D.B. Prior, and J.N. Suhayda, Processes of marine dispersal and deposition of suspended silts off the modern mouth of the Huanghe (Yellow River), *Cont. Shelf Res.*, *10*, 1-40, 1990.

C. Pirmez, Exxon Production Research Co., P.O. Box 2189, Houston, TX 77252-2189. (email: Carlos.Pirmez@EXXON.sprint.com)

M.S. Steckler, Lamont-Doherty Earth Observatory of Columbia University, 61 Route 9W, Palisades, NY 10964. (email: steckler@ldeo.columbia.edu)

L.F. Pratson, Institute of Arctic and Alpine Research, University of Colorado, 1560 30th Street, Boulder, CO 80303. (email: Lincoln.Pratson@colorado.edu)

(Received June 26, 1997; revised March 31, 1998;
accepted April 30, 1998.)